

Transiting Exoplanets: Linking Observations and Theory

Inaugural dissertation
of the Faculty of Science
University of Bern

presented by

Paula Sarkis

from Bickfaya, Lebanon

Supervisor of the doctoral thesis:
Prof. Dr. Christoph Mordasini

Physics Institute of the University of Bern

Transiting Exoplanets: Linking Observations and Theory

Inaugural dissertation
of the Faculty of Science
University of Bern

presented by

Paula Sarkis

from Bickfaya, Lebanon

Supervisor of the doctoral thesis:
Prof. Dr. Christoph Mordasini
Physics Institute of the University of Bern

Accepted by the Faculty of Science.

Bern, 12. June 2020

The Dean
Prof. Dr. Zoltan Balogh

For Berna, Joseph, Mimo, and Wissam
my reason to go back home



FIGURE 1: Just another day at the office ...

Acknowledgements

Many years from now I will read this and it will bring back so many memories, some of them may be forgotten. It all started in one of my favorite camps. Little I knew this camp will shape the rest of my life. 14 years later, here I am pursuing a degree in Astronomy. There are so many people I would like to thank for their support and encouragement throughout this amazing journey. Without them, my road would have been tougher.

I would like to thank my supervisors Christoph Mordasini and Thomas Henning. Thomas, you trusted me enough to offer me a PhD position and Christoph, you accepted me as a PhD student. I know both of you took that risk, which put a lot of pressure on me to try even harder and I hope I was up to the challenge. I might joke more often than I should but I am still serious about my work. I learned a lot from both of you and enjoyed the meetings we had. Thomas, you always reminded me to look at the big picture and Christoph, you always made sure I understood the tiny details.

Christoph, thank you for being a great supervisor. While we didn't meet in person as often as we'd want, you were always available via Skype and email. It was pleasure and fun working with you. I enjoyed the many discussions we had and learned a lot about theory from you. My trips to Bern were very productive and often needed to put me back on the right track. Thank you for your advice, support, and your reassurance. Your enthusiasm for the project kept me motivated. I enjoyed learning from you more about *completo*, which made me think of *completo*.

Thomas, I am very lucky to have you unofficially as my supervisor. Thank you for your support during my dark and tough days. Your motivation and support helped me overcome the difficulties and challenges I faced during my PhD. I am very grateful for giving me the chance to observe in La Silla, a place that inspired me throughout these years. Thank you for your guidance and the confidence you had in me. Your love and enthusiasm for your job is very inspiring.

Willy Benz, thanks for agreeing to be the master of the ceremony and for taking the time to read the thesis.

Martin Kürster, thank you for being a great advisor. I am grateful for your patience in answering in detail all my questions. I enjoyed the many discussions related to stellar activity. Your office door was always open and I learned a lot from you. I am grateful I

had the chance to work with you and I was always amazed how you understood what I terribly failed to explain.

Roland, thank you for making my trips to Chile fun and memorable. I like your enthusiasm in sharing your passion about observations. I always felt I'm welcomed in your office and I enjoyed the conversations we had about life and observations. An important mission of yours is to give students the opportunity to observe. We're lucky to have you at MPIA. Thank you for showing me that working hard and having fun can be a lifestyle. I am forever grateful for giving me the chance to see the re-coating of the mirror.

I cannot talk about my PhD without mentioning La Silla. This place turned out to be more than an observatory and a working place. I even spent more days at La Silla than at Bern. I will never forget the friendly people I met there. Specifically, I want to thank all the support astronomers from whom I learned all about observations: Angela, Markus, Paul, Regis, and Sam. I also would like to thank Simona who was the first to teach me to observe and had the courage to teach me how to drive a manual car! It was a pleasure learning from all of you. A special thanks goes to the TOs Javier and Mauricio. I enjoyed my first mountain biking lessons we had together to the solar panels and to the viscacha mt. Javier, I enjoyed all the conversations we had ranging from extremely funny to extremely serious topics. Ariel, thank you for enjoying listening to my favorite band the entire night. *The band is just fantastic. That is really what I think. Oh by the way, which one's Pink?* This place was my main source of inspiration during my PhD and always reminded me why I love ~~my job~~ Astronomy. I will miss La Silla the most.

I want to thank IMPRS, specifically Christian Fendt, for giving me the opportunity to be part of the graduate program in Heidelberg.

I also would like to thank Bert, Martin Kürster, and Martin Schlecker for reading and providing comments on parts of my thesis.

A special thanks to the people I met in Bern that made my trips more enjoyable and whom I had useful scientific discussions with: Caroline, Daniel Angerhausen, Diana, Gabriel, Jonas, Harry, Lokesh, Natacha, Oliver, Oza, Remo, and Thibaut. A special thanks to Esther and Andrea who I had many inspiring conversations with.

Thanks to the carmenes crew for making me feel like I belong to a group. Especially, thanks to Diana (Lady D!), Sepideh, Martin, Trifon, and Olga. I enjoyed the discussions we had and all the birthday celebrations/surprises we planned together. It was a pleasure and fun working with you all.

I am also grateful to my collaborators: Rafael, Nestor, Andres, Gabriel, Paul, and Trifon. It was nice working in a team and thanks for your many constructive feedback.

Morgan, thank you for answering my many questions about statistics.

Special thanks to my friends at MPIA and in Heidelberg who made this chapter of my life memorable. A big thank you goes to my burokollegen! Valera, my ex-burokollegen, you always inspired me with your positive thinking. Arianna and Josha, I enjoyed the board games nights at your place, thanks! Miriam (Keppler), Martin, and Gabriele vielen dank for the fun adventures we had together and for being there during my rough times. I can't wait to see what the future holds for all of us and looking forward for more adventures together. Gabriele, grazie mille for all the care after my shoulder surgery: thanks for cooking the best(?) Italian food, for the microwave, and for carrying my arm when I was in pain. I'm very happy you finally got that job in Bologna, congrats! Faustine, I enjoyed the times we spent together and merci beaucoup for preparing cheese fondue in September! Asmita, thanks for teaching me to cook Indian food. A special shout-out to Manuel (birthday-mate!) and the cool ARI peeps, I enjoyed the many music nights we had: Michael (Michpael?), Marta (Sara left), Sara (Sara right), and Jonas. Lady D!, thank you for your support during IF, I wouldn't have succeeded without you. Best of luck in your upcoming adventures. My amigo Marcelo, mucha gracias for always preparing the best pisco sour. Theo, thanks for giving me the chance to try paragliding for free, twice! Michpael, my music and concert buddy, thank you for all the concerts and trips we went to. Looking forward for many more. Based on experimental evidence, thank you for improving my alcohol tolerance. Bert and Chiara, I also enjoyed the concerts and the trips we went to together. Looking forward for more with Giulia. Bert and Martin, I will never forget my favorite train ride! Christian, thanks for the interesting music conversations and for your hospitality. Tracy, thanks for the company when needed.

I am also grateful to my friends back home that never stopped supporting me and made me look forward to my visits. You made me feel that dreaming big is normal.

Finally, my biggest thanks goes to my mom, dad, sister, and brother. Thank you for your kindness, encouragement, and sacrifices. Your support in pursuing my dreams is invaluable. Without you, I would not be the person I am today. Merci ktir! B7ebkon ktir, ya 2a2wa 3alam bel 3alam!

Here's to the future for the dreams of youth! – I Want It All – Queen

Contents

1	Introduction	1
1.1	The Hunt for Exoplanets	2
1.1.1	Direct Imaging	2
1.1.2	Gravitational Microlensing	3
1.1.3	The Transit Method	3
	Basic Parameters Inferred from the Transit Light Curve	5
1.1.4	The Radial Velocity Method	7
	High Precision Radial Velocity	8
	Radial Velocity Variability Due to Stellar Activity	11
	Activity Indicators	13
1.2	General Overview of Exoplanets	14
1.3	Thesis Overview	16
2	Exoplanet Surveys	19
2.1	The CARMENES Survey	19
2.1.1	The Spectrograph	19
2.1.2	Survey Highlights	20
2.2	The HATSouth Survey	22
2.2.1	FEROS	23
2.2.2	Survey Highlights	24
3	Extrasolar Giant Planets	29
3.1	Statistical Properties of Giant Planets Observations	30
3.1.1	Hot Jupiters	30
3.1.2	Warm/Cold Jupiters	31

3.1.3	Comparison Between Hot Jupiters and Long-Period Giant Planets	31
	Eccentricity Distribution	31
	Radius Distribution	33
3.2	Interior Models of Irradiated Giant Planets	34
3.2.1	Basic Structure Equations	34
3.2.2	Microphysics	36
	Equation of State	36
	Opacity	37
3.2.3	Atmospheric Boundary Conditions	38
3.2.4	Thermal Evolution of Giant Planets	40
3.3	The Mass-Radius Diagram: Expectations vs Reality	43
3.4	What Is Really the Difference Between Hot and Cold Jupiters?	46
3.5	Radius Anomaly of Hot Jupiters	47
3.6	Interior Structure of Hot Jupiters	48
4	Characterization of K2-18 with CARMENES	49
4.1	Results	50
4.2	Overview of the 9-day Signal	69
	4.2.1 New HARPS data and Re-analysis of HARPS and CARMENES data (Cloutier et al. 2019)	69
	4.2.2 Summary	71
4.3	Conclusion	72
5	Discovery and Characterization of HATS-59b,c	73
6	Linking Observations and Theory: The Radius Anomaly of Hot Jupiters	87
6.1	Method	87
6.2	Bloating Model	89
6.3	Assumptions	90
	6.3.1 Steady State Assumption	90
	6.3.2 Distribution of Heavy Elements	90
6.4	Updates to the Interior Structure Model	92
	6.4.1 The Effect of the Atmospheric Boundary Condition on the Radius	92
	6.4.2 Details of the Coupling	94

6.5	Conclusion of the Publication	96
6.6	Comparison to Thorngren Results	120
6.7	Disk Migration Within the Context of Planet Population Synthesis	121
6.7.1	Coupling Bloating Model to Planet Formation and Evolution Models	122
6.7.2	Synthetic Planet Populations	122
6.7.3	Results	123
	Stable and Unstable Configurations	123
	Rate of Hot Jupiters and the Mass-Radius Diagram	123
6.8	Summary	126
7	Summary and Outlook	127
	Bibliography	132

Chapter 1

Introduction

Is there anybody out there?

We live in exceptionally remarkable times where we can finally answer centuries-old long-standing philosophical questions. We are the first generation in the history of humankind that knows countless alien worlds exist.

The journey in finding these strange new worlds started in our own backyard, inspired by what we know about the closest planetary system, our Solar System. It is the most extensively studied planetary system and provides the basis for understanding the characteristics of these alien worlds and the physical processes that formed them. A thorough knowledge of the planets and dust in the Solar System provided clues on the origin of planetary systems in general. Even studying the composition and motion of the dust (e.g. [Hicks et al. 1972, 1974](#); [May 2007](#)) helped to shed light on the formation of our planetary systems and are the foundations for understanding the characteristics of planetary systems beyond the Solar System.

The second half of the twentieth century saw a revolution in astrophysics in general and in planetary astronomy specifically. The discovery of the first exoplanet is largely thanks to the improvement in the technology and in the Doppler shift technique. Fast-forwarding two decades, the search for extrasolar planets has grown extraordinarily rapidly with thousands of exoplanets discovered. The diversity of their properties sparked tremendous improvements in understanding how such planets form. The hunt for exoplanets will continue with many dedicated telescopes, instruments, and surveys.

1.1 The Hunt for Exoplanets

To date, thousands of exoplanets have been discovered using several methods that can be divided into direct and indirect detection methods. The latter is the main topic of this thesis and relies on inferring the existence of the planet based on effects in the data induced by the planet on the host star. The most important and successful methods are the radial velocity method, the transit technique, direct imaging, and microlensing. Each of the mechanisms have weaknesses and strengths that are important to address to have an unbiased and comprehensive overview of the demography of exoplanets. The methods are described below and special importance is given to the transit and radial velocity methods as these are the methods used in this thesis and when combined together they provide an important characteristics of the planet, namely its bulk density.

1.1.1 Direct Imaging

Direct imaging relies on observing the light coming directly from the planet, either emitted in the infrared or reflected in the visible. This method is technically very challenging since the planets are several orders of magnitude fainter than the host star and often the angular separation between the planet and the star is small. To overcome this, a combination of large telescopes, adaptive optics, and sophisticated image processing tools are needed to extract the planetary signal.

Despite the many challenges in detecting planets with this method, the first detection was by [Chauvin et al. \(2004\)](#) and since several have been discovered (e.g. [Keppler et al. 2018](#)), even multiple planets are also possible to detect ([Marois et al. 2008](#)). Direct imaging is sensitive to detecting Jupiter-like planets in wide orbits around young stars. Planets around young stars have relatively higher temperatures and are therefore self-luminous at infrared wavelengths, leading to higher thermal emission. Exoplanets detected using the direct imaging technique are important since they complement other detection techniques, which are sensitive to short-orbital period planets. The reader is referred to [Pueyo \(2018\)](#) for a review on the direct imaging technique.

1.1.2 Gravitational Microlensing

Microlensing is probably the most indirect and difficult method of detecting exoplanets (for a recent review see [Batista 2018](#)). With this technique, we neither detect the light of the planet nor the light of the host star. Gravitational microlensing occurs when the star acts like a lens, i.e. magnifying significantly the light of a distant background star. If the lensing star, i.e. the foreground star, hosts a planet, then the planet's gravity can also increase the brightness of the background star. Such events can last between hours and weeks.

The downside of the gravitational microlensing technique is that the microlensing events are rare and happen only once. Follow-up observations to refine the planetary parameters are therefore not possible. The only planetary parameters determined using this technique are the projected angular separation and the ratio of the planetary mass to the host star mass. This method is very effective, compared to other methods, in detecting low-mass planets at intermediate distances from the host star, typically beyond the snowline where giant planets are believed to be formed. For example, the first exoplanet detected by a microlensing event is 1.5 times more massive than Jupiter and has an orbital distance of ~ 3 AU ([Bond et al. 2004](#)). The first major discoveries however implied that cool Neptune-like planets are common ([Beaulieu et al. 2006](#); [Gould et al. 2006](#)) and may be even more common than gas giant planets. The Wide Field InfraRed Space Telescope (*WFIRST*; [Spergel et al. 2015](#)) is the first space-based mission dedicated to search for microlensing events and is scheduled to launch in mid-2020s. The mission will increase the number of low-mass planets at large orbital separations and hence, combined with planets detected with other techniques, will provide a much more complete overview of the demography of exoplanets.

1.1.3 The Transit Method

The transit technique is by far the most successful method in finding exoplanets, with thousands of transiting planets discovered to date. The transit method is one of the techniques used in this thesis and therefore a short overview is presented below. For a complete review the reader is referred to [Haswell \(2010\)](#), [Winn \(2010\)](#), and [Deeg & Alonso \(2018\)](#). The method relies on detecting a dip in the brightness of the star, which could be attributed to the presence of a planet passing in front of the host star. The first transiting

exoplanet was discovered around the Sun-like bright star HD209458 b (Henry et al. 2000; Charbonneau et al. 2000). The host star was previously known to host a planet via radial velocity measurements (Mazeh et al. 2000). With a 10% chance of the planet to transit its host star, the two teams carried out photometric observations to search for transits and confirm the planetary nature of the signal.

The first transiting planet with no prior knowledge of its existence, which was subsequently confirmed with radial velocity observations, was discovered three years later (Konacki et al. 2003), despite many efforts in searching for transiting exoplanets. For a thorough historical overview of the discovery of the first transiting exoplanets, first ground-based surveys, and lessons learned check Dunham (2018). The challenge in the transiting technique lies in the low probability for a transit to be observed, which is

$$P_{\text{transit}} \approx \frac{R_*}{a} \quad (1.1)$$

where R_* is the stellar radius and a is the semimajor axis (Winn 2010). Planets orbiting large stars at short orbital periods are the most probable to transit. For example, the probability for any of the planets in the Solar System to transit is less than 1%, except for Mercury which is $\sim 1.2\%$. Therefore, it is necessary to continuously monitor a large number of stars in order to catch a planetary transit.

For these reasons, many ground-based surveys rely on fully-automated and robotic telescopes to search for transiting exoplanets, such as TrES (Alonso et al. 2004), HAT-Net (Bakos et al. 2004), SuperWASP (Pollacco et al. 2006), HATSouth (see also Section 2.2 Bakos et al. 2013), and NGTS (Wheatley et al. 2018). This technique is efficient since thousands of stars are simultaneously observed at high cadence and homogeneously analyzed. Due to the limited photometric precision achievable from the ground, most transiting ground-based surveys detected close-in giant planets (e.g. O'Donovan et al. 2006; Collier Cameron et al. 2007; Bakos et al. 2007; Penev et al. 2013; Bayliss et al. 2018). Space-based missions like *CoRoT* (Baglin et al. 2006) but most importantly *Kepler* (Borucki et al. 2010) can achieve better photometric precision and thereby extended the discoveries to terrestrial rocky planets (e.g. Léger et al. 2009; Batalha et al. 2011) and multiple planetary systems (e.g. Holman et al. 2010; Lissauer et al. 2011a). Even the recently launched telescope *TESS* (Ricker et al. 2015), which began science operations in July 2018, already

started contributing to the discoveries of terrestrial planets (e.g. [Kostov et al. 2019](#)) with many more awaiting to be discovered. *TESS* along with the recently launched satellite CHaracterising ExOPlanet Satellite (*CHEOPS*; [Broeg et al. 2013](#); [Benz et al. 2018](#)) will yield accurate radii for many exoplanets ranging from Jupiter-like down to Earth-like planets. *CHEOPS* was launched in December 2019 and successfully completed three months of commissioning, exceeding expectations for its performance. Recently, the satellite observed its first exoplanet¹ and at the time of writing is ready for science.

Basic Parameters Inferred from the Transit Light Curve

In the following section we give important quantities that are often derived from the transit light curve. All the following equations are approximations and valid for planets on circular orbits and neglecting the effect of limb darkening. For the complete set of equations check [Haswell \(2010\)](#), [Winn \(2010\)](#), and [Perryman \(2011\)](#).

When the planet transits the host star the resulting dip in the flux F , also known as the transit depth δ , is

$$\delta = \frac{\Delta F}{F} \approx \left(\frac{R_p}{R_*}\right)^2 \quad (1.2)$$

where R_p and R_* are the planet and stellar radius, respectively. Determining the planet radius requires estimating the stellar radius precisely, which is often estimated using stellar evolution models. The transit technique is sensitive to detecting planets with large radii for a given stellar radius.

Another important parameter that can be estimated using the transit technique is the semimajor axis, which is related to the orbital period P , planet mass M_p and stellar mass M_* using Kepler's third law

¹<https://sci.esa.int/web/cheops/-/cheops-observes-its-first-exoplanets-and-is-ready-for-science>

$$\begin{aligned}
 a^3 &= \frac{G(M_* + M_p)}{4\pi^2} P^2 \\
 a^3 &\approx \frac{GM_*}{4\pi^2} P^2
 \end{aligned}
 \tag{1.3}$$

in the limit of $M_* \gg M_p$.

The transit duration T_{dur} is the time the planet spends transiting a star and can be expressed as (Haswell 2010):

$$T_{\text{dur}} = \frac{P}{\pi} \sin^{-1} \left(\frac{R_*}{a} \right) \tag{1.4}$$

assuming the planet crosses from one end of the diameter of the star to the other, i.e. impact parameter $b = 0$ and assuming an orbital inclination $i = 90^\circ$. A transit of Earth will therefore take 13 hours and for Jupiter it would take 25 hours. The transiting exoplanet with the longest known transit duration is EPIC248847494 b with a duration of 54 hours at 4.5 AU separation (Giles et al. 2018). However, the duration for most of the discovered transiting exoplanets is few hours. The transit duration can also be rewritten in terms of the stellar parameters (Perryman 2011)

$$T_{\text{dur}} \approx 13 \left(\frac{M_*}{M_\odot} \right)^{-1/2} \left(\frac{a}{1\text{AU}} \right)^{1/2} \left(\frac{R_*}{R_\odot} \right) \text{ hours.} \tag{1.5}$$

This is useful as one can compare the observed transit duration to the expected one. If the transit duration is significantly larger than the expected one, then the transit might be due to a low-mass star and not due to a planet. However, there have been cases of eccentric planets on short orbital periods such as HATS-19 (Bhatti et al. 2016), so this rule should be applied to preliminary analysis only.

Finally, two physical quantities can be inferred from the transit light curve, i.e. directly from observable quantities and without relying on theoretical stellar and/or planetary models. The first one is the stellar density (Sozzetti et al. 2007)

$$\frac{M_*}{R_*^3} = \frac{4\pi^2}{GP^2} \left(\frac{a}{R_*}\right)^3 - \left(\frac{M_p}{R_*^3}\right) \quad (1.6)$$

where G is the gravitational constant. The term on the left side is essentially the stellar density ρ_* . The first term on the right side is entirely computed using measurable quantities derived from the transit light curve, where a/R_* is expressed as (Winn 2010)

$$\frac{R_*}{a} \approx \frac{\pi}{\delta^{1/4}} \frac{\sqrt{T_{\text{dur}}\tau}}{P} \quad (1.7)$$

and τ is the ingress duration defined as the time it takes the planet to fully cover the star after the first contact. This quantity only depends on the geometry of the transit and is measured from the shape of the transit light curve. The second term on the right side in Equation (1.6) is several orders of magnitude smaller and thus can be ignored.

The second quantity is the planetary surface gravity g_p , which can be derived using observable quantities from transit observations combined with the semi-amplitude K (Southworth et al. 2007) derived from radial velocity measurements, see Section 1.1.4 and Equation (1.10)

$$g_p = \frac{2\pi K}{P \sin i} \left(\frac{1}{\delta}\right)^2 \left(\frac{a}{R_*}\right)^2. \quad (1.8)$$

1.1.4 The Radial Velocity Method

The first exoplanet discovered around a solar-type star, Peg 51 b (Mayor & Queloz 1995), was detected using the radial velocity (RV) method. This technique is one of the most successful techniques and has contributed to the discovery of several hundreds of planets orbiting nearby stars. It can also be credited to kick off the ongoing search and research of the exoplanet field. The method plays also an important role in transit searches as it is not only used to confirm the planetary nature of the transit signal but also to estimate the planet mass, which is needed to calculate the bulk density of the exoplanet. A short

overview is provided below since it is one of the techniques used in this thesis and for a complete review the reader is referred to [Wright \(2018\)](#).

The RV technique is based on detecting a periodic variation in the radial velocity of the host star due to dynamical interaction with a planetary companion. Due to the relative movement of the planet, the star moves away or towards the observer. The radial velocity is measured using the Doppler effect, which causes a shift in the wavelength of the spectral lines and is given by

$$\frac{\Delta\lambda}{\lambda_{\text{rest}}} = \frac{v_r}{c} \quad (1.9)$$

where $\Delta\lambda = \lambda_{\text{obs}} - \lambda_{\text{rest}}$ is the difference between the observed wavelength λ_{obs} and the wavelength of the same line if the star is at rest with respect to the observer λ_{rest} , v_r is the radial velocity, and c is the speed of light. Observing the star at several epochs allows us to detect variations in the radial velocity, which are induced by the pull of the planet. The planet mass M_p can then be derived using the semi-amplitude K , period P , eccentricity e , and the stellar mass M_* , using the following relation

$$K [\text{m s}^{-1}] = \frac{2\pi G}{\sqrt{1-e^2}} \left(\frac{P}{\text{yr}}\right)^{-1/3} \left(\frac{M_p \sin i}{M_J}\right) \left(\frac{M_*}{M_\odot}\right)^{-2/3} \quad (1.10)$$

For example, Jupiter induces a reflex motion of 12.5 m s^{-1} , while Earth only 0.09 m s^{-1} . It is evident that planets with high masses and short periods orbiting less massive stars lead to higher radial velocity semi-amplitudes, requiring thus less instrumental precision.

High Precision Radial Velocity

In order to detect low-mass planets, precise and stable radial velocity instruments are needed. The movement of the spectral lines correspond to a shift on the CCD detector of a fraction of a pixel. For example, a giant planet with a semi-amplitude on the order of tens of m s^{-1} causes the spectral lines to shift 10^{-2} pixel, which for a typical CCD pixel size of $15 \mu\text{m}$ corresponds to 150 nm . To achieve a precision better than 1 m s^{-1} however, one must be able to measure the motion of the stellar lines on the order of 10^{-3} pixel, i.e.

a fraction of a nanometer. This requires exquisite state-of-the-art spectrographs capable of achieving high precision radial velocity along with long term stability.

There are two main key developments that led to achieve long term high precision radial velocity. The first lies in the ability to obtain a spectrum with as many resolved lines as possible, i.e. a high-resolution spectrum. This was achieved by the active development of high resolution spectrographs dedicated to the search for exoplanets, such as HARPS (Pepe et al. 2000) installed at the 3.6 m telescope at La Silla, HARPS-N (Cosentino et al. 2012) mounted on the 3.6 m TNG telescope at La Palma, HIRES (Vogt et al. 1994) operating on the 10 m Keck Telescope on Mauna Kea, and FEROS (Kaufer & Pasquini 1998) on the MPG 2.2 m telescope in La Silla. Note that for the stability of HARPS and HARPS-N, it is crucial that there are no moving parts in the instrument, and the pressure and temperature are stabilized.

The second major development is the ability to precisely track long term instrumental drifts, which ensures the long term stability of the instrument. This was achieved by observing a calibration lamp, typically an iodine absorption cell (Butler et al. 1996), or through simultaneous observations of a ThAr emission lamp. Nowadays, often Fabry-Pérot etalons or laser frequency combs are employed. Fischer et al. (2016) provides an overview in the developments of high precision wavelength calibrators.

Many algorithms are used to compute the radial velocity of the star. One of the algorithms is the cross-correlation technique, which is applied on the observed spectrum to measure the wavelength shift of each line. This can be done either using a binary mask or a high signal-to-noise spectrum of the same target. The output of this procedure is a cross-correlation function (CCF) with a minimum close to the radial velocity of the star. To compute the radial velocity, a Gaussian function is fitted to the CCF with the mean taken to be the RV of the star. The more lines available in a spectrum, the more precise the CCF and thus the RVs are. This highlights the need not only for high-resolution instruments but also for broad wavelength coverage. The cross-correlation technique is used in many data reduction pipelines, such as CERES (Brahm et al. 2017), which was developed to automatically reduce, extract, and analyze spectra acquired with CORALIE, FEROS, HARPS, ... We use this technique to compute the RVs presented in Chapter 5 by cross-correlating the observed spectrum with a binary mask.

Another algorithm is based on least-squares fitting where the template used is the co-added spectra of the observed target (Anglada-Escudé & Butler 2012). This technique

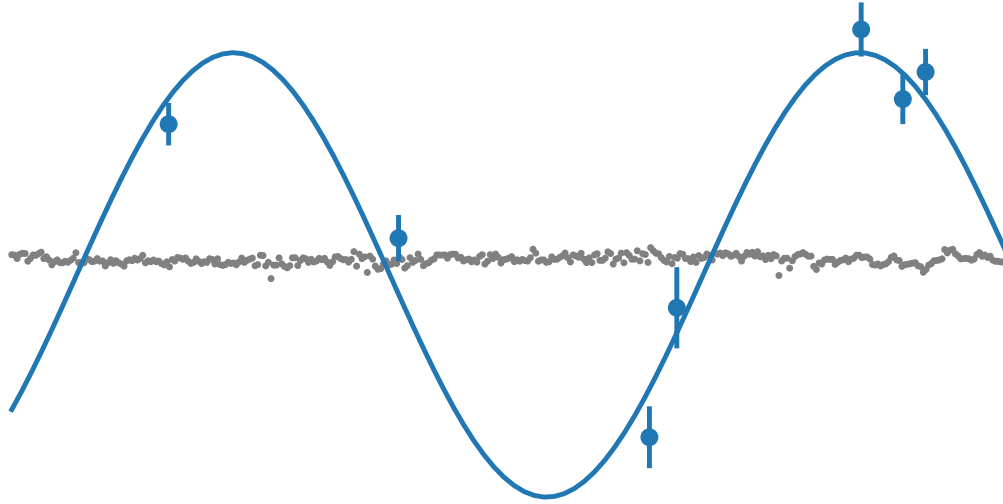


FIGURE 1.1: Outstanding and novel technological developments allowed the exploration of whole new worlds. Time series RV variations of WASP-1 b (115 m s^{-1} ; blue; Collier Cameron et al. 2007), compared on the same scale to the RV variations of HD 215152, which is known to host four super-Earths all with semi-amplitudes $< 1 \text{ m s}^{-1}$ (gray; Delisle et al. 2018). The vertical scale for both data sets is the same but the horizontal scale is not. WASP-1 b was detected with 7 RV measurements spanning just four days, while 373 precise RV measurements spanning 13 years were needed to extract the four planetary signals around HD 215152. This highlights the remarkable improvement in the precision and the challenges in detecting low-mass planets.

provides a significant increase in accuracy for M dwarfs but for G and K stars the difference is negligible. In Chapter 4 we present a planet discovery around an M dwarf and thus this approach is used.

With the current development of state-of-the-art instruments, current spectrographs achieve an RV precision of $0.5 - 1 \text{ m s}^{-1}$, which enabled the discovery of several low-mass

planets. To date, there are less than 20 planets detected with a signal less than 1 m s^{-1} (e.g. [Pepe et al. 2011](#); [Delisle et al. 2018](#); [Udry et al. 2019](#)) with the lowest one as low as 0.35 m s^{-1} ([Feng et al. 2017](#)). Figure 1.1 highlights the progress achieved in pushing the RV sensitivity down to 1 m s^{-1} and the challenges in detecting low-mass planets. With a period of 2.5 days and an amplitude of 115 m s^{-1} , 7 RV measurements spanning 4 days were enough to detect the signal of WASP-1 b ([Collier Cameron et al. 2007](#)). Improvements in the RV precision paved the way towards the detection of low-mass planets. [Delisle et al. \(2018\)](#) presented the discovery of four super-Earths orbiting HD 215152 with periods roughly 6, 7, 11, and 25 days and all with semi-amplitudes less than 1 m s^{-1} . The discovery is based on 373 RV measurements spanning 13 years, highlighting the improvement and the challenges in detecting such planetary systems. Additionally, long term stability is vital for the detection of low-mass planets. Long-period planets will likely be detected by radial velocity legacy surveys such as the CORALIE survey ([Queloz et al. 2000](#)), which has been running for 20 years, the HARPS survey ([Pepe et al. 2000](#); [Mayor et al. 2003](#)), which has contributed in the detection of more than 100 exoplanets, and the Anglo-Australian Planet Search (AAPS; [Tinney et al. 2001](#)) with a total time baseline of 18 years. The new state-of-the-art spectrograph Echelle SPectrograph for Rocky Exoplanets and Stable Spectroscopic Observations (ESPRESSO; [Pepe et al. 2010](#)) started operations in March 2018 and is designed to reach 10 cm s^{-1} precision, which will enable the detection of Earth-like planets.

Radial Velocity Variability Due to Stellar Activity

Despite this outstanding development in achieving high precision RVs coupled with long term stability, it is still challenging to detect low-amplitude signals. One limiting factor is that the measurements are so precise that the RVs are dominated by the intrinsic stellar variability. There are several sources for stellar variability each with different timescales, ranging from stellar oscillations with short times scales (5 – 15 min) to magnetic cycles that last years to decades for sun-like stars.

The largest source of variability is the presence of stellar active regions, such as spots and plages. Starspots appear darker because they have temperatures lower than the stellar surface. As the star rotates, light coming from the approaching hemisphere is blueshifted and light from the receding hemisphere is redshifted. If the surface has no spots, then these Doppler shifts cancel each other out. When a dark spots appears on the

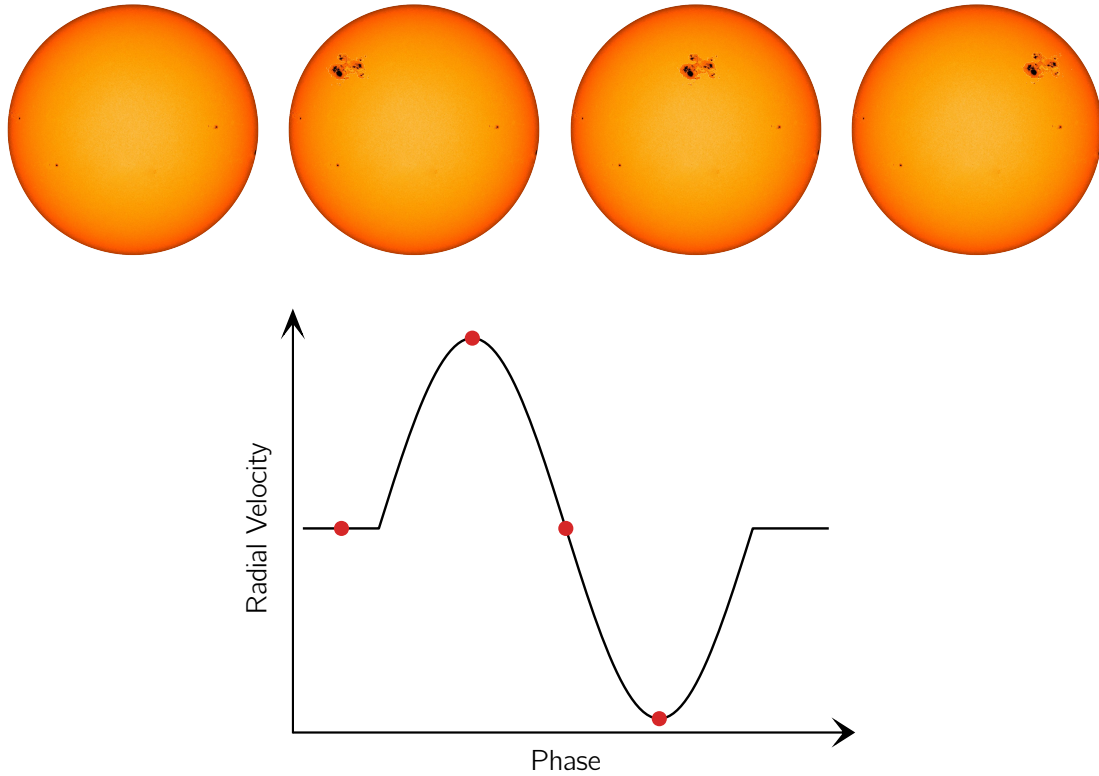


FIGURE 1.2: Diagram illustrating the RV variation induced by starspots as the star rotates. *The original sun image credit: SDO/NASA – For illustration purposes edited by: EmTee*

blueshifted limb, part of the flux of the star is blocked and the star appears to be redshifted. As the star continues to rotate, the spot is now visible on the redshifted hemisphere and the star appears to be blueshifted. Starspots thus induce RV variation as they cross the stellar surface disk, which could mimic the presence of a planet. This is illustrated in Figure 1.2.

Activity Indicators

Luckily there are diagnostic tools to distinguish whether the observed RV variations are due to a planetary signal or due to activity. Any correlation observed between the radial velocities and the activity indicators will most likely suggest that the RV variations are due to stellar spots, rather than due to a planet. These tools are used frequently to study the origin of the RV variations and to ensure that the RV variations are not caused by stellar activity.

The most common lines that are sensitive to activity are the Ca II H&K lines and the H α Balmer line in the optical and the Ca II infrared triplet (IRT) lines in the infrared. For example, [Hatzes \(2016\)](#) showed that the RV variations that were attributed to the planet Gl 581 d show a correlation with the H α index and thus most likely the signal is not due to a planet.

Another useful diagnostic tool is that a planet signal is wavelength independent, whereas the RV variations due to a spot have a smaller amplitude in the infrared. Comparing thus the RV amplitude in the visible (VIS) and the near-infrared (NIR) will give clues on the origin of the signal. This approach has been used to confirm signals due to planets (e.g. [Trifonov et al. 2015](#)) and due to stellar activity ([Prato et al. 2008](#); [Mahmud et al. 2011](#); [Crockett et al. 2012](#); [Carleo et al. 2018](#)). This gave rise to the importance of multi-wavelength RV observations in the search for exoplanets and led to the development of a new generation of spectrographs that can probe simultaneously the optical and near-infrared. The first spectrograph especially designed for multi-wavelength RV observations is CARMENES (see also Section 2.1; [Quirrenbach et al. 2014](#)), which started science operations in January 2016. Other instrument is GIARPS (GIANO-B in the NIR and HARPS-N in the VIS; [Claudi et al. 2017](#)) and the capability to observe simultaneously with NIRPS in the NIR ([Conod et al. 2016](#)) and HARPS in the VIS.

Leveraging of the broad wavelength coverage of CARMENES (0.52 – 1.71 μm). [Zechmeister et al. \(2018\)](#) recently presented a new activity diagnostic index, the chromatic index. It is motivated by the fact that the RV variations due to stellar spots typically decrease at redder wavelengths ([Reiners et al. 2010](#)). Thus, the chromatic index is a measure of the change of the RVs as a function of wavelength, where the RVs are computed for each echelle order.

Another novel approach to mitigate stellar activity was presented by [Dumusque \(2018\)](#).

It is based on computing RVs using individual spectral lines that are not sensitive to stellar activity. The method relies on high-resolution spectra of bright targets. First results are very promising as it was demonstrated that by measuring the RVs of each spectral line one can boost or mitigate the RV signal induced by stellar activity.

1.2 General Overview of Exoplanets

Each of the aforementioned detection methods has its own advantages and disadvantages. Each method probes a different parameter space, such as planet mass, radius, and orbital separation, and thus only provides a part of the bigger picture. It is important to study how they all complement each other and provide us with a complete overview of planet architecture. The contributions of each method are shown in the upper panel of Figure 1.3. The data is taken from the NASA Exoplanet Archive². The transit technique is by far the most successful method with more than 3000 contributions, largely due to *Kepler*. Both the transiting and the RV method are the most successful techniques detecting the majority of the planets.

The lower panel of Figure 1.3 shows the planet mass versus the orbital period color coded by the different detection methods. The plot clearly shows the biases inherent in each detection method. The transit method is biased towards detecting short-period planets, whereas the others methods are more sensitive towards longer-period planets. Note that the RV method is also biased toward short-period planets but these planets are not so frequent. While both microlensing and direct imaging are only sensitive towards long-period planets, the former is sensitive to lower mass planets. This highlights the importance of combining the different methods to have a complete overview of the demography of exoplanets.

The mass–period diagram highlights three different clusters. The low-mass planets (lower cluster) made up from rocky cores and small fraction of their mass is made up from hydrogen and helium. The giant planets (the two upper clusters) with masses roughly larger than $0.2 M_J$ can be further divided into three types: (i) the short-period planets known as hot Jupiters, (ii) the long period planets referred to as cold Jupiters, and (iii) the intermediate valley of planets between hot Jupiters and cold Jupiters, the warm Jupiters.

²<https://exoplanetarchive.ipac.caltech.edu/>

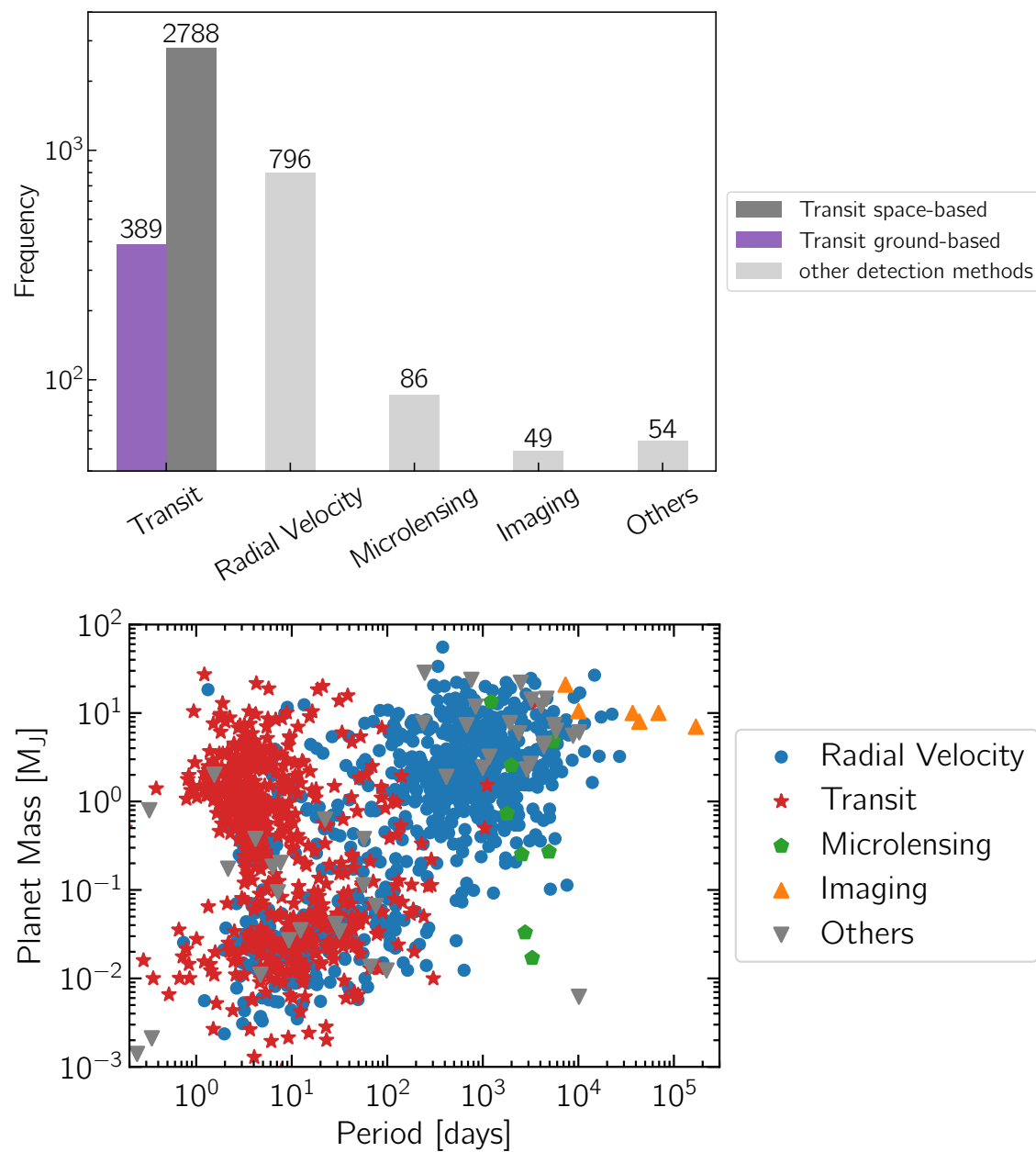


FIGURE 1.3: (*Upper*): The number of planets discovered by each detection method. (*Lower*): The planet mass versus the orbital period for all the planets detected to date with the different detection methods. The transiting and RV methods contributed to the discovery of most exoplanets.

Giant planets consist mostly of hydrogen and helium with a small fraction of their mass made up of heavy elements. Gas giant planets are one of the main focus of this thesis and in the Chapter 3 we provide a more detailed comparison between the different types of giant planets.

1.3 Thesis Overview

The focus of the thesis is not only to detect and characterize transiting exoplanets but also to link the observations to structure models, focused specifically on hot Jupiters. This provides further insights in their interiors and allows us to put constraints on the evolution of close-in giant planets. The first part of the thesis presents the observational work related to characterizing transiting exoplanets, while the second part is dedicated to the theoretical aspect of the thesis. Chapter 2 and Chapter 3 provide a general overview, while Chapters 4–6 present the publications.

The rest of the thesis is organized as follows:

In the context of discovering and characterizing new planetary systems, Chapter 2 presents two surveys that the author contributed to: CARMENES and HATSouth. The former uses the radial velocity method and the latter uses the transit method.

Chapter 3 provides an overview of extrasolar giant planets and covers both observations and theory. We also introduce the planet evolution model that is used later to link the observed properties of giant planets to interior structure models.

Chapter 4 presents the characterization of the system K2-18, within the CARMENES consortium. This system is suspected to have two low-mass planets around an active M dwarf. While the presence of the outer transiting planet is unquestionable, the existence of the inner non-transiting planet has been controversial and we provide an overview of that.

Chapter 5 reports the discovery and characterization of HATS-59, the first multi-planetary systems discovered with the HATSouth collaboration. The inner planet is a hot Jupiter on an eccentric orbit and the outer cold giant is a massive companion on a circular orbit.

Chapter 6 is devoted to the theoretical part of the thesis. We present our contribution towards understanding the radius anomaly of hot Jupiters and show evidence of three mechanisms that can explain their inflated radii.

Finally, in Chapter 7, we discuss and summarize the main findings.

My research, my job, is to find planets orbiting other stars
And I want to emphasize that there is no planet B for us
There's no substitute for Earth
Debra Fischer

Chapter 2

Exoplanet Surveys

There are many ongoing ground-based radial velocity and transiting surveys dedicated to discover and characterize extrasolar planets. This section highlights an RV survey, CARMENES, and a transiting survey, HATSouth, where the planets presented in this thesis in Chapter 4 and Chapter 5 are based on, respectively.

2.1 The CARMENES Survey

CARMENES (Calar Alto high-Resolution search for M dwarfs with Exoearths with Near-infrared and optical Echelle Spectrographs) is both an instrument and a survey ([Quirrenbach et al. 2014](#)).

2.1.1 The Spectrograph

The instrument is mounted on the 3.5 m telescope at Calar Alto Observatory in Spain and consists of two separate state-of-the-art echelle spectrographs, one operating in the visual (550 – 960 nm) and the other one in the near-infrared (960 – 1700 nm). The VIS spectrograph has a spectral resolution of $R = 94600$, while the NIR has a resolution of $R = 80400$ ([Quirrenbach et al. 2016](#)). The instrument was built following the scientific goal to detect low-mass planets in the habitable zone of M dwarfs. To mitigate stellar activity, simultaneous multi-wavelength RV observations are required, and thus the design of two spectrographs each operating at a different wavelength. The instrument belongs to the few ultra-stable high-resolution spectrographs developed specifically to achieve high

precision radial velocity on the order of 1 m s^{-1} . [Trifonov et al. \(2018\)](#) demonstrated that the precision of the VIS channel is similar to HARPS.

Both spectrographs are mechanically and thermally stabilized in order to achieve the 1 m s^{-1} precision. The main difference between both channels is the cooling system. The thermal stability of the instrument is crucial since changes in the temperature of mK translate into instrumental drifts on the order of few m s^{-1} . The VIS spectrograph is operated near room temperature with a temperature stability of $\pm 0.01 \text{ K}$ within 24 hours ([Quirrenbach et al. 2014](#)). The NIR spectrograph is actively stabilized at 140 K by an external heat exchanger that is fed by liquid nitrogen. The stability is within $\pm 0.01 \text{ K}$ over 24 hours.

Even with thermally stable instruments, an accurate wavelength calibration is essential to compute extremely precise RVs and to track any instrumental drifts. With CARMENES this is achieved by using hollow-cathode emission line lamps and a Fabry-Pérot (FP) system. To cover the entire broad wavelength range of both channels, several emission lamps are used: Th-Ne, U-Ar, and U-Ne lamps ([Quirrenbach et al. 2014](#)). These lamps are not used to produce the wavelength solution of the science frames but only to track the long-term stability of the instrument. The wavelength solution is obtained using the FP ([Bauer et al. 2015](#)), which is also used to monitor the short-term and long-term instrumental drifts.

2.1.2 Survey Highlights

CARMENES started science operations on January 2016 and the main science goal is to conduct a survey of ~ 300 M dwarfs to detect low-mass planets in the habitable zone (HZ; [Quirrenbach et al. 2014](#)). M dwarfs are ideal targets to search for planets in the HZ because they are numerous, at least 70% of the stars in the Milky Way are M dwarfs. More importantly, the semi-amplitude of an Earth-like planet around an M dwarf is larger than that around a Sun-like star, making it easier to find low-mass planets around M dwarfs. For example, an Earth-like planet around a Solar-like star induces an RV amplitude of 10 cm s^{-1} , which is still not possible to achieve with most of the spectrographs, compared to 1 m s^{-1} in the HZ of a mid-M dwarf. Finally, since M dwarfs are cooler, the habitable zone of these stars is at shorter orbital periods compared to Sun-like stars. For all these reasons, M dwarfs are well suited to search for Earth-like planets in the habitable zone.

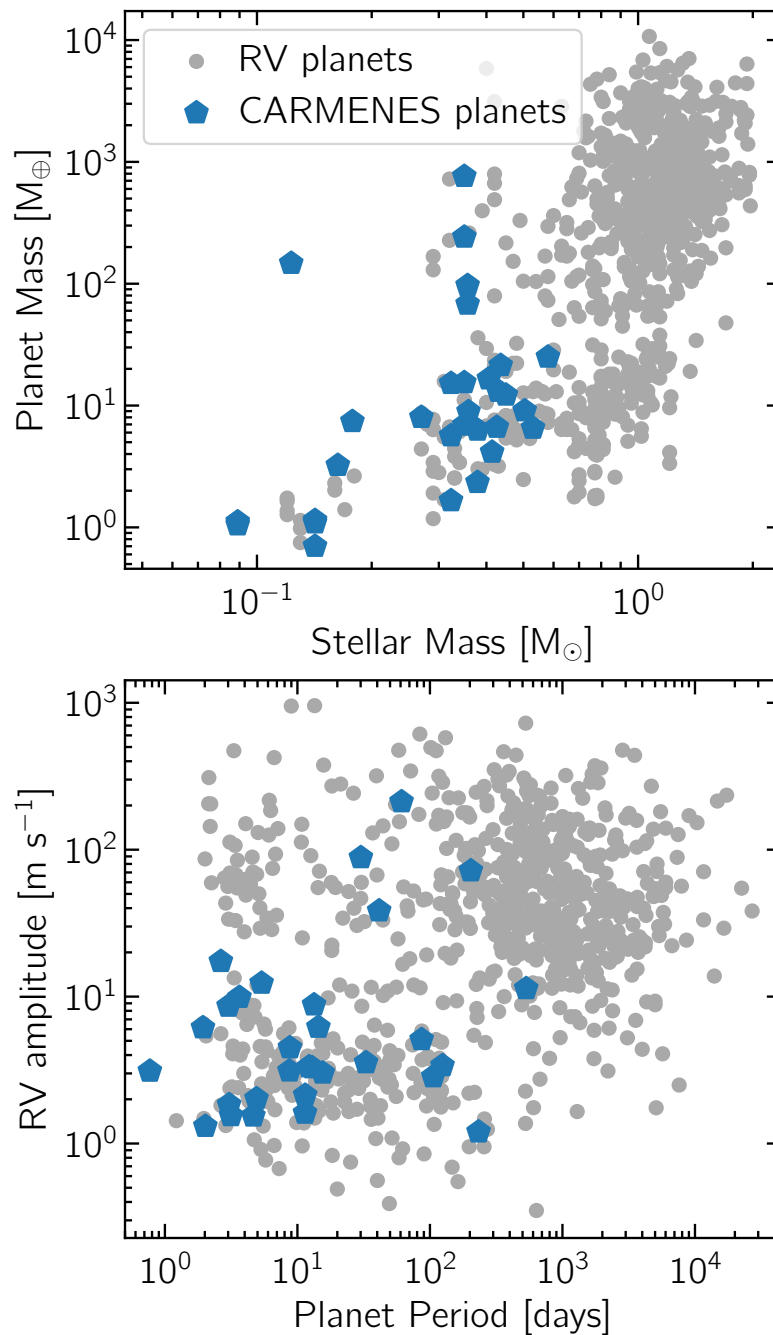


FIGURE 2.1: Diagram highlighting the properties of the exoplanets detected using CARMENES (blue) in comparison to planets detected with the radial velocity method by other surveys (gray). (*upper*) Planet mass versus stellar mass diagram and (*lower*) RV amplitude as a function of orbital period.

The CARMENES catalog consists of 324 M dwarfs with spectral types ranging from early-types (M0) to later types ($> M6$). With more than four years of operations, CARMENES has so far discovered and characterized 30 extrasolar planets out of which 6 have semi-amplitude less than 2 m s^{-1} . The properties of the CARMENES planets are highlighted in Figure 2.1 in a stellar mass–planet mass diagram (upper panel) and a planet period–RV amplitude diagram (lower panel). The first planet detected is a Neptune-like planet in the habitable zone of a nearby bright M0.0 V dwarf (Reiners et al. 2018).

One of the highlights is the nearby multi-planetary system YZ Ceti consisting of three Earth-like planets with minimum masses 0.7, 1.14, and $1.09 M_{\oplus}$ all detected with semi-amplitudes less than 2 m s^{-1} (Stock et al. 2020).

Two planets have also been announced around Teegarden’s Star, which is the brightest and one of the nearest (3.83 pc) ultra-cool dwarfs in the solar neighborhood (Zechmeister et al. 2019). These are the first planets discovered using the radial velocity method around a late-type M dwarf with stellar mass less than $0.1 M_{\odot}$. Both planets have minimum masses less than $1.2 M_{\oplus}$, RV amplitude below 2 m s^{-1} , and are in the habitable zone of the host star.

Another highlight is the super-Earth candidate ($3.2 M_{\oplus}$) orbiting near the snow line of Barnard’s Star, which is the closest single star at a distance of 1.8 pc (Ribas et al. 2018). The discovery was made possible thanks to a large RV data set from several spectrographs spanning 20 years.

Finally, the most recent discovery is a giant planet around the late type M dwarf GJ 3512 (Morales et al. 2019). The planet is on an eccentric orbit with a period of 204 days and a minimum mass of $0.46 M_{\text{J}}$. This discovery challenges planet formation models by core accretion since such models fail to explain the existence of such a massive planet around such a low-mass star.

In Chapter 4 we report the discovery of the first transiting exoplanet followed up with CARMENES, which was first discovered by the K2 mission (Montet et al. 2015).

2.2 The HATSouth Survey

This subsection is largely based on my contribution to the Fachbeirat Science Report 2019 (except for the FEROS Section).

The Hungarian-made Automated Telescope Network-South (HATSouth) is a network of fully automatic telescopes spread out in longitude (Chile, Namibia, and Australia) (Bakos et al. 2013). It is the first network that permits round the clock 24 hours continuous monitoring of a large field of view in the southern hemisphere. The main goal of the survey is to discover and characterize transiting exoplanets. To date, HATSouth has discovered 70 exoplanets covering a wide range of masses and radii.

HATSouth has been monitoring the sky since 2009, covering $\sim 17\%$ of the southern sky. The survey involves six units in total where each of the sites has two units installed (Las Campanas Observatory, Chile, the High Energy Spectroscopic Survey, Namibia, and Siding Spring Observatory, Australia). Each of these units has four 0.18 m diameter telescopes mounted on a common mount with a $8.2^\circ \times 8.2^\circ$ field of view. Observations are carried out with the Sloan r' filter with a 4-min cadence and each field is monitored on average for 3 months (some fields up to 6 months).

More than 2300 transiting candidates have been identified from the HATSouth survey light curves. After the identification of a possible transiting planet, spectroscopic and photometric follow-up observations are necessary to confirm or refute the planetary nature of the candidate. Photometric follow-up observations are important to obtain higher precision light curves, which allow us to determine precisely the physical parameters of the system and to rule out blend scenarios. Low-resolution spectroscopy is necessary to identify false positive scenarios, such as eclipsing binaries. If a candidate passes this vetting process, then high-resolution and high signal-to-noise spectra are acquired to measure the semi-amplitude of the RV variation due to the transiting planet.

2.2.1 FEROS

The bulk of the high-resolution follow-up within the HATSouth collaboration is done with FEROS. FEROS (Fiber-fed Extended Range Optical Spectrograph) is a state-of-the-art high-resolution echelle spectrograph mounted at the MPG 2.2 m telescope in La Silla, Chile (Kaufer & Pasquini 1998). It has a resolution of $R = 48000$, high efficiency (20%), and a broad wavelength coverage from 350 nm to 920 nm. The instrument is mechanically and thermally stable, which allows for a precise wavelength calibration and makes it suitable for the detection and characterization of exoplanets.

FEROS is fed by two fibres providing simultaneous spectra. The first one is fed to the science target and the second one can be fed either to the sky or to the wavelength calibration lamps. Within the HATSouth project, we use the latter mode and we calibrate the spectra using ThAr lamps. These lamps have many emission lines in the optical and are capable of achieving a precision of 1 m s^{-1} , making them ideal for our purposes.

To reduce the spectra and compute the radial velocities, we use CERES (Brahm et al. 2017), a dedicated pipeline which was developed within the HATSouth collaboration. This also allowed us to develop a very efficient observing strategy. The spectra obtained are reduced and analyzed immediately every night. This is useful to quickly discard false-positives and hence focus on promising targets. False-positives are identified either by having RV variations on the order of $\sim \text{km s}^{-1}$ or by showing double peaks in the CCF.

Although the precision of FEROS based on standard stars using the CERES pipeline is 7 m s^{-1} (Brahm et al. 2017), we were able to push its limits to reach 3 m s^{-1} for a bright $V = 8$ mag star (Espinoza et al. 2020). This was achieved by making sure the ThAr lamp is turned on 20 minutes before the beginning of the first exposure of the night and keeping it on all the night. The ThAr lamps however are not being produced anymore and our stock is running low, which is why we developed a Fabry-Pérot system that is yet to be commissioned (Roland Gredel, private communication). Furthermore, for the daytime wavelength calibrations, we take many exposures and select the best one as a reference, which is the one that produces the smallest RV offset between the science and calibration fibers. This potentially allows FEROS to join the few instruments that are capable of detecting super-Earths around bright targets.

2.2.2 Survey Highlights

HATSouth contributed some of the exciting exoplanet discoveries. Their physical properties in the mass–radius diagram and radius–equilibrium temperature diagram are highlighted in Figure 2.2. Additionally, Figure 2.3 compares the number of planets detected within the various ground-based transit surveys, such as WASP, HATNet, HATSouth, and other surveys. WASP is the most successful transit survey to date with 175 planets discovered. HATSouth is also playing a major and important role in contributing to the ever-growing list of transiting planet discoveries.

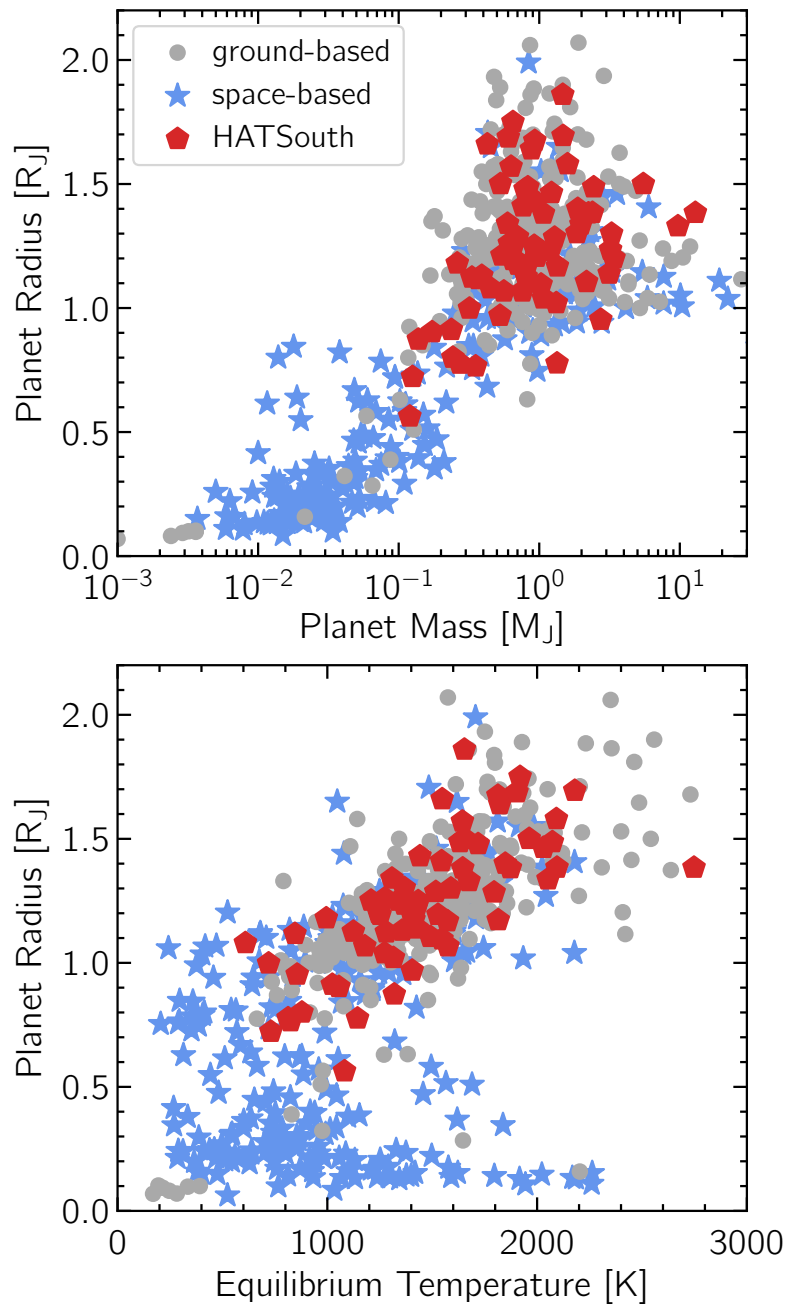


FIGURE 2.2: (*upper*) Planet mass–radius diagram and (*lower*) planet radius–equilibrium temperature diagram highlighting the planets discovered within the HATSouth collaboration (red pentagons) along with the planets discovered using ground-based surveys (gray circles) and space-based surveys (blue stars). HATSouth has contributed with many transiting exoplanets spanning a wide range of physical properties.

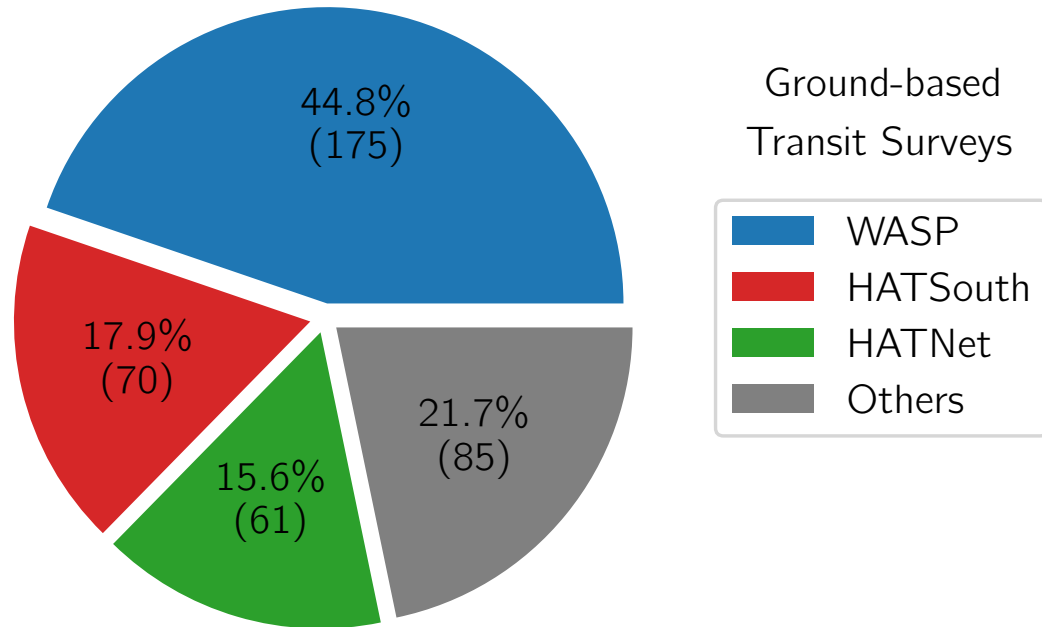


FIGURE 2.3: The number of planets detected within the various transiting ground-based surveys. HATSouth has contributed with 18% of the transiting exoplanets.

The characteristic of the HATSouth planets span a large region in parameter space, ranging from small planets $\sim 38 M_{\oplus}$ (HATS-7 b and HATS-8 b; [Bakos et al. 2015](#); [Bayliss et al. 2015](#), respectively) to massive ones $\sim 13 M_J$ (HATS-70 b; [Zhou et al. 2019](#)). Of particular interest is HATS-17b ([Brahm et al. 2016](#)), a transiting planet with a period of $P = 16.3$ days, the longest period ever discovered using ground-based telescopes, thanks to the 24 hours coverage of the same field of view of the automated network of telescopes. Another interesting system is HATS-71b ([Bakos et al. 2018](#)), only the third giant planet discovered transiting an M dwarf. The system was discovered using the HATSouth light

curves, and confirmed using several photometric, spectroscopic, and imaging ground-based facilities, as well as space-based photometry using data from *TESS*. This is the first system confirmed using *TESS* light curves and shows that combining ground-based and space-based light curves is an important step that we will follow in future confirmation of HATSouth candidates. Moreover, the survey has contributed to the detection of 55 hot Jupiters (e.g. [Mancini et al. 2015](#); [Ciceri et al. 2016](#); [Rabus et al. 2016](#); [Henning et al. 2018](#)) out of the 300¹ discovered using ground-based observations. Of particular interest is the system HATS-56 ([Espinoza et al. 2019](#)), where the radial velocities show a long term trend. If we assume that this trend is due to a second planet in the system, then the planet would be a super-Jupiter with $M \sin i \sim 5 M_J$ orbiting in the habitable zone of the host star. In Chapter 5 we report the discovery of HATS-59 b,c, the first multi-planet system discovered by the survey. The survey continues to play a leading role in the discovery and precise characterization of transiting exoplanets.

¹as of 16 March 2020

Chapter 3

Extrasolar Giant Planets

The great progress in exoplanetary research can be largely attributed to the advances in the technology that enabled these discoveries. We now know that planetary systems are extremely diverse – different masses, sizes, orbital periods, eccentricities, compositions, ... While the detection of individual planetary systems is exciting, studying the distribution of the physical properties of the entire exoplanet population provides a higher level of insight and is one of the most important outcomes of the combined individual discoveries. With several thousands of planets detected, the field moved from understanding single detections to rather studying the entire population and testing theories of planet formation and evolution. Such comparisons shed light on the most important physical mechanisms in planet formation and aid with understanding the diversity of systems discovered.

Giant planets are one of the main focus of this thesis with two contributions covering both aspects of observations and theory. Chapter 5 presents the discovery of a new multiplanet system, which consists of a hot Jupiter and a cold Jupiter. Additionally, Chapter 6 focuses on studying the population of close-in giant planets with the aim to understand their interior structure and evolution. In this chapter the observed properties of giant planets are presented along with highlighting the various populations. The general theory describing the planet interior structure and evolution is described. Finally, the observed properties are compared to theoretical predictions.

3.1 Statistical Properties of Giant Planets Observations

With almost 4000 confirmed exoplanets discovered using both the transit and radial velocity methods, it is now possible to look at the statistical distribution of the planetary systems. We focus on statistical properties related to extrasolar giant planets, specifically the two recognizable upper populations in Figure 1.3. The two distinct massive giant planet populations are: the close-in giant planets referred to as hot Jupiters (HJs) and the long period planets with periods $P > 100$ days referred to as cold Jupiters (CJs). Warm Jupiters (WJs) are at intermediate periods between hot Jupiters and cold Jupiters with periods $10 < P < 100$ days. WJs lie in a region known as the period valley first identified by radial velocity surveys (Udry et al. 2003; Jones et al. 2003) and later confirmed by Santerne et al. (2016) using *Kepler* data. The period valley could provide constraints on the migration history as it provides evidence for disk migration (Dawson & Johnson 2018). Briefly, as the planet migrates, if the migration timescale is similar to the disk lifetime, then the planet will halt and end up as a warm Jupiter. More details regarding the different migration scenarios are presented in Section 3.1.3. Ground-based transiting surveys, however, are biased towards detecting short-period planets, with HATS-17 b having the longest-period detected from the ground (16.3 days; Brahm et al. 2016). We therefore refrain from comparing WJs to CJs due to observational biases but rather treat them as a single population. The main goal is to compare the statistical properties of the population of hot Jupiters to warm/cold Jupiters.

3.1.1 Hot Jupiters

Hot Jupiters are defined as planets with masses roughly larger than $\sim 0.2 M_J$ and orbital periods less than ~ 10 days. Because of their short orbital periods, they are the easiest to detect. Indeed, most of the planets detected using ground-based surveys are hot Jupiters. Despite that, hot Jupiters are quite rare with an occurrence rate of 0.5 – 1% based on *CoRoT* data (Deleuil et al. 2018), *Kepler* data (Santerne et al. 2016), and radial velocity surveys (Mayor et al. 2011; Wright et al. 2012).

3.1.2 Warm/Cold Jupiters

Warm/Cold Jupiters have long orbital periods, typically $P > 10$ days. Transiting surveys are not sensitive to detecting long-period planets and thus most of them are detected by radial velocity surveys. Although fewer WJs and CJs have been detected compared to HJs, they are relatively more common with an occurrence rate of $\sim 1.5\%$ and $\sim 3\%$ for warm and cold Jupiters, respectively, based on radial velocity surveys (Mayor et al. 2011) and *Kepler* data (Santerne et al. 2016).

3.1.3 Comparison Between Hot Jupiters and Long-Period Giant Planets

In this Section, we compare the main physical properties of giant planets with masses $M_p > 0.2 M_J$. Hot Jupiters are defined as giant planets with $P < 10$ days while warm/cold Jupiters with $P > 10$ days. The upper panel of Figure 3.1 shows the period–eccentricity diagram for HJs (red) and warm/cold Jupiters (blue). The eccentricity and radius distributions are also presented in the bottom left and right panel, respectively.

Eccentricity Distribution

Hot Jupiters with periods $P < 1$ day have circular orbits while the further out HJs (1 – 10 days) tend to have a range of moderate eccentricities $0 < e < 0.6$. At even longer periods ($P > 10$ days) warm/cold Jupiters show a wide range of eccentricities even up to 0.95. The two different populations of eccentricities have been supported by Kipping (2013) who finds that splitting the population into two groups, short-period and long-period planets, results into two distinct Beta distributions.

Even if both populations show a wide range of eccentricities, only a dozen of HJs have eccentricities larger than 0.4 while many long-period planets have large eccentricities. The two distinct populations could be an indicator of different migration histories and therefore provide insights into their origins. Most of the HJs are on circular orbits, which could be due to the short tidal circularization timescales or due to disk migration. The non-zero eccentric orbits observed could be due to interactions with a distant planetary companion (e.g. Rasio & Ford 1996) or stellar companion (e.g. Fabrycky & Tremaine 2007; Naoz et al. 2012) that could potentially result in eccentric orbits. Ngo et al. (2016)

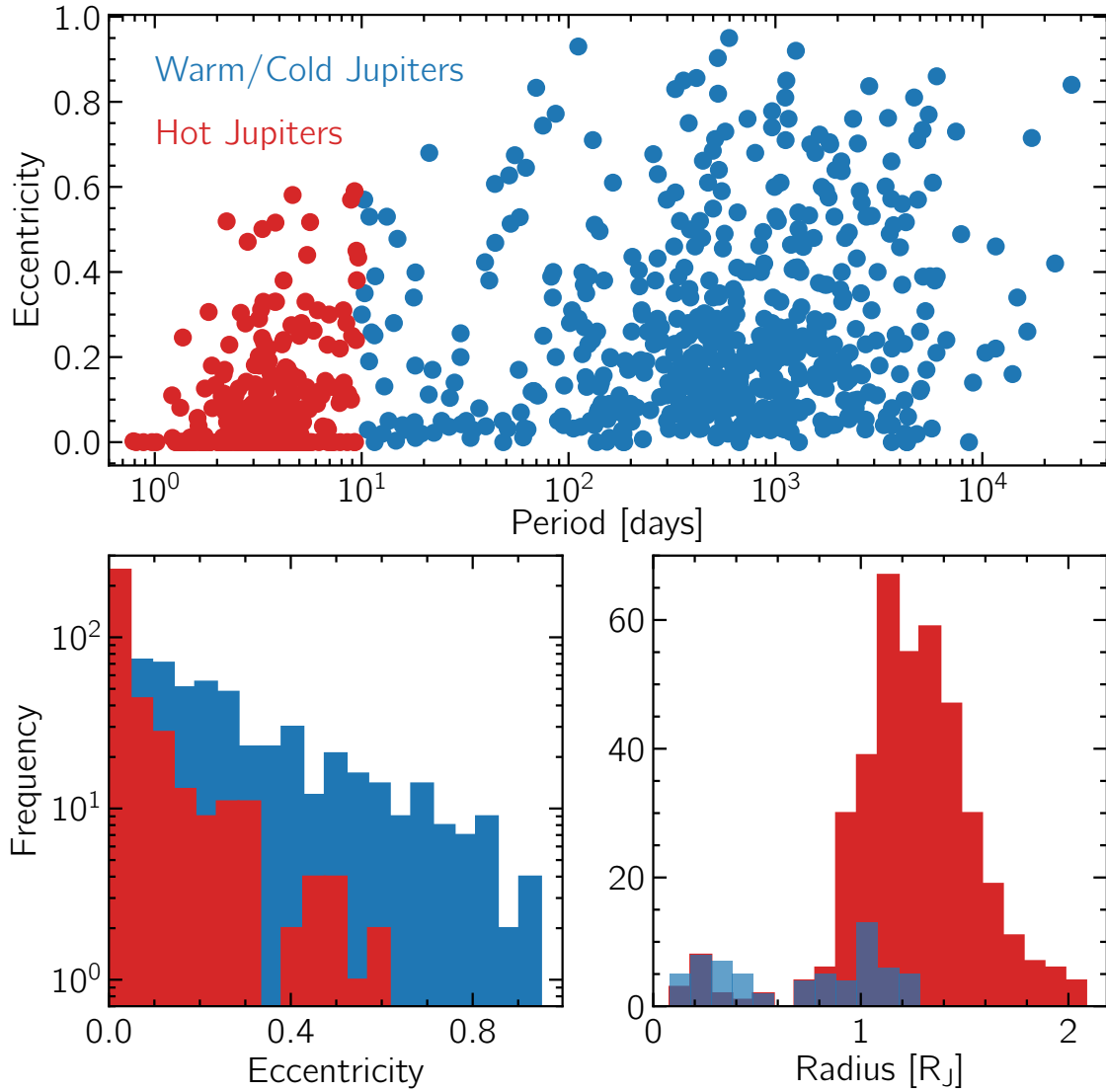


FIGURE 3.1: Comparison between warm/cold Jupiters (blue) and hot Jupiters (red). (*upper panel*) The period-eccentricity diagram. (*lower panel*) The eccentricity distribution (left) and radius distribution (right). Close-in planets tend to be on circular orbits and have large radii, while long-period planets tend to have a wide range of eccentricities 0 – 0.95 and radii not larger than $\sim 1.2 R_J$.

found that 47% of the hot Jupiters have stellar companions with semimajor axes between 50 and 2000 AU, however less than 20% are capable of exciting the eccentricities of hot Jupiters. Planet companions are also common for HJs with an occurrence rate of $\sim 50\%$ (Knutson et al. 2014; Bryan et al. 2016). It is possible that the outer planetary companions scatter inward the present HJs, leading to high eccentricity migration, and ending as HJs in eccentric orbits. This is also in-agreement with Dawson & Murray-Clay (2013), who suggested that hot Jupiters can form via two competing formation scenarios: disk migration and high eccentricity tidal migration excited by planet-planet scattering. In Chapter 5, I provide further observational evidence of the latter mechanism where I present the discovery of the HATS-59 system, composed of an inner hot Jupiter on an eccentric orbit with an outer gas giant planetary companion.

The eccentricity of warm/cold Jupiters on the other hand spans a wide range of eccentricities, which could mean several formation scenarios for those planets as well. Disk migration supports the planets observed on circular orbits and high eccentricity migration could potentially explain the planets on eccentric orbits where their orbits got excited by an outer companion. Anderson & Lai (2017) showed however that the latter mechanism can explain WJ planets with moderate eccentricities but fails to explain those with very large eccentricities. WJs and CJs are also likely to have a massive outer companion (Bryan et al. 2016) reinforcing the existence of two different formation scenarios: disk migration for planets on circular orbits and planet-planet scattering for planets on moderate eccentric orbits. Note however that if two or more giants form in a disk, even with disk migration the eccentricities of the planets will be excited.

Radius Distribution

Figure 3.1 compares the radius distribution for both hot Jupiters and warm/cold Jupiters. Due to observational biases, most of the warm Jupiters are discovered using the *Kepler* mission (Borucki et al. 2010), with only 5 systems detected using the HATNet, HATSouth, (Bakos 2018) and SuperWASP (Pollacco et al. 2006) transiting ground-based surveys. WJs and CJs tend to have small radii compared to their hot counterparts, with the largest radius $1.24 R_J$ (Kepler-39 b; Bonomo et al. 2017). Hot Jupiters on the other hand, tend to have relatively large radii with the largest planet as large as $2.085 R_J$ (HAT-P-17 b; Zhou et al. 2017). As I show in Section 3.3 and in Figure 3.2 the origin of the large radii of

hot Jupiters is one of the biggest mysteries in the exoplanet field and is the subject of Chapter 6.

3.2 Interior Models of Irradiated Giant Planets

Current observations of exoplanets are limited to few planetary parameters, such as the mass, radius, and orbital properties. Nevertheless, these properties are our primary window into the interior of extrasolar planets. Linking the observed properties to planetary structure models provides insights into the interior of such planets, such as their bulk composition. We outline below in Sections 3.2.1–3.2.4 the general theory describing the planetary structure and thermal evolution and provide links, when necessary, to the evolution model `complete021` (Mordasini et al. 2012b), which the work presented in Chapter 6 is based on. Then in Section 3.3 and Section 3.4, we provide clues on how linking the observed properties to interior structure models reveals the diversity of exoplanets and shows that major physical processes are missing in our theoretical models. The radius anomaly problem of hot Jupiters is introduced in Section 3.5. Section 3.6 provides a general overview on our current understanding of the interior structure of HJs.

3.2.1 Basic Structure Equations

In this work, we focus on giant planets, which we define as planets made up mostly of a massive hydrogen and helium envelope with a small fraction of heavy elements that is modeled as water H_2O . Under the assumption that the planets are spherical and symmetric, the first of the four equations governing the interior structure of giant planets is the mass conservation equation

$$\frac{dm}{dr} = 4\pi r^2 \rho \quad (3.1)$$

where r is the planet radius, m the planet mass inside r , and ρ the density.

The second equation describes hydrostatic equilibrium, which states that the gravitational acceleration is balanced by the pressure gradient. The equation of hydrostatic equilibrium is

$$\frac{dP}{dr} = -\frac{Gm}{r^2}\rho \quad (3.2)$$

where P is the pressure and G the gravitational constant.

The third equation, the energy transfer equation, describes the process by which the internal heat is transported from the deep interior to the surface of the planet. The equation for the energy transport is defined as

$$\frac{dT}{dr} = \frac{T}{P} \frac{dP}{dr} \nabla, \quad (3.3)$$

where T is the temperature and ∇ is the temperature gradient defined as

$$\nabla \equiv \frac{d \ln T}{d \ln P} = \min(\nabla_{\text{ad}}, \nabla_{\text{rad}}). \quad (3.4)$$

In the above equation, ∇_{ad} and ∇_{rad} are the temperature gradients in the convective and radiative layers, respectively. If energy is transported by convection, we assume it does so adiabatically and then $\nabla = \nabla_{\text{ad}}$ and is given by the equation of state (EOS). Otherwise, if energy is transported by radiation, then $\nabla = \nabla_{\text{rad}}$ and in the diffusion approximation is given as

$$\nabla_{\text{rad}} = \frac{3}{64\pi\sigma G} \frac{\kappa l P}{T^4 m} \quad (3.5)$$

where κ is the Rosseland mean opacity, l is the intrinsic luminosity, and σ is the Stefan-Boltzmann constant. To determine whether energy is transported via convection or radiation, we use the Schwarzschild criterion. In general, a relatively large amount of energy is transported from the deep interior of giant planets to the surface. This is because giant planets have hot interiors, leading to inner convective interiors and radiative outer layers.

Finally, the fourth equation is the energy equation

$$\frac{dl}{dr} = 4\pi r^2 \rho \left(\dot{\epsilon} - T \frac{dS}{dt} \right) \quad (3.6)$$

where t is the time, S is the specific entropy and $\dot{\epsilon}$ describes the sources of energy such as deuterium burning. For giant planets with masses less than $13 M_J$, it is safe to assume $\dot{\epsilon} \sim 0$ since deuterium burning becomes important for planets more massive than $13 M_J$ (Mollière & Mordasini 2012). In Chapter 6 we account for an additional heating term, L_{bloat} , that accounts for heat dissipated into the interior. This becomes important and relevant for hot Jupiters since as we showed in Section 3.1.3, HJs possess large radii. The second term in the brackets on the right hand side accounts for changes in the heat in a given layer, which could be due to thermal cooling or contraction. In general, integrating dl/dr radially from the center outwards accounts for the increase in luminosity per size dr . In our model however, we make the assumption that

$$\frac{dl}{dr} = 0, \quad (3.7)$$

that is we assume that the luminosity is constant in each layer and all the luminosity is emitted from the central core. This is possible because the basic structure equations (Equations 3.1, 3.2, and 3.3) are independent of l in the convective layers. l only enters in the radiative layers of the planet. This assumption was verified to be a good approximation as long as there is no strong heating in the outer layers and when the planet is nearly fully convective (Mordasini et al. 2012b).

3.2.2 Microphysics

Equation of State

The most abundant elements in the envelopes of irradiated giant planets are hydrogen and helium along with a small fraction of heavier elements. In the photosphere, hydrogen is in its molecular form where the pressure is as low as 1 mbar and temperatures around 500 – 2500 K (for warm and hot Jupiters). The pressure in the interior can reach up

to 1 – 10 Mbars and temperature up to 20000 – 30000 K where hydrogen and helium become fluid. It is thus crucial to derive accurate thermodynamic properties of matter under conditions similar to the interior of irradiated planets covering the wide range of pressure and temperature.

In `completeo21`, we use the SCvH EOS of H and He (Saumon et al. 1995) assuming a He mass fraction $Y = 0.27$. To account for the heavy element enrichment modeled as H_2O , we use the ANEOS. H/He and H_2O are mixed using the additive volume law (Mordasini 2020). Given the pressure, temperature, and fraction of heavy elements, the EOS outputs the density, entropy, adiabatic temperature gradient, specific energy, and the mean molecular weight.

Opacity

Another important microphysical ingredient to determine accurately the thermal evolution of a giant planet is the opacity. As we showed in Equation 3.4, the internal temperature gradient ∇ depends on the process that is transporting energy from the interior to the surface, which in turn depends on the opacity. Since the opacity increases in the interior of giant planets, energy is transported using convection. In these regions, the two main sources of opacity are the absorption of H_2^- and H^- .

Irradiated giant planets tend to have a radiative layer on top of the convective region, which controls the cooling and the contraction of the interior. In this region, the three dominant sources of opacity are water, methane, and collision-induced absorption by hydrogen molecules. This has been supported by observations as several elements and molecules have been detected in the atmosphere of hot Jupiters such as sodium Na (e.g. Charbonneau et al. 2002; Wyttenbach et al. 2015; Burton et al. 2015), potassium K (e.g. Wilson et al. 2015; Sedaghati et al. 2016), and water H_2O (e.g. Deming et al. 2013; Evans et al. 2016; Stevenson et al. 2016). This clearly shows that the atmosphere of giant planets cannot be assumed as a blackbody, which highlights the importance of coupling the atmosphere to a detailed non-gray atmospheric model. We discuss below the outer atmospheric boundary condition.

3.2.3 Atmospheric Boundary Conditions

The energy flux coming from the deep interior is radiated away in the atmosphere. Therefore, the cooling rate of a gas giant planet is regulated by the atmospheric boundary condition. Realistic atmospheres are necessary to compute accurately the evolution of a gas giant planet in order to correctly interpret the observed data.

The detection of the first exoplanet, 51 Peg b (Mayor & Queloz 1995) motivated the need for more realistic atmospheric models and sparked a substantial improvement in the atmospheric models. It was immediately realized that because of the close orbital separation between the planet and the host star, the heating from the stellar incident flux should be accounted for (e.g. Guillot et al. 1996; Burrows et al. 1997; Barman et al. 2001; Guillot & Showman 2002; Arras & Bildsten 2006). Compared to an isolated planet, the intense stellar radiation increases the photospheric temperature by nearly an order of magnitude. This in turn leads to an extended radiative zone in the outer layers pushing the top of the convective layer deeper into the atmosphere (Fortney et al. 2007). The main effect of irradiation is that it decreases the cooling rate and thus the contraction rate of irradiated giant planets (Burrows et al. 2000).

More sophisticated state-of-the-art atmospheric models have been incorporated in thermal evolution models. The pioneering work of Burrows et al. (1997) and then Chabrier et al. (2000); Baraffe et al. (2003); Fortney et al. (2008); Burrows et al. (2008) and recently Spiegel & Burrows (2013); Thorngren et al. (2016); Linder et al. (2019); Marleau et al. (2019) all include detailed non-gray atmospheric boundary conditions. There exist also analytical solutions of the radiative transfer approach for the semi-gray case, which accounts for the incoming flux in the visible and the outgoing intrinsic flux in the infrared. This model was developed by Guillot (2010) and incorporated in `complete021` by Jin et al. (2014). We describe below the semi-gray model, however in Section 6.4.1 we provide the motivation and details of coupling `complete021` to a fully non-gray atmospheric model using the `petitCODE` (Mollière et al. 2015, 2017).

In the case of irradiated gas giant planets, the intense stellar irradiation heats up the planet and produces an extended isothermal layer. Additionally, heat is transferred from the interior via radiation. The analytical semi-gray model was developed specifically for irradiated planets and thus accounts for both effects (Guillot 2010). The model provides an analytical relation relating the temperature at a given optical depth τ :

$$T^4 = \frac{3T_{\text{int}}^4}{4} \left\{ \frac{2}{3} + \tau \right\} + \frac{3T_{\text{eq}}^4}{4} \left\{ \frac{2}{3} + \frac{2}{3\gamma} \left[1 + \left(\frac{\gamma\tau}{2} - 1 \right) \times e^{-\gamma\tau} \right] + \frac{2\gamma}{3} \left(1 - \frac{\tau^2}{2} \right) E_2(\gamma\tau) \right\} \quad (3.8)$$

where T_{int} and T_{eq} are the intrinsic and equilibrium temperatures of the planet, respectively, and are defined below. γ is the ratio of the visible opacity to the thermal opacity ($\gamma = \kappa_v/\kappa_{\text{th}}$; Guillot 2010) and determines the amount of absorbed flux in the atmosphere. Jin et al. (2014) computed the values of γ as a function of T_{eq} by comparing the analytical model (Equation 3.8) to a non-gray model (Fortney et al. 2008) and the values are provided in Jin et al. (2014). E_2 is the exponential integral $E_n(z) \equiv \int_1^\infty t^{-n} e^{-zt} dt$ with $n = 2$.

The equilibrium temperature T_{eq} of a planet is defined as the stellar irradiation flux averaged over the entire planetary surface. In equation form and assuming zero albedo, the equilibrium temperature is

$$T_{\text{eq}} = T_* \sqrt{\frac{R_*}{2a}} \quad (3.9)$$

where T_* and R_* are the stellar temperature and radius, respectively, and a is the orbital separation between the planet and the host star. The intrinsic temperature T_{int} characterizes the energy released by the planet due to cooling and contraction and is expressed in terms of the intrinsic luminosity of the planet

$$L_{\text{int}} = 4\pi R_p^2 \sigma T_{\text{int}}^4 \quad (3.10)$$

where σ is the Stefan-Boltzmann constant and R_p the planetary radius. Knowing thus the equilibrium and the intrinsic temperature, one can determine the temperature of the planet as a function of optical depth using Equation 3.8.

3.2.4 Thermal Evolution of Giant Planets

Section 3.2.4 is adapted from Guillot & Gautier (2014).

In this section we study the cooling history of giant planets. In particular, we derive that at early stages of planet evolution most of the energy is radiated away and thus the planet undergoes fast contraction following the Kelvin-Helmholtz timescale. At later stages, electron degeneracy sets in, the planet contracts slowly and the source of luminosity is the thermal cooling of the ions. This has important consequences on the mass–radius diagram, where we show that observations tend to violate what is expected from theoretical models. This concept is known as the radius anomaly problem of hot Jupiters and points out that a physical mechanism occurs in hot Jupiters that is still not accounted for in the present standard thermal evolution models.

The thermal emission of giant planets is powered by their cooling and contraction. The process powering this thermal emission though changes with time depending on the state of the matter in the deep interior. Giant planets evolve from a high entropy, high θ , hot initial state to a low entropy, low θ , cold degenerate state. θ is the degeneracy parameter and is defined as

$$\theta = \frac{E_{\text{thermal}}}{E_{\text{Fermi}}} = \frac{T}{T_F}, \quad (3.11)$$

which is the ratio between the thermal energy and the Fermi energy and T_F is the Fermi temperature. θ sets whether the electrons are in a degenerate state or not. For $\theta > 1$ the electrons are non-degenerate, weakly coupled, and quantum effects can be ignored. For $\theta < 1$ the electrons are degenerate, strongly coupled, and electron interactions are important. To relate the state of matter to the source of thermal emission, it is useful to start from the virial theorem

$$\xi E_i + E_g = 0 \quad (3.12)$$

which can be used to connect the gravitational energy E_g to the internal energy E_i of a gravitationally bound object. For our purposes, ξ is computed using the EOS and depends on the state of gas.

Using the conservation of energy, the intrinsic luminosity of the planet L is

$$L = -\frac{dE_{\text{total}}}{dt} \quad (3.13)$$

$$= -\frac{d(E_g + E_i)}{dt} \quad (3.14)$$

$$= -\frac{d}{dt} \left(E_g - \frac{E_g}{\xi} \right) \quad (3.15)$$

$$= -\frac{\xi - 1}{\xi} \frac{dE_g}{dt} \quad (3.16)$$

where in the third equation we used Equation (3.12) and assuming that ξ is constant.

We can now use the virial theorem (Equation (3.12)) and the conservation of energy equation (Equation (3.16)) to understand the evolution of giant planets. For example, at the beginning of planet evolution, we can assume that the planet is a perfect H_2 gas and for a diatomic ideal gas $\xi = 3.2$. The gravitational energy decreases because the planet contracts and, using Equation (3.16), around 70% of the energy is radiated away and 30% goes into increasing the internal energy. This in turn increases the pressure and the density and heats up the planet.

As the planet contracts even further and the density increases, the interior becomes degenerate. The internal energy is then given by the energy of the ions and electrons $E_i = E_e + E_{\text{ion}}$ and $E_i \gg E_{\text{ion}}$. For a fully degenerate gas, $\xi = 2$, which implies that half of the energy emitted due to contraction is radiated away and the other half will increase the internal energy. The gravitational energy changes as a function of the planet density ρ

$$E_g \propto \frac{1}{R_p} \propto \rho^{1/3}. \quad (3.17)$$

The energy of the degenerate electrons is

$$E_e \propto \rho^{2/3}. \quad (3.18)$$

Converting for ρ in Equation (3.18) and substituting in Equation (3.17), we get

$$E_e \propto E_g^2. \quad (3.19)$$

Differentiating with respect to time, we get

$$\begin{aligned} \dot{E}_e &\propto 2E_g \dot{E}_g \times \frac{E_g}{E_g} \\ &\propto 2 \frac{E_g^2}{E_g} \dot{E}_g \end{aligned}$$

and using Equation (3.19), we get

$$\dot{E}_e \propto 2 \frac{E_e}{E_g} \dot{E}_g. \quad (3.20)$$

(the dot denotes derivative with respect to time). Applying the virial theorem Equation (3.12) with $\xi = 2$, this means that

$$E_i \approx E_e \approx -\frac{E_g}{2} \quad (3.21)$$

in the limit of $E_i \gg E_{\text{ion}}$. Replacing Equation (3.21) in Equation (3.20), we obtain

$$\dot{E}_e = -\dot{E}_g. \quad (3.22)$$

Finally, applying the conservation of energy, we have

$$\begin{aligned}
L &= -\frac{dE_{\text{total}}}{dt} \\
&= -(\dot{E}_g + \dot{E}_e + \dot{E}_{\text{ion}}) \\
&\approx -\dot{E}_{\text{ion}}
\end{aligned} \tag{3.23}$$

where Equation (3.22) was used in the last equation. This has important consequences, as it states that the gravitational energy lost due to contraction is fully absorbed by the degenerate electrons and the luminosity of the planet is powered by the thermal cooling of the ions.

To briefly summarize, in the early stages of planet evolution, the planet is very compressible and therefore the planet contracts fast, following the Kelvin-Helmholtz timescale. The luminosity is caused by the decrease in gravitational energy. As the evolution proceeds and contraction still following the Kelvin-Helmholtz timescale, the density increases and the electrons become degenerate in the inner part of the planet. In this regime, the planet's compressibility is smaller compared to its early evolution and the radiated energy is caused by the thermal cooling of the ions.

3.3 The Mass-Radius Diagram: Expectations vs Reality

As mentioned in the previous section, understanding the process powering the luminosity of the planet has major consequences on the theoretical mass-radius relation. The basic shape of the mass-radius relation can be understood using the polytropic mass-radius relation (Burrows & Liebert 1993)

$$R_p \propto K(n) M_p^\beta \tag{3.24}$$

where n is the polytropic index and K is a constant as a function of n determined using the EOS and β is

$$\beta = \frac{1 - n}{3 - n} \quad (3.25)$$

Low-mass planets are generally not compressible, therefore $n \approx 0$ and as such $R_p \propto M_p^{1/3}$ for a given material composition. For massive planets, the compression in the interior is high enough that the interior is supported by electron degeneracy and $n \approx 1.5$. In this regime, $R_p \propto M_p^{-1/3}$. Qualitatively, since low mass planets are not compressible the radius increases with increasing mass until a critical mass M_{cr} after which degeneracy sets in and the radius decreases with increasing mass.

In reality, K depends on the mass and on the composition of the planet. Additionally, not a single value of β is expected since this also depends on the planet mass and composition. Actually, estimating the mass–radius relation is a very active field of research (e.g. [Lissauer et al. 2011b](#); [Hadden & Lithwick 2014](#); [Weiss & Marcy 2014](#); [Rogers 2015](#); [Wolfgang et al. 2016](#); [Chen & Kipping 2017](#); [Ning et al. 2018](#)) and a lot of work has been devoted to estimate β . However, it is still fruitful to compare theoretical predictions to the actual observed properties of exoplanets. We select the theoretical mass–radius relation based on planet population synthesis (PPS) from [Mordasini et al. \(2012a\)](#). Planet population synthesis is a suite of physical models that account for all the known important physical processes of planet formation and evolution, where the main goal is to link the individual processes and compare the outcome to observed properties of extrasolar planets (for a recent review check [Mordasini 2018](#)). There are many effects leading to the observed diversity of exoplanets, such as different disk mass, disk lifetime, stellar mass, ... Planet population synthesis naturally accounts for this diversity and thus predictions of the mass–radius relation can be compared to observations. Figure 3.2 shows the mass–radius diagram of the observed exoplanets with measured masses and radii and for $M_p > 0.1 M_J$. The data was taken from the Transiting Extrasolar Planet Catalogue (TEPCat¹; [Southworth 2011](#)). The warm Jupiters with orbital periods larger than 10 days are indicated with a black circle. The gray solid line is the analytical mass–radius solution based on planet population synthesis. This can be regarded as the average relation based on various compositions and equilibrium temperatures for moderately irradiated

¹www.astro.keele.ac.uk/jkt/tepcat/

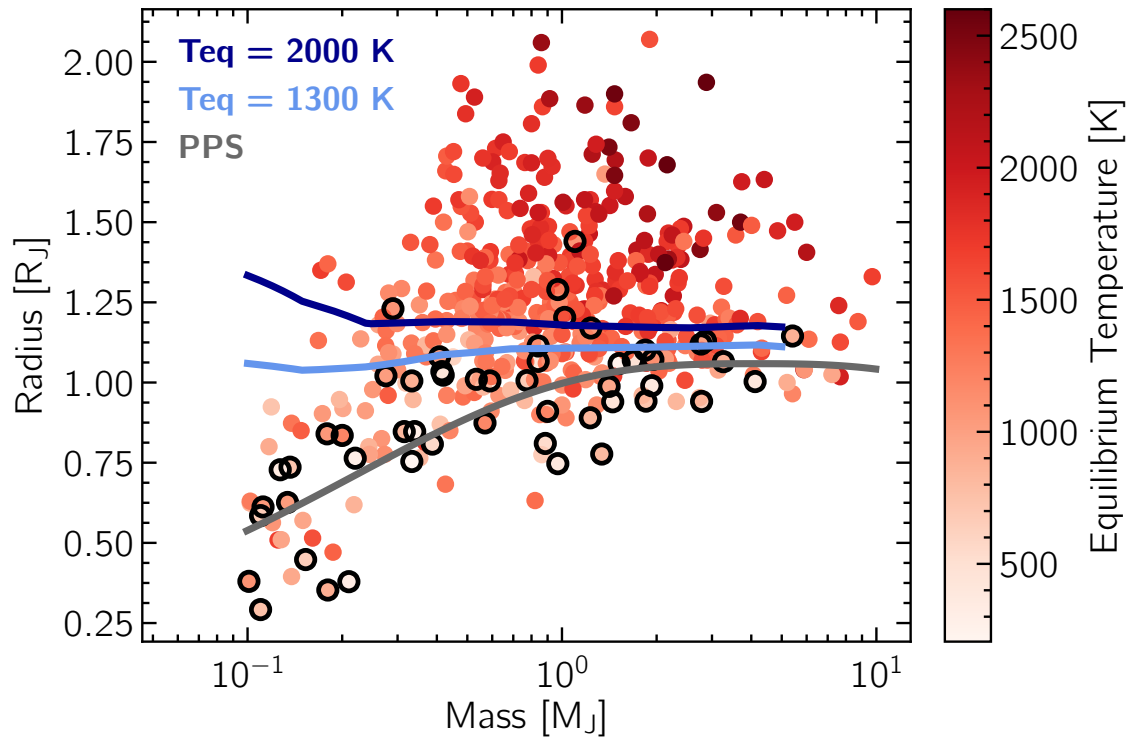


FIGURE 3.2: The mass–radius diagram for the observed exoplanets ($M > 0.1 M_J$) color coded by the equilibrium temperature. Warm Jupiters with periods > 10 days are highlighted by black circles. The gray line is the analytical expression based on planet population synthesis for planets with $0.1 < a/AU < 1$ (Mordasini et al. 2012a). The light and dark blue lines are the models of Fortney et al. (2007) with equilibrium temperatures of 1300 K and 2000 K, respectively, and made up entirely of H/He. The basic pattern of the mass–radius relation is conserved with an increase in radius until a critical mass, after which the radius decreases with increasing mass. Most of the planets however have radii larger than predicted by standard theoretical models.

planets. The blues lines are based on models of [Fortney et al. \(2007\)](#) at 4.5 Gyr for equilibrium temperatures of 1300 K and 2000 K and assuming the planets are made up entirely of hydrogen and helium, i.e. no heavy elements. The PPS relation leads to radii smaller than the models for the highly-irradiated planets. This is expected since the PPS models include a core, which leads to smaller radii and is based on planets with orbital distances larger than 0.1 AU. These planets thus are not subject to intense stellar irradiation, which also leads to smaller radii. It is evident that most of the planets detected have radii larger than predicted by theoretical models. Warm Jupiters tend to have radii smaller than their hot counterparts and on average in agreement with predictions based on planet population synthesis. The fact that the radii of most of the hot Jupiters violate theoretical predictions is known as the radius anomaly problem and points to a physical mechanism that is missing in our present modeling of hot Jupiters.

3.4 What Is Really the Difference Between Hot and Cold Jupiters?

In order to comprehend the nature of the physical mechanism missing in the standard thermal evolution models, it is important to understand the fundamental and physical differences between a hot Jupiter and a cold Jupiter. Specifically, how does the close proximity of hot Jupiters to their host stars affect their interior structure and atmospheric circulation. We discuss below briefly the differences that could provide insights into the inflation mechanism.

Recall that hot Jupiters are highly irradiated because of the intense stellar irradiation. This leads to a thick isothermal zone that extends to higher pressures, which retards cooling and thus contraction. Jupiter on the other hand has a thin radiative zone on top of the convective interior. Heating the atmosphere can significantly modify the evolution of an irradiated planet compared to an isolated or less irradiated planet, leading to relatively larger radii ([Fortney et al. 2007](#)). Another main difference is that hot Jupiters are tidally locked and therefore experience a strong asymmetric irradiation between the day-side and the night-side. This leads to large temperature gradients between both sides and also between the equator and the poles. The global temperature distribution is thus not as

homogeneous as is the case for Jupiter and for less irradiated exoplanets. Indeed, atmospheric circulation models of hot Jupiters suggest the presence of strong winds flowing from the hot side to the cool side (e.g. [Showman et al. 2015](#)), which was also confirmed via observations ([Snellen et al. 2010](#)). It is believed that these strong winds could be one of the main important parameters driving the large radii of hot Jupiters. Specifically, fast winds can transport heat into the interior, which increase the entropy of the planet and lead to large radii ([Arras & Bildsten 2006](#); [Marleau & Cumming 2014](#)).

3.5 Radius Anomaly of Hot Jupiters

The inflated radii of hot Jupiters is the subject of Chapter 6 in this thesis. We give a short overview of the current state of the field related to the ongoing efforts to solve the radius anomaly problem. We focus on what are the physical mechanisms proposed and how the trends inferred from observations are used to test the proposed theories.

The suggested mechanisms include delaying the cooling and contraction of the planet or depositing extra heat into the interior. Enhanced atmospheric opacity ([Burrows et al. 2007](#)) can for example delay contraction. Depositing extra heat into the interior can be done via dissipative mechanisms, such as atmospheric circulation and ohmic dissipation ([Guillot & Showman 2002](#); [Batygin & Stevenson 2010](#), respectively) or via advection ([Tremblin et al. 2017](#)). For a review on the different mechanisms, see [Baraffe et al. \(2014\)](#).

Trends in the observed parameters also reveal clues on important pieces that should be explored in the proposed models. One such important trend is the positive correlation observed between the planet radius and equilibrium temperature. It is well established that the level of irradiation is strongly correlated with the planet radius. The critical temperature is around 1000 K ([Demory & Seager 2011](#)), above which the planets are considered to be inflated and below which the mechanisms are not efficient. Any of the mechanisms then should be efficient at T_{eq} higher than 1000 K and should be able to explain the observed positive trend. Another clue from observations is the trend between the level of inflation and the planet mass. Lower-mass planets tend to be more inflated compared to massive planets ([Sestovic et al. 2018](#)).

While the proposed solutions can reproduce the radii of couple of hot Jupiters, each one should be able to account for all the observed radii. One approach to test the proposed theories is to check whether the observed trends can be explained or even reproduced.

Tremblin et al. (2017) followed this approach and showed that the advection of potential temperature can reproduce the positive correlation between the radius and equilibrium temperature. Recently, Thorngren & Fortney (2018) took a different approach and focused on testing theories related to heat transfer. Specifically, they assumed that the source of heat is the irradiation of the host star and quantified the fraction of the stellar irradiation ϵ that should be transported into the interior to reproduce the observed radii of hot Jupiters. Then, they compared the distribution between ϵ and T_{eq} to theoretical predictions. Thorngren & Fortney (2018) showed that shape of the pattern follows a Gaussian function, which was predicted by ohmic dissipation. The two competing theories are thus ohmic dissipation and advection of potential temperature. Thorngren & Fortney (2018) however argued that the latter does not predict the Gaussian function and thus cannot be the universal mechanism.

3.6 Interior Structure of Hot Jupiters

Within the context of transporting heat into the interior, the depth at which the extra energy is deposited is very important. It must be deposited below the radiative-convective boundary (RCB) in order for the planet to retain the heat and therefore maintain a large radius (Komacek & Youdin 2017). Otherwise, heat deposited in the radiative layers will be radiated away. As mentioned in Section 3.4, winds also are important to transport the energy into the interior. There should thus be a sweet spot in the convective regions of the planet where the winds are still fast enough to deposit the extra heat. Therefore knowing the location of the RCB is important.

Previous estimates of the location of the RCB pointed out that it is at 1000 bars (Fortney et al. 2007). However these models did not consider the high internal entropy hot Jupiters possess. A recent study by Thorngren et al. (2019) accounts for heat deposition and revealed for the first time that the pressure at the RCB (P_{RCB}) is a function of the equilibrium temperature and the planet surface gravity ($\log g$). P_{RCB} moves to lower pressures for the strongly irradiated planets and low $\log g$, reaching pressures around 1 bar, significantly lower than previous estimates. This correlation is a direct consequence of the trend observed between the radius and T_{eq} . Planets with high T_{eq} tend to have large radii, which also means high entropy and thus hot interiors. The high internal temperature will push the RCB high up in the atmosphere.

Chapter 4

Characterization of K2-18 with CARMENES

The first publication presented in the thesis is devoted to the observational project whose aim is to characterize transiting exoplanets. In this chapter we present the characterization of the K2-18 system using the CARMENES spectrograph. The transiting planet was first discovered by the *K2* mission ([Montet et al. 2015](#)) and then confirmed with *Spitzer* observations ([Benneke et al. 2017](#)). The transiting planet orbits around the M2.5 active star every 33 days, placing it thus in the temperate zone. It receives stellar irradiation similar to Earth, making it an interesting target for atmospheric characterization. Our aim is to measure the mass and density of the planet via radial velocity (RV) observations with CARMENES.

The system was also observed with the HARPS spectrograph ([Pepe et al. 2000](#)), where [Cloutier et al. \(2017\)](#) presented the mass and density of the transiting planet. Another signal was also dominant in the HARPS RV time series, which was attributed to a second non-transiting planet in the system. We first present our main results and the publication and then provide a comprehensive overview of the observational evidence for and against the planetary nature of the second controversial signal.

4.1 Results

We obtained simultaneous photometric and spectroscopic data that allows us to better characterize stellar activity. We find that the photometric and spectroscopic activity indicators (the calcium infrared triplet lines Ca II IRT and the H α lines) show a periodic variability consistent with the stellar rotation period estimated using the K2 photometric data (Stelzer et al. 2016; Cloutier et al. 2017). We take advantage that both data sets were taken simultaneously and compare the photometric and chromospheric variability. We find an anticorrelation, meaning that a maximum in the chromospheric variability, i.e. high Ca II emission, corresponds to a minimum in the photometric light curve. This is expected if the chromospheric active regions are located above a photometric spot.

We account for stellar activity in modeling the CARMENES RV data and derive a planetary semi-amplitude of $3.38^{+0.75}_{-0.76}$ m s⁻¹, corresponding to a mass of $M_b = 9.07^{+1.58}_{-1.49} M_{\oplus}$. Combining the mass estimate with the radius estimated from transit observations ($R_b = 2.37 \pm 0.22 R_{\oplus}$; Benneke et al. 2017), we find K2-18 b to be a volatile rich planet. Our results are in agreement with the values derived using the HARPS RV data (Cloutier et al. 2017). With a period of 33 days, K2-18 b is located in the temperate zone of the host star where water vapor may condense in the atmosphere to its liquid form. Indeed, the planet was later observed with the *Hubble Space Telescope*/WFC3 where water vapor and clouds were detected (Benneke et al. 2019; Tsiaras et al. 2019).

Despite the evidence of a second planet in the HARPS data (Cloutier et al. 2017) with a period of 9 days and a semi-amplitude of 4.63 ± 0.72 m s⁻¹, we did not find a significantly strong signal in the CARMENES residual RVs. We computed wavelength-dependent RVs by splitting up the wavelength regime into the shorter and longer wavelength parts, which we will refer to as the blue and red RVs, respectively. We find that the 9 day planetary signal is present only in the second half of the data and only in the blue RVs, which coincides with a higher level of stellar activity. We conclude we do not have strong evidence to confirm the existence of the second planet and interpret the signal as being due to stellar activity.

The detailed methods and results are presented below and were published in Sarkis et al. (2018b) in AJ, 155, 257.



The CARMENES Search for Exoplanets around M Dwarfs: A Low-mass Planet in the Temperate Zone of the Nearby K2-18

Paula Sarkis¹ , Thomas Henning¹, Martin Kürster¹, Trifon Trifonov¹ , Mathias Zechmeister², Lev Tal-Or², Guillem Anglada-Escudé^{3,4}, Artie P. Hatzes⁵, Marina Lafarga⁶, Stefan Dreizler², Ignasi Ribas⁶ , José A. Caballero^{7,8}, Ansgar Reiners², Matthias Mallonn⁹, Juan C. Morales⁶, Adrian Kaminski⁸, Jesús Aceituno¹⁰, Pedro J. Amado⁴, Victor J. S. Béjar^{11,12}, Hans-Jürgen Hagen¹³, Sandra Jeffers², Andreas Quirrenbach⁸, Ralf Launhardt¹ , Christopher Marvin², and David Montes¹⁴

¹ Max-Planck-Institut für Astronomie, Königstuhl 17, D-69117 Heidelberg, Germany; sarkis@mpia.de

² Institut für Astrophysik, Georg-August-Universität, Friedrich-Hund-Platz 1, D-37077 Göttingen, Germany

³ School of Physics and Astronomy, Queen Mary University of London, E1 4NS London, UK

⁴ Instituto de Astrofísica de Andalucía (CSIC), Glorieta de la Astronomía s/n, E-18008 Granada, Spain

⁵ Thüringer Landessternwarte, Sternwarte 5, D-07778 Tautenburg, Germany

⁶ Institut de Ciències de l'Espai (CSIC-IEEC), Campus UAB, c/de Can Magrans s/n, E-08193 Bellaterra, Barcelona, Spain

⁷ Centro de Astrobiología (CSIC-INTA), Campus ESAC, Camino Bajo del Castillo s/n, E-28692 Villanueva de la Cañada, Madrid, Spain

⁸ Landessternwarte, Zentrum für Astronomie der Universität Heidelberg, Königstuhl 12, D-69117 Heidelberg, Germany

⁹ Leibniz Institute for Astrophysics Potsdam (AIP), An der Sternwarte 16, D-14482 Potsdam, Germany

¹⁰ Centro Astronómico Hispano Alemán de Calar Alto (CSIC-MPG), C/Jesús Durbán Remón 22, E-4004 Almería, Spain

¹¹ Instituto de Astrofísica de Canarias, Via Láctea s/n, E-38205 La Laguna, Tenerife, Spain

¹² Departamento de Astrofísica, Universidad de La Laguna, E-38206 La Laguna, Tenerife, Spain

¹³ Hamburger Sternwarte, Gojenbergsweg 112, D-21029 Hamburg, Germany

¹⁴ Departamento de Astrofísica y Ciencias de la Atmósfera, Facultad de Ciencias Físicas, Universidad Complutense de Madrid, E-28040 Madrid, Spain

Received 2017 December 1; revised 2018 April 24; accepted 2018 April 25; published 2018 May 31

Abstract

K2-18 is a nearby M2.5 dwarf, located at 34 pc and hosting a transiting planet that was first discovered by the *K2* mission and later confirmed with *Spitzer Space Telescope* observations. With a radius of $\sim 2 R_{\oplus}$ and an orbital period of ~ 33 days, the planet lies in the temperate zone of its host star and receives stellar irradiation similar to that of Earth. Here we perform radial velocity follow-up observations with the visual channel of CARMENES with the goal of determining the mass and density of the planet. We measure a planetary semi-amplitude of $K_b \sim 3.5 \text{ m s}^{-1}$ and a mass of $M_b \sim 9 M_{\oplus}$, yielding a bulk density around $\rho_b \sim 4 \text{ g cm}^{-3}$. This indicates a low-mass planet with a composition consistent with a solid core and a volatile-rich envelope. A signal at 9 days was recently reported using radial velocity measurements taken with the HARPS spectrograph. This was interpreted as being due to a second planet. We see a weaker, time- and wavelength-dependent signal in the CARMENES data set and thus favor stellar activity for its origin. K2-18 b joins the growing group of low-mass planets detected in the temperate zone of M dwarfs. The brightness of the host star in the near-infrared makes the system a good target for detailed atmospheric studies with the *James Webb Space Telescope*.

Key words: stars: activity – stars: individual (K2-18) – stars: low-mass

1. Introduction

The search for exoplanets around M dwarfs has expanded steadily over recent years because it allows the first detections of low-mass planets in their habitable zones. Because of their low masses and small radii, compared to Sun-like stars, relatively large radial velocity (RV) amplitudes and transit depths can occur. Moreover, the low luminosity of M dwarfs implies that the planets in the habitable zones of these stars are located closer to the star and at shorter orbital periods. Indeed, the recent discoveries of Earth-like low-mass planets orbiting in the habitable zones of M stars have demonstrated the importance of these targets (e.g., Crossfield et al. 2015; Bonfils et al. 2018; Dittmann et al. 2017; Gillon et al. 2017), with perhaps the most exciting discovery being the detection of a potentially habitable planet orbiting our stellar neighbor Proxima Centauri (Anglada-Escudé et al. 2016).

However, a major challenge in detecting low-mass planets around M dwarfs is the activity of their host stars. Common features of activity are dark starspots and bright plage regions, both of which can break the flux balance between the blueshifted approaching hemisphere and the redshifted

receding hemisphere. As a result, active regions may produce distortions in the spectral lines that give rise to RV variations. Such activity signals could obscure or hinder the detection of low-mass planets or even mimic the presence of a false planetary signal. They often appear at the stellar rotation period and its harmonics (Boisse et al. 2011). For example, Robertson et al. (2014) and Hatzes (2016) showed that the RV variations associated with GJ 581d correlate with the $H\alpha$ index, which is a magnetic activity indicator. This is an indication that GJ 581d is most likely not a planet and its RV signal is a harmonic of the stellar rotation period (but see Anglada-Escudé & Tuomi 2015).

There are several ongoing and future precise RV surveys whose main goal is to search for terrestrial planets around M dwarfs, including CARMENES (Quirrenbach et al. 2014), HPF (Mahadevan et al. 2012), IRD (Tamura et al. 2012), NIRPS (Bouchy et al. 2017), and SPIRou (Artigau et al. 2014). Stellar activity poses a challenge in finding these planets. It is even more difficult to disentangle the planetary signal from the activity signal when the orbital period of the planet is close to that of the stellar activity. The stellar rotation

periods of early M dwarfs often coincide with the orbital periods of planets in their habitable zones (Newton et al. 2016). Therefore, correcting for stellar activity requires the rotational period to be accurately known. Contemporaneous photometry is thus crucial to determine the rotational period and to differentiate between planetary and activity signals. Another powerful way is to obtain RV measurements at different wavelengths. This enables the comparison between the blue part and the red part of the spectrum, where, unlike a wavelength-independent Keplerian signal, RV signals due to activity are wavelength dependent (Reiners et al. 2010).

In this work, we aim to estimate the mass and hence the density of the transiting planet K2-18 b by analyzing the RV signals obtained with CARMENES. The host star is a nearby M2.5 V star. K2-18 b receives approximately the same level of stellar irradiation as Earth and orbits in the temperate zone, where water could exist in its liquid form. Two planetary transits were observed with *Kepler* as part of the K2 mission during Campaign 1 (Montet et al. 2015). Later, Benneke et al. (2017) confirmed the planetary nature of the transit signal by observing the same transit depth at a different wavelength, 4.5 μm , with the *Spitzer Space Telescope*. These observations validated the signal seen in the K2 photometry and ruled out the alternative scenario of two long-period planets with similar sizes, each transiting once during the K2 observations.

Cloutier et al. (2017) presented precise RV follow-up observations of K2-18 performed with the HARPS spectrograph (Mayor et al. 2003). They estimated the mass and density of K2-18 b and additionally reported the discovery of a second nontransiting planet in the system. In this paper we first present the results of independent RV observations and analysis of the system. Second, we compare the results of both CARMENES and HARPS campaigns, and finally we combine both data sets to refine the parameters of the system.

For this study, observations were carried out with the high-resolution spectrograph CARMENES (Quirrenbach et al. 2014), which is the first operational spectrograph that is designed to obtain precise RVs in the visible and in the near-infrared (NIR) simultaneously. Its design was motivated by the scientific goal of detecting low-mass planets in the habitable zone of 324 M dwarfs (Reiners et al. 2018b). Trifonov et al. (2018) demonstrated that CARMENES is indeed capable of discovering rocky planets around low-mass stars. Reiners et al. (2018a) reported the discovery of the first CARMENES exoplanet from the survey around HD 147379b, an M0.0V star. We also acquired simultaneous photometric observations in the Johnson *B* and Cousins *R* filters to estimate the stellar rotation period.

As the optimization of the NIR channel to the precision required to carry out such studies is still ongoing, we concentrate on the data taken in the visual channel (VIS), which contains several activity indicators and covers redder orders than HARPS. Where appropriate, we will address the data obtained by the visual channel as CARMENES-VIS and address the instrument as a whole as CARMENES.

The paper is structured as follows: In Section 2 we present the spectroscopic and photometric data sets. In Section 3 we estimate the stellar rotation period and analyze the stellar activity. Section 4 describes different tests that we performed to analyze the RV data set and compare our results with the results of Cloutier et al. (2017). In Section 5 we refine the planetary parameter by combining both CARMENES and

HARPS data sets. In Section 6 we discuss our results, and we give our conclusions in Section 7.

2. Data

2.1. Radial Velocities

CARMENES (Calar Alto search for M dwarfs with Exo-earths with Near-infrared and optical Echelle Spectrographs) is a pair of high-resolution echelle spectrographs (Quirrenbach et al. 2014) mounted on the 3.5 m telescope of the Calar Alto Observatory (CAHA) in Spain. The VIS channel covers the wavelength range from 0.52 to 0.96 μm and has a spectral resolution $R = 94,600$ (Quirrenbach et al. 2016), with a demonstrated precision similar to HARPS and better than Keck/HIRES (Trifonov et al. 2018).

We monitored K2-18 between 2016 December and 2017 June with CARMENES. In total 58 spectra were obtained that were reduced and extracted using the CARACAL pipeline (Caballero et al. 2016; Zechmeister et al. 2018). The pipeline implements the standard method for reducing a spectrum, i.e., each spectrum was corrected for bias, flat-field, and cosmic rays, followed by a flat-relative optimal extraction of the 1D spectra (Zechmeister et al. 2014) and wavelength calibration. In order to get precise RVs, we use the data products from the SERVAl pipeline (Zechmeister et al. 2018), which uses a least-squares fitting algorithm. Following the approach by Anglada-Escudé & Butler (2012), a high signal-to-noise ratio spectrum is constructed by a suitable combination of the observed spectra and used as a template to measure the RVs. The SERVAl-estimated RVs were additionally corrected for small night-to-night systematic zero-point variations, as explained in Trifonov et al. (2018). The origin of the offsets is still unclear, but they are probably due to systematics in the wavelength solution and a slow drift in the calibration source during the night. The time series is shown in the left panel of Figure 6. The optical differential RV measurements and the activity indicators (see Section 3) used in the analysis are reported in Table 6.

2.2. Photometry

We monitored the host star K2-18 for photometric variability with the robotic 1.2 m twin-telescope STELLA on Tenerife (Strassmeier et al. 2004) and its wide-field imager WiFSIP. From 2017 February until 2017 June, we obtained blocks of four exposures in Johnson *B* and four exposures in Cousins *R* over 33 nights. The exposure time was 120 s in *B* and 60 s in *R*. The data reduction was performed identically to previous host star monitoring campaigns with STELLA (Mallonn et al. 2015; Mallonn & Strassmeier 2016). The bias and flat-field correction was made with the STELLA data reduction pipeline. We performed aperture photometry with the software Source Extractor (Bertin & Arnouts 1996). For differential photometry we divided the flux of the target by the combined flux of an ensemble of comparison stars. The flux of these stars was combined after giving them an optimal weight according to the scatter in their light curves (Broeg et al. 2005). We verified that the selection of comparison stars did not significantly affect the variability signal seen in the differential light curve of K2-18. The nightly observations were averaged, and a few science frames were discarded owing to technical problems. The final light curves contain 29 data points in *B* and 28 data points in *R* and are shown in Figure 1.

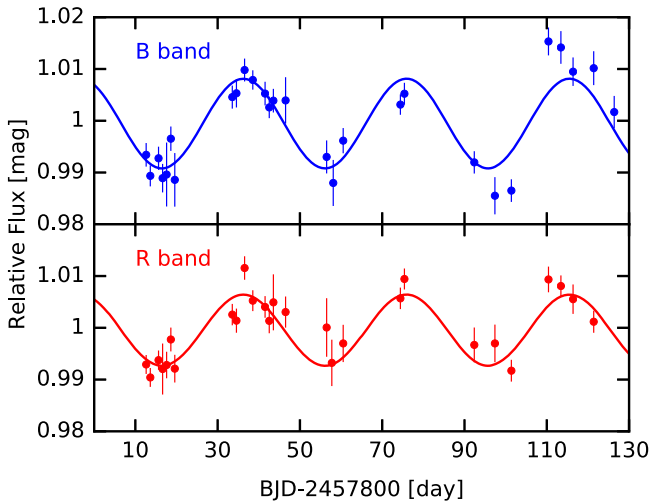


Figure 1. WFSIP/STELLAR differential photometry of K2-18 taken in *B* (top panel) and in *R* (bottom panel). The solid curves show the best sine fit to the data. The star shows photometric variations with a semi-amplitude of 0.86% in the *B* band and 0.69% in the *R* band.

3. Rotation Period and Stellar Activity

The presence of active regions on the surface of a star can produce RV variations and hence mimic the presence of a planet (Robertson et al. 2014, 2015; Hatzes 2016). A common way to distinguish whether the RV signal is due to a planet or due to activity is to check for periodicities in the activity indicators and for photometric variability. We present first the analysis of the stellar photometric variability (Section 3.1), then we present the analysis of the spectroscopic activity indicators (Section 3.2), and finally we compare the chromospheric and photospheric variability (Section 3.3).

3.1. Photometric Variability

Active regions, in the form of dark spots and bright plages, rotate with the stellar surface and produce photometric as well as RV variability. The observed RV signal is often detected at the stellar rotation period (P_{rot}) and its harmonics ($P_{\text{rot}}/2$, $P_{\text{rot}}/3$, ...) (Boisse et al. 2011). Its amplitude and phase may also vary in time owing to the evolution of the active regions. Therefore, contemporaneous photometry and RV observations are important to determine the stellar rotation period and to differentiate between a planetary and stellar activity signals.

The photometric and spectroscopic observations were performed during the same observational season in 2017. In order to estimate the stellar rotation period, we followed the classical approach by applying the Generalized Lomb–Scargle periodogram (GLS; Zechmeister & Kürster 2009) to the photometric data sets. The GLS analysis showed a peak at ~ 40 days in the *B* band and a peak at ~ 39 days in the *R* band. To assess the false-alarm probability (FAP) of the signals, we applied the bootstrap randomization technique (Bieber et al. 1990; Kürster et al. 1997). This is done by computing the GLS of a set obtained by randomly shuffling the observed magnitudes with the times of observations. We repeated this 10,000 times, and the FAP is defined as the number of times where the periodogram of the randomized data sets shows a GLS power as high as or higher than that of the original data set. We found that the FAP is $< 10^{-4}$ in the *B* band and $\text{FAP} = 2 \times 10^{-4}$ in the *R* band. The top panel of Figure 2

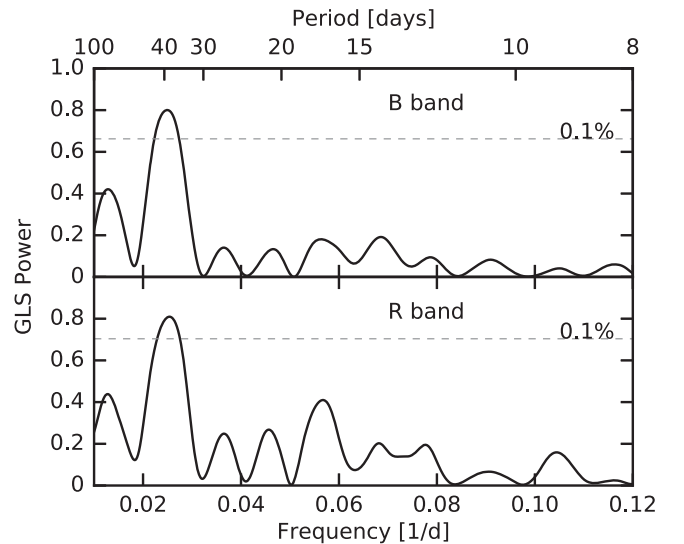


Figure 2. GLS periodogram of the *B* (top panel) and *R* (bottom panel) photometric data sets. The horizontal line indicates the 0.1% FAP level. Both data sets show a significant peak at ~ 40 days, indicating the stellar rotation period.

shows the periodogram of the data taken with the *B* filter, and the bottom panel shows the periodogram of those taken with the *R* filter.

To get a better estimate of the stellar rotation period, we fit both bands simultaneously with a sine wave function and forced both light curves to have the same frequency (f_{BR}) and phase (ϕ_{BR}), but we allowed the offsets (γ_B and γ_R) and amplitudes (A_B and A_R) to be different for each band. In total we fit for six parameters (f_{BR} , ϕ_{BR} , γ_B , γ_R , A_B , and A_R) and performed a Markov Chain Monte Carlo (MCMC) using the `emcee` ensemble sampler (Foreman-Mackey et al. 2013). We adopted flat uniform priors for all parameters and estimate the rotation frequency to be $0.02524 \pm 0.00032 \text{ day}^{-1}$ (39.63 ± 0.50 days). This value is in agreement with the one estimated using the *K2* photometry, where Cloutier et al. (2017) derived a value of $38.6_{-0.4}^{+0.6}$ days using Gaussian processes and Stelzer et al. (2016) derived a value of 40.8 days using an autocorrelation function (private comm.).

We estimated a photometric variability of $8.7 \pm 0.5 \text{ mmag}$ in *B* and a smaller variability of $6.9 \pm 0.5 \text{ mmag}$ in *R*. This difference is expected when the photometric variability is due to cool spots, since the contrast between the spots and the photosphere decreases at redder wavelengths. Figure 1 shows the photometric variations in the *B* filter (in blue) and the *R* filter (in red) and the best-fit model. In Tables 4 and 5 we provide the differential photometry in *B* and *R* bands, respectively.

3.2. Spectroscopic Indicators

The most common and widely used spectroscopic activity indicators can be divided into two different types: the chromospheric and the photospheric ones. The chromospheric activity indicators measure the excess of flux in the cores of, e.g., Ca II H and K, calcium infrared triplet (Ca II IRT), Na I doublet, and H α lines. The cores of these lines have their origin in the stellar chromosphere, and hence they trace stellar magnetic activity. The photospheric activity indicators measure the degree of asymmetry in the line profile. The presence of spots on the photosphere distorts the spectral lines, and therefore periodic variability of the FWHM and bisector span

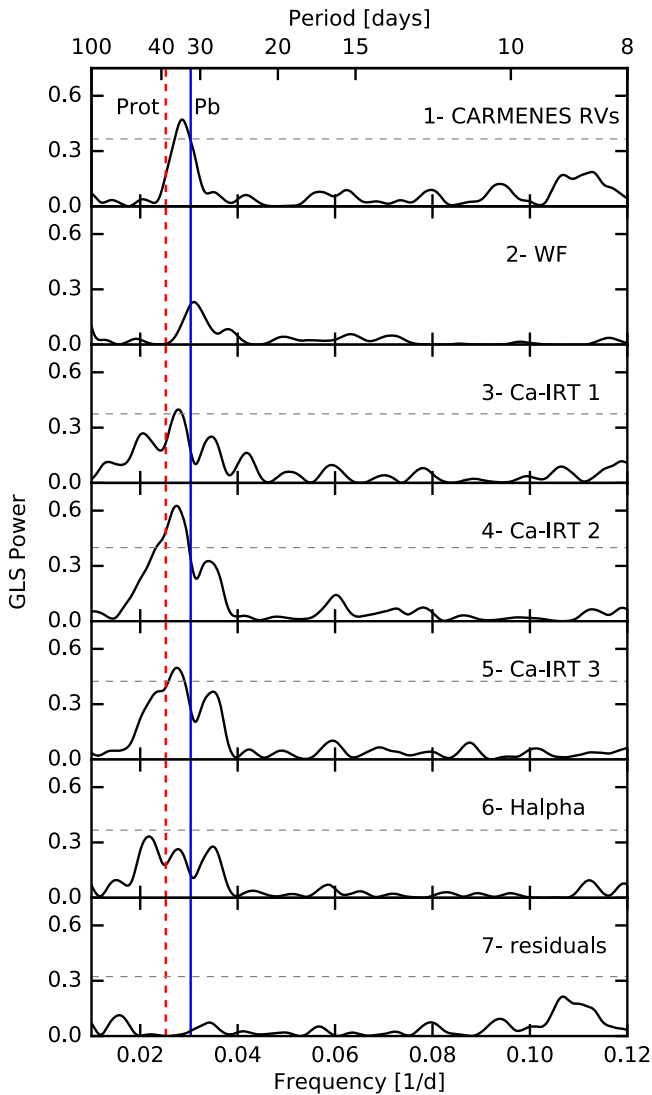


Figure 3. From top to bottom: GLS periodogram of the RVs, window function, the three Ca II IRT lines, H α line, and the RV residuals. The blue solid line shows the orbital period of the planet, P_b , and the red dashed line indicates the stellar rotation period, P_{rot} . The dashed horizontal lines show the 0.1% FAP. Excess power in the RVs close to the orbital period of the planet indicates the presence of the RV signal of the planet in the data. Prominent peaks in the Ca II IRT and H α lines hint at the rotation period of the star.

(BS) of the cross-correlation function (CCF) could indicate the presence of spots. Zechmeister et al. (2018) recently showed that the chromatic index is also an important photospheric indicator (see below).

The SERVAl pipeline provides the line indices of the Ca II IRT, H α , and Na I doublet. The three Ca II IRT lines are centered at 8498.02, 8542.09, and 8662.14 Å; the H α line is centered at 6562.81 Å; and the Na I D lines are centered at 5889.95 and 5895.92 Å. The pipeline also computes the differential line width (dLW) and the chromatic RV index. The former is a measure of the relative change of the width of the average absorption line, and the latter is a measure of the wavelength dependency on the RV. We refer the reader to Zechmeister et al. (2018) for a detailed description of how the various activity diagnostics are computed.

We performed a period search analysis using GLS to search for a significant periodicity that could be related to stellar activity. Figure 3 (panels 3–6) displays the periodograms of the

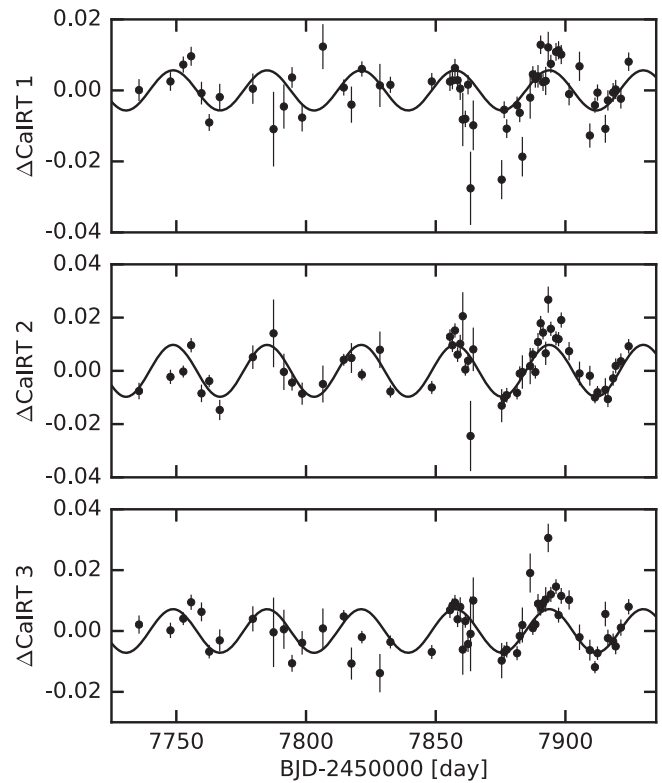


Figure 4. Time series of the three Ca II IRT lines. The black curve shows the best fit to the data using a sinusoidal fit of which we estimate a period of ~ 36 days.

indicators that show a significant peak. Although we inspected a wide range of frequencies, we only show the frequency range of interest that covers the stellar rotation frequency, the planetary frequency of the transiting planet, and the potential 9-day signal (see Section 4.3). All three Ca II IRT indices show a clear dominant peak at ~ 36 days with $\text{FAP} = 3 \times 10^{-4}$, $< 10^{-4}$, and $= 10^{-4}$ for the Ca II IRT 1, Ca II IRT 2, and Ca II IRT 3 lines, respectively, which was determined via bootstrap. The H α periodogram shows three peaks at 29, 36, and 45 days, with $\text{FAP} = 3.7 \times 10^{-3}$ at 36 days. The origin of the signal of both indicators is consistent, within the frequency resolution, with the rotational period of the star derived from photometry (Section 3.1). Similar to the photometric data, we fit the Ca II IRT indices simultaneously with a sine wave function, forcing them to have the same frequency and phase, but allowed the offsets and amplitudes to vary. Figure 4 shows the Ca II IRT line indices along with the best-fit sinusoidal model. The Na I doublet and dLW periodograms, however, are free from significant peaks even though the Na I lines were expected to be good activity indicators for early M dwarfs (Gomes da Silva et al. 2011; Robertson et al. 2015). We report the data of the activity indicators in Table 6.

In addition to the indicators provided by SERVAl, we computed the CCF for each spectrum by cross-correlating the spectrum with a weighted binary mask that was built by co-adding all the observed spectra of the star itself. We selected around 4000 deep, narrow, and unblended lines, which were weighted according to their contrast and inverse FWHM. We computed one CCF for each spectral order, and the final CCF was computed by combining all the individual CCFs according to signal-to-noise ratio. A Gaussian function was fitted to the combined CCF. From this, the FWHM and BS were derived. A

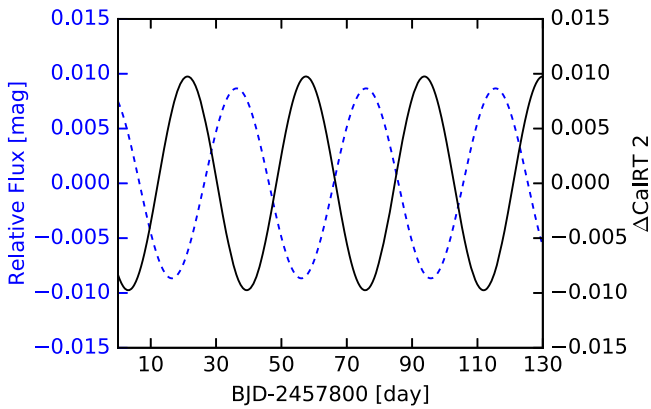


Figure 5. The blue dashed curve shows the photometric variability of K2-18 in the B band with a period of ~ 40 days. This is the same model shown in Figure 1. The solid black curve is the best sine fit of the Ca II IRT 2 line with a period of ~ 36 days. During this time interval, the two curves are 180° out of phase and show an anticorrelation between the photosphere and the chromosphere, especially in the second half of the data set.

period analysis of the FWHM and BS does not show significant periods. The lines in a typical M dwarf spectrum are blended and, thus, may mask changes in the FWHM and BS, which could be the reason why these indicators do not show a variability. Another reason is probably the low projected rotational velocity of the star ($v \sin i$). Reiners et al. (2018b) imposed an upper limit on $v \sin i$ at 2 km s^{-1} . However, from the stellar radius and rotation period (Table 2), we estimate a true equatorial velocity v of only 0.53 km s^{-1} . The spot-BS relationship from Saar & Donahue (1997) predicts, for $v \sin i = 0.53 \text{ km s}^{-1}$, a bisector variability of 0.01 m s^{-1} , which is too small to measure.

3.3. Photospheric versus Chromospheric Variations

The star shows photometric variability with a stellar rotation period of 39.63 ± 0.50 days. The semi-amplitude is 0.87% in the B band and 0.69% in the R band. K2-18 also shows chromospheric variability in the Ca II IRT and $H\alpha$ lines with a period consistent with the rotation period derived from photometry within the frequency resolution. Figure 5 shows the variations of the Ca II IRT second index and the best-fit model (solid black curve) and the photometric variability of K2-18 in the B band (dashed blue curve). There is an anticorrelation between the photometric and the chromospheric variability. The chromosphere shows variations that are 180° out of phase with the photosphere. Similar trends are seen with the first and third Ca II IRT indices and the $H\alpha$ line. This demonstrates that for high Ca II emission values, a minimum in the photometric light curve is observed. This is expected if active chromospheric regions are present on top of a photospheric spot. This is not the first time that an anticorrelation between the chromosphere and photosphere of M dwarfs is observed. Bonfils et al. (2007) reported an anticorrelation for GJ 674, which is also an early M2.5 dwarf. It would be worth checking whether the anticorrelation will hold for late M dwarfs.

We conclude that K2-18 is a moderately active star and there is an anticorrelation between the photospheric and chromospheric variations, which is consistent with the previous results of Radick et al. (1998) for younger, more active stars. Finally, although $H\alpha$ is a good activity indicator (Kürster et al. 2003; Hatzes et al. 2015; Robertson et al. 2015; Jeffers et al. 2018),

the Ca II IRT lines show a significantly stronger peak compared to $H\alpha$. Ca II IRT lines are thus good chromospheric activity proxies (see discussion by Martin et al. 2017) and provide a promising approach to detect stellar activity signals in M dwarfs, where the signal-to-noise ratio is too low to measure Ca II H and K lines, especially for mid- and late M dwarfs. This is also in agreement with the findings of Robertson et al. (2016).

4. RV Analysis

4.1. Periodogram Analysis of the RVs

Benneke et al. (2017) analyzed the *K2* and *Spitzer* light curves and derived an orbital period of $P = 32.939614^{+0.000101}_{-0.000084}$ days. To ensure that we have detected the planet signal with high significance, we performed a periodogram analysis for the RVs obtained with CARMENES-VIS. The RV measurements show a peak at 34.97 days with an FAP $< 10^{-4}$ (Figure 3, panel 1). This peak is approximately the mean of the planetary orbital frequency and the stellar rotation frequency (0.02524 day^{-1}), as measured in Section 3.1. The peak in the periodogram is therefore not centered at the orbital period of the planet, but is shifted halfway between the stellar rotation frequency and the planetary orbital frequency. This shows that the RVs are contaminated by stellar activity, which is conceivable since the star is moderately active (Section 3).

To assess the FAP of the planetary signal and, hence, to confirm the detection of the planet, we applied the bootstrap randomization technique. Unlike the previous analysis where we computed the GLS for the randomly shuffled data set (see Section 3.1), this time we fitted an adapted model to the randomized data points. The model employed the known ephemeris of the planet from Benneke et al. (2017), assumed zero eccentricity, and had only the RV semi-amplitude K_b and the RV zero-point (offset) as free parameters. We performed this 100,000 times and found that the FAP to infer a K_b amplitude as large as (or larger than) the one estimated from the original data is $< 10^{-5}$ and the FAP to get a χ^2 as small as (or smaller than) the one from the original fit and finding at the same time that K_b is positive is also $< 10^{-5}$. This ensures that given the known ephemeris of the planet, we are confident that there is a signal at the known ephemeris, which can be a combination of the planet and activity signals. In Section 4.2 we address several tests that we performed to check whether the RVs and, therefore, the planetary amplitude are affected by activity.

Signals that are sampled at discrete times can produce fake signals in the periodogram that are due instead to observational patterns. In order to check for periodicities due to sampling, we applied the GLS on the window function (WF), which is a periodogram analysis of the observation times. The GLS shows a peak at 32.2 days (Figure 3, panel 2) which is very close to the orbital period of the planet. The reason for that peak is because we aimed to observe the star on a daily basis. However, some nights were lost as a result of bad weather, and more importantly, during dark nights, roughly for a couple of lunar cycles, another instrument was mounted on the telescope, and no observations were carried out with CARMENES. This pattern could have caused the peak in the WF that is close to the lunar synodic cycle.

The presence of a peak in the WF would lead to the detection of the wrong frequency when there is a signal in the

data. Dawson & Fabrycky (2010) showed that the reported periods of 55 Cnc e and HD 156668 b from their respective discovery papers were actually wrong and affected by daily aliases. In the case of K2-18 b, first we have evidence that the star is moderately active (Section 3), and as a result, we anticipate the presence of a signal in the RVs close to the stellar rotation frequency. Second, the planet transits (Montet et al. 2015; Benneke et al. 2017), and therefore we expect another signal in the data close to the orbital period of the planet. However, the proximity of the stellar rotation frequency to the planetary orbital one makes separating them challenging, since the frequencies are not resolved given the time span of the data set.

Given the presence of the peak in the WF and assuming the presence of one signal in the data (either the planetary signal or the stellar rotational period), is it possible to retrieve the signal at the right frequency? To answer this question, we generated a single synthetic sinusoidal signal sampled at times identical to the real RVs. The uncertainty of every point corresponded to the uncertainties derived from the RVs. We generated two different sets, each with an amplitude of 3 m s^{-1} , one set using the stellar rotation frequency and a second set using the planetary frequency. Finally, for the synthetic data generated using the rotational frequency, instead of fixing the phase, we covered a grid of phases $[-\pi, -0.9\pi, \dots, \pi]$. For the planetary signal we assumed that the phase is well constrained. We then did a periodogram analysis for each set and could recover a peak at the true frequency. This test shows that even though the WF shows a peak, we can still retrieve the signal at the right frequency (planet frequency or the stellar rotation frequency) given the data sampling. Hence, the data set is not affected by aliases.

In short, the planet’s orbital period is 32.94 days (Benneke et al. 2017), and the stellar rotation period is ~ 40 days. Not only are the RVs affected by activity, but the WF also shows a peak close to 32.2 days, caused by observational patterns in the way the data were sampled. Previous studies (Robertson & Mahadevan 2014; Vanderburg et al. 2016) showed the difficulty in detecting RV planets in orbits close to the stellar rotation period. Hatzes (2013) and Rajpaul et al. (2016) demonstrated that the WF can give rise to fake signals in the periodogram that mimicked the presence of a planet around α Cen B, which was reported by Dumusque et al. (2012). In the case of K2-18 b, the planet transits, and hence its existence is undeniable. However, a closer look at the WF is needed to check whether the RV signal of the planet is present in the data. This case demonstrates the difficulty in detecting nontransiting low-mass planets not only at orbits close to the stellar rotation period but also when observational patterns are present in the data.

4.2. Orbital Analysis of K2-18 b

We performed joint modeling of the photometric light curves obtained with STELLA and the RV measurements. Similar to Section 3.1, we modeled the photometric data of both bands with a sine wave function and fit for f_{BR} , ϕ_{BR} , γ_B , γ_R , A_B , and A_R . We adopted uniform priors for the phase and offsets of the stellar photometric variability. For f_{BR} , A_B , and A_R we adopted Gaussian priors centered at 0.02524 day^{-1} , 8.7 mmag , and 6.9 mmag , respectively, and with a standard deviation of 0.00032 day^{-1} and 0.5 mmag for both amplitudes (see Section 3.1). We fit the RV measurements with a Keplerian model assuming a circular orbit

($e = 0$) and using the combined K2 and *Spitzer* ephemeris, i.e., we fixed the mid-transit time T_0 and P_b to the values derived photometrically by Benneke et al. (2017) since these parameters are tightly constrained. We accounted for stellar activity in the RV data by assuming that it has a sinusoidal function whose frequency is constrained from the photometric light curves. We let the phase of the stellar activity ϕ_{act} free and thus fit for the phase, amplitude K_{act} , and frequency f_{BR} of the stellar activity. We adopted noninformative priors for the offset, ϕ_{act} , K_{act} , and K_b . The joint analysis was then performed using *emcee* (Foreman-Mackey et al. 2013), and in total we fit for 10 parameters: 6 parameters for the photometric data (mentioned above) and 5 parameters for the RV data (γ , K_b , ϕ_{act} , K_{act} , and f_{BR}); the stellar rotation frequency is the same in both data sets.

The best-fit model gave a planetary semi-amplitude of $K_b = 3.60^{+0.53}_{-0.51} \text{ m s}^{-1}$ and a stellar activity semi-amplitude of $K_{\text{act}} = 2.72 \pm 0.50 \text{ m s}^{-1}$, corresponding to a planetary mass of $M_b = 9.07^{+1.58}_{-1.49} M_{\oplus}$, using $M_* = 0.359 \pm 0.047 M_{\odot}$. Figure 13 shows the joint and marginalized posterior constraints on the model parameters. Using the transit depth, R_b/R_* , and stellar radius, R_* , as reported in Benneke et al. (2017) and provided in Table 2, we derive a planetary radius $R_b = 2.37 \pm 0.22 R_{\oplus}$ ¹⁵ this corresponds to a planetary density of $\rho_b = 4.18^{+1.71}_{-1.17} \text{ g cm}^{-3}$. The $v \sin i$ and spot filling factor estimated from photometry yield an RV semi-amplitude of 2.7 m s^{-1} for spots using the relationship by Hatzes (2002), which is in excellent agreement with the one estimated using the RV data. The planetary semi-amplitude value is consistent with the one derived using HARPS RVs by Cloutier et al. (2017) at the 1σ level. The best-fit model and the phased RVs are shown in Figure 6. We report the stellar and planetary parameters used in this study and the median values of all the parameters, along with the 16th and 84th percentiles of the marginalized posterior distributions, in Table 2.

To further test whether the activity signal is due to cool spots, we compared the phase shift between the photometric light curve and the RV signal due to activity. Figure 7 shows the phase-folded photometric light curve in the *B* band in blue and the RV signal in black. When the spot is at the center of the stellar surface (minimum in the photometric light curve), the contribution of the spot to the RV signal is close to zero. As the spot moves along the stellar surface to the receding redshifted limb (zero in the photometric light curve), the star appears to be blueshifted (minimum in the RV curve). Therefore, the phase shift is $\sim 90^\circ$. This is expected if the variations are due to cool spots, which is also consistent with the multiwavelength photometry analysis (Section 3.1). This is only considering the *flux* effect of dark spots. In general, the RV variations in active regions are induced by two different physical processes: first, the asymmetry in the stellar line profiles created by starspots, and second, the suppression of the convective blueshift effect due to the presence of strong magnetic fields that inhibit convection inside active regions. The convective blueshift effect could explain why the RV curve appears shifted a bit vertically at the minimum phase of the photometric light curve.

Even though the star shows periodic photometric variability, there is evidence that the chromosphere does not show strict

¹⁵ Given the 10% measurement uncertainty on the stellar radius, we expect a 10% measurement uncertainty on the planetary radius. However, Benneke et al. (2017) reported a value on the order of 1%.

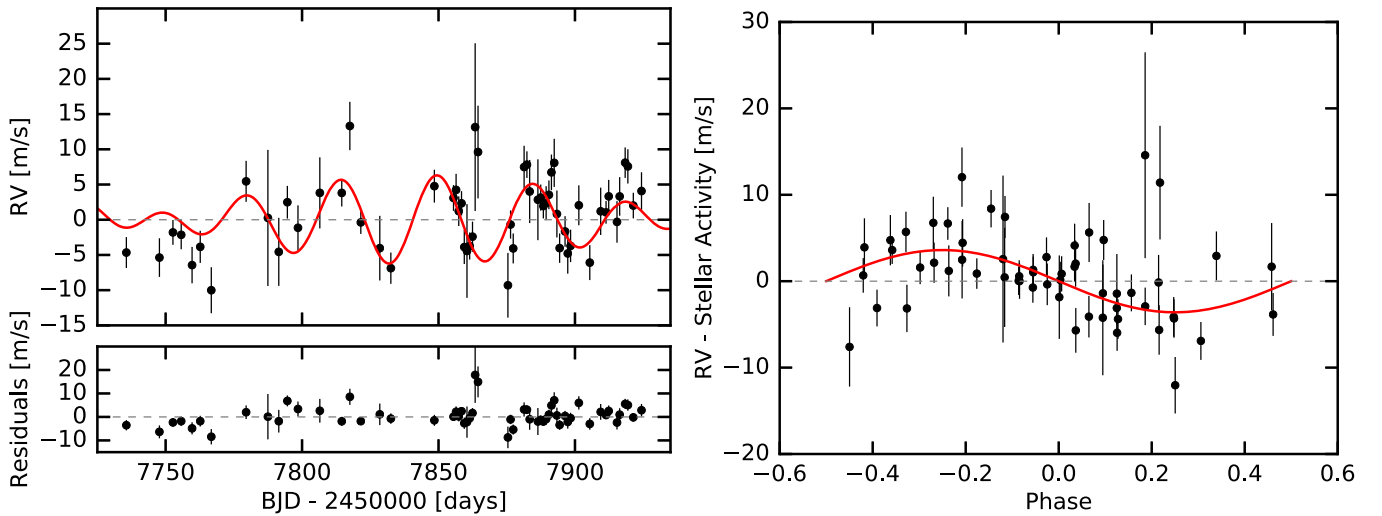


Figure 6. Left: CARMENES-VIS RVs modeled with a circular Keplerian signal of K2-18 b plus stellar activity modeled with a periodic sine function (red line), and the residuals to the best-fit model. Right: phase-folded activity-corrected RVs along with the best-fit planetary model.

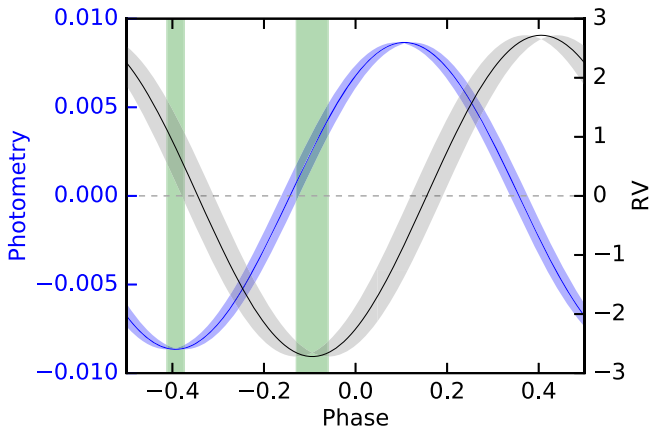


Figure 7. Phase-folded photometric light curve in the *B* band (blue) and RV signal due to activity (black), along with their 1σ uncertainties. To aid the eye, the minima of both curves are shaded in green. Within the error bars the phase shift between the two curves is 90° , as expected if the photometric and RV signals are due to cool spots crossing the visible stellar surface as the star rotates.

periodic sine-like variability (see Section 4.3 and Figure 4, where some points deviate from the best-fit curve, especially Ca II IRT 1 and Ca II IRT 3). Therefore, modeling the RV signal of stellar activity by a periodic sinusoidal function might not be the best approach. However, we next argue that the derived planetary semi-amplitude is not dependent on our choice of the model used to account for stellar activity. We performed several tests to check this dependency. First, following Baluev (2009), we accounted for stellar activity by adding a constant white-noise term often referred to as the RV jitter term, σ_{jitter} . The jitter term is treated as an additional source of Gaussian noise with variance σ_{jitter}^2 and is added in quadrature to the estimated RV uncertainties (Ford 2006). We derived a planetary semi-amplitude $K_b = 3.38^{+0.75}_{-0.76} \text{ m s}^{-1}$ and an RV jitter $\sigma_{\text{jitter}} = 3.02^{+0.57}_{-0.53} \text{ m s}^{-1}$. The planetary semi-amplitude derived using this model is in agreement with the one derived previously, within the 1σ error bars.

Second, to check whether the RVs are affected by stellar activity, we looked for correlations between the raw RVs and the

Table 1
Planetary Semi-amplitudes K_b Derived for the Full, First Half, and Second Half of the Data Set Using the Full- λ RVs, the Blue RVs, and the Red RVs

K_b (m s^{-1})	Full Set	First Set	Second Set
Full- λ RVs	3.35 ± 0.47	3.23 ± 0.66	3.10 ± 0.68
Blue RVs	3.46 ± 0.55	3.71 ± 0.79	$2.71^{+0.80}_{-0.77}$
Red RVs	3.29 ± 0.46	2.77 ± 0.65	3.44 ± 0.64

various activity indicators mentioned in Section 3.2. The top panels of Figure 12 in the Appendix show the measured RVs plotted against the activity indicators and color-coded according to the stellar rotational phase. We did not find a linear correlation between any of these quantities and the measured RVs. However, there is a slight indication that the color-coded data points follow a circular path, especially for Ca II IRT 2, but not with high significance. We further repeated the same analysis after the removal of the planetary signal and still did not find any significant correlations with the activity indicators. The results are shown in the bottom panel of Figure 12. Despite detecting a signal close to the stellar rotational period in both the RVs and the Ca II IRT lines, no evident linear or circular correlation is seen, indicating that the relation is quite complex.

Third, we ignored activity and fit the RVs with a single Keplerian signal and fixed T_0 and P_b to the known photometric values. We estimated a planetary semi-amplitude $K_b = 3.35 \pm 0.47 \text{ m s}^{-1}$, which is also in agreement with the previous results. We further divided the data set into two, each containing 29 data points, and repeated the same analysis for the first and second halves of the data. We found similar planetary semi-amplitudes in both cases, and the values are given in Table 1.

As a final test,¹⁶ we looked at the RV measurements in the red and blue orders of CARMENES-VIS. If the RVs are dominated by activity due to active regions on the stellar surface, then the planetary semi-amplitude in the blue part of

¹⁶ Cloutier et al. (2017) demonstrated that the planetary semi-amplitude derived by implementing a Gaussian process model (Model 1 in their Table 2) is consistent at the 1σ level with the model that neglects any contribution from stellar activity (their Model 4). Also the covariance amplitude is in agreement with zero within the error bars $0.1^{+2.8}_{-0.1} \text{ m s}^{-1}$.

Table 2
Stellar and Planetary Parameters for the System K2-18

Parameter	Value		
Stellar Parameters			
P_{rot} (days)	39.63 ± 0.50		
M_* (M_{\odot}) ^a	0.359 ± 0.047		
R_* (R_{\odot}) ^a	0.411 ± 0.038		
T_* (K) ^a	3457 ± 39		
[Fe/H] (dex) ^a	0.12 ± 0.16		
Transit Parameters			
R_b/R_* (%) ^a	$5.295^{+0.061}_{-0.059}$		
T_0 (BJD) ^a	$2457264.39144^{+0.00059}_{-0.00066}$		
P_b (days) ^a	$32.939614^{+0.000101}_{-0.000084}$		
R_b (R_{\oplus}) ^b	2.37 ± 0.22		
i (deg) ^a	$89.5785^{+0.0079}_{-0.0088}$		
Models			
	Planet only	Planet + sine	Planet + jitter
Radial Velocity Parameters			
K_b (m s^{-1})	3.35 ± 0.47	$3.60^{+0.53}_{-0.51}$	$3.38^{+0.75}_{-0.76}$
K_{act} (m s^{-1})	...	2.72 ± 0.50	...
σ_{jitter} (m s^{-1})	$3.02^{+0.57}_{-0.53}$
e	0 (fixed)	0 (fixed)	0 (fixed)
Planet Parameters			
a (au) ^a	$0.1429^{+0.0060}_{-0.0065}$	$0.1429^{+0.006}_{-0.0065}$	$0.1429^{+0.006}_{-0.0065}$
M_b (M_{\oplus})	$8.43^{+1.44}_{-1.35}$	$9.06^{+1.58}_{-1.49}$	$8.49^{+2.08}_{-1.97}$
T_{eq} (K)	283 ± 15	283 ± 15	283 ± 15
ρ_b (g cm^{-3})	$3.89^{+1.58}_{-1.08}$	$4.18^{+1.71}_{-1.17}$	$3.90^{+1.77}_{-1.24}$

Notes.

^a Parameters based on Benneke et al. (2017).

^b Recalculated the value using R_b/R_* and R_* as derived by Benneke et al. (2017).

the spectrum should be more affected by activity, whereas the red part should be less affected. As a result, if the star is active, a single Keplerian fit to the data should yield different planetary semi-amplitudes for different orders. The RV measurements for K2-18 are available at 42 orders. We calculated an RV weighted mean average for the first and second half of the orders, which we will refer to as the *blue* RVs and as the *red* RVs, respectively, and are reported in Table 6. The blue orders cover the wavelength range from 561 to 689 nm, whereas the red orders cover the range from 697 to 905 nm. We also ignored activity and fit separately the blue and red RVs with a Keplerian model with T_0 and P_b fixed. We did this analysis for the full CARMENES-VIS data set, the first half, and the second half. So, in total we repeated this analysis six times, all of which yielded similar planetary semi-amplitudes within the error bars. The values are reported in Table 1, where we denote the original full wavelength coverage RVs as full- λ RVs. We conclude that the RVs are not dominated by stellar activity and that the estimation of the planetary semi-amplitude is robust and does not depend on the choice of model used to account for stellar activity.

We also computed the results of Table 1 using a Keplerian model plus a sinusoidal model to account for activity, where we fit for the stellar rotation frequency. We find that the planetary semi-amplitude is consistent within 1σ when computed for the

full data, first half, and second half for the full spectral coverage, the red orders, and the blue orders with one exception, the planetary amplitude computed for the second half in the red order. However, the value is in agreement at the 2σ level. Even though we expect the activity semi-amplitudes to be different in different orders, the semi-amplitudes derived are consistent either at the 1σ or at the 2σ level. This could be explained by the low-amplitude signals in both order ranges, which are on the order of $2.7 \pm 0.73 \text{ m s}^{-1}$, i.e., a higher precision would be required to differentiate between the activity semi-amplitudes in different orders.

4.3. Search for a Second Planet

Cloutier et al. (2017) used 75 HARPS RV measurements spanning approximately three seasons of observations to estimate the mass of K2-18 b and to search for additional planetary signals. They reported a nontransiting planet, K2-18 c, with a period of 8.962 ± 0.008 days and a semi-amplitude of $4.63 \pm 0.72 \text{ m s}^{-1}$. The signal of K2-18 c is stronger than that of K2-18 b (see Figure 2 in Cloutier et al. 2017).

We searched for the signal of the second planet in the CARMENES-VIS data set. As mentioned in Section 4, the periodogram only shows one strong peak at 34.97 days, the combined signal of the ~ 33 -day-period planet and the stellar rotation period. The second strongest peak is around 9 days, with an FAP $> 5\%$ and significantly weaker than in the HARPS data. We then subtracted the signal of the 33-day-period planet and stellar activity from the RVs and performed again a period analysis. We still did not find a strong signal at the period of the supposed second (inner) planet (Figure 3, panel 7).

In order to examine whether the absence of the 9-day signal in the CARMENES-VIS data set is due to bad sampling, we generated a synthetic RV data set assuming that there are two planets in the system and using the real observing times of CARMENES. We set the values of the orbital period, semi-amplitude, and time of inferior conjunction of both planets as derived by Cloutier et al. (2017): $P_b = 32.93963$ days, $P_c = 8.962$ days, $K_b = 3.18 \text{ m s}^{-1}$, $K_c = 4.63 \text{ m s}^{-1}$, $T_{0,b} = 2,457,264.39157$ BJD, and $T_{0,c} = 2,457,264.55$ BJD. We further assumed that the uncertainty is the sum of the observational error and a random noise (drawn from a normal distribution centered at 0 and a standard deviation of 0.25 m s^{-1}) to attribute to the stellar jitter determined by Cloutier et al. (2017). We then did a periodogram analysis and could recover an extremely strong peak at 8.98 days with an FAP $< 0.1\%$. This shows that our analysis is not affected by poor time sampling.

We also examined whether the 9-day signal could be caused by stellar activity, since the period is near the fourth harmonic of the stellar rotation period (39.63 days—Section 3; Cloutier et al. 2017). We divided the full CARMENES-VIS data set into two, each consisting of 29 data points, and did a periodogram analysis for each set of the RVs, Ca II IRT, and H α lines. Figure 8 shows the periodograms for both data sets. The top left and top right panels show the periodograms of the activity indicators and RVs, respectively, for the first half of the CARMENES-VIS data set. Similarly, the bottom panels show the periodograms for the second half of the data set. The dashed line in the periodograms of the activity indicators shows the stellar rotation period, P_{rot} , while the dashed line in the RV

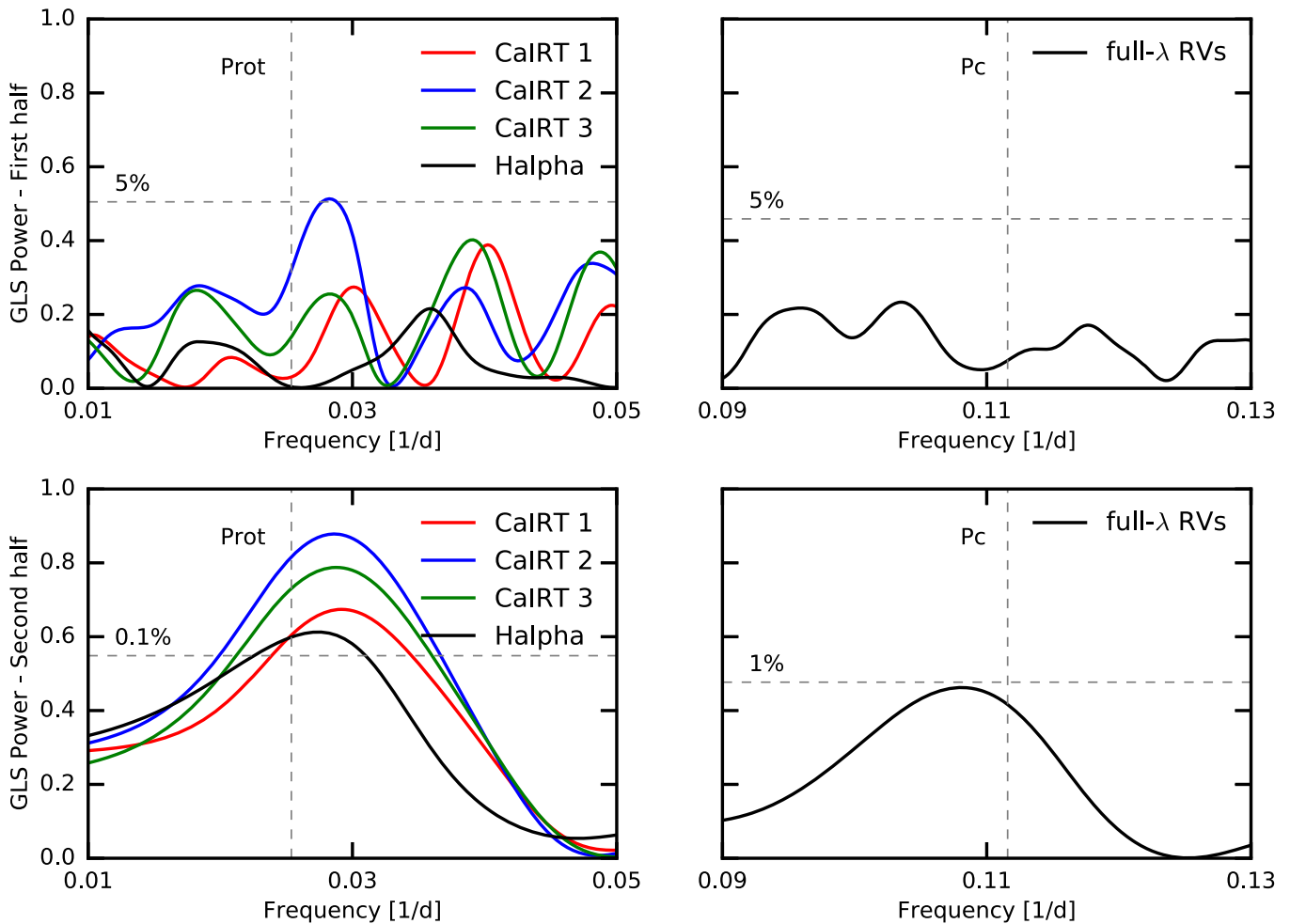


Figure 8. Periodograms of the first (top panels) and second (bottom panels) halves of the Ca II IRT and $H\alpha$ lines (left panels) and CARMENES-VIS RVs (right panels). The dashed lines on the left and right show the stellar rotational period P_{rot} and the claimed period of the inner planet P_c , respectively. The signal of the inner planet is only present in the second half of the data set, when all the spectroscopic indicators show a single significant signal at P_{rot} .

periodograms indicates the period of the inner planet, P_c , as estimated by Cloutier et al. (2017). Note that for the activity indicators only the periodogram region near the rotation period is shown, whereas for the RVs only the region around the 9-day signal is displayed. The different levels of FAPs are indicated in the plot. The first half of the RV data set does not show a power at the orbital period of the supposed inner planet. That is also true when the Ca II IRT and $H\alpha$ lines do not show a consistent peak. The second Ca II IRT index is the only indicator that shows a somewhat stronger peak with an FAP of $\sim 1\%$. The other indicators do not show a prominent peak, and notably $H\alpha$ shows no power at the stellar rotation period. The signal of the 9-day period appears only in the second half of the RV data set, which occurs at the same time when all the Ca II IRT and $H\alpha$ lines show a prominent peak at the stellar rotation period with an FAP $< 0.1\%$, demonstrating that the level of activity increased in this set. This indicates that the signal of the 9-day planet is absent when the star is less active and is present only when the level of activity increases significantly. We thus conclude that the presence of the 9-day signal correlates with the Ca II IRT and $H\alpha$ lines.

This is further illustrated in Figure 9, which shows the periodograms of the full- λ RVs and the blue and red RVs of

CARMENES-VIS, which are calculated as explained in Section 4.2. The periodogram for the blue RVs, red RVs, and full- λ RVs is shown in blue, red, and black, respectively. The legend indicates the period with the highest power for the different sets of RVs. The blue, red, and full- λ RVs show a single peak in the first half of the data set (top panel) close to 36 days. In the second half, interestingly the periodogram of the blue RVs shows the highest GLS power close to 9 days, while the red and full- λ RVs show the highest power close to the orbital period of the 33-day-period planet. This further demonstrates that when the level of stellar activity increased, the blue RVs show a period at the fourth harmonic of the stellar rotation period, while the red RVs do not. This is in line with the notion that RV variations due to photometric starspots are wavelength dependent and more prominent in the blue part of the spectrum, while the variations get smaller at redder wavelengths (Reiners et al. 2010). On the other hand, the RV variation of a planetary signal is wavelength independent and should be constant at all wavelengths. This shows the importance of multiwavelength RV measurements to differentiate planetary from stellar activity signals.

Notably, in the second half of the data set, when the star is relatively more active, the red and full- λ RVs show peaks much

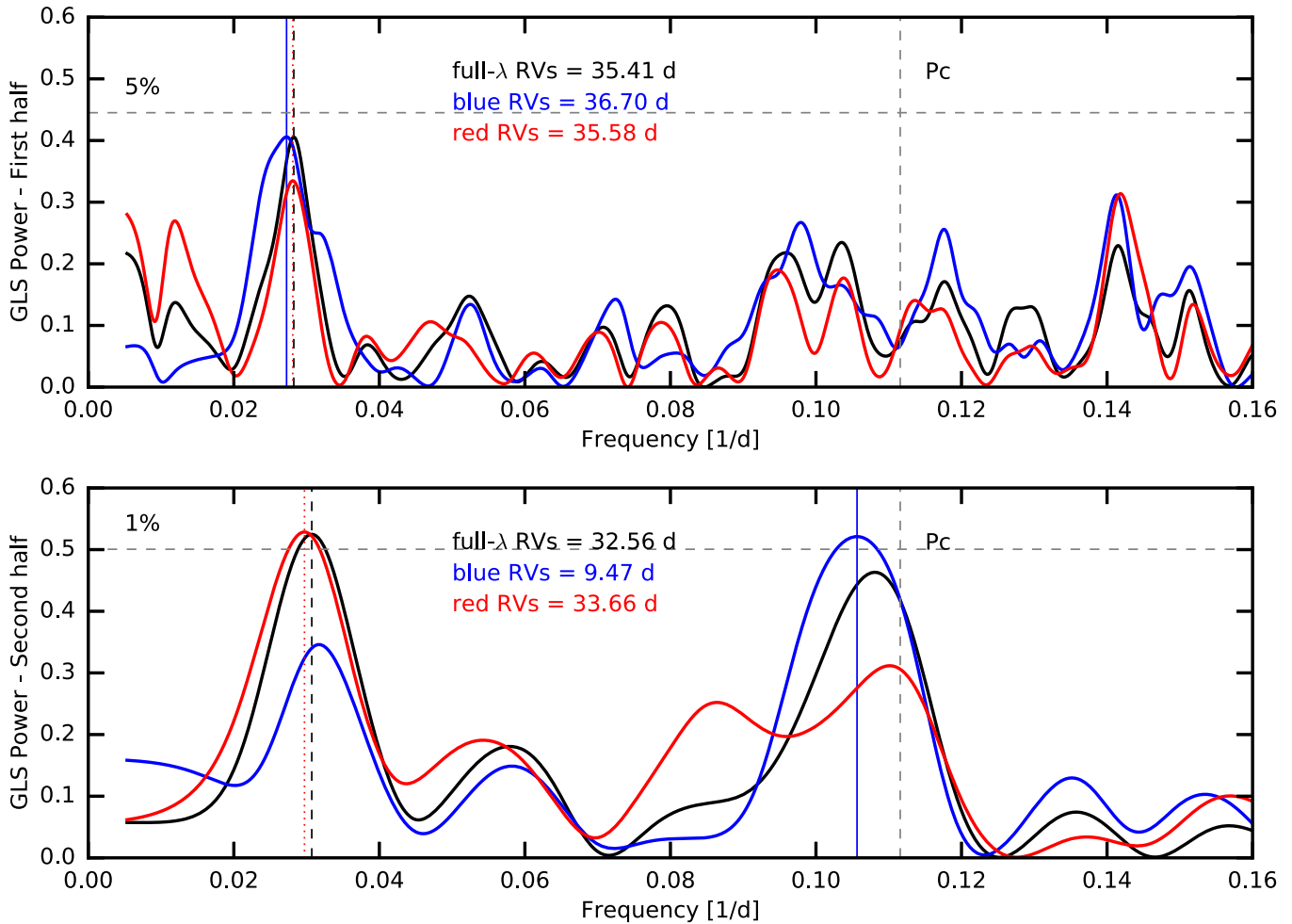


Figure 9. Periodograms of the first (top panel) and second (bottom panel) halves of the data set of the full- λ RVs, blue RVs, and red RVs. The dashed, solid, and dotted lines indicate the peak with the highest GLS power for the full- λ RVs, blue RVs, and red RVs, respectively. The signal of the inner planet P_c is only prominent in the second half of the data set, when the star shows a high level of activity.

closer to the orbital period of the planet and are not shifted in value toward that of the stellar rotation. It seems that the contribution of activity to the RVs appears near the fourth harmonic of the stellar rotation period, and this set shows a clean planetary signal.

We conclude that, although we found evidence of the second planet signal announced recently by Cloutier et al. (2017), the peak is not significant in the CARMENES-VIS data set with an FAP $> 5\%$. The signal is also time and color variable and correlates with stellar activity. Given the sampling and the time baseline of our observations, we conclude that we do not have enough evidence to confirm the presence of the second inner planet, and there is a strong indication that the signal is intrinsic to the star. This also could explain why no transits were observed by *K2* (Cloutier et al. 2017), although this can also be explained by misaligned orbits.

5. Joint HARPS and CARMENES Analysis

In this section, we combine both the HARPS and CARMENES-VIS data sets to refine the parameters of the system, in particular to put constraints on the eccentricity. The joint HARPS (75 observations) and CARMENES-VIS (58

observations) data sets contain a total of 133 RV measurements with a time baseline of 807 days. A periodogram analysis for the WF of the combined set reveals a peak at ~ 372 days (Figure 10, top panel). This is expected since the data set spans three seasons with gaps in between. However, if there is a signal in the raw RVs at frequency f_s , then in the periodogram aliases will likely appear at $f_{\text{alias},n} = f_s + nf_{\text{WF}}$, where n is an integer and f_{WF} is the frequency at which the WF shows a peak (also known as the sampling frequency; Dawson & Fabrycky 2010). Considering that the RV signal due to the transiting planet is present in the data, then $f_{\text{alias},1} = 1/32.9396 - 1/372.01 = 0.02767 \text{ day}^{-1}$ (~ 36.14 days). For $n = 2$, $f_{\text{alias},2} = 0.02498 \text{ day}^{-1}$ (~ 40.03 days). This means that an alias of the orbital frequency of the planet is right at the stellar rotation frequency. Similarly, the aliases of the stellar rotation frequency are also approximately at 33 and 36 days. It is a coincident that the alias of one signal is close to the real frequency of the other signal. It is also by chance that the aliases of both signals meet at 36 days. So these aliases interfere and give a higher GLS power at this frequency. The aliases are shown in the bottom panel of Figure 10.

We performed a Keplerian fit for the combined HARPS and CARMENES-VIS RVs using the publicly available python

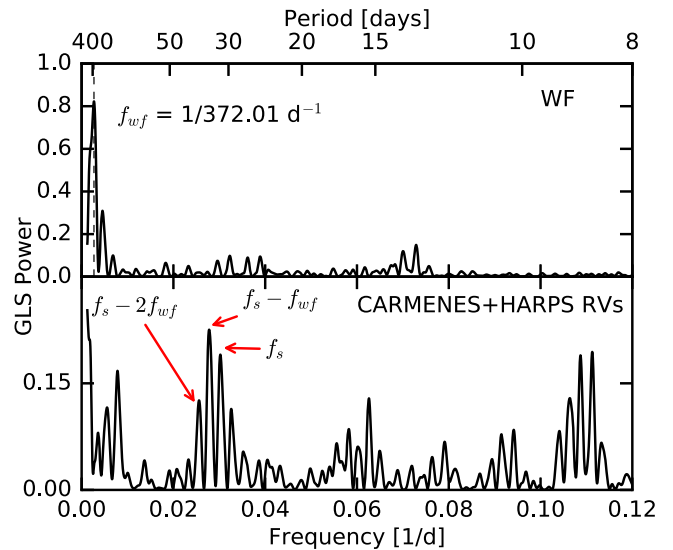
Table 3

Orbital and Planetary Parameters for the System K2-18 b for the Combined HARPS and CARMENES-VIS Data Sets

Parameter	Value
Orbital Parameters	
T_0 (BJD)	$2,457,264.39144 \pm 0.00065$
P_b (days)	$32.939623^{+0.000095}_{-0.000100}$
K_b (m s^{-1})	$3.55^{+0.57}_{-0.58}$
e_b	0.20 ± 0.08
ω_b (rad)	$-0.10^{+0.81}_{-0.59}$
Planetary Parameters	
R_p (R_{\oplus}) ^b	2.37 ± 0.22
i (deg) ^a	$+0.0079$ -0.0088
a (au) ^a	$0.1429^{+0.006}_{-0.0065}$
M_b (M_{\oplus})	$8.92^{+1.70}_{-1.60}$
$T_{\text{eq, b}}$ (K)	284 ± 15
ρ_b (g cm^{-3})	$4.11^{+1.72}_{-1.18}$
Other Parameters	
γ_{CARMENES} (m s^{-1})	-3.40 ± 0.56
γ_{preHARPS} (m s^{-1})	$656.4^{+1.8}_{-1.9}$
$\gamma_{\text{postHARPS}}$ (m s^{-1})	$653.86^{+0.61}_{-0.59}$
σ_{CARMENES} (m s^{-1})	$2.78^{+0.61}_{-0.53}$
σ_{preHARPS} (m s^{-1})	$2.5^{+2.5}_{-1.7}$
$\sigma_{\text{postHARPS}}$ (m s^{-1})	$3.06^{+0.69}_{-0.64}$

Notes.^a Parameters based on Benneke et al. (2017).^b Recalculated the value using R_b/R_* and R_* as derived by Benneke et al. (2017).

package RadVel¹⁷ (Fulton et al. 2018). RadVel is capable of modeling RV data taken with different instruments and uses a fast Keplerian equation solver written in C and the emcee ensemble sampler (Foreman-Mackey et al. 2013). The optical fibers of the HARPS spectrograph were upgraded in 2015 June (Lo Curto et al. 2015). Consequently, this affected the RV offset, and therefore we treated the data taken pre- and post-fiber upgrade separately by accounting for a different velocity offset for each data set (γ_{preHARPS} and $\gamma_{\text{postHARPS}}$). We account for stellar activity by adding an RV jitter term. Three independent jitter terms (σ_{preHARPS} , $\sigma_{\text{postHARPS}}$, σ_{CARMENES}) were added in quadrature to the formal error bars of each instrument and were allowed to vary. We followed Ford (2005) and fit for $\sqrt{e} \cos \omega$ and $\sqrt{e} \sin \omega$ instead of the eccentricity e and argument of periastron ω to increase the rate of convergence. We thus fit for 11 parameters: the planetary semi-amplitude K_b , $\sqrt{e} \cos \omega$, $\sqrt{e} \sin \omega$, planetary orbital period P_b , time of conjunction T_c , the velocity offsets for the CARMENES, HARPS pre-fiber, and HARPS post-fiber upgrade, γ_{CARMENES} , γ_{preHARPS} , and $\gamma_{\text{postHARPS}}$, and for σ_{preHARPS} , $\sigma_{\text{postHARPS}}$, and σ_{CARMENES} . We assign Gaussian priors on P_b and T_c , adopt uniform uninformative priors on the jitter and offset terms, and measure $e = 0.20 \pm 0.08$ and $K_b = 3.55^{+0.57}_{-0.58} \text{ m s}^{-1}$. This translates into a planetary mass $M_b = 8.92^{+1.70}_{-1.60} M_{\oplus}$, consistent with the previous analysis using only the CARMENES-VIS data set (Section 4.2). The median values and the 68% credible intervals are reported in Table 3. The joint and marginalized posterior constraints on the model

**Figure 10.** Periodogram of the WF (top) and RVs for the combined HARPS and CARMENES data set (bottom). The WF shows a significant peak at the sidereal year. The aliases of the planetary signal are indicated by the red arrows.

parameters are shown in Figure 14, and Figure 15 shows the eccentricity distribution.

6. Discussion

Using the CARMENES-VIS data only, we detected K2-18 b with a semi-amplitude of $K = 3.60^{+0.53}_{-0.51} \text{ m s}^{-1}$, in agreement with the value estimated by Cloutier et al. (2017) using data taken with HARPS. We then combined the CARMENES-VIS and HARPS data sets to refine the planetary parameters, particularly to put constraints on the eccentricity. We derived a semi-amplitude of $K_b = 3.55^{+0.57}_{-0.58} \text{ m s}^{-1}$ and eccentricity $e = 0.20 \pm 0.08$, indicating that the planet is on a slightly eccentric orbit. This implies a mass $M_b = 8.92^{+1.70}_{-1.60} M_{\oplus}$ that, combined with the radius estimate we derived in Section 4.2 ($R_b = 2.37 \pm 0.22 R_{\oplus}$), leads to a bulk density of $\rho_b = 4.18^{+1.71}_{-1.17} \text{ g cm}^{-3}$. However, the radius estimate could be affected by systematic errors due to stellar contamination (Rackham et al. 2018). Consequently, this leads to systematic errors in the derived density.

We put the parameters of K2-18 b in the context of discovered exoplanets of similar sizes and masses. Figure 11 shows the position of K2-18 b on the mass–radius diagram in comparison with the other discovered exoplanets¹⁸ with radii less than $4 R_{\oplus}$, with masses smaller than $32 M_{\oplus}$, and with masses and radii determined with a precision better than 30%. Theoretical two-layer models obtained from Zeng et al. (2016) are overplotted. It can be seen that K2-18 b can have a composition consistent with $\sim 100\%$ water (H_2O) or $\sim 50\%$ H_2O and $\sim 50\%$ rock (MgSiO_3), indicating that this planet could be water rich. However, it is well known that there are a wide range of possible compositions for a given mass and radius, all of which include low-density volatiles such as water and H/He (Lopez et al. 2012; Jin & Mordasini 2018). The radius of K2-18 b can be thus explained by a silicate and iron core along with an H/He envelope or with a water envelope. This is in agreement with Rogers (2015) and Wolfgang & Lopez (2015), who showed that most planets with radii larger than $1.6 R_{\oplus}$ are not rocky.

¹⁷ <https://github.com/California-Planet-Search/radvel>¹⁸ Data taken on November 6 from the NASA Exoplanet Archive, <http://exoplanetarchive.ipac.caltech.edu>.

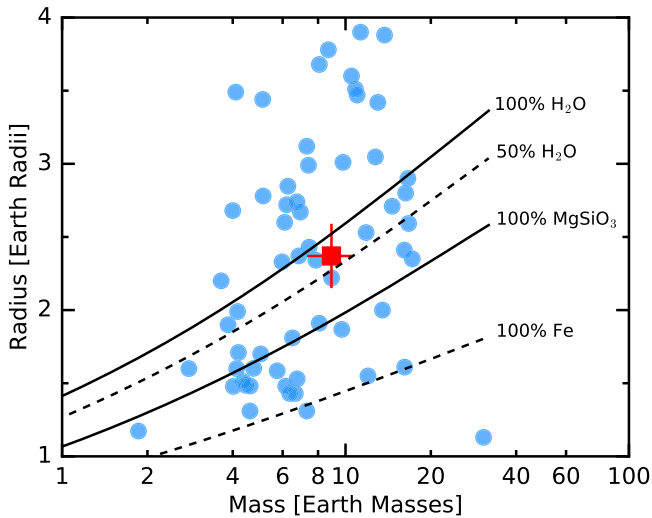


Figure 11. Mass–radius diagram for well-characterized transiting exoplanets. K2-18 b (red square) and theoretical models (Zeng et al. 2016) are overplotted. The composition of the planet is consistent with 50% H₂O and 50% MgSiO₃.

Transiting low-mass planets in the temperate zone of M stars are potential prime targets for detailed atmospheric characterization. K2-18 b lies in the temperate zone of its host star (Kopparapu et al. 2013, 2014) and receives stellar irradiation similar to that of Earth. In addition to that, the brightness of the star in the NIR ($J = 9.8$ mag and $K = 8.9$ mag) and its close distance make K2-18 b a good candidate for detailed atmospheric characterization with observations of secondary transits. The *James Webb Space Telescope* will be able to simultaneously observe from 0.6 to 2.8 μm and thus can provide robust detections of water absorption bands in the NIR (if any) for this bright target.

7. Conclusions

K2-18 b was first discovered as part of the *K2* mission (Montet et al. 2015). Later, Benneke et al. (2017) confirmed the presence of the planet by detecting a third transit light curve of the same depth using *Spitzer*. We obtained contemporaneous photometric and spectroscopic observations to model jointly stellar activity and the Keplerian signal of K2-18 b. We found the stellar rotation period P_{rot} to be close to the planetary orbital period, in agreement with *K2* photometry (Stelzer et al. 2016; Cloutier et al. 2017). The simultaneous photometric data, along with the precise RV observations, were a key to disentangling these two signals. Coincidentally, the WF also shows a peak close to the orbital period of the planet. We performed several tests to assess whether the RV signal due to the planet is detected in the RV data and to test whether stellar activity affects the determination of the planetary amplitude. Our analysis highlights the difficulty in detecting nontransiting low-mass planets in the presence of uneven sampling and, more importantly, when the planetary signal is close to the stellar rotation period.

Using data taken with HARPS, Cloutier et al. (2017) claimed that the system hosts two planets: (i) an outer planet, K2-18 b, with an amplitude of $K_b = 3.18 \pm 0.71 \text{ m s}^{-1}$, and (ii) an inner nontransiting planet, K2-18 c, which has a higher signal compared to K2-18 b and a period of 8.962 ± 0.008 days. While the existence of K2-18 b is in agreement with results

derived with the CARMENES-VIS data, the 9-day signal in our data set is not significant and is only present in the blue part of the spectrum when the star is showing high activity levels. We thus believe that the signal is time and color variable and is correlated with the chromospheric stellar activity. K2-18 c is mostly an artifact of stellar activity and not a bona fide planet. This analysis underscores the importance of multiwavelength RV observations, in particular the value of comparing the blue and red orders of active stars to check the consistency of planetary signals across all orders of the echelle spectrum.

Disentangling the signal of a low-mass planet from the stellar RV signal is still challenging. Following Vanderburg et al. (2016), we also encourage future studies to perform a combined analysis of simultaneous photometry, multiwavelength RV observations, and analysis of the activity indicators to overcome these challenges and to test the reliability of signals present in the data.

CARMENES is an instrument for the Centro Astronómico Hispano-Alemán de Calar Alto (CAHA, Almería, Spain). CARMENES is funded by the German Max-Planck-Gesellschaft (MPG), the Spanish Consejo Superior de Investigaciones Científicas (CSIC), the European Union through FEDER/ERF FICTS-2011-02 funds, and the members of the CARMENES Consortium (Max-Planck-Institut für Astronomie, Instituto de Astrofísica de Andalucía, Landessternwarte Königstuhl, Institut de Ciències de l’Espai, Institut für Astrophysik Göttingen, Universidad Complutense de Madrid, Thüringer Landessternwarte Tautenburg, Instituto de Astrofísica de Canarias, Hamburger Sternwarte, Centro de Astrobiología, and Centro Astronómico Hispano-Alemán), with additional contributions by the Spanish Ministry of Economy, the German Science Foundation (DFG), the states of Baden-Württemberg and Niedersachsen, and the Junta de Andalucía. P.S. would like to thank Christoph Mordasini for his helpful comments on an early draft and Sudeshna Boro-Saikia for her help on calculating the calcium indices of the HARPS data set. I.R. and J.C.M. acknowledge support by the Spanish Ministry of Economy and Competitiveness (MINECO) and the Fondo Europeo de Desarrollo Regional (FEDER) through grant ESP2016-80435-C2-1-R, as well as the support of the Generalitat de Catalunya/CERCA program. A.P.H. acknowledges the support of the Deutsche Forschungsgemeinschaft (DFG) grant HA 3279/11-1. J.A.C., P.J.A. and D.M. acknowledge support by the Spanish Ministry of Economy and Competitiveness (MINECO) from projects AYA2016-79425-C3-1, 2, 3-P. V.J.S.B. is supported by program AYA2015-69350-C3-2-P from Spanish Ministry of Economy and Competitiveness (MINECO). We thank the anonymous referee for useful comments that improved the paper.

Software: astropy (Astropy Collaboration et al. 2013), corner (Foreman-Mackey 2016), emcee (Foreman-Mackey et al. 2013), matplotlib (Hunter 2007), RadVel (Fulton et al. 2018).

Appendix Additional Figures and Tables

The Appendix comprises Figures 12, 13, 14, and 15 as well as Tables 4, 5, and 6.

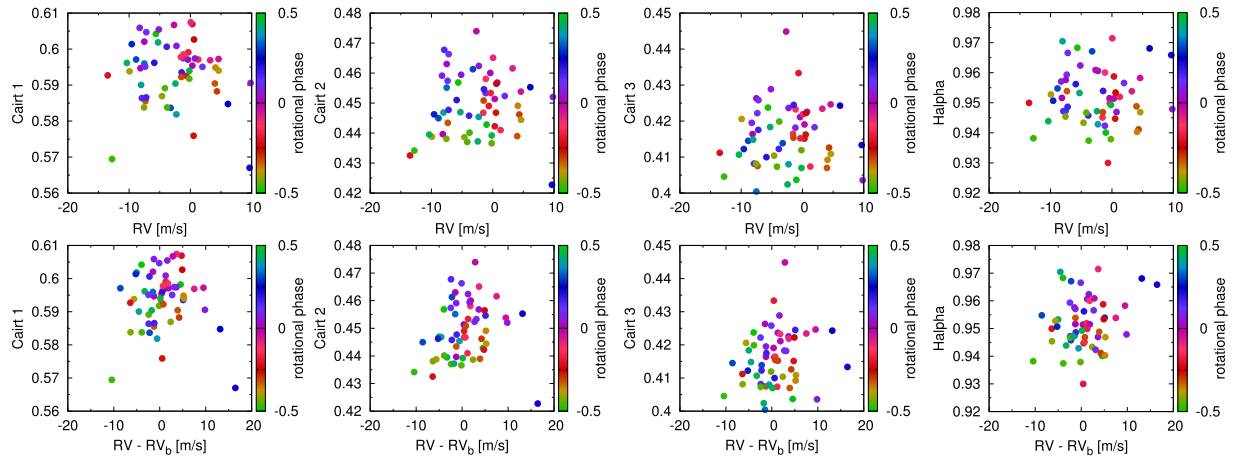


Figure 12. Top panels: measured RVs plotted against various stellar activity indicators phase-folded using the stellar rotation period of 39.63 days. Bottom panels: same as the top panels, but after subtracting the planetary signal. None of the activity indicators show a statistically significant linear or circular correlation with the raw RVs or the residuals.

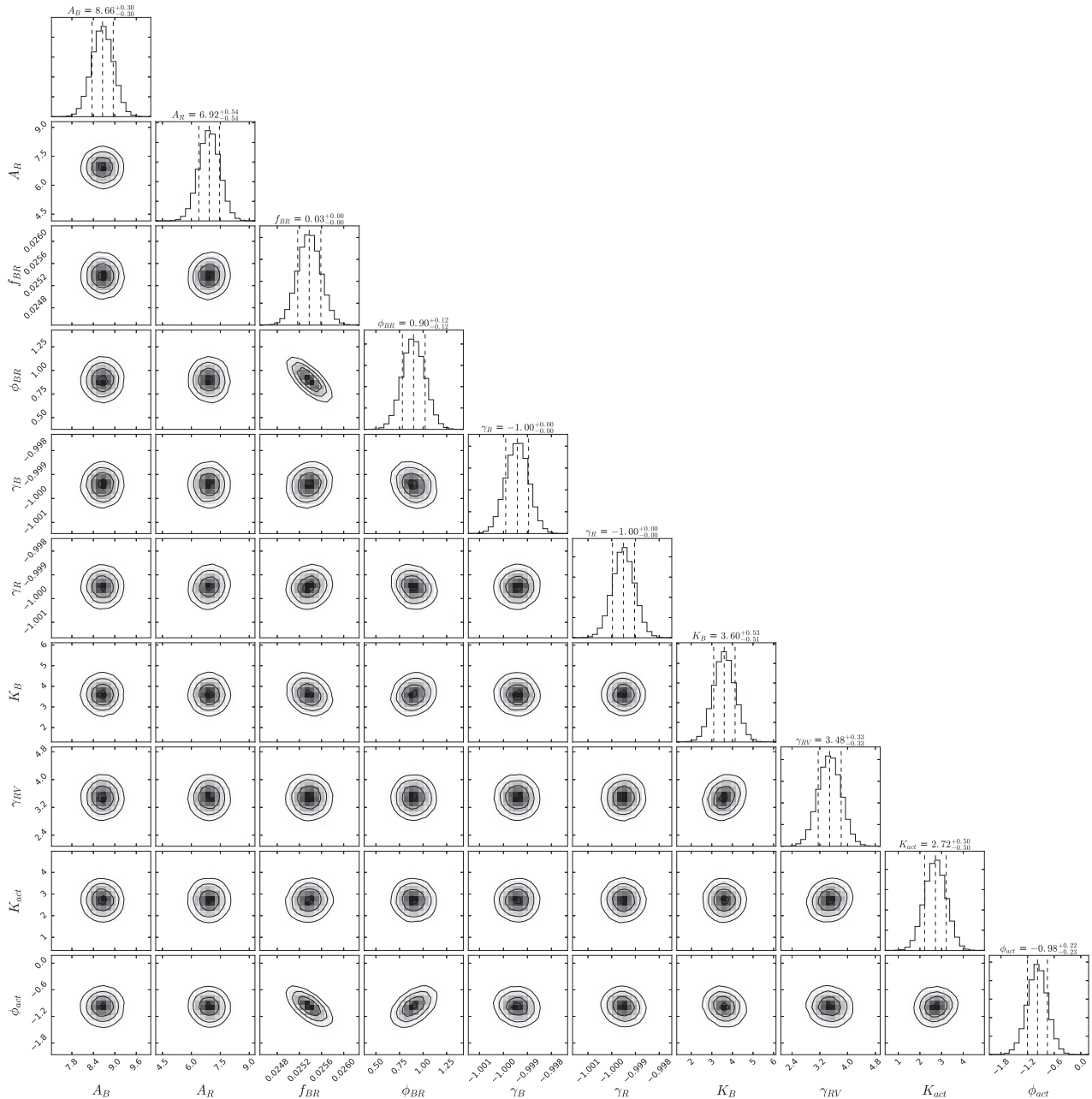


Figure 13. Marginalized posterior distributions on the model parameters from the joint analysis of the photometry and CARMENES RV measurements.

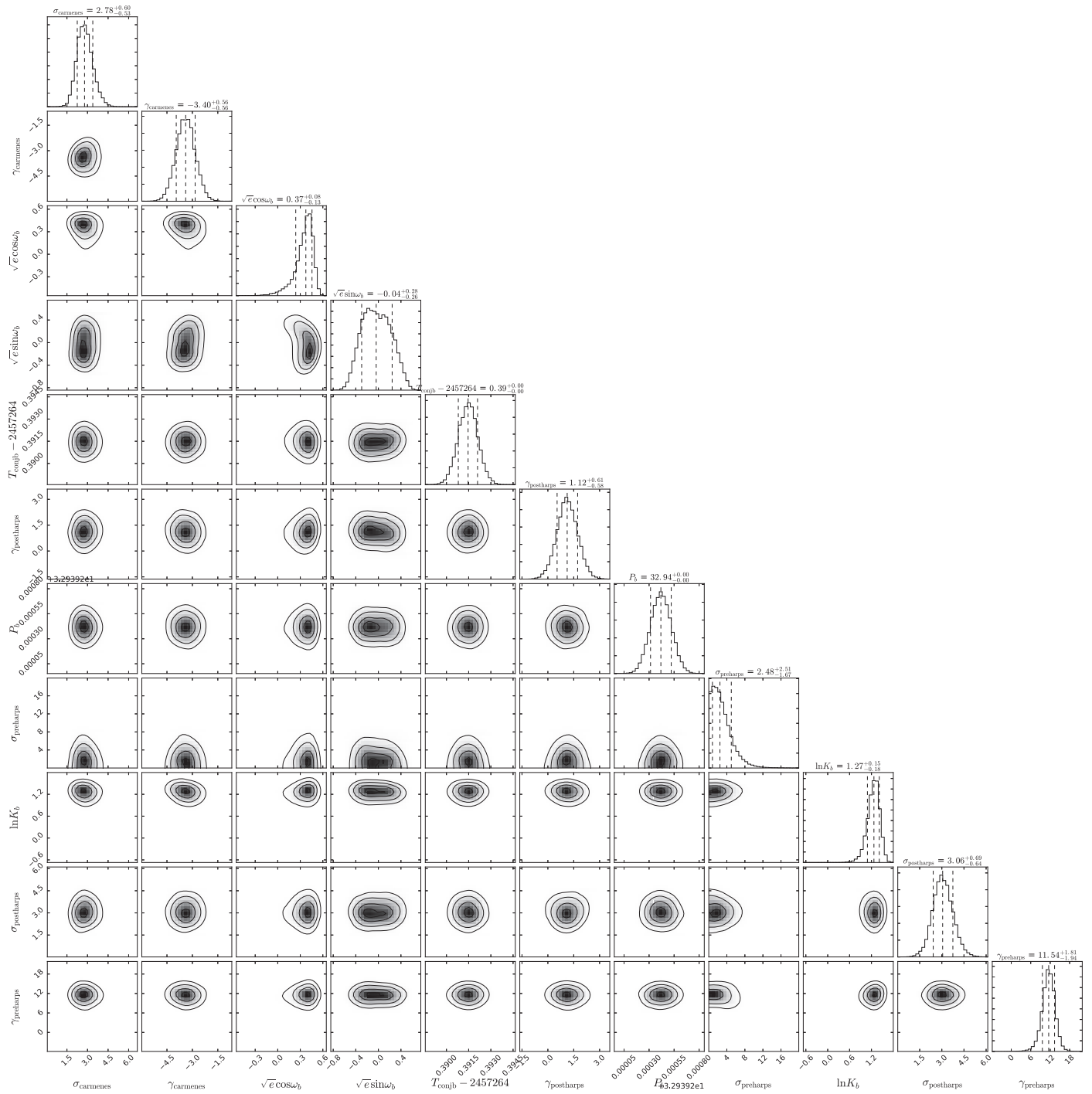


Figure 14. Marginalized posterior distributions on the model parameters of the RV measurements using CARMENES and HARPS data.

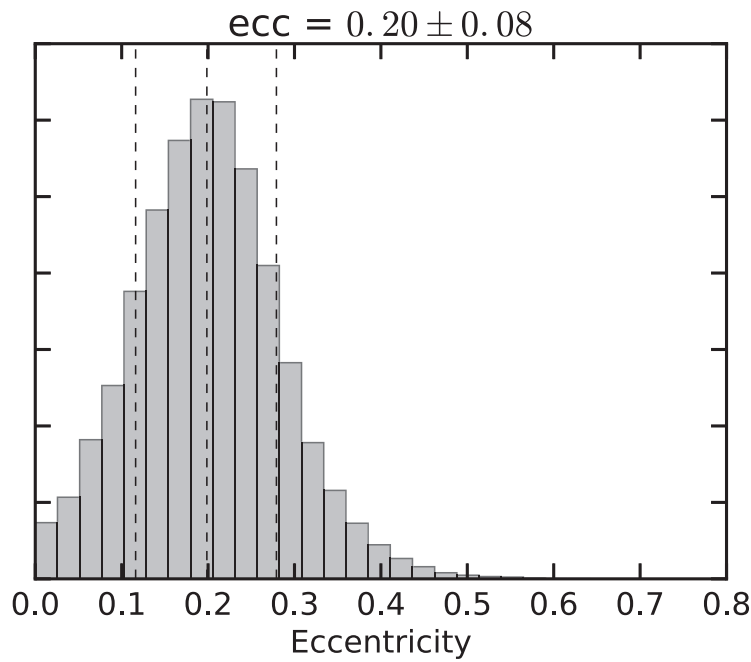


Figure 15. Posterior distribution of e calculated from $\sqrt{e} \cos \omega_b$ and $\sqrt{e} \sin \omega_b$. The vertical lines show the 16th, 50th, and 84th percentile.

Table 4

WiFSIP Photometry in the Johnson B Filter

BJD $-2,450,000$ (days)	ΔB (mag)	σ_B (mag)
7812.628906	0.9934	0.0023
7813.632812	0.9894	0.0020
7815.636719	0.9928	0.0022
7816.625000	0.9889	0.0028
7817.597656	0.9896	0.0062
7818.628906	0.9965	0.0024
7819.585938	0.9886	0.0052
7833.562500	1.0046	0.0022
7834.570312	1.0053	0.0027
7836.550781	1.0098	0.0022
7838.546875	1.0079	0.0019
7841.531250	1.0052	0.0023
7842.546875	1.0026	0.0021
7843.546875	1.0039	0.0023
7846.515625	1.0039	0.0045
7856.492188	0.9930	0.0032
7858.097656	0.9880	0.0044
7860.515625	0.9962	0.0024
7874.417969	1.0031	0.0020
7875.398438	1.0052	0.0021
7892.378906	0.9920	0.0022
7897.390625	0.9855	0.0036
7901.390625	0.9865	0.0022
7910.410156	1.0153	0.0027
7913.429688	1.0142	0.0032
7916.386719	1.0095	0.0028
7921.402344	1.0102	0.0033

Table 5

WiFSIP Photometry in the Cousins R Filter

BJD $-2,450,000$ (days)	ΔR (mag)	σ_R (mag)
7812.628906	0.9929	0.0018
7813.632812	0.9904	0.0018
7815.636719	0.9937	0.0019
7816.628906	0.9920	0.0049
7817.601562	0.9928	0.0026
7818.628906	0.9977	0.0023
7819.585938	0.9921	0.0027
7833.562500	1.0026	0.0021
7834.570312	1.0014	0.0023
7836.554688	1.0115	0.0023
7838.546875	1.0052	0.0020
7841.531250	1.0040	0.0021
7842.546875	1.0013	0.0024
7843.550781	1.0049	0.0054
7846.515625	1.0030	0.0030
7856.496094	1.0001	0.0057
7857.753906	0.9932	0.0045
7860.515625	0.9970	0.0036
7874.417969	1.0057	0.0021
7875.398438	1.0094	0.0020
7892.378906	0.9967	0.0034
7897.394531	0.9970	0.0036
7901.390625	0.9917	0.0021
7910.414062	1.0093	0.0025
7913.433594	1.0081	0.0020
7916.386719	1.0055	0.0028
7921.406250	1.0012	0.0021

Table 6
Radial Velocities Obtained with CARMENES and the Spectroscopic Activity Indicators

BJD -2,450,000 (days)	RV (m s ⁻¹)	σ_{RV} (m s ⁻¹)	Blue RV (m s ⁻¹)	σ_{blue} (m s ⁻¹)	Red RV (m s ⁻¹)	σ_{red} (m s ⁻¹)	Ca II IRT 1 (dex)	σ_{CaIRT1} (dex)	Ca II IRT 2 (dex)	σ_{CaIRT2} (dex)	Ca II IRT 3 (dex)	σ_{CaIRT3} (dex)	H α (dex)	$\sigma_{H\alpha}$ (dex)
7735.617860	-8.14	2.20	-5.15	2.95	-10.17	2.45	0.5947	0.0031	0.4396	0.0031	0.4164	0.0030	0.9516	0.0028
7747.734170	-8.86	2.74	-9.81	2.67	-8.15	2.27	0.5971	0.0026	0.4450	0.0027	0.4145	0.0025	0.9548	0.0026
7752.685530	-5.28	1.76	-7.02	2.14	-3.99	1.87	0.6018	0.0023	0.4470	0.0022	0.4183	0.0021	0.9533	0.0022
7755.711910	-5.63	2.05	-3.51	2.64	-7.15	2.24	0.6042	0.0027	0.4569	0.0027	0.4237	0.0025	0.9683	0.0026
7759.696560	-9.93	2.58	-8.25	3.36	-11.08	2.70	0.5938	0.0032	0.4388	0.0033	0.4206	0.0031	0.9528	0.0034
7762.686550	-7.33	2.28	-6.37	2.30	-8.08	1.98	0.5855	0.0024	0.4434	0.0023	0.4075	0.0022	0.9539	0.0023
7766.737730	-13.49	3.27	-12.96	3.95	-13.82	3.12	0.5927	0.0037	0.4325	0.0038	0.4112	0.0036	0.9500	0.0037
7779.501760	1.97	2.91	-1.12	4.15	3.97	3.34	0.5951	0.0043	0.4524	0.0044	0.4183	0.0041	0.9566	0.0041
7787.481300	-3.23	9.66	-30.21	12.65	9.81	8.79	0.5837	0.0105	0.4613	0.0127	0.4138	0.0114	0.9671	0.0116
7791.467500	-8.05	4.83	-15.53	6.46	-3.63	4.95	0.5900	0.0062	0.4468	0.0068	0.4148	0.0064	0.9705	0.0065
7794.611520	-1.00	2.32	-4.83	2.95	1.63	2.47	0.5982	0.0029	0.4428	0.0030	0.4037	0.0028	0.9401	0.0029
7798.500510	-4.63	3.19	-6.88	4.10	-3.19	3.28	0.5869	0.0039	0.4387	0.0042	0.4104	0.0039	0.9434	0.0040
7806.509160	0.33	5.05	-2.15	7.19	1.73	5.41	0.6069	0.0063	0.4423	0.0069	0.4151	0.0066	0.9587	0.0068
7814.550200	0.32	1.93	1.40	2.16	-0.47	1.89	0.5954	0.0023	0.4514	0.0022	0.4191	0.0021	0.9514	0.0021
7817.513200	9.82	3.43	10.42	5.75	9.50	4.36	0.5906	0.0051	0.4520	0.0056	0.4036	0.0053	0.9479	0.0054
7821.529830	-3.86	1.64	-5.67	2.08	-2.43	1.84	0.6006	0.0022	0.4458	0.0022	0.4123	0.0021	0.9458	0.0021
7828.484510	-7.52	4.59	-14.18	6.96	-3.86	5.16	0.5960	0.0061	0.4551	0.0068	0.4004	0.0063	0.9473	0.0066
7832.533410	-10.36	2.22	-12.34	2.23	-8.90	1.94	0.5962	0.0023	0.4395	0.0023	0.4107	0.0021	0.9439	0.0022
7848.477660	1.28	2.33	4.47	2.51	-0.88	2.08	0.5971	0.0024	0.4410	0.0025	0.4074	0.0023	0.9520	0.0024
7855.492080	-0.39	1.83	2.47	2.80	-2.28	2.27	0.5971	0.0027	0.4600	0.0028	0.4211	0.0026	0.9515	0.0026
7856.441020	0.75	2.28	-1.34	2.72	2.07	2.18	0.5974	0.0025	0.4568	0.0026	0.4226	0.0024	0.9469	0.0025
7857.414140	-2.27	2.10	-3.74	2.70	-1.26	2.22	0.6009	0.0026	0.4624	0.0027	0.4236	0.0025	0.9606	0.0025
7858.429730	-1.15	1.72	-2.99	2.94	-0.02	2.30	0.5974	0.0027	0.4533	0.0028	0.4181	0.0026	0.9424	0.0027
7859.444190	-7.37	2.41	-9.47	3.53	-6.08	2.77	0.5951	0.0032	0.4574	0.0034	0.4222	0.0032	0.9593	0.0032
7860.428910	-7.92	6.65	-25.00	10.06	0.76	7.17	0.5864	0.0075	0.4677	0.0090	0.4082	0.0083	0.9472	0.0080
7861.419190	-7.22	1.92	-8.54	2.31	-6.30	1.93	0.5866	0.0023	0.4477	0.0023	0.4175	0.0022	0.9486	0.0022
7862.453700	-5.89	2.14	-8.13	2.95	-4.41	2.40	0.5962	0.0027	0.4510	0.0028	0.4100	0.0026	0.9562	0.0028
7863.426410	9.66	11.91	4.14	15.66	12.35	10.86	0.5670	0.0103	0.4228	0.0132	0.4133	0.0123	0.9659	0.0121
7864.480200	6.13	6.58	16.88	9.80	1.15	6.66	0.5847	0.0070	0.4553	0.0082	0.4243	0.0076	0.9681	0.0079
7875.429690	-12.79	4.59	-10.20	6.83	-14.18	5.02	0.5694	0.0055	0.4342	0.0062	0.4046	0.0058	0.9382	0.0058
7876.398880	-4.16	2.00	-5.11	2.49	-3.47	2.04	0.5891	0.0024	0.4370	0.0024	0.4073	0.0023	0.9467	0.0023
7877.374190	-7.56	2.13	-8.94	2.81	-6.69	2.23	0.5838	0.0026	0.4381	0.0027	0.4081	0.0026	0.9454	0.0026
7881.362850	4.00	3.02	2.38	2.61	5.10	2.16	0.5904	0.0024	0.4390	0.0025	0.4070	0.0023	0.9488	0.0024
7882.390120	4.34	1.89	-0.42	2.80	7.28	2.21	0.5883	0.0026	0.4462	0.0027	0.4126	0.0025	0.9412	0.0026
7883.401660	0.53	4.48	-2.95	7.00	2.36	5.06	0.5759	0.0056	0.4468	0.0063	0.4162	0.0058	0.9447	0.0057
7886.415260	-0.65	5.74	-16.16	7.95	6.84	5.52	0.5926	0.0059	0.4490	0.0068	0.4333	0.0064	0.9300	0.0062
7887.447050	-0.34	1.85	-1.02	2.38	0.13	1.89	0.5991	0.0023	0.4534	0.0024	0.4152	0.0022	0.9499	0.0023
7888.414710	-1.54	1.76	-3.15	2.51	-0.51	2.00	0.5978	0.0024	0.4468	0.0025	0.4164	0.0023	0.9451	0.0024
7889.433290	-1.13	2.41	-2.06	3.27	-0.53	2.58	0.5985	0.0032	0.4580	0.0034	0.4233	0.0032	0.9600	0.0032
7890.451800	0.05	2.04	1.14	2.58	-0.62	2.05	0.6074	0.0026	0.4651	0.0027	0.4219	0.0025	0.9715	0.0026
7891.373770	3.25	2.53	4.26	2.48	2.98	1.99	0.5969	0.0025	0.4616	0.0026	0.4234	0.0024	0.9538	0.0024
7892.398400	4.59	3.42	-3.05	4.61	8.60	3.36	0.5972	0.0040	0.4538	0.0044	0.4246	0.0041	0.9582	0.0042
7893.377370	-2.67	3.33	-6.62	4.96	-0.59	3.59	0.6067	0.0044	0.4740	0.0049	0.4449	0.0047	0.9609	0.0049
7894.381700	-7.52	2.09	-9.92	2.42	-6.01	1.98	0.6021	0.0025	0.4630	0.0027	0.4263	0.0025	0.9576	0.0025
7896.370090	-5.15	2.17	-4.23	2.38	-5.61	1.93	0.6054	0.0025	0.4594	0.0026	0.4289	0.0024	0.9624	0.0024
7897.357930	-8.27	2.87	-7.76	2.58	-8.60	2.12	0.6059	0.0026	0.4591	0.0027	0.4195	0.0024	0.9571	0.0025
7898.391440	-7.20	2.30	-3.54	2.66	-9.76	2.24	0.6047	0.0027	0.4663	0.0028	0.4258	0.0026	0.9666	0.0027

Table 6
(Continued)

BJD $-2,450,000$ (days)	RV (m s^{-1})	σ_{RV} (m s^{-1})	Blue RV (m s^{-1})	σ_{blue} (m s^{-1})	Red RV (m s^{-1})	σ_{red} (m s^{-1})	Ca II IRT 1 (dex)	σ_{CaIRT1} (dex)	Ca II IRT 2 (dex)	σ_{CaIRT2} (dex)	Ca II IRT 3 (dex)	σ_{CaIRT3} (dex)	H α (dex)	$\sigma_{\text{H}\alpha}$ (dex)
7901.415500	-1.43	2.83	-1.90	3.36	-1.28	2.56	0.5935	0.0032	0.4546	0.0034	0.4245	0.0032	0.9539	0.0033
7905.431390	-9.57	2.48	-10.72	4.20	-8.89	3.28	0.6014	0.0041	0.4462	0.0044	0.4122	0.0042	0.9507	0.0041
7909.422030	-2.29	3.36	-0.58	3.85	-3.36	2.85	0.5819	0.0034	0.4454	0.0037	0.4080	0.0034	0.9429	0.0036
7911.388840	-2.44	1.61	-0.28	2.08	-3.84	1.69	0.5904	0.0021	0.4372	0.0022	0.4024	0.0020	0.9472	0.0021
7912.363270	-0.17	2.34	0.24	2.34	-0.40	1.86	0.5940	0.0023	0.4392	0.0023	0.4070	0.0022	0.9493	0.0022
7915.399610	-3.79	2.95	-2.82	4.28	-4.43	3.43	0.5838	0.0039	0.4401	0.0043	0.4199	0.0040	0.9374	0.0039
7916.378800	-0.18	2.74	-2.60	3.11	1.45	2.52	0.5918	0.0029	0.4366	0.0030	0.4119	0.0028	0.9379	0.0029
7918.393180	4.62	2.17	4.93	2.63	4.34	2.26	0.5940	0.0027	0.4444	0.0028	0.4109	0.0026	0.9468	0.0026
7919.379830	4.09	2.43	6.14	2.62	2.58	2.31	0.5949	0.0027	0.4491	0.0028	0.4092	0.0026	0.9403	0.0025
7921.378720	-1.47	1.82	-1.19	2.64	-1.70	2.23	0.5922	0.0028	0.4508	0.0029	0.4154	0.0027	0.9469	0.0026
7924.380800	0.59	2.67	0.00	2.67	0.90	2.25	0.6027	0.0026	0.4565	0.0027	0.4222	0.0025	0.9534	0.0026

ORCID iDs

Paula Sarkis  <https://orcid.org/0000-0001-8128-3126>
 Trifon Trifonov  <https://orcid.org/0000-0002-0236-775X>
 Ignasi Ribas  <https://orcid.org/0000-0002-6689-0312>
 Ralf Launhardt  <https://orcid.org/0000-0002-8298-2663>

References

- Anglada-Escudé, G., Amado, P. J., Barnes, J., et al. 2016, *Natur*, 536, 437
 Anglada-Escudé, G., & Butler, R. P. 2012, *ApJS*, 200, 15
 Anglada-Escudé, G., & Tuomi, M. 2015, *Sci*, 347, 1080
 Artigau, É., Kouach, D., Donati, J.-F., et al. 2014, *Proc. SPIE*, 9147, 914715
 Astropy Collaboration, Robitaille, T. P., Tollerud, E. J., et al. 2013, *A&A*, 558, A33
 Baluev, R. V. 2009, *MNRAS*, 393, 969
 Benneke, B., Werner, M., Petigura, E., et al. 2017, *ApJ*, 834, 187
 Bertin, E., & Arnouts, S. 1996, *A&AS*, 117, 393
 Bieber, J. W., Seckel, D., Stanev, T., & Steigman, G. 1990, *Natur*, 348, 407
 Boisse, I., Bouchy, F., Hébrard, G., et al. 2011, *A&A*, 528, A4
 Bonfils, X., Astudillo-Defru, N., Díaz, R., et al. 2018, *A&A*, arXiv:1711.06177
 Bonfils, X., Mayor, M., Delfosse, X., et al. 2007, *A&A*, 474, 293
 Bouchy, F., Doyon, R., Artigau, É., et al. 2017, *Msngr*, 169, 21
 Broeg, C., Fernández, M., & Neuhäuser, R. 2005, *AN*, 326, 134
 Caballero, J. A., Guàrdia, J., López del Fresno, M., et al. 2016, *Proc. SPIE*, 9910, 99100E
 Cloutier, R., Astudillo-Defru, N., Doyon, R., et al. 2017, *A&A*, 608, A35
 Crossfield, I. J. M., Petigura, E., Schlieder, J. E., et al. 2015, *ApJ*, 804, 10
 Dawson, R. I., & Fabrycky, D. C. 2010, *ApJ*, 722, 937
 Dittmann, J. A., Irwin, J. M., Charbonneau, D., et al. 2017, *Natur*, 544, 333
 Dumusque, X., Pepe, F., Lovis, C., et al. 2012, *Natur*, 491, 207
 Ford, E. B. 2005, *AJ*, 129, 1706
 Ford, E. B. 2006, *ApJ*, 642, 505
 Foreman-Mackey, D. 2016, *JOSS*, 1
 Foreman-Mackey, D., Hogg, D. W., Lang, D., & Goodman, J. 2013, *PASP*, 125, 306
 Fulton, B. J., Petigura, E. A., Blunt, S., & Sinukoff, E. 2018, *PASP*, 130, 044504
 Gillon, M., Triaud, A. H. M. J., Demory, B.-O., et al. 2017, *Natur*, 542, 456
 Gomes da Silva, J., Santos, N. C., Bonfils, X., et al. 2011, *A&A*, 534, A30
 Hatzes, A. P. 2002, *AN*, 323, 392
 Hatzes, A. P. 2013, *ApJ*, 770, 133
 Hatzes, A. P. 2016, *A&A*, 585, A144
 Hatzes, A. P., Cochran, W. D., Endl, M., et al. 2015, *A&A*, 580, A31
 Hunter, J. D. 2007, *CSE*, 9, 90
 Jeffers, S. V., Schoefer, P., Lamert, A., et al. 2018, arXiv:1802.02102
 Jin, S., & Mordasini, C. 2018, *ApJ*, 853, 163
 Kopparapu, R. K., Ramirez, R., Kasting, J. F., et al. 2013, *ApJ*, 765, 131
 Kopparapu, R. K., Ramirez, R. M., SchottelKotte, J., et al. 2014, *ApJL*, 787, L29
 Kuerster, M., Schmitt, J. H. M. M., Cutispoto, G., & Dennerl, K. 1997, *A&A*, 320, 831
 Kürster, M., Endl, M., Rouesnel, F., et al. 2003, *A&A*, 403, 1077
 Lo Curto, G., Pepe, F., Avila, G., et al. 2015, *Msngr*, 162, 9
 Lopez, E. D., Fortney, J. J., & Miller, N. 2012, *ApJ*, 761, 59
 Mahadevan, S., Ramsey, L., Bender, C., et al. 2012, *Proc. SPIE*, 8446, 84461S
 Mallonn, M., & Strassmeier, K. G. 2016, *A&A*, 590, A100
 Mallonn, M., von Essen, C., Weingrill, J., et al. 2015, *A&A*, 580, A60
 Martin, J., Fuhrmeister, B., Mittag, M., et al. 2017, *A&A*, 605, A113
 Mayor, M., Pepe, F., Queloz, D., et al. 2003, *Msngr*, 114, 20
 Montet, B. T., Morton, T. D., Foreman-Mackey, D., et al. 2015, *ApJ*, 809, 25
 Newton, E. R., Irwin, J., Charbonneau, D., Berta-Thompson, Z. K., & Dittmann, J. A. 2016, *ApJL*, 821, L19
 Quirrenbach, A., Amado, P. J., Caballero, J. A., et al. 2014, *Proc. SPIE*, 9147, 91471F
 Quirrenbach, A., Amado, P. J., Caballero, J. A., et al. 2016, *Proc. SPIE*, 9908, 990812
 Rackham, B. V., Apai, D., & Giampapa, M. S. 2018, *ApJ*, 853, 122
 Radick, R. R., Lockwood, G. W., Skiff, B. A., & Baliunas, S. L. 1998, *ApJS*, 118, 239
 Rajpaul, V., Aigrain, S., & Roberts, S. 2016, *MNRAS*, 456, L6
 Reiners, A., Bean, J. L., Huber, K. F., et al. 2010, *ApJ*, 710, 432
 Reiners, A., Ribas, I., Zechmeister, M., et al. 2018a, *A&A*, 609, L5
 Reiners, A., Zechmeister, M., Caballero, J. A., et al. 2018b, *A&A*, 612, A49
 Robertson, P., Bender, C., Mahadevan, S., Roy, A., & Ramsey, L. W. 2016, *ApJ*, 832, 112
 Robertson, P., & Mahadevan, S. 2014, *ApJL*, 793, L24
 Robertson, P., Mahadevan, S., Endl, M., & Roy, A. 2014, *Sci*, 345, 440
 Robertson, P., Roy, A., & Mahadevan, S. 2015, *ApJL*, 805, L22
 Rogers, L. A. 2015, *ApJ*, 801, 41
 Saar, S. H., & Donahue, R. A. 1997, *ApJ*, 485, 319
 Stelzer, B., Damasso, M., Scholz, A., & Matt, S. P. 2016, *MNRAS*, 463, 1844
 Strassmeier, K. G., Granzer, T., Weber, M., et al. 2004, *AN*, 325, 527
 Tamura, M., Suto, H., Nishikawa, J., et al. 2012, *Proc. SPIE*, 8446, 84461T
 Trifonov, T., Kürster, M., Zechmeister, M., et al. 2018, *A&A*, 609, A117
 Vanderburg, A., Plavchan, P., Johnson, J. A., et al. 2016, *MNRAS*, 459, 3565
 Wolfgang, A., & Lopez, E. 2015, *ApJ*, 806, 183
 Zechmeister, M., Anglada-Escudé, G., & Reiners, A. 2014, *A&A*, 561, A59
 Zechmeister, M., & Kürster, M. 2009, *A&A*, 496, 577
 Zechmeister, M., Reiners, A., Amado, P. J., et al. 2018, *A&A*, 609, A12
 Zeng, L., Sasselov, D. D., & Jacobsen, S. B. 2016, *ApJ*, 819, 127

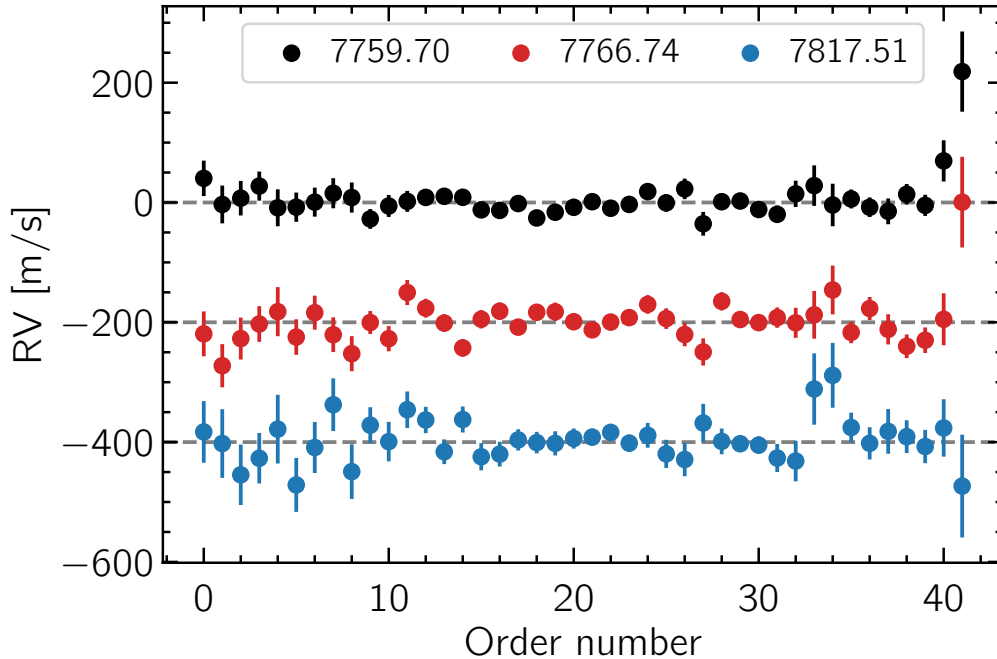


FIGURE 4.1: Radial velocity for each order for the three anomalous RV measurements color coded by the date the measurements were taken. The measurements look reasonable and we could not identify why these RV measurements could suppress the 9-day signal.

4.2 Overview of the 9-day Signal

4.2.1 New HARPS data and Re-analysis of HARPS and CARMENES data (Cloutier et al. 2019)

As mentioned in the publication, 75 spectra were obtained with HARPS and 58 spectra with CARMENES. K2-18 was further observed with HARPS and 31 new RVs were presented in Cloutier et al. (2019) who report that they also detect the 9-day signal with the new

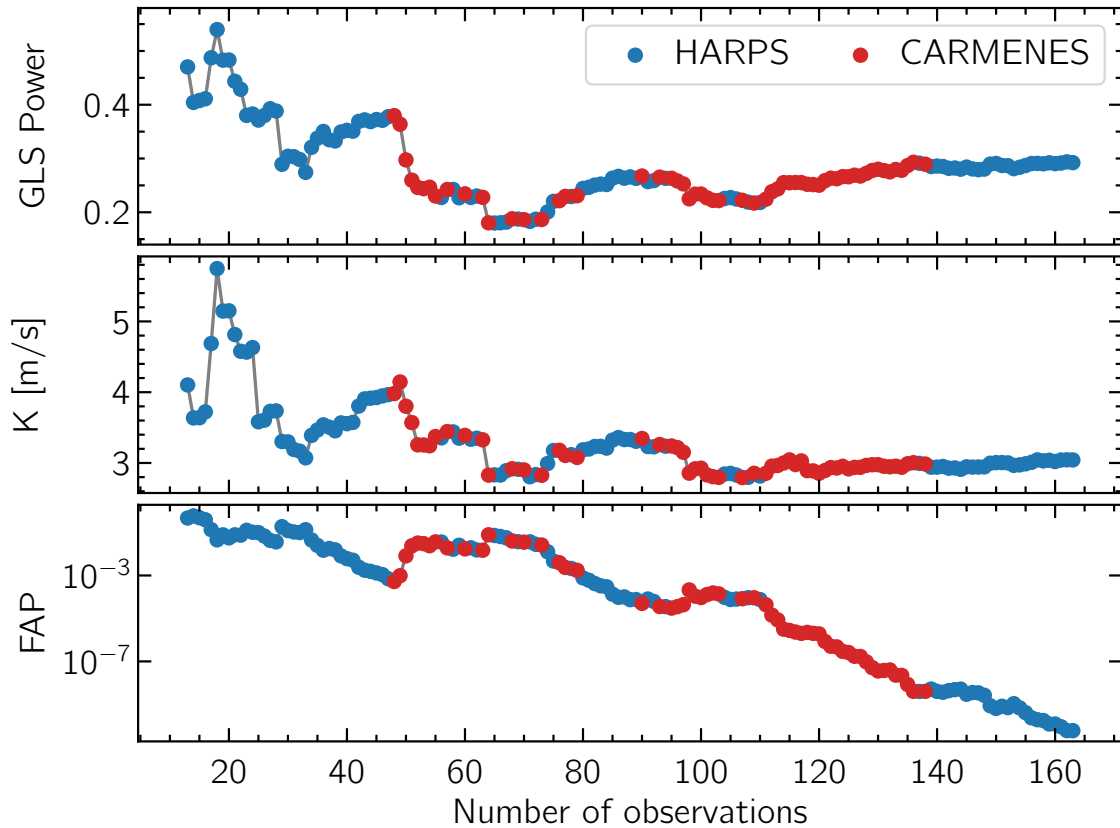


FIGURE 4.2: GLS power, amplitude, and FAP of the 9-day signal as a function of the number of observations. The steady decrease in the FAP indicates that the significance of the signal increases as more observations are added.

This supports the planetary nature of the signal.

observations. [Cloutier et al. \(2019\)](#) analyzed both CARMENES and HARPS data sets and concluded the existence of the second planet. They provided evidence that there are three anomalous RV measurements that suppressed the signal in the CARMENES data. They did this by removing a single RV measurement at a time from the entire CARMENES data and re-computing a Bayesian generalized Lomb–Scargle periodogram (BGLS; [Mortier et al.](#)

2015). The removal of any of the anomalous RV measurements increases the significance of the 9-day signal (see their Figure 3). Finally, upon the removal of the three anomalous RV measurements and re-computing the BGLS for the entire CARMENES data set, the 9-day signal becomes significant (see their Figure 2).

We inspected the individual RV orders of the three anomalous RV measurements, which are presented in Figure 4.1. We could not find a reason why these RV measurements might suppress the 9-day signal, especially that the quality of the measurements is similar to the other RV measurements.

We combined both HARPS and CARMENES data sets to study the evolution of the 9-day signal. Figure 4.2 shows the evolution with the number of measurements of the GLS power, amplitude, and FAP of the 9-day signal for the combined HARPS (blue) and CARMENES (red) data. This was done by looking at the residuals, i.e. after removing the planetary signal at ~ 33 days. The FAP of the signal decreases as more data is added while the amplitude and the GLS power are stable for $N > 100$. The same pattern is seen when analyzing separately either HARPS or CARMENES data, yet the signal is not significant in CARMENES. The stability and significance of the signal seen in HARPS data suggest that indeed the source of the signal is a planet, in agreement with the findings of Cloutier et al. (2017) and Cloutier et al. (2019). This conclusion however cannot justify the chromatic dependence of the 9-day signal observed with CARMENES.

4.2.2 Summary

To conclude, the HARPS measurements support the planetary nature of the 9-day signal. The CARMENES data favor two planets only when the 3 anomalous measurements are omitted, whereas the full time-series does not suggest a second planet at 9-days. The planet hypothesis cannot explain the color dependence of the signal seen in the CARMENES data, which coincides with high level of stellar activity.

If the source of the signal is indeed a planet, then the fewer CARMENES measurements compared to HARPS and the sub-optimal time-sampling as shown by Cloutier et al. (2019) could explain why the signal was not detected. In this case, more CARMENES RV measurements are needed to detect the planetary signal.

4.3 Conclusion

In this Chapter we presented the characterization of the K2-18 system based on 58 RV measurements from CARMENES and also by combining both HARPS and CARMENES data. We showed that the star is an active M-dwarf showing photometric and chromospheric variability. While the existence of the second planet is debatable, the transiting planet is a low-mass planet in the temperate zone of the host star receiving irradiation similar to Earth.

How could I know, how could I know?
That I'll get lost in space to roam forever
Lost In Space – Avantasia

Chapter 5

Discovery and Characterization of HATS-59b,c

Within the context of characterizing transiting exoplanets, this chapter presents the first multiplanet system discovered within the HATSouth survey. The inner transiting planet is a hot Jupiter with a planet mass of $0.806 \pm 0.069 M_J$ and a radius of $1.126 \pm 0.077 R_J$. While the structure of the hot Jupiter is typical to its class, the orbital parameters, specifically the eccentric orbit ($e = 0.129 \pm 0.049$) makes it an interesting system. Disk migration and high orbital migration have been proposed to explain the existence of close-in giant planets. The former predicts circular and aligned orbits (Lin et al. 1996) while the latter results in eccentric and misaligned orbits (Fabrycky & Tremaine 2007; Naoz et al. 2012). The eccentric orbit of HATS-59 b is potentially due to scattering by a distant massive companion. Indeed, the radial velocities suggest an outer massive companion, HATS-59 c, with $m \sin i = 12.70 \pm 0.87 M_J$ and a period of 1422 days.

While Knutson et al. (2014) and Bryan et al. (2016) found that almost half of the hot Jupiters have a planetary companion, to-date only 9 companions have their orbits fully resolved. This is mainly due to the lack of long-term RV monitoring required for such detections. The RV data we collected for this systems span 5 years where half of them were obtained with FEROS. FEROS played a critical role in enabling the detection of the outer companion and highlights the importance of RV follow-up campaigns.

The presence of an inward Jupiter-like planet along with an outer massive companion poses a challenge for planet formation models based on the core accretion paradigm. It is not clear whether core accretion can form such planets. The architecture of this system

will be valuable to understand the migration mechanisms of hot Jupiters and will help constrain the formation of gas giant planets.

We present the paper highlighting the discovery and characterization of the multi-planet system, HATS-59 b,c. The paper was published in [Sarkis et al. \(2018a\)](#) in AJ, 155, 257.



HATS-59b,c: A Transiting Hot Jupiter and a Cold Massive Giant Planet around a Sun-like Star*

P. Sarkis¹ , Th. Henning¹, J. D. Hartman² , G. Á. Bakos^{2,21,22} , R. Brahm^{3,4} , A. Jordán^{1,3,4}, D. Bayliss⁵ , L. Mancini^{1,6,7} , N. Espinoza^{1,3,4}, M. Rabus^{1,3}, Z. Csabry², W. Bhatti² , K. Penev⁸ , G. Zhou⁹, J. Bento¹⁰, T. G. Tan¹¹, P. Arriagada¹² , R. P. Butler¹³ , J. D. Crane¹³ , S. Shectman¹³, C. G. Tinney^{14,15} , D. J. Wright^{14,15}, B. Addison¹⁶, S. Durkan¹⁷ , V. Súc³ , L. A. Buchhave¹⁸ , M. de Val-Borro¹⁹, J. Lázár²⁰, I. Papp²⁰, and P. Sári²⁰

¹Max Planck Institute for Astronomy, Heidelberg, Germany; sarkis@mpia.de

²Department of Astrophysical Sciences, Princeton University, NJ 08544, USA

³Instituto de Astrofísica, Facultad de Física, Pontificia Universidad Católica de Chile, Av. Vicuña Mackenna 4860, 7820436 Macul, Santiago, Chile

⁴Millennium Institute of Astrophysics, Av. Vicuña Mackenna 4860, 7820436 Macul, Santiago, Chile

⁵Department of Physics, University of Warwick, Coventry CV4 7AL, UK

⁶Department of Physics, University of Rome Tor Vergata, Via della Ricerca Scientifica 1, I-00133 Rome, Italy

⁷INAF–Astrophysical Observatory of Turin, via Osservatorio 20, I-10025 Pino Torinese, Italy

⁸Physics Department, University of Texas at Dallas, 800 W Campbell Rd. MS WT15, Richardson, TX 75080, USA

⁹Harvard-Smithsonian Center for Astrophysics, Cambridge, MA 02138, USA

¹⁰Research School of Astronomy and Astrophysics, Australian National University, Canberra, ACT 2611, Australia

¹¹Perth Exoplanet Survey Telescope, Perth, Australia

¹²Department of Terrestrial Magnetism, Carnegie Institution for Science, Washington, DC 20015, USA

¹³The Observatories of the Carnegie Institution for Science, 813 Santa Barbara St., Pasadena, CA 91101, USA

¹⁴Australian Centre for Astrobiology, School of Physics, University of New South Wales, NSW 2052, Australia

¹⁵Exoplanetary Science at UNSW, School of Physics, University of New South Wales, NSW 2052, Australia

¹⁶Mississippi State University, Department of Physics & Astronomy, Hilburn Hall, Starkville, MS 39762, USA

¹⁷Astrophysics Research Centre, Queens University, Belfast, Belfast, Northern Ireland, UK

¹⁸DTU Space, National Space Institute, Technical University of Denmark, Elektrovej 328, DK-2800 Kgs. Lyngby, Denmark

¹⁹Astrochemistry Laboratory, Goddard Space Flight Center, NASA, 8800 Greenbelt Rd., Greenbelt, MD 20771, USA

²⁰Hungarian Astronomical Association, 1451 Budapest, Hungary

Received 2018 May 13; revised 2018 August 24; accepted 2018 August 29; published 2018 October 18

Abstract

We report the first discovery of a multi-planetary system by the HATSouth network, HATS-59b,c, a planetary system with an inner transiting hot Jupiter and an outer cold massive giant planet, which was detected via radial velocity. The inner transiting planet, HATS-59b, is on an eccentric orbit with $e = 0.129 \pm 0.049$, orbiting a $V = 13.951 \pm 0.030$ mag solar-like star ($M_* = 1.038 \pm 0.039 M_\odot$ and $R_* = 1.036 \pm 0.067 R_\odot$) with a period of 5.416081 ± 0.000016 days. The outer companion, HATS-59c is on a circular orbit with $m \sin i = 12.70 \pm 0.87 M_J$ and a period of 1422 ± 14 days. The inner planet has a mass of $0.806 \pm 0.069 M_J$ and a radius of $1.126 \pm 0.077 R_J$, yielding a density of $0.70 \pm 0.16 \text{ g cm}^{-3}$. Unlike most planetary systems that include only a single hot Jupiter, HATS-59b,c includes, in addition to the transiting hot Jupiter, a massive outer companion. The architecture of this system is valuable for understanding planet migration.

Key words: photometric – planetary systems – stars: individual (HATS-59) – techniques: spectroscopic

Supporting material: machine-readable table

1. Introduction

During the past decade, the number of exoplanets has increased steadily and by now more than 3500 exoplanets have been

statistically validated. Exoplanets are very common and have a wide variety of properties (for a review, see Winn & Fabrycky 2015), which offer a unique opportunity to constrain their formation and evolution (Mordasini et al. 2016; Jin & Mordasini 2018). Hot Jupiters, i.e., gas giant planets on short orbital periods, still pose many challenges for planet formation models. It is believed that such planets formed beyond the iceline, several au from the central star, and migrated inwards through interactions with the disk (e.g., Lin et al. 1996). However, disk migration predicts circular and aligned orbits (e.g., Goldreich & Tremaine 1980; Artymowicz 1993) and cannot explain the existence of several hot Jupiters that have been found on retrograde or misaligned orbits (for a review see Winn & Fabrycky 2015). Alternative scenarios have been thus proposed, which involve interactions with a third distant body or planet–planet scattering that can result in eccentric and misaligned orbits (Kozai 1962; Lidov 1962; Nagasawa et al. 2008; Li et al. 2014; Petrovich 2015).

One approach to put constraints on the different migration mechanisms is to measure the spin–orbit alignment via the

* The HATSouth network is operated by a collaboration consisting of Princeton University (PU), the Max Planck Institute für Astronomie (MPIA), the Australian National University (ANU), and the Pontificia Universidad Católica de Chile (PUC). The station at Las Campanas Observatory (LCO) of the Carnegie Institute is operated by PU in conjunction with PUC, the station at the High Energy Spectroscopic Survey (H.E.S.S.) site is operated in conjunction with MPIA, and the station at Siding Spring Observatory (SSO) is operated jointly with ANU. This paper includes data gathered with 6.5 m *Magellan* Telescopes located at Las Campanas Observatory, Chile, and the MPG 2.2 m, the NTT, and the Euler 1.2 m telescopes at the ESO Observatory in La Silla. This paper uses observations obtained with facilities of the Las Cumbres Observatory Global Telescope. Based in part on observations made with the 3.9 m Anglo-Australian Telescope and the ANU 2.3 m Telescope both at SSO. Based in part on observations made with the facilities of the Las Cumbres Observatory Global Telescope, the Perth Exoplanet Survey Telescope, and the Nordic Optical Telescope.

²¹ Packard Fellow.

²² MTA Distinguished Guest Fellow, Konkoly Observatory.

Rossiter-McLaughlin effect (e.g., Queloz et al. 2000; Zhou et al. 2015). Another approach is to search for planetary or stellar companions at large separations, which could have influenced the dynamical evolution of the inner planet. Knutson et al. (2014) performed a long-term radial velocity monitoring of 51 systems known to host a hot Jupiter, with the goal to detect further planetary companions. They estimated an occurrence rate of $51\% \pm 10\%$ for companions with masses between 1 and $13M_J$ and orbital semimajor axes between 1 and 20 au. Ngo et al. (2015) presented the results on searching for stellar companions around 50 out of the 51 selected systems from Knutson et al. (2014) study. They corrected for survey incompleteness and reported a stellar companion fraction of $48\% \pm 9\%$. Combining the results of both studies, Ngo et al. (2015) estimated that $72\% \pm 16\%$ of hot Jupiters are part of multi-planet and/or multi-star systems.

In this work, we report the discovery of HATS-59b,c, the first multi-planet system detected by the HATSouth survey (Bakos et al. 2013). The star hosts an inner hot Jupiter detected via its transits and an outer cold massive giant planet detected via the radial velocity variations of the host star. The possibility of additional outer planetary companions to transiting hot Jupiter has been proposed by, e.g., Rabus et al. (2009) and in fact, there have been only a few transiting planets with an outer planetary companion for which a full orbit was detected via radial velocity, such as HAT-P-13b,c (Bakos et al. 2009), HAT-P-17b,c (Howard et al. 2012), Kepler-424b,c (Endl et al. 2014), WASP-41b,c (Neveu-VanMalle et al. 2016), WASP-47b,c (Hellier et al. 2012; Becker et al. 2015; Neveu-VanMalle et al. 2016), and WASP-53b,c (Triaud et al. 2017). Among all the systems with a transiting hot Jupiter known to have outer companions, HAT-P-13 c and WASP-53b,c are the only massive planetary companions with a minimum mass greater than HATS-59 c. The few detections of companions around transiting planets is due, to some extent, by the lack of radial velocity follow-up observations. Hot Jupiters in multi-planet systems provide a unique opportunity to place observational constraints on migration models and also could be used to probe the tidal love number of the hot Jupiter (Buhler et al. 2016; Hardy et al. 2017), which in turn constrains the planetary interior structure (Batygin et al. 2009). Therefore, monitoring these systems is very interesting for planet formation and interior structure models.

The paper is structured as follows: In Section 2, we show the planetary signal detected by the HATSouth network and present the photometric and spectroscopic follow-up observations that allowed us to characterize the system. In Section 3, we derive the stellar parameters and jointly model the data to derive the planetary parameters. Our results are finally summarized in Section 4.

2. Observations

2.1. Photometry

2.1.1. Photometric Detection

The HATS-59 system was identified by the HATSouth instruments as potentially hosting a transiting planet. The star (Table 3) was observed between UT 2010 January 19 and UT 2010 August 10 using the HS-1, HS-3, and HS-5 units at the Las Campanas Observatory (LCO) in Chile, the H.E.S.S. site in Namibia, and the Siding Springs Observatory (SSO) in Australia, respectively. A total of 3113, 4690 and 658 of useful

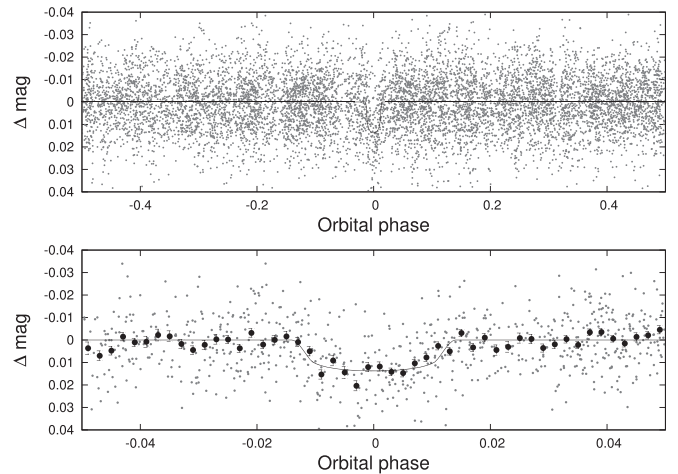


Figure 1. The discovery light curve of HATS-59 phase-folded with a period of $P = 5.4160810$ days (see Section 3). The lower panel shows the transit where the filled black points show the light curve binned in phase with a bin size of 0.002. The solid lines in both panels show the best-fit transit model.

Table 1
Differential Photometry of HATS-59

BJD (2 400 000+)	Mag ^a	σ_{Mag}	Mag (orig) ^b	Filter	Instrument
55372.26299	-0.01448	0.00725	...	<i>r</i>	HS/G563.1
55274.77568	0.01224	0.00650	...	<i>r</i>	HS/G563.1
55296.44071	0.01384	0.00668	...	<i>r</i>	HS/G563.1
55274.77891	-0.01225	0.00628	...	<i>r</i>	HS/G563.1
55296.44428	-0.00169	0.00659	...	<i>r</i>	HS/G563.1
55274.78240	-0.01307	0.00627	...	<i>r</i>	HS/G563.1
55296.44754	-0.00042	0.00652	...	<i>r</i>	HS/G563.1
55274.78561	0.00435	0.00643	...	<i>r</i>	HS/G563.1
55296.45080	-0.00521	0.00660	...	<i>r</i>	HS/G563.1
55372.27744	0.00356	0.00771	...	<i>r</i>	HS/G563.1

Notes. The data are also available on the HATSouth website at <http://www.hatsouth.org>.

^a The out-of-transit level has been subtracted. For the HATSouth light curve (rows with “HS” in the Instrument column), these magnitudes have been detrended using the EPD and TFA procedures prior to fitting a transit model to the light curve. The magnitudes of the follow-up light curves (rows with an Instrument other than “HS”) have been detrended with the EPD procedure, which was carried out simultaneously with the transit fit.

^b Raw magnitude values for the follow-up light curve without applying the EPD procedure.

(This table is available in its entirety in machine-readable form.)

images were obtained with the HS-1, HS-3, and HS-5 telescopes, respectively, using the Sloan *r* filter with an exposure time of 240 s.

Similar to previous HATSouth discoveries, all the photometry data were reduced to trend-filtered light curves using the aperture photometry pipeline described by Penev et al. (2013). Systematic variations were removed using the External Parameter Decorrelation (EPD; Bakos et al. 2010) and the Trend Filtering Algorithm (TFA; Kovács et al. 2005). Then a transit search was performed using the Box Least Squares (BLS; Kovács et al. 2002) fitting algorithm and a period of 5.4161 was detected (Figure 1; the data is provided in Table 1). The rms scatter after subtracting the best-fit model transit is 0.012 mag. The star was then flagged as a planet-host candidate

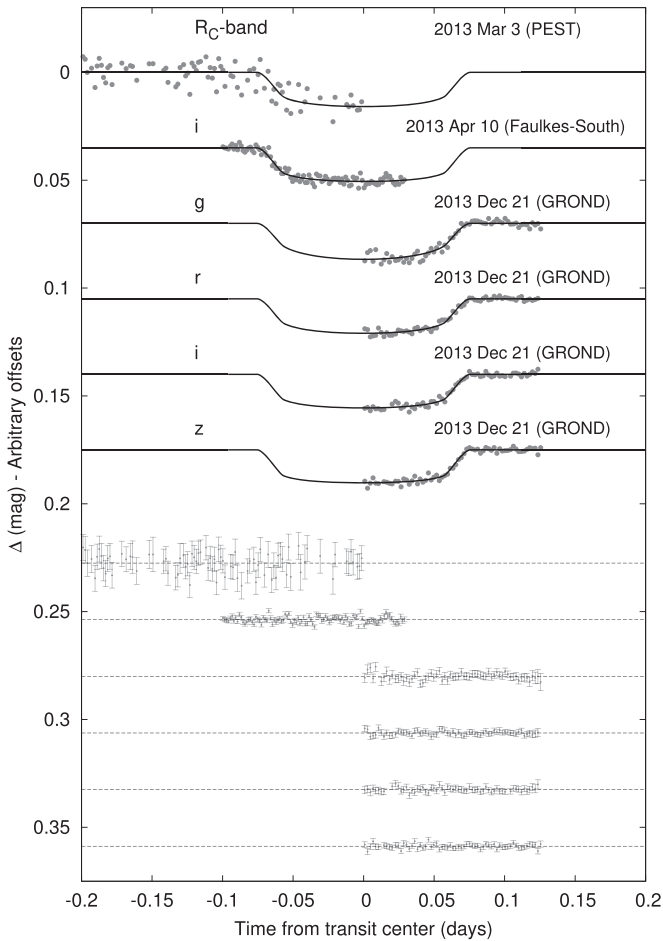


Figure 2. Unbinned follow-up transit light curve of HATS-59 compared to the best-fit transit model along with the residuals. The facilities and filters used, and the dates of each event are listed.

and approved for further follow-up photometric and spectroscopic observations.

2.1.2. Photometric Follow Up

In order to confirm that the transit signals detected in the discovery light curve are due to a transiting planet, we obtained photometric follow-up observations of three transit events. These light curves allow us to refine the ephemeris of the system and to determine precise parameters of the system. All the photometric data are provided in Table 1 and the follow-up light curves are shown in Figure 2 along with the best-fit model and residuals.

An ingress was observed with the 0.3 m Perth Exoplanet Telescope (PEST) on 2013 March 3, using the R_C filter. The photometric precision of the light curve was 5.0 mmag with a cadence of 130 s. Another ingress was observed on 2013 April 10 using the Faulkes Telescope South (FTS), which is a fully automated telescope operated as part of the Las Cumbres Observatory Global Telescope (LCOGT; Brown et al. 2013). The transit was observed in the i -band filter achieving a photometric precision of 1.6 mmag with a cadence of 113 s. An egress was obtained on 2013 December 21 with the multiband imager GROND (Greiner et al. 2008), mounted on the 2.2 m telescope in La Silla Observatory, using four different filters (g , r , i , z). The light curve had a precision of 1.7 mmag in the g band, 1.0 mmag in r , 1.1 mmag in i , and 1.1 mmag in z , with

a cadence of 168 s. The details of the data reduction for these facilities are described in Penev et al. (2013), Mohler-Fischer et al. (2013), and Zhou et al. (2014a).

2.2. Spectroscopic Observations

HATS-59 was spectroscopically observed between 2011 April and 2016 March to confirm the planetary nature of the transit signals and to estimate the mass and therefore the density of the planet. Furthermore, the long radial velocity (RV) monitoring of the star allowed us to detect an outer companion with a longer orbital period than the transiting planet. We present the RV used to characterize the system in Figure 5 and provide the data in Table 2.

2.2.1. Reconnaissance Spectroscopy

Reconnaissance low-resolution spectroscopic follow-up observations are important to rule out various false positive scenarios, such as a primary giant star, or large RV variations indicating that the transiting object is itself a star. Reconnaissance spectroscopic observations were carried out with WiFeS (Dopita et al. 2007), a spectrograph mounted on the ANU 2.3 m telescope. We obtained a single $R = 3000$ spectrum to estimate the stellar atmospheric parameters $T_{\text{eff},*}$, $[\text{Fe}/\text{H}]$, and $v \sin i$ and were used to confirm that the star is a dwarf. In order to rule out large RV variations (at the level of $\sim 2 \text{ km s}^{-1}$), we obtained 7 spectra with a resolution of $R = 7000$. The spectra were extracted and reduced following Bayliss et al. (2013). Another reconnaissance spectrum was observed with the FIES spectrograph at the Nordic Optical Telescope (Telting et al. 2014), where it was reduced following Buchhave et al. (2010). We did not find large RV variations and thus ruled out the possibility that this system might be an eclipsing binary displaying a large radial velocity amplitude. We therefore proceeded with acquiring high-precision RV observations to characterize the system.

2.2.2. High-precision Radial Velocities

We carried out an intensive RV follow-up campaign to measure, with high precision, the semi-amplitude of the RV variations due to the transiting planet. The RV observations showed variations in phase with the transit ephemeris of the interior planet. They, additionally, showed evidence for a large amplitude sinusoidal variation with a period of ~ 1400 days. We next describe the observations and the data reduction of all the spectrographs used in this analysis.

We obtained nine spectra with the CORALIE spectrograph (Queloz et al. 2001) at the Euler 1.2 m telescope at La Silla. We also obtained five spectra with the Planet Finder Spectrograph (PFS; Crane et al. 2010) on the *Magellan* Clay 6.5 m telescope and seven spectra with CYCLOPS on the 3.9 m Anglo-Australian Telescope. Most of the spectra used in this analysis, most importantly for the discovery of the second outer companion, were obtained with FEROS on the MPG 2.2 m (Kaufer & Pasquini 1998) in La Silla Observatory. Twenty-four spectra were acquired with FEROS, which is a high-resolution echelle spectrograph (Kaufer & Pasquini 1998). All the spectra acquired with FEROS and CORALIE were reduced, extracted, and analyzed using the CERES pipeline (Brahm et al. 2017a). The radial velocities of the PFS spectra calibrated with an I2-cell, were computed by matching a template spectrum. For more information, we refer the reader to Butler et al. (1996). Details on

Table 2
Relative Radial Velocities and Bisector Span Measurements of HATS-59

BJD (2 450 000+)	RV ^a (m s ⁻¹)	σ_{RV} ^b (m s ⁻¹)	BS (m s ⁻¹)	σ_{BS}	Phase	Instrument
5722.48192	-156.41	34.00	-25.0	68.0	0.163	FEROS
5725.50346	72.59	41.00	-64.0	82.0	0.721	FEROS
5736.54834	-43.41	29.00	10.0	58.0	0.760	FEROS
5737.51083	-49.41	31.00	7.0	62.0	0.938	FEROS
5738.54029	-166.41	33.00	-52.0	66.0	0.128	FEROS
5754.47565	-35.41	48.00	-29.0	96.0	0.070	FEROS
5756.49554	-36.41	45.00	-111.0	90.0	0.443	FEROS
5757.52534	97.59	52.00	-177.0	104.0	0.633	FEROS
5934.15946	104.14	109.00	0.246	CYCLOPS
5934.86914	72.59	33.00	8.0	66.0	0.377	FEROS
5936.80355	219.59	27.00	4.0	54.0	0.735	FEROS
5938.23445	22.14	177.00	0.999	CYCLOPS
5938.87128	69.59	30.00	-11.0	60.0	0.116	FEROS
5939.81042	39.59	31.00	-6.0	62.0	0.290	FEROS
5943.16020	244.14	82.00	0.908	CYCLOPS
5969.77597	130.39	36.00	-61.0	72.0	0.822	Coralie
5988.70024	74.59	28.00	0.0	56.0	0.317	FEROS
6056.06292	136.14	29.00	0.754	CYCLOPS
6057.03928	318.14	27.00	0.934	CYCLOPS
6059.00663	65.14	73.00	0.298	CYCLOPS
6059.08191	46.14	30.00	0.312	CYCLOPS
6375.71072	224.59	24.00	87.0	48.0	0.773	FEROS
6376.71477	101.59	26.00	237.0	52.0	0.958	FEROS
6424.70951	229.59	40.00	-90.0	80.0	0.820	FEROS
6427.67642	54.59	69.00	-123.0	138.0	0.367	FEROS
6464.53773	-119.61	50.00	43.0	100.0	0.173	Coralie
6465.53888	85.39	43.00	65.0	86.0	0.358	Coralie
6694.77700	-71.73	6.28	0.684	PFS
6696.82969	-214.95	4.90	0.063	PFS
6697.75879	-248.73	4.86	0.234	PFS
6700.82214	-101.76	5.72	0.800	PFS
6703.71677	-296.25	8.71	0.334	PFS
6727.73071	24.39	48.00	-95.0	96.0	0.768	Coralie
6728.62473	-128.61	36.00	-61.0	72.0	0.933	Coralie
6729.69322	-197.61	37.00	76.0	74.0	0.131	Coralie
6730.68884	-209.61	46.00	-119.0	92.0	0.314	Coralie
6731.74803	-109.61	55.00	104.0	110.0	0.510	Coralie
6732.69422	-158.61	41.00	15.0	82.0	0.685	Coralie
7182.46643	32.59	11.00	16.0	22.0	0.729	FEROS
7185.59484	-117.41	19.00	-27.0	38.0	0.306	FEROS
7462.66518	204.59	11.00	-28.0	22.0	0.464	FEROS
7463.86306	302.59	16.00	-37.0	32.0	0.685	FEROS
7464.73538	254.59	14.00	-29.0	28.0	0.846	FEROS

Notes.^a Relative RVs, with γ_{RV} subtracted.^b Internal errors not accounting for astrophysical/instrumental jitter.

the data reduction and analysis are described in previous HATSouth discovery papers, e.g., Jordán et al. (2014), Zhou et al. (2014b), Hartman et al. (2015). For details of the data reduction of CYCLOPS spectra, see Penev et al. (2013).

2.3. Lucky Imaging

High spatial resolution imaging were obtained as part of the follow-up campaign using the Astralux Sur camera (Hippler et al. 2009) on the New Technology Telescope (NTT), at La Silla Observatory in Chile. The lucky imaging observations are useful to identify close stellar companions that could affect the transit depth. The observations were carried out with the SDSS z' filter on 2015 December 23 and reduced following Espinoza

et al. (2016) but we used instead the plate scale derived in Janson et al. (2017) of $15.2 \text{ mas pixel}^{-1}$, which is a better estimate than the one estimated in our previous work. Figure 3 shows the final reduced image and Figure 4 shows the contrast curve, where no resolved companion is detected within $2''$.

3. Analysis

3.1. Properties of the Parent Star

It is important to characterize the host star in order to measure precise planetary parameters. We used ZASPE (Brahm et al. 2017b) to get an initial estimate of the atmospheric parameters ($T_{\text{eff}\star}$ [Fe/H] $v \sin i$, and $\log g_{\star}$). The parameters were determined using the FEROS spectra, which

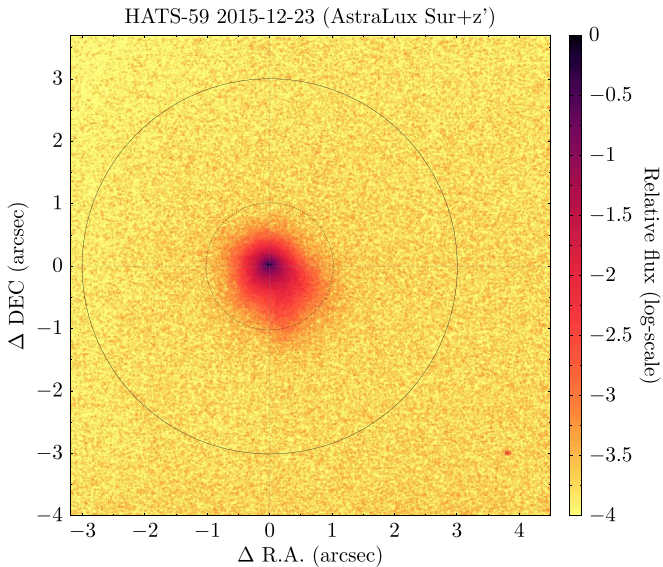


Figure 3. Astralux Sur lucky image of HATS-59 using z' . Circles of $1''$ and $3''$ radii are shown. No neighboring companion is detected within $2''$.

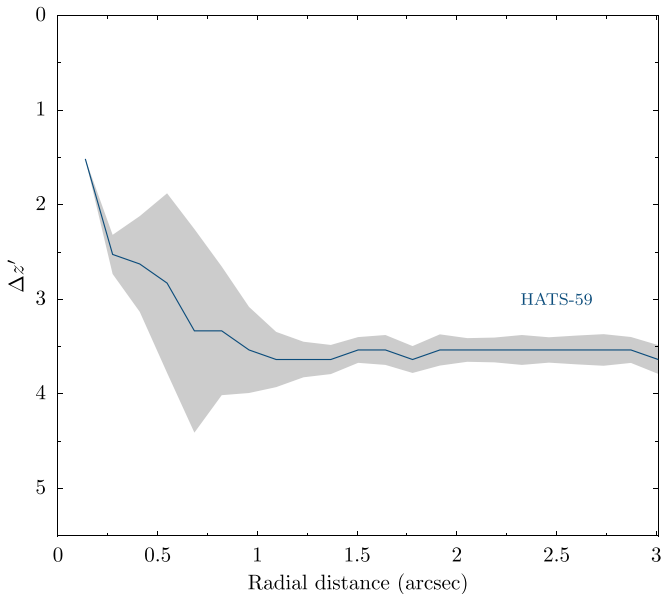


Figure 4. Contrast curve for of HATS-59 using the Astralux Sur z' observations. Gray bands show the uncertainty given by the scatter in the contrast in the azimuthal direction at a given radius.

were co-added to obtain a high signal-to-noise ratio spectrum. ZASPE determines the stellar parameters via least-squares minimization against a grid of synthetic spectra in the spectral regions most sensitive to changes in the parameters (5000 \AA and 6000 \AA).

We then followed Sozzetti et al. (2007) to determine the fundamental stellar parameters (M_* , R_* , L_* , age, etc.). In particular, we used the stellar density ρ_* determined from the photometric light curve, combined with the $T_{\text{eff}*}$ and $[\text{Fe}/\text{H}]$ measurements, to characterize the host star. The parameters were obtained by combining the spectroscopic and photometric parameters with the Yonsei–Yale stellar evolution models (Y²; Yi et al. 2001). This provided a revised estimate of $\log g_*$, which was fixed in a second iteration of ZASPE that returned the final values of the stellar parameters.

We estimate a mass of $1.038 \pm 0.039 M_{\odot}$ and a radius of $1.036 \pm 0.067 R_{\odot}$. HATS-59 is at a reddening-corrected distance of $630 \pm 43 \text{ pc}$. The distance estimated using isochrone fitting is in agreement with the distance estimated using *Gaia* data. Figure 6 shows the location of the star on the $T_{\text{eff}*}-\rho_*$ diagram and the stellar parameters are provided in Table 3.

3.2. Excluding Blend Scenarios

It is important to perform a blend analysis to confirm the planetary nature of the transiting signal and to rule out a stellar eclipsing binary system as a cause of the signal. Using the photometric data, the blend analysis was carried out following Hartman et al. (2012). We find that although blended stellar eclipsing binary models can be found that fit the available photometric data, these models would produce obviously composite spectroscopic cross-correlation functions (CCFs) that are inconsistent with the observed CCFs. For example, in all cases the spectral line bisector spans (BSs) computed from the simulated CCFs have scatter in excess of 900 m s^{-1} , with a maximum simulated value of 4.54 km s^{-1} , whereas the scatter of the measured FEROS BSs is $\sim 100 \text{ m s}^{-1}$. Similarly the RVs of the simulated CCFs are in excess of 500 m s^{-1} , whereas the observed FEROS RVs have a scatter of 130 m s^{-1} (dominated by the planetary signals). We conclude that the transiting signals are indeed due to a planet, and HATS-59 is not a blended stellar eclipsing binary.

3.3. Global Modeling of the Data

To measure the orbital and physical properties of the planets, we modeled all the photometric data (the HATSouth and follow-up photometric data) and the high-precision RV measurements following Pál et al. (2008), Bakos et al. (2010) and Hartman et al. (2012).

All the photometric light curves were modeled using the Mandel & Agol (2002) transit models with fixed quadratic limb-darkening coefficients taken from Claret (2004). For the HATSouth discovery photometric light curves, we also considered a dilution factor for the transit depth that accounts for possible blends from neighboring stars and possible over-correction introduced by the trend filtering algorithm (TFA; removes trends shared with other stars; Bakos et al. 2010; Kovács et al. 2005). As for the photometric follow-up light curves, the systematic trends were corrected by including a quadratic trend to the transit model. We also added a linear trend, with up to three parameters, to reconstruct the shape of the PSF. This trend compensates for changes in the PSF during the observations, which could be due to poor guiding, non-photometric conditions, or changes in the seeing during the transit observations.

We fit the RVs, taken with different spectrographs, with a Keplerian orbit allowing the zero-point and the RV jitter, for each instrument, to vary independently in the fit. This ensures that the best-fitting model is self-consistent with the data set. Our RVs support the existence of a second planet on top of the transiting one, and therefore models with two planets were considered in the modeling. We considered four different scenarios where one or both of the planets had a fixed circular orbit, or was allowed to have non-zero eccentricity. To choose between the different scenarios, we estimated the Bayesian evidence for each model following Weinberg et al. (2013), and

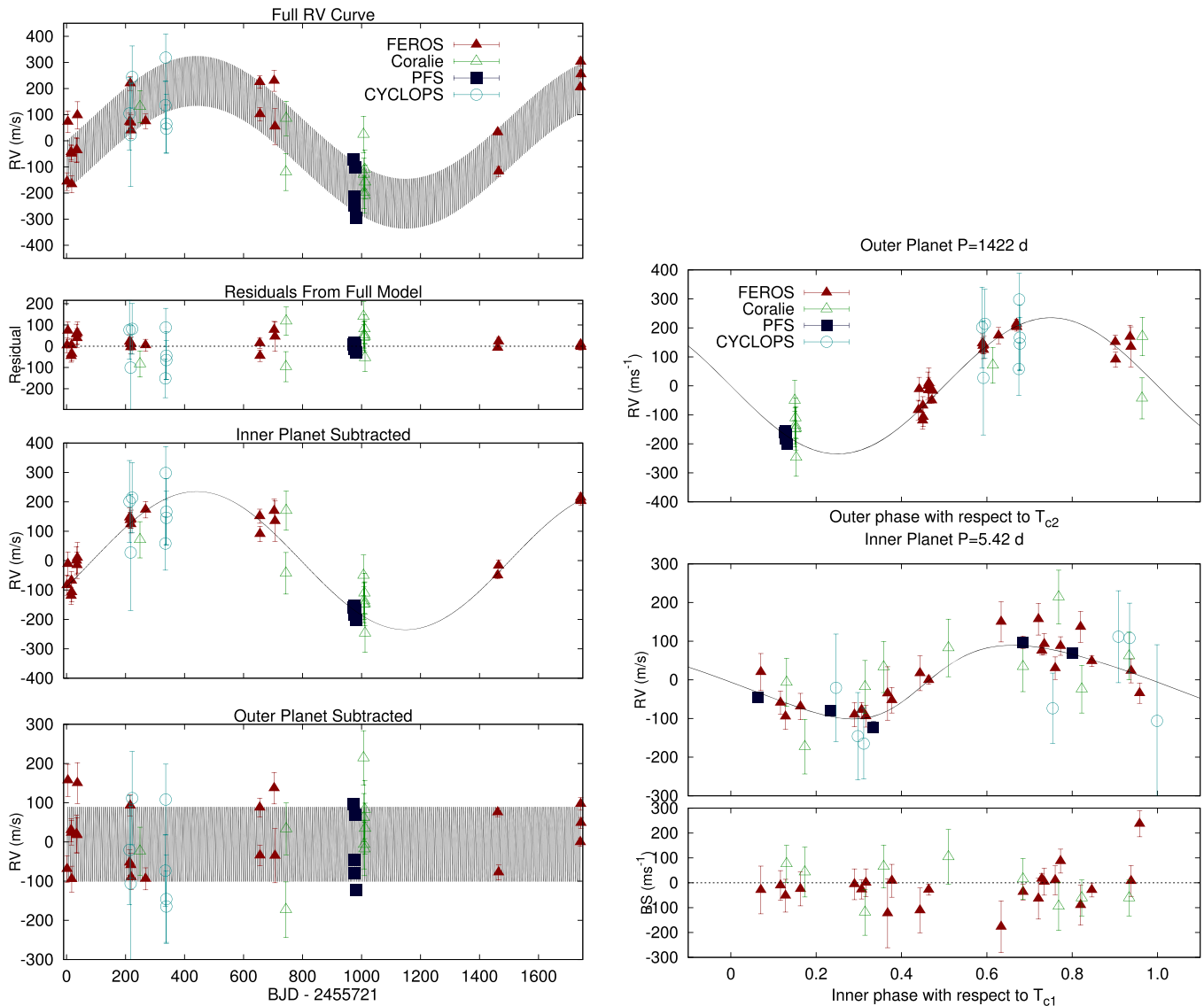


Figure 5. Top left: FEROS, Coralie, PFS, and CYCLOPS high-precision RV measurements, together with our best-fit two-planet orbit model, plotted as a function of time. The center-of-mass velocity has been subtracted. The error bars include the jitter which is varied independently for each instrument in the fit. Left, second panel: $RV O - C$ residuals from the two-planet model, plotted as a function of time. Left, third panel: RV residuals after subtracting only the model variation due to the inner planet, plotted as a function of time. Left, bottom panel: RV residuals after subtracting only the model variation due to the outer planet, plotted as a function of time. Top right: RV residuals after subtracting only the model variation due to the inner planet, plotted as a function of phase of the outer planet. Here zero phase is the time of inferior conjunction for the outer planet. Right, second panel: RV residuals after subtracting only the model variation due to the outer planet, plotted as a function of phase of the inner planet. Right, bottom panel: Spectral line bisector spans (BSs) plotted as a function of phase of the inner planet. Note the different vertical scales of all of the panels.

then adopted the model with the highest evidence, which we find to be a model in which the interior transiting planet has a non-zero eccentricity, while the exterior planet has a circular orbit. The evidence for this model is a modest factor of 2.4 times greater than the evidence for the model in which both planets are assumed to have circular orbits, 7 times greater than the model in which the interior planet is circular and the exterior planet has an eccentric orbit, and 19 times greater than the model in which both planets have non-zero eccentricities.

The posterior distributions for each parameter and hence the median parameters along with their 1σ uncertainties were estimated using the differential evolution Markov Chain Monte Carlo procedure (DEMCMC; ter Braak 2006) and are provided in Table 4. We find that the transiting planet HATS-59b has a mass of $0.806 \pm 0.069 M_J$, a radius of $1.126 \pm 0.077 R_J$, and a non-zero eccentricity of $e = 0.129 \pm 0.049$. For the second

planet, which we dub HATS-59c, we find that it is well fit by a circular Keplerian orbit with $P = 1422 \pm 14$ days, $K = 224 \pm 14 \text{ m s}^{-1}$, implying a minimum mass for the companion of $m \sin i = 12.70 \pm 0.87 M_J$, where i is the orbital inclination of HATS-59c.

4. Discussion

We present the discovery of HATS-59, the first multi-planet system detected by the HATSouth survey. The inner planet, HATS-59b, is a transiting hot Jupiter on an eccentric orbit, completing one revolution every ≈ 5 days. The outer planet, HATS-59c, is a cold massive giant planet on a circular orbit with a period of 1422 days. We note the $m \sin i$ for HATS-59b, c is very close to the theoretical limit for deuterium burning for a solar metallicity object, and thus it may be a very low mass

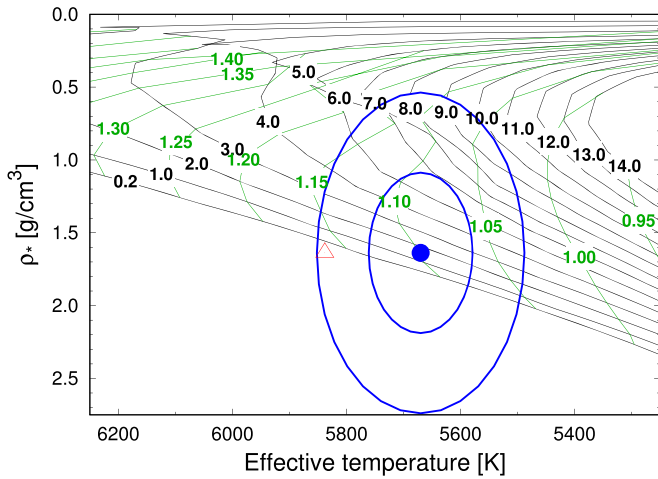


Figure 6. Model isochrones (black solid lines) from Yi et al. (2001) for the measured metallicity of HATS-59. The age of each isochrone in Gyr is labeled in black font. We also show evolutionary tracks for stars of fixed mass (dashed green lines) with the mass of each tracked labeled in solar mass units in green font. The adopted values of $T_{\text{eff}*}$ and ρ_* are shown using the filled blue circle together with their 1σ and 2σ confidence ellipsoids (blue lines). The initial values of $T_{\text{eff}*}$ and ρ_* from the first ZASPE and light curve analysis are represented with the red open triangle.

brown dwarf rather than a giant exoplanet, although the distinction is unlikely to change the physical characteristics of the object.

4.1. Possible Formation Scenarios of HATS-59b,c

The architecture of HATS-59b,c poses a challenge for planet formation and migration scenarios. Can core accretion explain the presence of a hot Jupiter and a massive gas giant in the same system? Schlaufman (2018) found that planets with $M > 10M_J$ do not preferentially orbit metal-rich solar-like stars, suggesting that these objects most likely did not form via core accretion but via gravitational instability. The architecture of HATS-59b,c hence suggests that both core accretion and gravitational instability could have occurred in the same system, which was also previously suggested by Triaud et al. (2017) for WASP-53bc and WASP-81bc.

The current water iceline is around 2.92 au, suggesting that both HATS-59b and HATS-59c formed beyond the iceline and then migrated inwards to their present locations. The presence of HATS-59c, a massive companion close to the deuterium burning limit (Mollière & Mordasini 2012), could have scattered HATS-59b inwards resulting in its present eccentric orbit. Due to its mass, type-II migration is reduced even below the viscous limit for HATS-59c (Baruteau et al. 2014), resulting in only little inward migration, potentially explaining its long period.

4.2. Transit Timing Variations

Variations in the times of transits can be attributed to the presence of a secondary planet in the system (e.g., Agol et al. 2005; Mancini et al. 2016; Almenara et al. 2018). The maximum transit variation expected for the inner planet is on the order of 10^{-10} s, undetectable with current instruments. However, this depends on the mutual inclination between the inner and outer planet.

Table 3
Stellar Parameters for HATS-59

Parameter	Value	Source
Identifying Information		
R.A. (h:m:s)	1 ^h 21 ^m 18 ^s .00	2MASS
Decl. (d:m:s)	−22°23′17″.4	2MASS
R.A.p.m. (mas yr ^{−1})	−24.16 ± 0.047	Gaia DR2
Decl.p.m. (mas yr ^{−1})	0.92 ± 0.03	Gaia DR2
Parallax (mas)	1.52 ± 0.03	Gaia DR2
GSC ID	GSC 6090-00133	GSC
2MASS ID	2MASS 11211786-2223174	2MASS
Spectroscopic properties		
$T_{\text{eff}*}$ (K)	5670 ± 91	ZASPE ^a
[Fe/H]	0.180 ± 0.064	ZASPE
$v \sin i$ (km s ^{−1})	2.80 ± 0.61	ZASPE
γ_{RV} (m s ^{−1})	−10887 ± 11	FEROS
Photometric properties		
B (mag)	14.727 ± 0.020	APASS
V (mag)	13.951 ± 0.030	APASS
g (mag)	14.286 ± 0.030	APASS
r (mag)	13.725 ± 0.030	APASS
i (mag)	13.551 ± 0.040	APASS
J (mag)	12.590 ± 0.024	2MASS
H (mag)	12.299 ± 0.030	2MASS
K_s (mag)	12.238 ± 0.030	2MASS
G (mag)	13.785	Gaia DR2
Derived properties		
M_* (M_{\odot})	1.038 ± 0.039	$Y^2 + \rho_* + \text{ZASPE}^b$
R_* (R_{\odot})	1.036 ± 0.067	$Y^2 + \rho_* + \text{ZASPE}$
$\log g_*$ (cgs)	4.422 ± 0.053	$Y^2 + \rho_* + \text{ZASPE}$
ρ_* (g cm^{-3}) ^c	1.59 ± 0.54	Light curves
ρ_* (g cm^{-3}) ^c	1.31 ± 0.24	$Y^2 + \text{Light curves} + \text{ZASPE}$
L_* (L_{\odot})	0.99 ± 0.16	$Y^2 + \rho_* + \text{ZASPE}$
M_V (mag)	4.86 ± 0.19	$Y^2 + \rho_* + \text{ZASPE}$
M_K (mag, ESO)	3.24 ± 0.14	$Y^2 + \rho_* + \text{ZASPE}$
Age (Gyr)	4.3 ± 2.3	$Y^2 + \rho_* + \text{ZASPE}$
A_V (mag) ^d	0.091 ± 0.074	$Y^2 + \rho_* + \text{ZASPE}$
Distance (pc)	654 ± 14	Gaia DR2

Notes.

^a ZASPE = “Zonal Atmospheric Stellar Parameter Estimator” method for the analysis of the FEROS high-resolution spectra (Brahm et al. 2017b). Similar to previous works, these parameters rely primarily on ZASPE, but they also have a small dependence on the iterative analysis of the isochrone search and global modeling of the data. For more information see the text.

^b Y^2 Isochrones (Yi et al. 2001) + $\rho_* + \text{ZASPE}$ = the stellar density which is used as a luminosity indicator, and the ZASPE results.

^c Two different values for ρ_* are listed. The first is determined from the global fit to the light curves and RV data, without imposing a constraint that the parameters match the stellar evolution models. The second value results from restricting the posterior distribution to combinations of $\rho_* + T_{\text{eff}*} + [\text{Fe}/\text{H}]$ that match to a Y^2 stellar model.

^d The star extinction in the V band determined by comparing the expected magnitude from Isochrones + $\rho_* + \text{ZASPE}$ model for the star to the catalog broad-band photometry listed in the table. The extinction law is from Cardelli et al. (1989).

4.3. The Inner Transiting Planet HATS-59b

In Figure 7, we plot the masses and radii of all the transiting exoplanets having these parameters measured with a precision better than 20%. HATS-59b lies in a densely populated region of the parameter space, where numerous non inflated giant

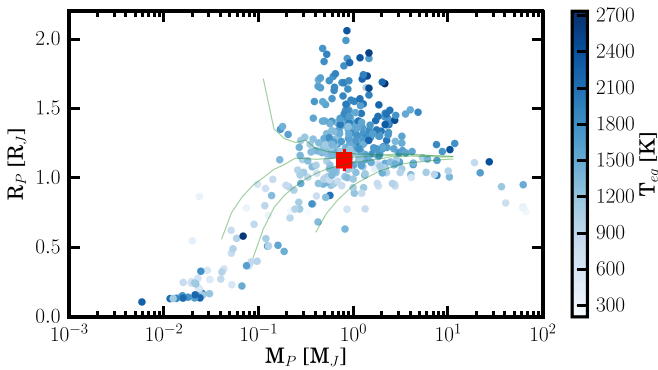


Figure 7. Mass–radius diagram for the full population of well characterized transiting planets color coded by their equilibrium temperature. HATS-59b is shown in red. The Fortney et al. (2007) models of planetary structure are also plotted as green lines. The four models correspond to gaseous planets with $a = 0.045$ au, age = 4.3 Gyr, and core masses of 0, 25, 50, and $100 M_{\oplus}$.

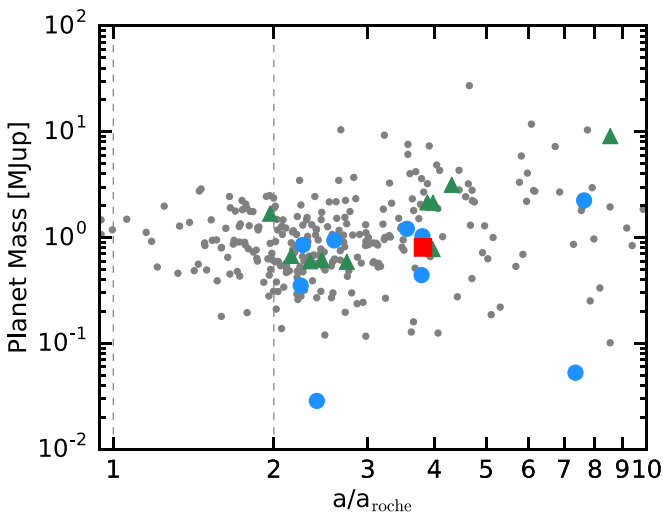


Figure 8. Planetary mass vs. a/a_{roche} for single (small gray circles), known multi-planetary systems (blue circles), and systems showing a linear trend (green triangles). HATS-59b is shown as a red square. Most of the multi-planetary systems have $a/a_{\text{roche}} > 2$, which supports the high eccentricity migration scenario.

planets with similar properties have been detected. In terms of structure, HATS-59b is similar to HAT-P-29 b ($M_p = 0.78 M_J$, $R_p = 1.11 R_J$, and $P = 5.7$ days; Buchhave et al. 2011); and K2-115 b, ($M_p = 0.84 M_J$, $R_p = 1.12 R_J$, and $P = 20.3$ days; Shporer et al. 2017), however with a significantly shorter period.

We compare the mass and radius of HATS-59b to the theoretical models of Fortney et al. (2007), for a hydrogen–helium dominated planets with different core masses, at a distance of 0.045 au, and an age of 4.3 Gyr. We find that its composition is consistent with a gas-dominated planet with a core mass $M_c < 25 M_{\oplus}$. However, these models assume that all the solid material is located inside the core. According to Thorngren et al. (2016), HATS-59b could have a larger amount of heavy elements in its interior ($\sim 50 M_{\oplus}$) if they are predominantly mixed in the gaseous envelope.

4.3.1. Possible Migration Scenarios of HATS-59b

Hot Jupiters are thought to form beyond the iceline and migrate inwards via disk or high eccentricity migration, where the latter requires an outer planetary or stellar companion.

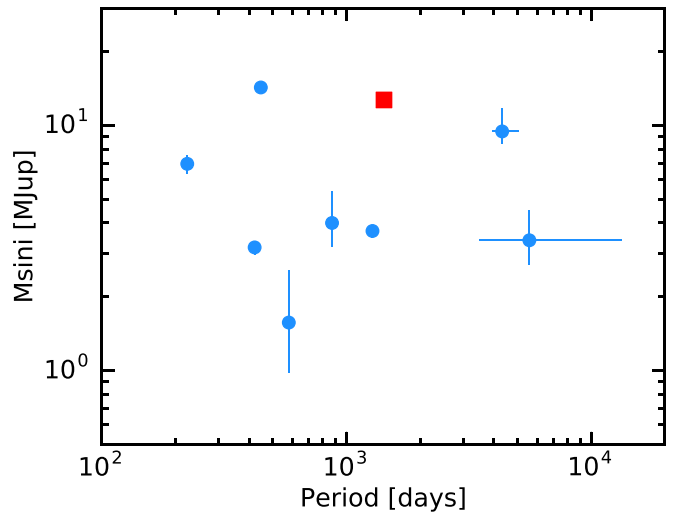


Figure 9. $M \sin i$ vs. period for the outer companions where the orbit was fully observed (blue circle). HATS-59c (red square) has the third longest period, where only nine companions have been characterized.

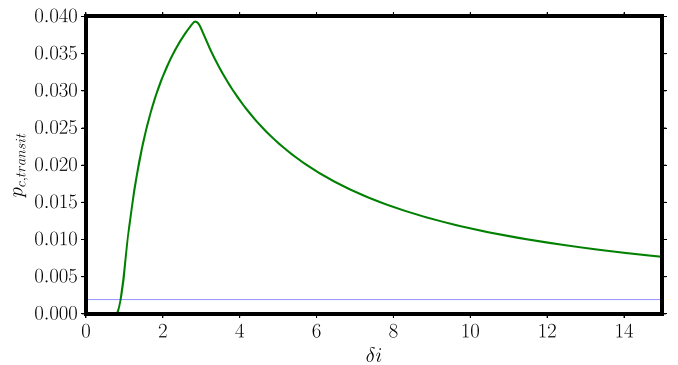


Figure 10. Transit probability for HATS-59c for an aligned configuration with HATS-59b as a function of the maximum separation in inclination between both planets. The blue line shows the a priori probability for HATS-59c to transit. A maximum probability of $\approx 4\%$ would occur if the orbital plane of HATS-59c is inclined around 3 deg with respect to that of HATS-59b.

Observations of the projected spin–orbit angle via the Rossiter–McLaughlin (RM) effect provides an approach to distinguish between these migration scenarios. Disk migration predicts circular and aligned orbits, whereas the high eccentricity migration can produce a broad range of obliquities, depending mostly on the scattering mechanism and on the effectiveness of tidal interactions at damping obliquities.

The amplitude of the RM effect scales with $v \sin i$, the projected rotational velocity of the star. We predict an RM amplitude of $23\text{--}36 \text{ m s}^{-1}$ for $v \sin i = 2.2\text{--}3.4 \text{ km s}^{-1}$. Measuring the RM amplitude for this faint star ($V = 13.951 \pm 0.030$ mag), is challenging but plausible using HIRES (Vogt et al. 1994; Wang et al. 2018) on the Keck telescope or with the new high-resolution spectrograph, ESPRESSO (Pepe et al. 2014) at the Very Large Telescope.

Disk migration predicts that planets can migrate up until they reach the planet–star Roche separation (a_{roche}), the critical distance within which a planet would start losing mass (Faber et al. 2005). On the other hand, high-eccentricity migration predicts planets will circularize at a semimajor axis greater than $2a_{\text{roche}}$. This mechanism would require that hot Jupiters are excited to eccentric orbits, often by being scattered by a distant

Table 4
Parameters for the Planets HATS-59b,c

Parameter	HATS-59b Value ^a	HATS-59c Value ^a
Light curve parameters		
P (days)	5.416081 ± 0.000016	1422 ± 14
T_c (BJD) ^b	$2456620.66527 \pm 0.00052$	2456521 ± 11
T_{14} (days) ^b	0.1497 ± 0.0017	0.957 ± 0.054
$T_{12} = T_{34}$ (days) ^b	0.0186 ± 0.0016	0.0863 ± 0.0011
a/R_*	12.66 ± 0.77	518 ± 32
ζ/R_* ^c	15.23 ± 0.13	...
R_p/R_*	0.1116 ± 0.0021	...
b^2	$0.209^{+0.054}_{-0.056}$...
$b \equiv a \cos i/R_*$	$0.457^{+0.056}_{-0.066}$...
i (deg)	88.10 ± 0.33	...
Limb-darkening coefficients ^d		
c_1, g (linear term)	0.5965	...
c_2, g (quad-ratic term)	0.2045	...
c_1, R	0.3628	...
c_2, R	0.3129	...
c_1, r	0.3896	...
c_2, r	0.3085	...
c_1, i	0.2930	...
c_2, i	0.3208	...
c_1, z	0.2259	...
c_2, z	0.3232	...
RV parameters		
K (m s ⁻¹)	92.1 ± 7.8	224 ± 14
e^e	0.129 ± 0.049	<0.083
ω	227 ± 29	...
$\sqrt{e} \cos \omega$	-0.233 ± 0.084	...
$\sqrt{e} \sin \omega$	$-0.25^{+0.18}_{-0.11}$...
$e \cos \omega$	-0.082 ± 0.034	...
$e \sin \omega$	-0.090 ± 0.065	...
FEROS RV jitter (m s ⁻¹) ^f	<20.7	...
Coralie RV jitter (m s ⁻¹) ^f	58 ± 44	...
PFS RV jitter (m s ⁻¹) ^f	24 ± 14	...
CYCLOPS RV jitter (m s ⁻¹) ^f	93 ± 40	...
Planetary parameters		
M_p (M_J)	0.806 ± 0.069	...
$M_p \sin i$ (M_J)	...	12.70 ± 0.87
R_p (R_J)	1.126 ± 0.077	...
$C(M_p, R_p)^g$	0.05	...
ρ_p (g cm ⁻³)	0.70 ± 0.16	...
$\log g_p$ (cgs)	3.195 ± 0.069	...
a (au)	0.06112 ± 0.00076	2.504 ± 0.035
T_{eq} (K) ^h	1128 ± 40	175.9 ± 6.4

massive companion, and survived the tidal dissipation process required to circularize their final orbits (Faber et al. 2005; Ford 2006).

Many distant planetary companions to hot Jupiters have been detected (Knutson et al. 2014). In Figure 8, we show planetary mass plotted against a/a_{roche} , where

$$a_{\text{roche}} = 2.7R_p \left(\frac{M_*}{M_p} \right)^{1/3}, \quad (1)$$

Table 4
(Continued)

Parameter	HATS-59b Value ^a	HATS-59c Value ^a
Θ^i	0.0841 ± 0.0093	...
$\langle F \rangle$ (erg s ⁻¹ cm ⁻²) ^j	$(3.66 \pm 0.53) \times 10^8$	$(2.16 \pm 0.32) \times 10^5$

Notes.

^a We provide the median value and the 68.3% (1σ) confidence intervals for all the parameters. Reported results assume an eccentric orbit for HATS-59b and a circular orbit for HATS-59c.

^b Reported times are in Barycentric Julian Date calculated directly from UTC, without correction for leap seconds. T_c : Reference epoch of mid transit that minimizes the correlation with the orbital period. Note that HATS-59c has not been observed to transit. We list here the time of mid transit, implied by the orbital solution, in the event that the orbital inclination permits transits. T_{14} : total transit duration, time between first to last contact; $T_{12} = T_{34}$: ingress/egress time, time between first and second, or third and fourth contact. For HATS-59c T_{14} and T_{12} are calculated assuming central transits ($i = 90^\circ$ orbit) and a Jupiter radius for the planet.

^c Reciprocal of the half duration of the transit used as a jump parameter in our MCMC analysis in place of a/R_* . It is related to a/R_* by the expression $\zeta/R_* = a/R_*(2\pi(1 + e \sin \omega))/(P\sqrt{1 - b^2}\sqrt{1 - e^2})$ (Bakos et al. 2010).

^d Values for a quadratic law, adopted from the tabulations by Claret (2004) according to the spectroscopic (ZASPE) parameters listed in Table 3.

^e For HATS-59c, we list the 95% confidence upper-limit on the eccentricity. All the other parameters are estimated assuming a circular orbit for this planet.

^f Astrophysical or instrumental error added in quadrature to the original RV errors. This term is varied in the fit independently for each instrument assuming a prior that is inversely proportional to the jitter.

^g Correlation coefficient between the planetary mass M_p and radius R_p determined from the parameter posterior distribution via $C(M_p, R_p) = \langle (M_p - \langle M_p \rangle)(R_p - \langle R_p \rangle) \rangle / (\sigma_{M_p} \sigma_{R_p})$, where $\langle \cdot \rangle$ is the expectation value, and σ_x is the std. dev. of x .

^h Planet equilibrium temperature averaged over the orbit, calculated assuming a Bond albedo of zero, and that flux is reradiated from the full planet surface.

ⁱ The Safronov number is given by $\Theta = \frac{1}{2}(V_{\text{esc}}/V_{\text{orb}})^2 = (a/R_p)(M_p/M_*)$ (see Hansen & Barman 2007).

^j Incoming flux per unit surface area, averaged over the orbit.

Table 5
Future Transit Windows

Date (UT)	Sun RA distance (hr)
2021 May 30	6.8
2025 Apr 21	9.4
2029 Mar 13	12.2

for all hot Jupiters whose mass and radii are determined with a precision better than 30% (small gray circles). Blue circles show all the hot Jupiters with a fully resolved orbit of the outer planetary companion and green triangle represent the systems whose RVs show a linear trend, taken from Knutson et al. (2014). The position of HATS-59b is shown with a red square. All but one multi-planet system have $a/a_{\text{roche}} > 2$, HAT-P-7b, with a value a/a_{roche} only slightly lower than 2. The available data on hot Jupiters with companions indicate that high eccentricity migration could be the main mechanism for placing the gas giant on a close-in orbit in these systems.

We compare the parameters of HATS-59c to all the detected planetary companions whose orbit is fully resolved. Figure 9

shows the position of HATS-59c (red square) on the minimum mass-period diagram with the other discovered companions (blue circles). With a period of 1422 days, HATS-59c has the third longest period, indicating how few outer companions to transiting hot Jupiters have been characterized due to the lack of RV follow-up observations. All of the companions have minimum masses above $1 M_J$, which is most likely due to selection effects with a detection limit of $\sim 20 \text{ m s}^{-1}$ for a planet orbiting a Sun analog.

4.4. Possible Transits of HATS-59c

As was stated in the previous section, knowing the mutual inclination between HATS-59b and HATS-59c can be useful to further clarify the possible migration path of this system. The host star is too faint for the GAIA mission to be able to measure the astrometric signal of HATS-59c. However, the inclination of HATS-59c with respect to the plane of the sky could be measured if it also transits its star. While the a priori probability of transit for HATS-59c is $\sim 0.2\%$, if we consider that the two planets are co-planar, then the probability of transit raises by one order of magnitude. Figure 10 shows the transit probability of HATS-59c for different assumed maximum mutual inclinations (δ_i) between the orbital plane of the planets. The probabilities were computed following the formalism of Beatty & Seager (2010). The maximum probability (3.8%) occurs if the mutual inclination between the planets is around 3 deg.

The future transit windows for HATS-59c are listed in Table 5. In this table, we indicate the center of the transit window and the distance of the target from the Sun at the time of putative transit center. Currently, the width of the transit window is quite large (>50 days) due to the large uncertainties in the ephemeris. Long-term RV monitoring of the system would be useful to further constrain the width of the transit window.

Development of the HATSouth project was funded by NSF MRI grant NSF/AST-0723074, operations have been supported by NASA grants NNX09AB29G, NNX12AH91H, and NNX17AB61G, and follow-up observations receive partial support from grant NSF/AST-1108686. P.S. would like to thank Bertram Bitsch for useful discussions. A.J. acknowledges support from FONDECYT project 1171208, BASAL CATA PFB-06, and project IC120009 “Millennium Institute of Astrophysics (MAS)” of the Millennium Science Initiative, Chilean Ministry of Economy. R.B. acknowledges support from project IC120009 “Millennium Institute of Astrophysics (MAS)” of the Millennium Science Initiative, Chilean Ministry of Economy. L.M. acknowledges support from the Italian Minister of Instruction, University and Research (MIUR) through FFABR 2017 fund. J.H. acknowledges support from NASA grant NNX14AE87G. V.S. acknowledges support from BASAL CATA PFB-06. A.V. is supported by the NSF Graduate Research Fellowship, Grant No. DGE 1144152. This work has made use of data from the European Space Agency (ESA) mission *Gaia* (<https://www.cosmos.esa.int/gaia>), processed by the *Gaia* Data Processing and Analysis Consortium (DPAC, <https://www.cosmos.esa.int/web/gaia/dpac/consortium>). Funding for the DPAC has been provided by national institutions, in particular the institutions participating in the *Gaia* Multilateral Agreement. This work is based on observations made with ESO Telescopes at the La Silla Observatory. This paper also uses observations obtained with facilities of the Las Cumbres

Observatory Global Telescope. We acknowledge the use of the AAVSO Photometric All-Sky Survey (APASS), funded by the Robert Martin Ayers Sciences Fund, and the SIMBAD database, operated at CDS, Strasbourg, France. Operations at the MPG 2.2 m Telescope are jointly performed by the Max Planck Gesellschaft and the European Southern Observatory. The imaging system GROND has been built by the high-energy group of MPE in collaboration with the LSW Tautenburg and ESO. We thank the MPG 2.2 m telescope support team for their technical assistance during observations.

ORCID iDs

P. Sarkis  <https://orcid.org/0000-0001-8128-3126>
 J. D. Hartman  <https://orcid.org/0000-0001-8732-6166>
 G. Á. Bakos  <https://orcid.org/0000-0001-7204-6727>
 R. Brahm  <https://orcid.org/0000-0002-9158-7315>
 D. Bayliss  <https://orcid.org/0000-0001-6023-1335>
 L. Mancini  <https://orcid.org/0000-0002-9428-8732>
 W. Bhatti  <https://orcid.org/0000-0002-0628-0088>
 K. Penev  <https://orcid.org/0000-0003-4464-1371>
 P. Arriagada  <https://orcid.org/0000-0002-3578-551X>
 R. P. Butler  <https://orcid.org/0000-0003-1305-3761>
 J. D. Crane  <https://orcid.org/0000-0002-5226-787X>
 C. G. Tinney  <https://orcid.org/0000-0002-7595-0970>
 S. Durkan  <https://orcid.org/0000-0002-3663-3251>
 V. Suc  <https://orcid.org/0000-0001-7070-3842>
 L. A. Buchhave  <https://orcid.org/0000-0003-1605-5666>

References

- Agol, E., Steffen, J., Sari, R., & Clarkson, W. 2005, *MNRAS*, 359, 567
 Almenara, J. M., Díaz, R. F., Hébrard, G., et al. 2018, *A&A*, 615, A90
 Artymowicz, P. 1993, *ApJ*, 419, 166
 Bakos, G. Á., Csabry, Z., Penev, K., et al. 2013, *PASP*, 125, 154
 Bakos, G. Á., Howard, A. W., Noyes, R. W., et al. 2009, *ApJ*, 707, 446
 Bakos, G. Á., Torres, G., Pál, A., et al. 2010, *ApJ*, 710, 1724
 Baruteau, C., Crida, A., Paardekooper, S.-J., et al. 2014, in *Protostars and Planets VI*, ed. H. Beuther et al. (Tucson, AZ: Univ. Arizona Press), 667
 Batygin, K., Bodenheimer, P., & Laughlin, G. 2009, *ApJL*, 704, L49
 Bayliss, D., Zhou, G., Penev, K., et al. 2013, *AJ*, 146, 113
 Beatty, T. G., & Seager, S. 2010, *ApJ*, 712, 1433
 Becker, J. C., Vanderburg, A., Adams, F. C., Rappaport, S. A., & Schwengeler, H. M. 2015, *ApJL*, 812, L18
 Brahm, R., Jordán, A., & Espinoza, N. 2017a, *PASP*, 129, 034002
 Brahm, R., Jordán, A., Hartman, J., & Bakos, G. 2017b, *MNRAS*, 467, 971
 Brown, T. M., Baliber, N., Bianco, F. B., et al. 2013, *PASP*, 125, 1031
 Buchhave, L. A., Bakos, G. Á., Hartman, J. D., et al. 2010, *ApJ*, 720, 1118
 Buchhave, L. A., Bakos, G. Á., Hartman, J. D., et al. 2011, *ApJ*, 733, 116
 Buhler, P. B., Knutson, H. A., Batygin, K., et al. 2016, *ApJ*, 821, 26
 Butler, R. P., Marcy, G. W., Williams, E., et al. 1996, *PASP*, 108, 500
 Cardelli, J. A., Clayton, G. C., & Mathis, J. S. 1989, *ApJ*, 345, 245
 Claret, A. 2004, *A&A*, 428, 1001
 Crane, J. D., Shectman, S. A., Butler, R. P., et al. 2010, *Proc. SPIE*, 7735, 773553
 Dopita, M., Hart, J., McGregor, P., et al. 2007, *Ap&SS*, 310, 255
 Endl, M., Caldwell, D. A., Barclay, T., et al. 2014, *ApJ*, 795, 151
 Espinoza, N., Bayliss, D., Hartman, J. D., et al. 2016, *AJ*, 152, 108
 Faber, J. A., Rasio, F. A., & Willems, B. 2005, *Icar*, 175, 248
 Ford, E. B. 2006, *ApJ*, 642, 505
 Fortney, J. J., Marley, M. S., & Barnes, J. W. 2007, *ApJ*, 659, 1661
 Goldreich, P., & Tremaine, S. 1980, *ApJ*, 241, 425
 Greiner, J., Bornemann, W., Clemens, C., et al. 2008, *PASP*, 120, 405
 Hansen, B. M. S., & Barman, T. 2007, *ApJ*, 671, 861
 Hardy, R. A., Harrington, J., Hardin, M. R., et al. 2017, *ApJ*, 836, 143
 Hartman, J. D., Bayliss, D., Brahm, R., et al. 2015, *AJ*, 149, 166
 Hartman, J. D., Bakos, G. Á., Béky, B., et al. 2012, *AJ*, 144, 139
 Hellier, C., Anderson, D. R., Collier Cameron, A., et al. 2012, *MNRAS*, 426, 739

- Hippler, S., Bergfors, C., Wolfgang, B., et al. 2009, *Msngr*, **137**, 14
- Howard, A. W., Marcy, G. W., Bryson, S. T., et al. 2012, *ApJS*, **201**, 15
- Janson, M., Durkan, S., Hippler, S., et al. 2017, *A&A*, **599**, A70
- Jin, S., & Mordasini, C. 2018, *ApJ*, **853**, 163
- Jordán, A., Brahm, R., Bakos, G. Á, et al. 2014, *AJ*, **148**, 29
- Kaufer, A., & Pasquini, L. 1998, *Proc. SPIE*, **3355**, 844
- Knutson, H. A., Fulton, B. J., Montet, B. T., et al. 2014, *ApJ*, **785**, 126
- Kovács, G., Bakos, G., & Noyes, R. W. 2005, *MNRAS*, **356**, 557
- Kovács, G., Zucker, S., & Mazeh, T. 2002, *A&A*, **391**, 369
- Kozai, Y. 1962, *AJ*, **67**, 591
- Li, G., Naoz, S., Kocsis, B., & Loeb, A. 2014, *ApJ*, **785**, 116
- Lidov, M. L. 1962, *P&SS*, **9**, 719
- Lin, D. N. C., Bodenheimer, P., & Richardson, D. C. 1996, *Natur*, **380**, 606
- Mancini, L., Lillo-Box, J., Southworth, J., et al. 2016, *A&A*, **590**, A112
- Mandel, K., & Agol, E. 2002, *ApJL*, **580**, L171
- Mohler-Fischer, M., Mancini, L., Hartman, J. D., et al. 2013, *A&A*, **558**, A55
- Mollière, P., & Mordasini, C. 2012, *A&A*, **547**, A105
- Mordasini, C., van Boekel, R., Mollière, P., Henning, T., & Benneke, B. 2016, *ApJ*, **832**, 41
- Nagasawa, M., Ida, S., & Bessho, T. 2008, *ApJ*, **678**, 498
- Neveu-VanMalle, M., Queloz, D., Anderson, D. R., et al. 2016, *A&A*, **586**, A93
- Ngo, H., Knutson, H. A., Hinkley, S., et al. 2015, *ApJ*, **800**, 138
- Pál, A., Bakos, G. Á, Torres, G., et al. 2008, *ApJ*, **680**, 1450
- Penev, K., Bakos, G. Á, Bayliss, D., et al. 2013, *AJ*, **145**, 5
- Pepe, F., Ehrenreich, D., & Meyer, M. R. 2014, *Natur*, **513**, 358
- Petrovich, C. 2015, *ApJ*, **805**, 75
- Queloz, D., Eggenberger, A., Mayor, M., et al. 2000, *A&A*, **359**, L13
- Queloz, D., Mayor, M., Udry, S., et al. 2001, *Msngr*, **105**, 1
- Rabus, M., Alonso, R., Belmonte, J. A., et al. 2009, *A&A*, **494**, 391
- Schlaufman, K. C. 2018, *ApJ*, **853**, 37
- Shporer, A., Zhou, G., Fulton, B. J., et al. 2017, *AJ*, **154**, 188
- Sozzetti, A., Torres, G., Charbonneau, D., et al. 2007, *ApJ*, **664**, 1190
- Telting, J. H., Avila, G., Buchhave, L., et al. 2014, *AN*, **335**, 41
- ter Braak, C. J. F. 2006, *Statistics and Computing*, **16**, 239
- Thorngren, D. P., Fortney, J. J., Murray-Clay, R. A., & Lopez, E. D. 2016, *ApJ*, **831**, 64
- Triaud, A. H. M. J., Neveu-VanMalle, M., Lendl, M., et al. 2017, *MNRAS*, **467**, 1714
- Vogt, S. S., Allen, S. L., Bigelow, B. C., et al. 1994, *Proc. SPIE*, **2198**, 362
- Wang, S., Addison, B., Fischer, D. A., et al. 2018, *AJ*, **155**, 70
- Weinberg, M. D., Yoon, I., & Katz, N. 2013, arXiv:1301.3156
- Winn, J. N., & Fabrycky, D. C. 2015, *ARA&A*, **53**, 409
- Yi, S., Demarque, P., Kim, Y.-C., et al. 2001, *ApJS*, **136**, 417
- Zhou, G., Bayliss, D., Hartman, J. D., et al. 2014a, *MNRAS*, **437**, 2831
- Zhou, G., Bayliss, D., Hartman, J. D., et al. 2015, *ApJL*, **814**, L16
- Zhou, G., Bayliss, D., Penev, K., et al. 2014b, *AJ*, **147**, 144

In theory, theory and practice are the same.

In practice, they are not.

Albert Einstein

Chapter 6

Linking Observations and Theory: The Radius Anomaly of Hot Jupiters

The second part of this thesis deals with planet evolution theory. It mainly focuses on the radius anomaly problem of hot Jupiters, as introduced in Section 3.3. Our main goal is to constrain which of the several mechanisms proposed can explain the radii of all of the observed hot Jupiters.

We also present our small contribution to understanding the origin of hot Jupiters, specifically can we rule out disk migration as the formation mechanism. As mentioned in Section 3.1.3, several mechanisms can explain the eccentricity distribution of hot Jupiters. This is directly related to the formation and migration of the close-in giant planets. The two competing theories are disk migration (e.g. [Lin et al. 1996](#)) and high eccentricity migration (e.g. [Rasio & Ford 1996](#); [Fabrycky & Tremaine 2007](#); [Naoz et al. 2012](#)). While this is a very big and active field of research and cannot be addressed in a small section, in Section 6.7 we present our contribution to the migration of hot Jupiters within the context of planet population synthesis.

6.1 Method

We want to link the observed properties of hot Jupiters and their host stars to the interior structure model `complete021`. This allows us to test the theories proposed to explain the large radii of hot Jupiters. The mechanisms suggested have been tested on a couple of planets but it is essential to prove whether they can explain the radii of the entire

population. We thus address the radius anomaly problem within a statistical framework and do not make an attempt to model in details any of the mechanisms. Specifically, we aim to quantify the internal luminosity (L_{int}) of the planet that explains the observed properties (planet mass, radius, and equilibrium temperature). However, the observed parameters have uncertainties that can be significant and thus we develop a Bayesian framework that allows us to incorporate these uncertainties and infer a distribution for the internal luminosity.

The most recognized theories include energy transport to the interior that heats the planet and therefore leads to a large radius. While the source of energy is still an open question, one of the competing theories suggest the source of heat could be the stellar irradiation of the host star. Within this context, we convert the internal luminosity into a heating efficiency ϵ , which is defined as the fraction of the stellar irradiation transported into the interior. A by-product of our model is also the interior structure of the planet, specifically we keep track of the internal temperature (T_{int}) and the pressure of the radiative-convective boundary (P_{RCB}). We then study the general distribution of the internal luminosity as a function of the planet radius, and of ϵ , T_{int} , and P_{RCB} as a function of the planet equilibrium temperature (T_{eq}).

Before I started the PhD, there was no evidence of a single mechanism that can explain the entire population of hot Jupiters. The mechanisms proposed were tested on a couple of planets but there were no studies focusing on comparing them systematically. Moreover, little was known about the T_{int} and P_{RCB} . One of the main goals of this thesis is to use a statistical approach to study the full sample of hot Jupiters, rather than to model a specific mechanism. During that time, the work of [Thorngren & Fortney \(2018\)](#) showed evidence of ohmic dissipation. Also, the study of [Thorngren et al. \(2019\)](#) provided an in-depth analysis on the internal temperature and on the depth of the RCB. Our work and approach is similar to [Thorngren & Fortney \(2018\)](#) and to [Thorngren et al. \(2019\)](#) but with a main fundamental difference. We compare our methods and results to both of Thorngren studies in Section 6.6. We note however that our study is independent of their work and we only became aware of their results during the thesis.

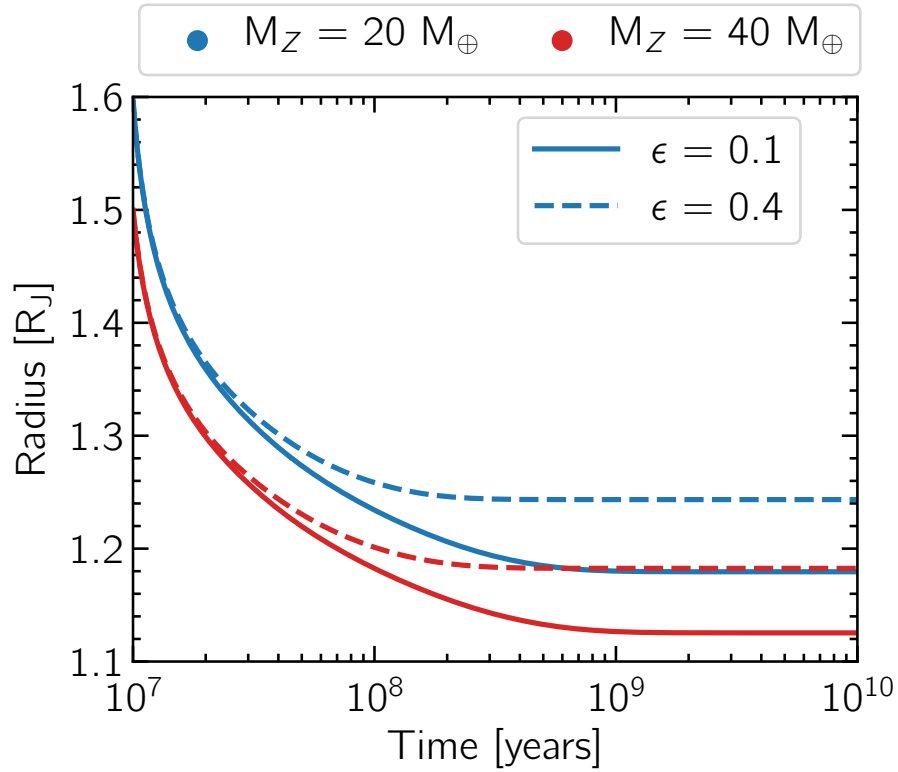


FIGURE 6.1: Radius evolution for a $1 M_J$ planet highlighting the effect of the heating efficiency (solid and dashed lines) and the amount of heavy elements in the core (blue and red lines). While the higher the efficiency the larger the radius, the more heavy elements the smaller the planet. The plot also shows the degeneracy between the heating efficiency and the amount of heavy elements.

6.2 Bloating Model

As mentioned in the previous section our aim is to estimate L_{int} and then convert it into a heating efficiency ϵ . However, several tests were done to confirm that this is plausible since this approach is based on the assumption that the planet is at steady state.

This assumption is addressed in Section 6.3.1 but for now we introduce the method of accounting for extra heat into the interior.

We include a parametrized bloating model to deposit a fraction of the stellar irradiation in the interior defined as

$$L_{\text{bloat}} = \epsilon F \pi R_p^2 \quad (6.1)$$

where L_{bloat} is the bloating luminosity and F is the stellar incident flux. In this model, ϵ is an input parameter. We assume that the extra energy is deposited in the interior and that the heating efficiency is constant in time. Figure 6.1 shows an example of the radius evolution for a $1 M_J$ planet for different heating efficiency (solid and dashed line) and different amount of heavy elements (blue and red lines). It is evident that higher efficiency leads to larger radii and the more heavy elements the smaller the radius is.

6.3 Assumptions

6.3.1 Steady State Assumption

In the rest of this chapter, we do not calculate the evolution of the planet, rather we assume that the planet is in steady state. This is motivated by the evolution of the radius presented in Figure 6.1. It is clear that the planet has reached steady state at a relatively young age. Hot Jupiters are more than 1 Gyr old and hence this assumption holds for all the planets.

6.3.2 Distribution of Heavy Elements

Figure 6.1 shows a clear degeneracy between the heating efficiency and the amount of heavy elements in the core. For the same radius, increasing the amount of heavy elements can be compensated by increasing the amount of heat deposited in the interior. In order to break this degeneracy, we use the heavy element mass – mass relation, which was developed by [Thorngren et al. \(2016\)](#) for warm Jupiters.

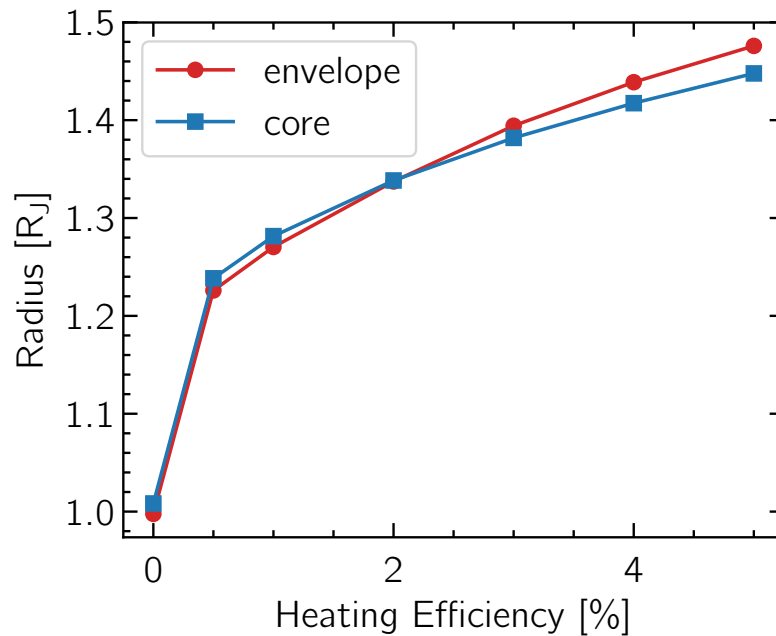


FIGURE 6.2: Planet radius as a function of heating efficiency for models where the heavy elements are in the core (blue squares) or in the envelope (red circles). The distribution of heavy elements has negligible effect on the planet radius.

We studied the effect of distributing the heavy elements entirely in the core or in the envelope for different heating efficiency for HD 209458 b. It is visible in Figure 6.2 that the location of the heavy elements has little effect on the planet radius with a maximum relative change in the radius about 2%. For the remainder of the chapter and except when mentioned, the heavy elements are distributed homogeneously in the envelope of the planet and we do not account for a central core.

6.4 Updates to the Interior Structure Model

6.4.1 The Effect of the Atmospheric Boundary Condition on the Radius

It is well established that the close proximity of hot Jupiters to their host star affects their cooling and contraction, which demanded the use of more realistic atmospheric boundary conditions. As mentioned in Section 3.2.3, we updated the atmospheric model from the semi-gray (SG) analytical one (Guillot 2010) to a fully non-gray model using the `petitCODE` (Mollière et al. 2015, 2017). In this section, we provide the main motivation behind our approach.

As pointed out in Equation (3.8), the semi-gray models depends on T_{eq} , T_{int} , and most importantly on γ , which regulates how much of the incoming flux is absorbed in the upper atmosphere. The values of γ were determined by matching the interior adiabat of the atmosphere using the analytical models of Guillot (2010) to a detailed fully non-gray model (Fortney et al. 2008) for $T_{\text{int}} = 200$ K and for several T_{eq} values. The results of γ for a given T_{eq} are tabulated in Jin et al. (2014). However, for our specific study concerning the large radii of hot Jupiters, it is believed that these planets possess hot interiors with $T_{\text{int}} > 200$ K. Using the tabulated values of γ will thus lead to incorrect outer boundary conditions, leading to different radii.

In order to study the effect of the atmospheric model on the radius, we compare the pressure–temperature (PT) profiles derived using the semi-gray to the non-gray model for a fiducial planet with an internal temperature of 500 K, equilibrium temperature of 1500 K, and surface gravity $\log g = 3$. We then compare the radii obtained under both atmospheric models. Despite the fact that both models use the same input parameters, Figure 6.3 shows the difference in the PT profiles between the previously calibrated SG model (blue line) and the one from `petitCODE` (thick green line). The dashed lines indicate the convective zones, while the solid ones indicate the radiative regions. The PT profile using the γ values as tabulated by Jin et al. (2014) does not match the one using the `petitCODE` models, leading to discrepancy in the radius with a relative change on the order of $\sim 7\%$. On the other hand, if we manually calibrate the SG model against the `petitCODE` PT profile (black line), we get $\gamma = 0.6$ and the radius is matched to within $\sim 1\%$.

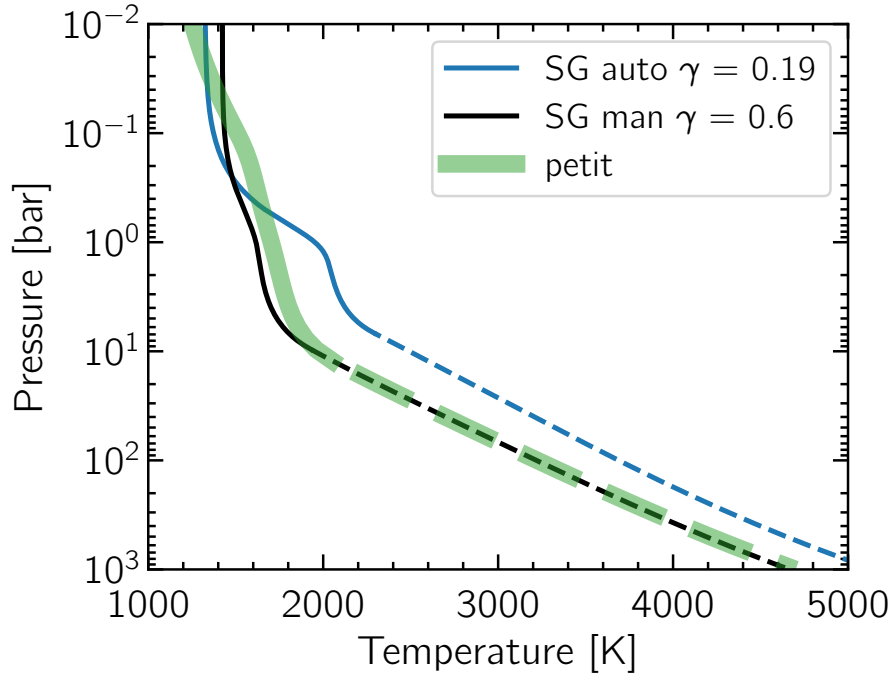


FIGURE 6.3: Pressure–Temperature profiles for the non-gray `petitCODE` model (thick green) and for the semigray (SG) model calibrated using the tabulated values from [Jin et al. \(2014\)](#) (blue) and the SG models calibrated manually to match the interior adiabat as given by the `petitCODE` models (black). The dotted lines show the convective regions, while the solid lines indicate the radiative regions.

Figure 6.4 shows the evolution of the radius of HD 209458 b using `petitCODE` (solid lines) and SG (dashed line) models. The gray square and the error bars indicate the radius and age of the planet. While a heating efficiency $\epsilon = 0.7\%$ is needed to reproduce the radius of HD 209458 b using the SG models, $\epsilon = 3\%$ is required using the `petitCODE` models. This is significantly different and further motivates the need to couple the structure model to a more realistic fully non-gray model.

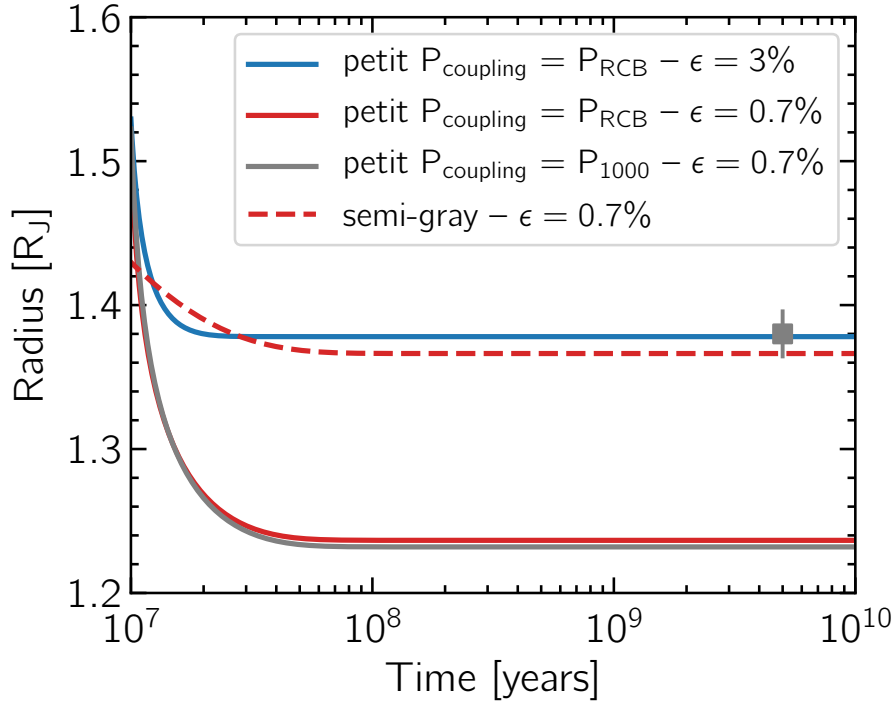


FIGURE 6.4: The radius evolution of HD 209458 b using the semi-gray and `petitCODE` models. The gray square indicates the observed radius and age of the planet. For a fixed heating efficiency $\epsilon = 0.7\%$, there is a significant difference between the `petitCODE` and semi-gray models. $\epsilon = 3\%$ and $\epsilon = 0.7\%$ is needed to reproduce the radius of HD 209458 b using the `petitCODE` and SG models, respectively. P_{coupling} at 1000 bar or following the RCB layer has little effect on the radius (for more details see Section 6.4.2).

6.4.2 Details of the Coupling

While the main concept of coupling the interior to atmospheric models is simple, the pressure at which the coupling is done requires careful analysis. The basic idea is to match the convective interior adiabat of the atmosphere to the convective layers of the planet.

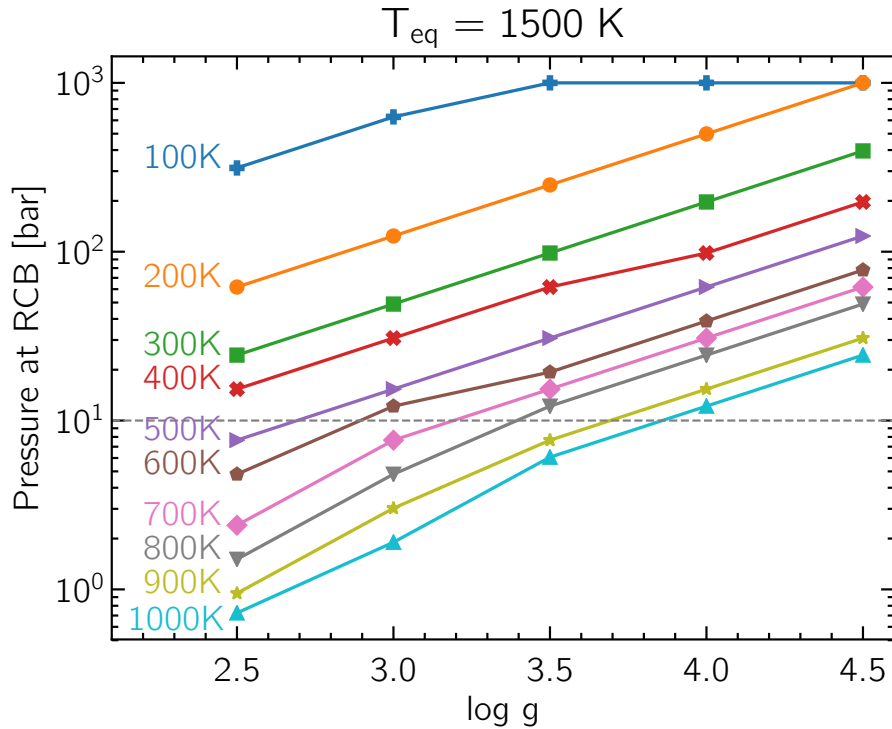


FIGURE 6.5: Pressure at the radiative-convective boundary (RCB) as a function of $\log g$ and T_{int} (color coded) for planets with $T_{\text{eq}} = 1500 \text{ K}$. While all the atmospheres of the planets with $T_{\text{int}} < 400 \text{ K}$ are adiabatic at $P_{\text{RCB}} = 10 \text{ bar}$, this is not the case for planets with higher T_{int} and low $\log g$.

Previous methods involved choosing a fixed pressure e.g. at 50 bar (Linder et al. 2019) or a fixed optical depth (Chabrier & Baraffe 1997). For cold low-mass planets the coupling can be made at any pressures as long as it is done in the convective region of the planet and the error on the radius from neglecting the above layers is negligible (Linder et al. 2019). For hot Jupiters however, the outward structure cannot be neglected because the pressure at the RCB can sometimes be at 100 or even 1000 bar. Additionally, the pressure at the RCB changes in time and is different for planets with different T_{eq} , T_{int} , and $\log g$.

Figure 6.5 shows the pressure at the RCB for $T_{\text{eq}} = 1500$ K and for different T_{int} and $\log g$. For example, coupling the atmosphere and the interior at $P = 10$ bar is reasonable for planets with $T_{\text{int}} < 400$ K and for planets with high $\log g$ and T_{int} values. But for planets with low $\log g$ and high T_{int} the atmosphere is not adiabatic at such pressures. In order to choose a universal rule that applies for all the hot Jupiters, we studied the effect of coupling either at 1000 bar or following the RCB. Figure 6.4 confirms that the change in the radius is negligible for a heating efficiency $\epsilon = 0.7\%$. For the rest of this chapter, the coupling is done following the RCB and the outward structure is calculated assuming hydrostatic equilibrium.

6.5 Conclusion of the Publication

We find that the large radii of hot Jupiters indeed can be explained by high internal luminosity, which can be as high as 4 orders of magnitude more luminous than Jupiter. We also studied the effect of the high internal luminosity on the interior structure of the planet. We find that the internal temperature is higher than previous estimates, ranging between 200 K and 800 K for the planets with the highest equilibrium temperature. As a consequence of the hot interior, the RCB layer moves to low pressures, reaching as low as 3 bar for the most irradiated planets. This is significantly high up in the atmosphere compared to previous estimates of 1000 bar, which is based on models that do not account for the high internal entropy (Fortney et al. 2007). This has important consequences on the heating mechanism as it provides constraints at which pressure the heat should be deposited. In the context of the proposed mechanisms, we provide evidence for the first time that three mechanisms can explain the large radii of hot Jupiters: ohmic dissipation, advection of potential temperature, and thermal tides.

The method and results are presented in details in the paper below, which was submitted to *Astronomy & Astrophysics* on the 6th of May 2020.

Evidence of Three Mechanisms Explaining the Radius Anomaly of Hot Jupiters

P. Sarkis^{1,2}, C. Mordasini¹, Th. Henning², G. D. Marleau^{3,1,2}, and P. Mollière²

¹ Physikalisches Institut, Universität Bern, Gesellschaftsstrasse 6, CH-3012 Bern, Switzerland

² Max-Planck-Institut für Astronomie, Königstuhl 17, Heidelberg 69117, Germany

³ Institut für Astronomie und Astrophysik, Universität Tübingen, Auf der Morgenstelle 10, D-72076 Tübingen, Germany

Received May 6, 2020/ Accepted —

ABSTRACT

Context. The anomalously large radii of hot Jupiters are still not fully understood, and all of the proposed explanations are based on the idea that these close-in giant planets possess hot interiors. Most of the mechanisms proposed have been tested on a handful of exoplanets.

Aims. We approach the radius anomaly problem by adopting a statistical approach. We want to infer the internal luminosity for the sample of hot Jupiters, study its effect on the interior structure, and put constraints on which mechanism is the dominant one.

Methods. We develop a flexible and robust hierarchical Bayesian model that couples the interior structure of exoplanets to the observed properties of close-in giant planets. We apply the model to 314 hot Jupiters and infer the internal luminosity distribution for each planet and study at the population level (i) the mass–luminosity–radius distribution and as a function of equilibrium temperature the distributions of the (ii) heating efficiency, (iii) internal temperature, and the (iv) pressure of the radiative–convective–boundary (RCB).

Results. We find that hot Jupiters tend to have high internal luminosity with $10^4 L_J$ for the largest planets. As a result, we show that all the inflated planets have hot interiors with internal temperature ranging from 200 K up to 800 K for the most irradiated ones. This has important consequences on the cooling rate and we find that the RCB moves to low pressures between 3 and 100 bar. Assuming that the ultimate source of the extra heating is the irradiation from the host star, we also illustrate that the heating efficiency increases with increasing equilibrium temperature, reaches a maximum of 2.5% at ~ 1860 K, beyond which the efficiency decreases, in agreement with previous results. We discuss our findings in the context of the proposed heating mechanisms and illustrate that ohmic dissipation, advection of potential temperature, and thermal tides are in agreement with certain trends inferred from our analysis and thus all three models can explain aspects of the observations.

Conclusions. We provide new insights on the interior structure of hot Jupiters and show that with our current knowledge it is still challenging to firmly identify the universal mechanism driving the inflated radii.

Key words. Stars: planetary systems – Planets and satellites: formation – Planets and satellites: interiors

1. Introduction

Two decades of observational and theoretical exploration have revealed that the anomalously large radii of close-in transiting giant planets holds firmly (e.g. Laughlin et al. 2011; Weiss et al. 2013). The radii of hot Jupiters are larger than what is predicted by standard interior structure models (Guillot & Showman 2002). Observations reveal that there is a strong correlation between the observed radii and the stellar incident flux (e.g. Enoch et al. 2012), with a threshold around $\sim 2 \times 10^8 \text{ erg s}^{-1} \text{ cm}^{-2}$, corresponding to an equilibrium temperature of about 1000 K (Demory & Seager 2011; Miller & Fortney 2011), below which the physical mechanism becomes inefficient. Sestovic et al. (2018) further demonstrated that the inflation extent is mass dependent, where the planets with the largest anomalous radii have masses less than $\sim < 1 M_J$.

There has been a lot of investigations to explain the discrepancy between the observations and theoretical models. The proposed mechanisms can be divided into two categories: (i) slowing down cooling and contraction or (ii) depositing extra heat into the interior. Burrows et al. (2007) showed that slowing down the cooling and thus delaying contraction can be achieved by in-

creasing the atmospheric opacity. Another way to delay contraction is to reduce the heat transport efficiency due to compositional gradients (Chabrier & Baraffe 2007).

It is well established that heating up the interior of the planet increases its entropy and thus its radius (Arras & Bildsten 2006; Marleau & Cumming 2014). The source of heat is still not constrained and possible sources could be tidal dissipation of an eccentric orbit (e.g. Bodenheimer et al. 2001), advection of potential temperature, which is a consequence of the strong stellar irradiation (Tremblin et al. 2017; Sainsbury-Martinez et al. 2019), or dissipative processes powered by the stellar irradiation flux. The latter has received a lot of attention and the mechanism to transport fraction of the stellar incident flux into the interior is still an open question. One mechanism is atmospheric circulation, which leads to thermal dissipation of kinetic energy into the interior (Guillot & Showman 2002; Showman & Guillot 2002). Another mechanism is ohmic dissipation (Batygin & Stevenson 2010; Batygin et al. 2011; Perna et al. 2010a; Huang & Cumming 2012; Wu & Lithwick 2013; Ginzburg & Sari 2016), where the irradiation drives fast winds through the planet’s magnetic fields, giving rise to currents that dissipate ohmically in the interior. Other mechanisms are thermal tides (Arras & Socrates 2010) and the mechanical greenhouse (Youdin & Mitchell 2010).

Send offprint requests to: Paula Sarkis, e-mail: paula.sarkis@space.unibe.ch

Some of these mechanisms come with a lot of approximations and uncertainties. For example, an important uncertain parameter in atmospheric circulation, ohmic dissipation, and advection of potential temperature is the wind speeds and the effect of magnetic drag in damping the winds (Perna et al. 2010a,b). Another uncertainty is how deep the wind zone extends, which is important to constrain the pressures at which the extra heat should be dissipated. Wu & Lithwick (2013) illustrate that if the wind zone is at shallow pressures, then a significantly larger heating efficiency is needed to achieve the same interior heating, compared to heating at deeper pressures. Komacek & Youdin (2017) argued that the extra heat should be deposited in the convective layers or at the radiative–convective–boundary (RCB), otherwise it will be re-radiated away. Huang & Cumming (2012) deposited the extra heat in the radiative layers and as a consequence showed that the RCB moves to deeper pressures. Fortney et al. (2007) showed that RCB is located at pressures of 1000 bar, where little is known about the wind speeds at such deep pressures. However, the Fortney et al. (2007) models were developed for irradiated planets and do not consider the high internal entropy that hot Jupiters are believed to possess.

All the mechanisms proposed have been tested and applied on single or a handful of planets. It is yet to be demonstrated that these mechanisms can explain the radii of all the observed hot Jupiters. Within this context, in this paper we approach the radius inflation problem from a statistical point of view, similar to the approach of Thorngren & Fortney (2018) (hereafter TF18). We do not model any of the previously mentioned mechanisms but rely solely on the interior structure model. We develop a hierarchical Bayesian model that allows us to couple the interior structure models to the observed physical properties of hot Jupiters while incorporating the measurement uncertainties. Our approach naturally accounts for non-Gaussian likelihoods. We first apply our model on the individual planets to infer the internal luminosity that reproduces the observed physical properties of hot Jupiters, namely radius, mass, and equilibrium temperature. Second, as a consequence of the high internal entropy, we find that the interior tends to be hot and show that the RCB moves to shallow pressures. Finally, we compare our findings to the proposed mechanisms and show that ohmic dissipation (Batygin & Stevenson 2010), advection of potential temperature (Tremblin et al. 2017), and thermal tides (Arras & Socrates 2010) can explain the anomalously large radii of hot Jupiters.

In a recent study, TF18 showed that the heating efficiency ϵ increases as a function of equilibrium temperature until a maximum of $\sim 2.5\%$ is reached at around 1500 K, beyond which it decreases. The basic shape of $\epsilon(T_{\text{eq}})$ provides evidence for ohmic dissipation. Building on the functional form of $\epsilon(T_{\text{eq}})$, Thorngren et al. (2019) (hereafter T19) studied the effect of central heating on the interior structure of hot Jupiters and found that the internal temperature is much hotter than previous estimates, which pushes the RCB to lower pressures. Our approach is similar to TF18 but rather than modeling the extra heating as a function of ϵ , we do not assume explicitly a source for the extra heat. Instead, we consider the planet reached steady state and compute the internal luminosity given the planet mass, radius, and equilibrium temperature. The advantage of this approach is twofold: first, we can compare our results to heating mechanisms where the source of extra heat is not the stellar irradiation, and second, we self-consistently study the effect of high internal entropy on the interior structure of hot Jupiters, namely the internal temperature and pressure of the RCB. We note, however, that both approaches should lead to the same results. We also convert the internal luminosity to a heating efficiency ϵ and com-

pare our results to TF18 in Section 5.3. We show that our results are qualitatively similar using a larger sample focused on FGK main-sequence stars and using an independent interior structure model.

The outline of this paper is as follows. Section 2 provides an overview of the sample selection criteria. In Section 3 we present the interior structure model used in this analysis. In Section 4 we outline the probabilistic framework used to link observations and theory and derive the basic equation which our method is based on (Equation (32)). Readers interested in the results can safely skip to Section 5 where we present the results of our analysis. We discuss the results and the shortcomings of our approach in Section 6 and conclude in Section 7.

2. Sample Selection

For the purpose of our study, we required that all the planets have measured masses and radii. Sestovic et al. (2018) showed that the radii of planets with masses less than $0.37 M_J$ do not show a clear dependence on the stellar incident flux. Photoevaporation plays an important role in the evolution of such low-mass close-in planets (Owen & Jackson 2012; Jin et al. 2014). Baraffe et al. (2004) also showed that these planets are subject to undergo Roche-lobe overflow. We therefore restrict our analysis to planets with masses $0.37 < M_p < 13 M_J$ with semi-major axis $a < 0.1$ au. In our study, we make no attempt to correct for selection effects where it is still challenging to detect “medium-inflated” hot Jupiters around F stars using ground-based surveys (see the discussion in Section 6.5).

Lopez & Fortney (2016) suggested that giant planets around stars leaving the main-sequence experience a high level of irradiation that could ultimately increase their radii. However, other studies argued that ohmic heating cannot re-inflate planets after they have already cooled (Wu & Lithwick 2013; Ginzburg & Sari 2016). A handful of re-inflated planets have been discovered around giant stars (Grunblatt et al. 2016, 2017; Hartman et al. 2016). Since different mechanisms can be at play around evolved stars, we exclude such planets and only consider hot Jupiters around solar-like stars. Specifically, we consider stars with stellar temperature $T_* = 4000 - 7000$ K and surface gravity $\log g = 4 - 4.9$.

The data was taken from the Transiting Extrasolar Planet Catalogue (TEPCat¹; Southworth 2011), last accessed on November 2018. The aforementioned constraints on the planet mass, semi-major axis, and stellar temperature and surface gravity, lead to a final sample consisting of 314 hot Jupiters. The equilibrium temperature (T_{eq}) values in the literature are often not homogeneous, where different teams use different assumptions for the albedo and heat redistribution. To mitigate this, we compute the equilibrium temperature for all the planets assuming a circular orbit, zero albedo, and full heat redistribution from the day-side to the night-side (Guillot 2010)

$$T_{\text{eq}} = T_* \sqrt{\frac{R_*}{2a}} \quad (1)$$

where T_* and R_* are the stellar temperature and radius, respectively, and a is the semi-major axis. Figure 1 displays the selected targets in the equilibrium temperature–radius (left panel) and mass–radius (right panel) diagrams color coded by the en-

¹ www.astro.keele.ac.uk/jkt/tepcat/

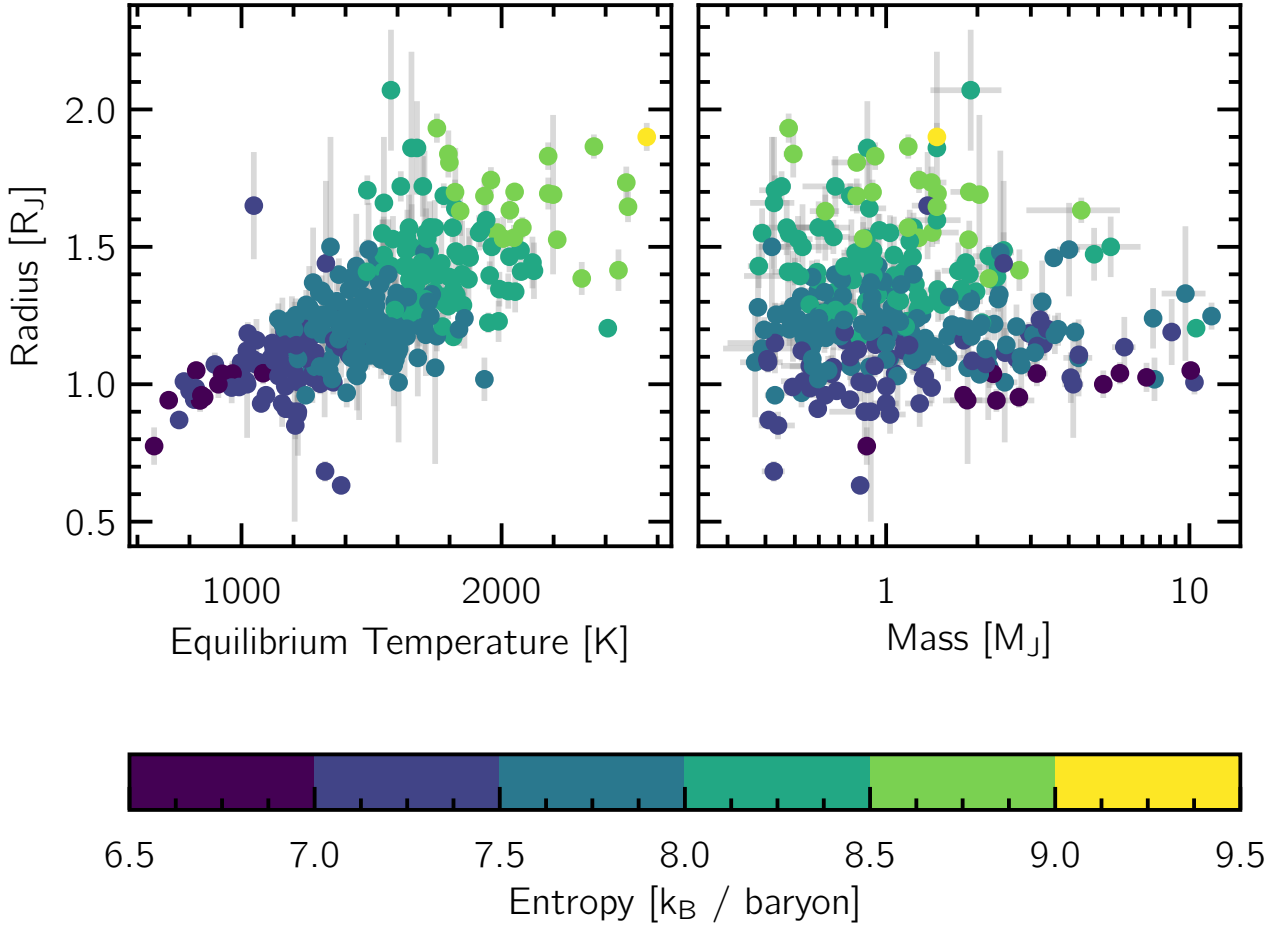


Fig. 1. Equilibrium temperature–radius diagram (*left panel*) and mass–radius diagram (*right panel*) colored by entropy for the 314 hot Jupiters selected for our analysis. The entropy was computed using the observed physical properties and an assumed heavy-element fraction of 0.2. Planets with large radii tend to have high internal entropy, with a weak dependence on planetary mass.

trophy². The entropy was calculated for all the planets given the observed physical properties of each system and assuming the fraction of heavy element is 20% the planet mass. Note that this value was chosen arbitrarily and for the rest of the results presented in this paper, we use the mass–heavy-element mass relation (Thorngren et al. 2016, see also Section 3.2). It is evident that larger internal entropy leads to larger radii as noted by previous work (e.g. Arras & Bildsten 2006; Spiegel & Burrows 2013; Marleau & Cumming 2014), with a weaker dependence on planetary mass. Planets with the largest radii have high equilibrium temperatures, masses below 1 M_J , and high entropy in their deep convective interior. There is thus a compelling evidence from observations that the proximity to the star, planet mass, and the incident stellar flux play a major role in keeping hot Jupiters at high entropy.

² When comparing to other work, it is crucial to use the same entropy zero-point or to correct for this. See Footnote 2 of Mordasini et al. (2017).

3. Interior Structure Model

The primary way to gain insights into the interior structure of exoplanets is typically derived from theoretical structure models by matching the observed mass and radius. Such models are often used to constrain the planet bulk composition. Given the age of the host star and the mass of the planet, the amount of heavy elements is determined by matching the observed radius with the radius predicted from structure models. This has been applied to warm Jupiters (e.g. Thorngren et al. 2016), sub-Neptunes (e.g. Valencia et al. 2013), and super-Earths (e.g. Dorn et al. 2019) but is challenging to apply for hot Jupiters because the radii are inflated.

The aim of our study is to characterize the interior structure of hot Jupiters within a probabilistic framework. This allows us to gain insights into the physical properties governing the interior. We are specifically interested in inferring the internal luminosity of the planets based on the observed mass, radius, and equilibrium temperature. This in turn will provide constraints on the heating efficiency, internal temperature, and the pressure at the radiative–convective–boundary (RCB). The standard interior structure model is briefly outlined in Section 3.1 and we discuss in Section 3.2 our approach to account for heat dissipa-

tion. The main model assumptions and limitations are addressed in Section 3.3.

3.1. Standard Model

The planetary evolution model `complete21` was presented in Mordasini et al. (2012) and several modifications have been introduced since such as photoevaporation (Jin et al. 2014; Jin & Mordasini 2018) and coupling the interior to a non-gray atmospheric model (Linder et al. 2019; Marleau et al. 2019). In the following sections, we provide a brief description of the code relevant to our work and discuss in Section 3.3 the limitations of the model.

The internal structure of a gas giant planet is modeled using the 1D equations below. Equation (2) defines the conservation of mass. We assume that the planet is in hydrostatic equilibrium (Equation 3) and that the luminosity is constant with radius (Equation 4). Mordasini et al. (2012) showed that the latter assumption does not significantly affect the evolution of the planet when the heating occurs deep, as we assume (see below). Finally, Equation (5) is the energy transport equation describing the transport of energy either via radiation or convection.

$$\frac{dm}{dr} = 4\pi r^2 \rho \quad (2)$$

$$\frac{dP}{dr} = -\frac{Gm}{r^2} \rho \quad (3)$$

$$\frac{dl}{dr} = 0 \quad (4)$$

$$\frac{dT}{dr} = \frac{T}{P} \frac{dP}{dr} \nabla \quad (5)$$

In the above equations, r is the planetary radius as measured from the center, m the total mass inside r , ρ density, P pressure, T temperature, l planet internal luminosity, G the gravitational constant, and ∇ is the temperature gradient which depends on the process energy is transported and defined as

$$\nabla \equiv \frac{d \ln T}{d \ln P} = \min(\nabla_{\text{ad}}, \nabla_{\text{rad}}). \quad (6)$$

Qualitatively, if a shell inside the planet is convectively unstable, then energy is transported by convection and we assume that the temperature gradient $\nabla = \nabla_{\text{ad}}$ is given by the equation of state (EOS). If the shell is convectively stable, then the energy is carried via radiation and $\nabla = \nabla_{\text{rad}}$. ∇_{rad} is calculated in the diffusion approximation

$$\nabla_{\text{rad}} = \frac{3}{64\pi\sigma G} \frac{\kappa l P}{T^4 m} \quad (7)$$

where κ is the opacity as given by Freedman et al. (2014) and σ is the Stefan-Boltzmann constant. We check if a given layer is convective by applying the Schwarzschild criterion. Note in Section 3.1.1 we provide the details of coupling `complete21` to a fully non-gray atmospheric model (`petitCODE`; Mollière et al. 2015, 2017) and hence the radiative structure is calculated using `petitCODE`.

We use the classical SCvH EOS of hydrogen and helium (Saumon et al. 1995) with a He mass fraction $Y = 0.27$. Our model does not include a central core and all the heavy elements are homogeneously mixed in the gaseous envelope, see Section 3.3.1 for a discussion on the distribution of heavy elements. We model the heavy elements as water and adopt the widely used EOS of water ANEOS (Thompson 1990; Mordasini 2020). H/He and water are mixed according to the additive volume law (Baraffe et al. 2008). The transit radius is defined at $P = 20$ mbar.

3.1.1. Atmospheric Model

The atmospheric boundary conditions control the cooling rate of irradiated giant planets. The evolution of the planet and its final structure are thus sensitive to the upper boundary conditions (Guillot & Showman 2002). Jin et al. (2014) calibrated the semi-gray model of Guillot (2010) against the fully non-gray atmospheric models of Fortney et al. (2008) in order to determine the value of γ , the ratio of the optical to the infrared opacity. They used a nominal value of $T_{\text{int}} = 200$ K. For our study, hot Jupiters are thought to be inflated due to dissipation or advection of heat into the interior, which thus leads to $T_{\text{int}} > 200$ K. Hence, using the tabulated values of Jin et al. (2014) will lead to different PT structures and therefore alter significantly the interior structure of the planet. Indeed, we find that for $T_{\text{eq}} = 1500$ K, $T_{\text{int}} = 500$ K, and $\log g = 3$, the relative change in the radius between using the improved version of the semi-gray model and using a non-gray model is around $\sim 7\%$, where the semi-gray model tend to lead to larger radii. It is essential then to have realistic atmospheric boundary conditions by using wavelength dependent radiative transfer atmospheric models.

Following a similar approach to Linder et al. (2019), we compute a grid of fully non-gray atmospheric models calculated using the `petitCODE` (Mollière et al. 2015, 2017). We included the following line absorbers CH_4 , H_2O , CO_2 , HCN , CO , H_2 , H_2S , NH_3 , OH , C_2H_2 , PH_3 , Na , K , TiO , VO , and SiO , and the following pseudo-continuum absorbers H_2 - H_2 Collision Induced Absorption, H_2 -He Collision Induced Absorption, H^- bound-free, H^- free-free, H_2 Rayleigh scattering, and He Rayleigh scattering. The reference for these opacities can be found in Mollière et al. (2019). These grids are then used to relate the planet atmospheric temperature and pressure to the planet internal structure. The atmospheric grid was calculated assuming solar composition and covering a range of 2.5–4.5 in $\log g$, 500–2700 K in equilibrium temperature, and 100–1000 K in internal temperature. The equilibrium temperature and surface gravity were chosen to cover the range of all the hot Jupiters selected in our sample.

The coupling between the atmosphere and the interior is done in the interior adiabat, following the first convective layer below the RCB. Details are given in Marleau et al. (2019). For a given $\log g$, equilibrium temperature, and internal temperature, the corresponding pressure and temperature were used as boundary conditions to calculate the inward interior structure. The outward structure was calculated using the `petitCODE` structure and assuming hydrostatic equilibrium (Equation 3) between the pressure at the coupling point and 20 mbar, i.e. the pressure at which the transit radius is defined. We verify that coupling at a high fixed pressure, $P = 1000$ bar, or following the RCB layer does not significantly affect the transit radius with relative change around $\sim 0.3\%$.

The atmospheric PT structures assume constant $\log g$. In fact, $\log g$ changes slightly in the radiative layers. Assuming

that the change in $\log g$ in the radiative layers during the planet evolution is around ~ 0.05 , then the change in entropy is only around ~ 0.05 kB/baryon for an internal temperature (T_{int}) of 700 K and an equilibrium temperature (T_{eq}) of 2500 K. It would take a change of 0.5 in $\log g$ to have a significant change in entropy (around 0.5 kB/baryon for $T_{\text{int}}=700$ K and $T_{\text{eq}}=2500$ K). We confirm that the change in entropy is negligible across the entire grid except for models with $T_{\text{eq}} > 2500$ K, $T_{\text{int}} > 700$ K, and $\log g < 3.5$. In our sample, only WASP-12 b has $T_{\text{eq}} = 2580$ K and $\log g = 3.0$ (Collins et al. 2017) where the change in entropy is between 0.06 - 0.08 kB/baryon. The radius of only one planet in our sample could be slightly underestimated, and therefore a constant $\log g$ in the PT structures is not a strong assumption.

3.2. Heat Dissipation

It is well established that, compared to cold Jupiter-like planets, the high internal entropy of a hot Jupiter increases its radius (Spiegel & Burrows 2013; Marleau & Cumming 2014). For example, the planet interior can gain entropy through ohmic or tidal heating. In this work, we do not attempt to model a mechanism to transport heat into the interior. We assume the planet is in steady state and thus do not calculate the planetary thermal evolution. We use the planet mass, radius, and equilibrium temperature (technically the stellar luminosity and the semimajor axis) from observations along with the mass–heavy–element–mass relation from Thorngren et al. (2016), to quantify the present internal luminosity L_{int} of the planet. At steady state, L_{int} is identical to the extra heating power deposited and thus

$$L_{\text{int}} = \epsilon F \pi R_p^2 \quad (8)$$

$$F = \sigma T_*^4 \left(\frac{R_*}{a} \right)^2 \quad (9)$$

where ϵ is the fraction of stellar irradiation transported into the interior, i.e. the heating efficiency, σ is the Stefan-Boltzmann constant, R_p the planetary radius, and F is the flux the planet receives at the substellar point as a function of the stellar temperature T_* , stellar radius R_* , and the semi-major axis a (Guillot 2010). We assume that the heat dissipated is absorbed at $\tau = 2/3$ and deposited at the center of the planet. Komacek & Youdin (2017) showed that heating at any depths larger than 10^4 bar yields nearly similar radii. However see the discussion relevant to this assumption in Section 3.3.2. Our definition agrees well with TF18, where they also deposit the extra heat at the center.

3.3. Model Assumptions/Limitations

3.3.1. Distribution of Heavy Elements

The distribution of heavy elements in the interior of exoplanets is still an open question. Some models assume for simplicity that all the heavy elements are in the core (Mordasini et al. 2012). For warm Jupiters, Thorngren et al. (2016) set an upper limit of $10 M_{\oplus}$ of heavy elements in the core and the rest is mixed homogeneously in the envelope. Current models developed to explain the anomalously large radii of hot Jupiters mix all the heavy elements in the envelope and do not include a central core (e.g. TF18; Komacek & Youdin 2017).

From the *Juno* mission, we now know that Jupiter has a diluted core (Wahl et al. 2017) based on the measurements of Jupiter’s low-order gravitational moments (Folkner et al. 2017), yet these findings are challenging to explain from standard formation models (Muller et al. 2020). Even though the interior

structures are highly affected by the chosen equation of state, the prediction of an enriched envelope still holds (Wahl et al. 2017). Planet formation models based on core accretion and that include the effect of envelope enrichment, also suggest that gas giant planets can be formed, notably at an accelerated rate (Venturini et al. 2016). Envelope enrichment compared to the Sun has also been observed for all of our four giant planets (Guillot & Gautier 2014).

In this work, all the heavy elements are mixed homogeneously in the convective part of the interior and are made up entirely of water. A central core is therefore not included. We compare the effect of the distribution of the heavy elements in the core versus in the envelope on the transit radius of the planet and hence on the heating efficiency ϵ . We find that for HD209458 b, $42 M_{\oplus}$ distributed in the core or in the envelope do not change significantly the radius when we account for heating in the interior. The absolute relative change in the radius is less than 2% for ϵ ranging between 0 – 5%. These results are also in agreement with Thorngren et al. (2016), which reached the same conclusion without accounting for heat dissipation. The median relative uncertainties on the radii measurements from observations in our sample is 4.3%, thus the distribution of the heavy elements has little effect on the inference of L_{int} and therefore ϵ . We also show in Section 5 that the uncertainty on the heating efficiency is mainly dominated by the amount of heavy elements in the planet rather than their distribution within the planet.

3.3.2. Depth of Internal Heating

In our model, we assume that the heat is deposited in the interior of the planet. However, the pressures at which heat is deposited is still not constrained. Within the context of ohmic dissipation (Batygin & Stevenson 2010), the depth of internal heating is mainly dominated by the electrical conductivity profile and by the depth of the wind zone. The layers that contribute the most are the layers close to the RCB. At lower pressures heat is re-radiated, whereas at higher pressures ohmic heating is not efficient due to the high conductivity there (Batygin & Stevenson 2010; Batygin et al. 2011). Huang & Cumming (2012) deposit the extra heat in the radiative layers and do not include ohmic heating below pressures of 10 bar. Under these assumptions, the RCB moves to higher pressures. Wu & Lithwick (2013) showed that heat deposited at deep layers requires significantly less heating efficiency in comparison to depositing the extra heat at shallow pressures. For planetary parameters similar to TrEs-4 b and using the same heating efficiency, the model of Batygin & Stevenson (2010) yields a planetary radius of $1.9 R_J$, while under a similar model Wu & Lithwick (2013) yields $1.6 R_J$. Differences in the radial profiles of the conductivity and wind might explain this difference. This however shows the difficulty in comparing models under the same heating mechanism but using different assumptions.

Komacek & Youdin (2017) studied systematically the effect of varying the depth of heating on the radius and found that heat deposited in the convective layers can explain the radii of hot Jupiters. Modest heating at pressures larger than 100 bar is enough, on condition that the heating is applied at an early age while the interior at such pressures is still convective. Heating at any pressure deeper than 10^4 bar leads to similar radii.

All the results we show are based on the assumption that heat is deposited in the deep interior. Therefore, the heating efficiencies we compute could be underestimated. This potentially has also an effect on the interior structure of hot Jupiters, where we show that the RCB moves to lower pressures.

4. Statistical Model

Our goal is to estimate the internal luminosity and heating efficiency for the individual planets and for the population of hot Jupiters, while accounting for the uncertainties on the observed parameters. In this section, we describe the method used to infer the distribution of the internal luminosity and thus the heating efficiency for each planet, by establishing a probabilistic framework to link the observed planetary radius to the predicted one from the theoretical model described in Section 3. We start by describing how the internal luminosity for each individual planet is computed in Section 4.1. We will refer to this step as the *lower level* of the hierarchical model. In Section 4.2, we then combine the individual posterior samplings to study the global distribution of the full population. This will be referred to as the *upper level* of the hierarchical model.

4.1. Lower Level of the Hierarchical Model: Inferring L_{int} for Each Planet

For each planet n ($n = 1, 2, \dots, N$), the planetary radius $R_{p,n}$ depends in our model on the planetary mass $M_{p,n}$, the fraction of heavy elements $Z_{p,n}$, the planet internal luminosity $L_{\text{int},n}$, and the stellar incident flux $F_{p,n}$, which further depends on the stellar luminosity $L_{*,n}$ and on the semi-major axis a_n . In what follows, all the quantities refer to the individual hot Jupiter’s physical parameters. In this framework, we define ω_n , the parameters that determine the planetary radius for each individual hot Jupiter

$$\omega_n \equiv (M_{p,n}, Z_{p,n}, L_{\text{int},n}, L_{*,n}, a_n) \quad (10)$$

and thus the predicted radius from the theoretical models $R_{t,n}$ is a deterministic function of ω_n , where $R_{t,n} = f(\omega_n)$. $R_{t,n}$ is determined using the internal structure model described in Section 3. Given the observed planetary mass, semi-major axis, and stellar luminosity, and using the mass–heavy-element mass relation from Thorngren et al. (2016), we aim to infer the distribution of $L_{\text{int},n}$ that reproduces the observed radius. We thus intend to answer the question: What is the internal luminosity of the planet given the observable parameters and our assumption on the fraction of heavy elements? Therefore, we define the likelihood function, the probability to observe the data given a specific set of model parameters, as

$$P(\mathbf{D}_n | \omega_n) = P(R_{p,n} | M_{p,n}, Z_{p,n}, L_{\text{int},n}, L_{*,n}, a_n). \quad (11)$$

Finally, the posterior probability function, the probability of the parameters ω_n given the data \mathbf{D}_n , is

$$P(\omega_n | \mathbf{D}_n) \propto P(\mathbf{D}_n | \omega_n) P(\omega_n) \quad (12)$$

$$\begin{aligned} &\propto P(R_{p,n} | M_{p,n}, Z_{p,n}, L_{\text{int},n}, L_{*,n}, a_n) \\ &\quad \times P(M_{p,n}, Z_{p,n}, L_{\text{int},n}, L_{*,n}, a_n) \end{aligned} \quad (13)$$

$$\begin{aligned} &\propto P(R_{p,n} | M_{p,n}, Z_{p,n}, L_{\text{int},n}, L_{*,n}, a_n) \\ &\quad \times P(Z_{p,n} | M_{p,n}) P(M_{p,n}) P(L_{\text{int},n}) P(L_{*,n}) P(a_n). \end{aligned} \quad (14)$$

In the last line in Equation (14) we assume that $L_{\text{int},n}$, $L_{*,n}$, and a_n are independent of each other and that $Z_{p,n}$ depends on $M_{p,n}$ following the mass–heavy-element mass relation (Thorngren et al. 2016). This inference allows us to account for data uncertainties. The semi-major axis is known precisely from observations and

hence we fix the value to the observed one. We then marginalize over $M_{p,n}$, $Z_{p,n}$, and $L_{*,n}$ to infer the distribution of the internal luminosity. We assume that the distribution of each of the observed parameter is a Gaussian distribution centered on the true quantity with a scatter given by the measurement uncertainties. Following the standard statistical notation, we can write

$$M_{p,n} | M_{\text{pt},n}, \sigma_{M_{p,n}} \sim \mathcal{N}(M_{\text{pt},n}, \sigma_{M_{p,n}}) \quad (15)$$

$$Z_{p,n} | M_{p,n}, \alpha, \beta, \sigma_Z \sim \mathcal{N}(\alpha M_{p,n}^{\beta-1}, \sigma_Z) \quad (16)$$

$$L_{*,n} | L_{\text{st},n}, \sigma_{L_{*,n}} \sim \mathcal{N}(L_{\text{st},n}, \sigma_{L_{*,n}}) \quad (17)$$

$$R_{p,n} | R_{t,n}, \sigma_{R_{p,n}} \sim \mathcal{N}(R_{t,n}, \sigma_{R_{p,n}}) \quad (18)$$

$$\epsilon \sim \mathcal{U}(0\%, 5\%) \quad (19)$$

where α , β , and σ_Z are the values taken from the mass–heavy-element mass relation established by Thorngren et al. (2016). We use $\alpha = 57.9/317.828$, $\beta = 0.61$, and $\sigma_Z = 10^{1.82}/317.828$ where $1M_J = 317.828 M_\oplus$ and M_p is in Jovian mass M_J . Here, $y | \mu, \sigma \sim \mathcal{N}(\mu, \sigma)$ implies that y is drawn from a normal distribution \mathcal{N} with mean μ and standard deviation σ . \mathcal{U} denotes that ϵ is sampled from a uniform distribution. We perform the inference twice each time using a different prior for the internal luminosity

$$L_{\text{int},n} | a, b \sim \mathcal{LU}(a, b) \quad (20a)$$

$$L_{\text{int},n} | a, b \sim \mathcal{U}(10^a, 10^b) \quad (20b)$$

where we set $\tau_0 = (a, b) = (0, 5)$. \mathcal{LU} and \mathcal{U} implies that L_{int} is drawn from a log-uniform and uniform distribution, respectively, and L_{int} is in Jovian luminosity L_J . Note that in our analysis, we do not sample ϵ , we sample L_{int} and at each step in the Markov Chain Monte Carlo (MCMC) compute ϵ using

$$\epsilon = \frac{4L_{\text{int},n} a_n^2}{L_{*,n} R_{p,n}^2}, \quad (21)$$

which was obtained by combining Equations (8) and (9) and the relation between the stellar luminosity and flux. We further set a uniform prior on ϵ over the range 0 – 5% (Equation (19)).

In Equation (20a), $L_{\text{int},n}$ is sampled from a log-uniform distribution \mathcal{LU} . We choose this prior because the internal luminosity covers a wide range of values and little is known about the true underlying distribution. This prior however does not lead to a uniform distribution in ϵ (see Section 4.1.1 and the right panel of Figure 3 for details), we therefore also consider a prior distribution uniform in linear space (Equations (20b)). The distribution of ϵ is uniform under this prior. In Section 4.1.1 we show in detail how the choice of prior on the internal luminosity affects the prior on ϵ and we discuss its effect on the inference. Finally, we can use the structure models to compute the internal temperature T_{int} . As discussed in Section 3.1.1, the atmospheric models were computed for T_{int} between 100 and 1000 K. We therefore set an upper limit of $T_{\text{int}} < 1000$ K in order to avoid extrapolation.

The statistical model described in Equations (15)–(20b) and setting $T_{\text{int}} < 1000$ K contain all the relevant distributions to evaluate Equation (14). All the results shown in Section 5, were produced by running MCMC using emcee (Foreman-Mackey et al. 2013). For each planet, we ran MCMC with 50 walkers each with 1000 steps and discard the first half as burn-in. At each iteration we compute the heating efficiency ϵ using Equation (21). Using 25,000 samples we then marginalize over

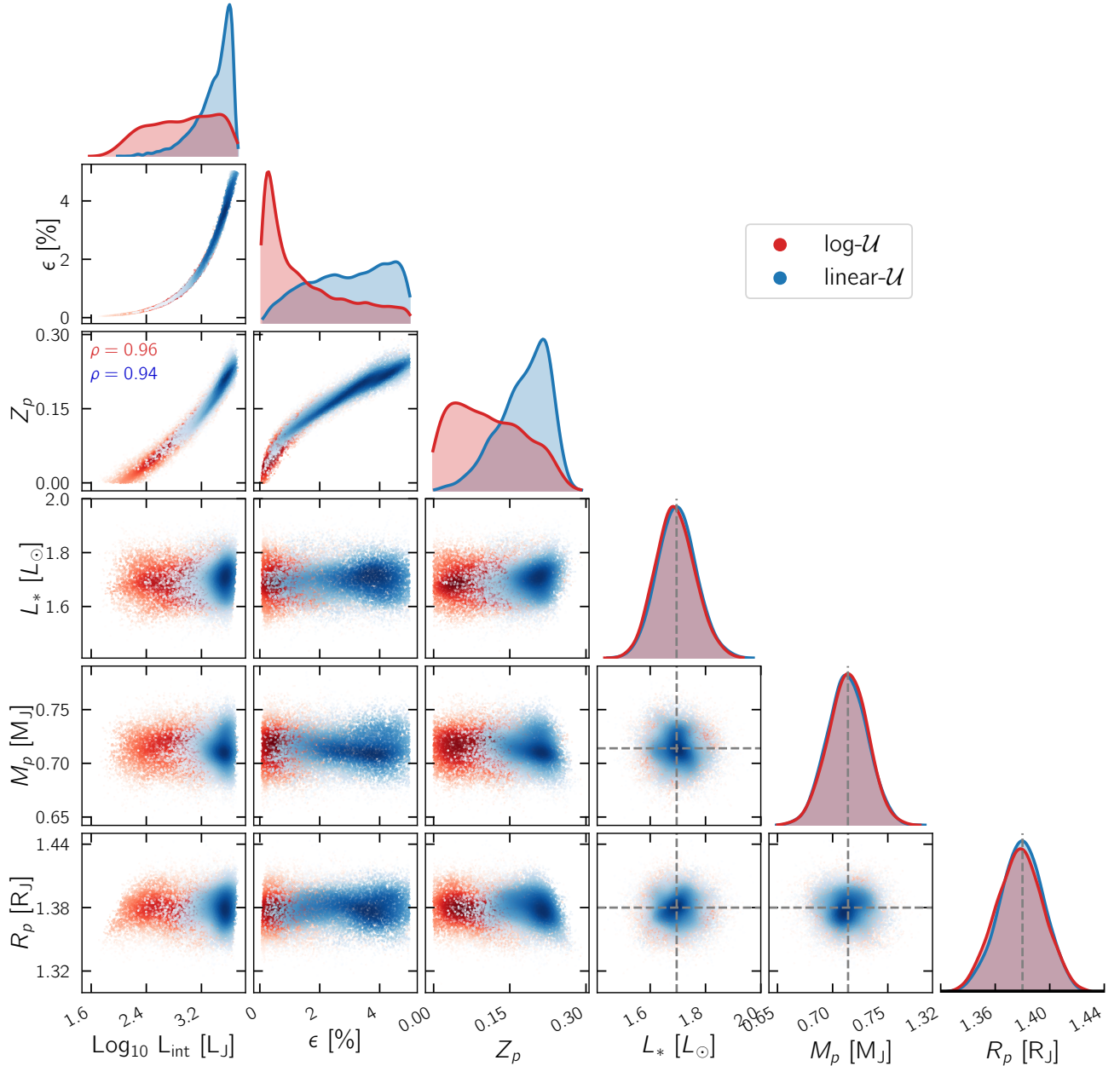


Fig. 2. The posterior distributions inferred for HD209458 b using our model (Equation (14)). The gray dashed lines show the observed value for the relevant parameters. The effect of using different prior distribution leads to different posterior distributions for L_{int} , ϵ , and Z_p . The inferred posterior distributions for the other parameters (L_* , M_p , and R_p) are almost identical for both priors since they are constrained well from observations.

the nuisance parameters and infer the posterior distribution of $L_{\text{int},n}$ and of ϵ . The average acceptance ratio was around ~ 0.5 for almost all the planets in the sample.

As a by-product of this analysis, we also keep track of the PT profiles and thus infer the distribution of the pressure at the RCB and the planet internal temperature T_{int} . This is useful to gain insights on the interior structure of hot Jupiters and we present the analysis in Section 5.4.

4.1.1. Choice of Prior on the Internal Luminosity

In the lower level of the hierarchical model (Section 4.1), we use non-informative uniform distributions in log and linear space as prior for the internal luminosity. It is worth studying the effect of the prior distribution on the final results. Figure 2 shows the marginalized distributions for HD209458 b using the two different priors. The luminosity distribution is shown in log-scale for both distributions for illustrative purposes. Red shows the samples using a log-uniform distribution while blue using a uniform distribution in linear space. Note the strong correlation between

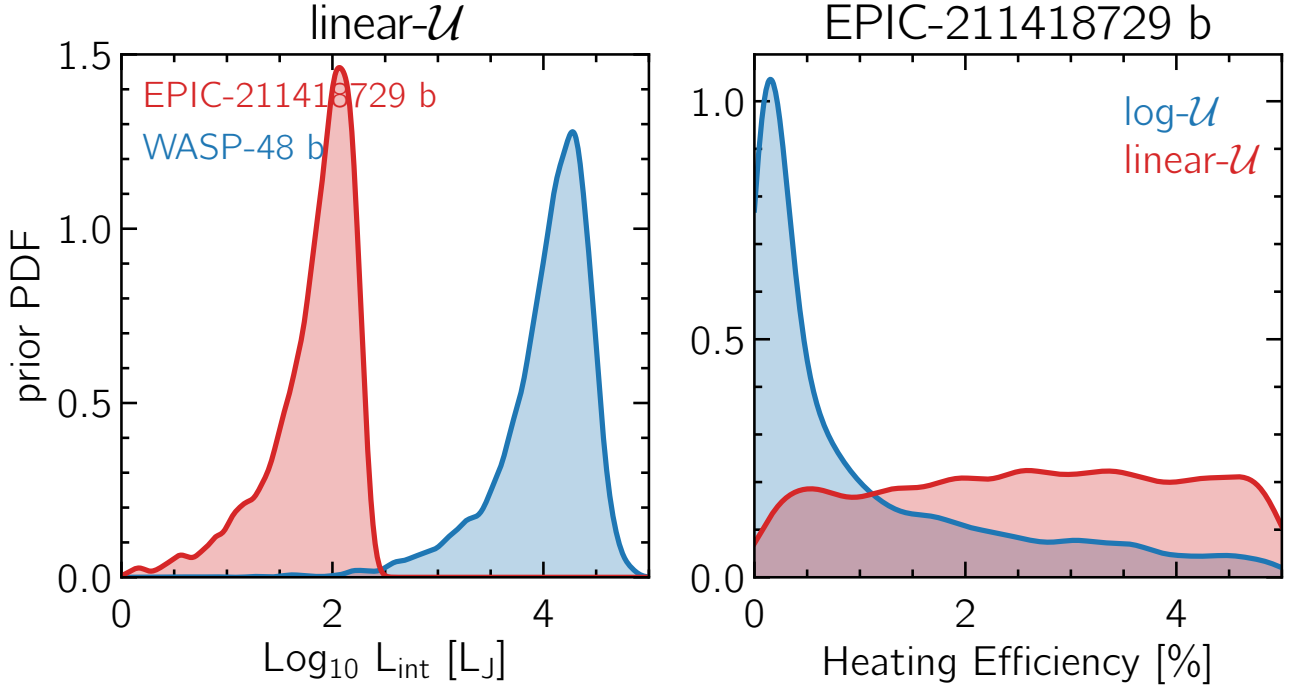


Fig. 3. (Left): PDF of the prior on the internal luminosity distributions for WASP-48 b and EPIC-211418728 b under the linear- \mathcal{U} prior. The systems were chosen arbitrarily for illustrative purposes. Even if we initially set a uniform prior between 10^a and $10^b L_J$, with $a = 0$ and $b = 5$, the *actual* prior distributions for each planet are not similar and have different a and b values. Notice the log scale for better visualization. (Right): The heating efficiency prior distribution for EPIC-211418728 b. Assuming log-uniform prior distribution on L_{int} leads to biases towards smaller values on ϵ .

the fraction of heavy elements Z_p and the internal luminosity with a Pearson correlation coefficient $\rho > 0.9$. The observed parameters (R_p , M_p , and L_*) are reproduced in both cases and the distributions look almost identical. But the distributions of L_{int} , the main parameter of interest, are different leading thus to different distributions in heating efficiency ϵ . We are in a regime where the data size is small and the choice of the prior distribution is important and dominates the inference. Note that Figure 2 shows the radius distribution even though we do not sample this parameter. This is useful to validate the model and to check that it predicts the observed data. Such plots are referred to as posterior predictive plots and we will apply them in Section 5.1 to validate the model for each planet.

Ideally, we would want to learn about the internal luminosity of the planet by relying entirely on the observed parameters while the choice of the prior should have minor effects on the posterior inference. Even though both distributions are non-informative, the data is not enough that the prior dominates. To put it in another way, more data is needed to be able to infer the distribution of L_{int} independently of the choice of prior. Unfortunately, the physical parameters that can be observed for exoplanets in general and transiting planets specifically are very limited. One promising avenue might be inferring precisely the internal temperature, which was for the first time recently estimated for WASP-121 b (Sing et al. 2019) with $T_{\text{int}} = 500$ K. In our results for WASP-121 b, the T_{int} distributions look similar using both priors and therefore it is not possible to put tighter constraints on L_{int} . Another promising approach is to put tighter constraints on the planet mass–heavy-element mass relation, which translates to tighter constraints on L_{int} due to the

large degeneracy between L_{int} and Z_p . This can be achieved by increasing the number of confirmed transiting warm Jupiters, i.e. giant planets with $T_{\text{eq}} < 1000$ K. Such relatively cool planets are not inflated (Demory & Seager 2011). This allows to infer the fraction of heavy elements for such planets and re-calibrate the relation between the planet mass and fraction of heavy elements, similar to what was done by Thorngrén et al. (2016) but with a larger sample.

It is important to explicitly mention that given the setup of the statistical model, the *prior* distributions for the individual planets are not the same because of the imposed upper limit of $\epsilon = 5\%$, which further depends on the observed parameters (Equation (21)). This can be understood by looking at the bottom line in Equation (14)³, where it is clear that each planet has different L_* , M_p , a , and Z_p distributions due to differences in the observed physical properties. We confirm this by sampling the prior probability density function (PDF), i.e. by running the model on an empty data set \mathbf{D}_n for two different planets EPIC-211418729 b and WASP-48 b. By not sampling \mathbf{D}_n in Equation (14), we effectively sample the prior PDF. The left panel of Figure 3 illustrates this concept where we show that the internal luminosity prior distributions are different under the linear-uniform prior for both planets. Note though the log scale for better visualization. For EPIC-211418729 b, L_{int} larger than $10^{2.5} L_J$ are not sampled and thus are ruled out. This cutoff in the distribution at high L_{int} values is a consequence of the upper limit imposed on ϵ and the low stellar luminosity which translates to low T_{eq} . With an equilibrium temperature roughly of

³ The top line in Equation (14) is the likelihood PDF and the bottom line is the prior PDF.

$T_{\text{eq}} = 700$ K, a heating efficiency of 5% for EPIC-211418729 b is equivalent to a maximum $L_{\text{int}} = 10^{2.5} L_J$. On the other hand, WASP-48 b with $T_{\text{eq}} = 2000$ K (i.e. high L_*), an upper limit of 5% on the heating efficiency is equivalent to a maximum of $L_{\text{int}} \sim 10^5 L_J$. Note that for WASP-48 b low L_{int} values are not ruled out but are less probable. To summarize, even if the initial prior imposed on L_{int} is $\mathcal{U}(10^a, 10^b)$ with $a = 0$ and $b = 5$, the actual prior distributions for the individual planets are different with different a and b values. This is a consequence of the additional prior on ϵ ($\epsilon < 5\%$). Planets with low T_{eq} , their distributions are truncated at high L_{int} values (with $b < 5$). While this is not the case for planets with high T_{eq} (with $b = 5$). The importance of a and b is relevant for the discussion in Section 4.2.

It is also worth studying the consequence of using different L_{int} priors (\mathcal{U} and \mathcal{LU}) on the heating efficiency ϵ prior PDF since the relationship between the two parameters is deterministic following Equation (21). We follow the same procedure described in the previous paragraph, i.e. we run the model on an empty data set for EPIC-211418729 b. The right panel of Figure 3 shows samples from the prior distribution on ϵ for EPIC-211418729 b using the linear-uniform and log-uniform cases. It is evident that a log-uniform prior distribution on L_{int} does not lead to a uniform prior on ϵ and the inference is biased towards small ϵ values. Whereas this is not the case when assuming a linear-uniform prior on L_{int} . We want to stress that this holds for almost all of the planets in our sample and not only for EPIC-211418729 b, which was chosen arbitrarily.

From a statistical point of view, a log-uniform prior distribution is favored because of the large range of values and it is therefore easier to explore the entire parameter space in log space. However, this prior leads to biases in the ϵ distribution. To mitigate this, in the following section (Section 4.2) we develop a flexible hierarchical Bayesian model that accounts for the choice of prior. We study the population distributions under both priors in Section 5 and show that the inference at the population level is *independent* on the choice of prior.

4.2. Upper Level of the Hierarchical Model: Population Level Posterior Samplings

In Section 4.1, we inferred the distributions of L_{int} , ϵ , T_{int} , and pressure at the RCB (P_{RCB}) for each planet individually. In this Section, we derive the equations needed to study the general distribution of the (i) internal luminosity as a function of planet radius, (ii) heating efficiency, (iii) internal temperature, and (iv) pressure at the RCB as a function of T_{eq} . Thus, (i), (iii), and (iv) provide insights into the interior structure of hot Jupiters, while (ii) gives insights into the efficiency of transporting energy into the interior, similar to what TF18 derived. In what follows, we derive the key equation which the inference is based on (Equation (32)) but first provide the motivation and simple description of the method.

We aim to use the single distributions we inferred in the lower level of the hierarchical model to infer the set of population parameters τ , which we will refer to as hyperparameters. We derive the general form of the full posterior distribution below but for now we refer to Equation (26) to motivate our work. In this equation N is the total number of planets, $p(\tau)$ is the prior probability distribution on the hyperparameters, $p(\omega_n)$ and $p(\mathbf{D}_n | \omega_n)$ are the prior and likelihood distributions for the individual planets, respectively. It is evident that the population posterior distribution is a strong function of the prior imposed at the lower level of the hierarchical model to the power of N ,

the number of planets. Therefore, it is crucial to make sure that the distribution we infer for the population has physical origins rather than is an output of the choice of prior. Hence, in order to account for the prior distribution imposed at the lower level of the hierarchical model, we apply the ‘‘importance sampling trick’’. We follow closely the pioneering work established by Hogg et al. (2010) (see also the Appendix of Price-Whelan et al. 2018). This method has been used by Foreman-Mackey et al. (2014) to infer the occurrence rate of planets as a function of period and radius and by Rogers (2015) to infer the radius at which the composition transition from rocky super-Earth to volatile-rich sub-Neptunes. Briefly, we re-weight the individual posterior samples by the ratio of the value of the hyperparameters τ evaluated given the new hyperprior distribution to the old prior on which the individual sampling is based on evaluated at the old default τ_0 values. We describe below how to compute the marginal likelihood distribution.

The likelihood for all N planets given τ is

$$p(\{\mathbf{D}_n\} | \tau) = \prod_n^N p(\mathbf{D}_n | \tau) \quad (22)$$

$$= \prod_n^N p(\mathbf{D}_n | \omega_n) p(\omega_n | \tau) \quad (23)$$

$$= p(\omega_n)^N \prod_n^N p(\mathbf{D}_n | \omega_n) \quad (24)$$

where we assume that the likelihood for individual planets are independent. Notice that Equation (23) is product of the likelihoods for a single planet (see also Equation (14)) and is independent of the hyperparameters τ . The full posterior distribution is then

$$p(\tau | \{\mathbf{D}_n\}) \propto p(\tau) p(\{\mathbf{D}_n\} | \tau) \quad (25)$$

$$\propto p(\tau) p(\omega_n)^N \prod_n^N p(\mathbf{D}_n | \omega_n) \quad (26)$$

It is evident in Equation (26) that the posterior distribution for the full population scales with $p(\omega_n)^N$, the default prior on which the individual sampling is based on. In this approach for simplicity we assume that $p(\omega_n)$ is the same for all planets, however, as we showed in Section 4.1.1 this is not the case. Our main intention here is to show that the choice of prior at the lower level of hierarchical model is important as it scales to the power of the number of planets N . Hence, we derive below the marginal likelihood distribution by applying the ‘‘importance sampling trick’’.

For each n of N planets, we obtain K posterior samples of the parameters that determine the planetary radius $\theta_n = (M_{\text{p},n}, Z_{\text{p},n}, L_{*,n}, a_n)$ and $L_{\text{int},n}$. Following similar notation to Section 4.1 and for brevity, we define the full set of parameters as

$$\omega_n = (\theta_n, L_{\text{int},n}) = (\theta_n, y_n). \quad (27)$$

We use the individual posterior samplings to compute the likelihood of the hierarchical model. For a single planet, the likelihood given the hyperparameters τ is

$$p(\mathbf{D}_n | \tau) = \int p(\mathbf{D}_n | \omega_n) p(\omega_n | \tau) d\omega_n \quad (28)$$

$$= \int p(\mathbf{D}_n | \omega_n) p(\omega_n | \tau) \frac{p(\omega_n | \mathbf{D}_n, \tau_0)}{p(\omega_n | \mathbf{D}_n, \tau_0)} d\omega_n \quad (29)$$

$$\propto \int \frac{p(\omega_n | \tau)}{p(\omega_n | \tau_0)} p(\omega_n | \mathbf{D}_n, \tau_0) d\omega_n. \quad (30)$$

where in the last equation we applied Bayes' theorem on the posterior distribution $p(\omega_n | \mathbf{D}_n, \tau_0)$, which is the posterior distribution for a single planet computed using Equation (14). The set of parameters from which the previous inference was generated is denoted by τ_0 . For example, as described in the previous section, the parameters describing the distribution of L_{int} are $\tau_0 = (a, b) = (0, 5)$. We can then apply the Monte Carlo integral approximation to estimate the marginalized likelihood distribution over θ

$$p(\mathbf{D}_n | \tau) \approx \frac{1}{K} \sum_k \frac{p(y_{nk} | \tau)}{p(y_{nk} | \tau_0)}. \quad (31)$$

Essentially, we are assuming that all the probability integrals can be approximated as sums over samples. In case of infinite samples, this approximation becomes exact. Having derived the marginalized likelihood distribution for a single planet (Equation 31), the full marginal likelihood is then the product of the individual likelihoods

$$p(\{\mathbf{D}_n\} | \tau) \approx \prod_n \frac{1}{K} \sum_k \frac{p(y_{nk} | \tau)}{p(y_{nk} | \tau_0)}. \quad (32)$$

We can then choose a prior probability distributions for the hyperparameter τ and the posterior probability distribution is

$$p(\tau | \{\mathbf{D}_n\}) \propto p(\tau) \prod_n p(\mathbf{D}_n | \tau) \quad (33)$$

$$\approx p(\tau) \prod_n \frac{1}{K} \sum_k \frac{p(y_{nk} | \tau)}{p(y_{nk} | \tau_0)}. \quad (34)$$

Inside the sum, the numerator is the new probability distribution that we want to infer given a new set of hyperparameters τ , while the denominator is the value of the default prior on which the single posterior samples is based at the previously assumed values of τ_0 . We then re-weight the y_{nk} posterior samples by the ratio. This approach of using the posterior samples from the lower level of the hierarchical model like data in the upper level has been first addressed by [Hogg et al. \(2010\)](#) (see also [Foreman-Mackey et al. 2014](#), and [TF18](#)). Ideally, the inference of τ and ω_n for all the planets should be done simultaneously, however this is computationally very expensive as it involves solving $4N + m$ integrals, where N is the number of planets and m is the number of hyperparameters in our model.

Equation (32) is the main equation we use to infer the general distributions of (i), (ii), (iii), and (iv) defined at the beginning of this Section. We use Kernel Density Estimation (KDE) to estimate the probability density function (PDF) of each of the previously inferred distributions to compute $p(y_{nk} | \tau)$, where we discuss below the functional forms. Note that even though we define a flat distribution for the internal luminosity,

Equations (20a) and (20b), and set $\tau_0 = (a, b) = (0, 5)$, this is not strictly the case because additionally we truncate the heating efficiency $0 < \epsilon < 5\%$ and require $100 < T_{\text{int}} < 1000$ K. Also, as noted in Section 4.1.1, each planet has a different prior probability distribution, leading thus to different values of τ_0 for each planet (for an example see left panel of Figure 3). Therefore to evaluate $p(y_{nk} | \tau_0)$, we sample Equation (14) for each planet on an empty data set similar to what was done in Section 4.1.1 and then estimate the PDF using KDE.

For each of the four distributions, we define the general form $y_{nk} = g(x_{nk})$, specifically $y_{nk} =$

$$L_{\text{int},nk} = g(R_{p,nk}) \quad (35)$$

$$\epsilon_{nk} = g(T_{\text{eq},nk}) \quad (36)$$

$$T_{\text{int},nk} = g(T_{\text{eq},nk}) \quad (37)$$

$$P_{\text{RCB},nk} = g(T_{\text{eq},nk}) \quad (38)$$

where $R_{p,nk}$ and $T_{\text{eq},nk}$ are the samples of the individual posterior distributions for the planetary radius and equilibrium temperature, respectively. The latter was computed at each iteration in the MCMC at the lower level of the hierarchical model and the values were stored.

We summarize below the computational procedure. First, at each iteration in the MCMC we sample the hyperparameters τ and evaluate the function $y_{nk} = g(x_{nk})$ using the sampled values of τ . Second, we compute $p(y_{nk} | \tau)$ and $p(y_{nk} | \tau_0)$ using the pre-computed KDE functions. Finally, we evaluate the log-likelihood of Equation (32)

$$\ln p(\{\mathbf{D}_n\} | \tau) \approx \sum_n \left[\ln \left(\sum_k \frac{p(y_{nk} | \tau)}{p(y_{nk} | \tau_0)} \right) - \ln N \right] \quad (39)$$

$$\approx \sum_n \left[\ln \left(\sum_k \exp(\ln p(y_{nk} | \tau) - \ln p(y_{nk} | \tau_0)) \right) - \ln N \right] \quad (40)$$

where in the last equation we compute the log of the sum of exponentials (log-sum-exp trick). In practice, this is numerically more stable compared to evaluating Equation (39).

For all the results presented below, we use `emcee` to sample from the posterior probability distribution (Equation (34)) where we specify the functional forms of $g(x_{nk})$ in Section 5. In what follows, we draw $K = 2000$ random samples from the single posterior samples when evaluating the mass–luminosity–radius relation. For the other relations we set $K = 1$ and use the observed T_{eq} values. This is possible since the equilibrium temperature is often well constrained from observations. We verified that accounting for the uncertainties does not effect the results. We adopt 44 walkers and run the sampler for 4000 iterations where the first half are discarded as burn-in and retain only every 20th sample in the chain to produce independent samples. We monitored convergence by computing the acceptance ratio and by visually inspecting the trace plots and corner plots. Note that for each relation, we execute this procedure twice, each time using the samples drawn under the different prior, log-uniform \mathcal{LU} and uniform \mathcal{U} . By running this process twice, in Section 5 we show that the results are not biased by the choice of prior, unlike the lower level of the hierarchical model. This further confirms that the distributions are physical and robust.

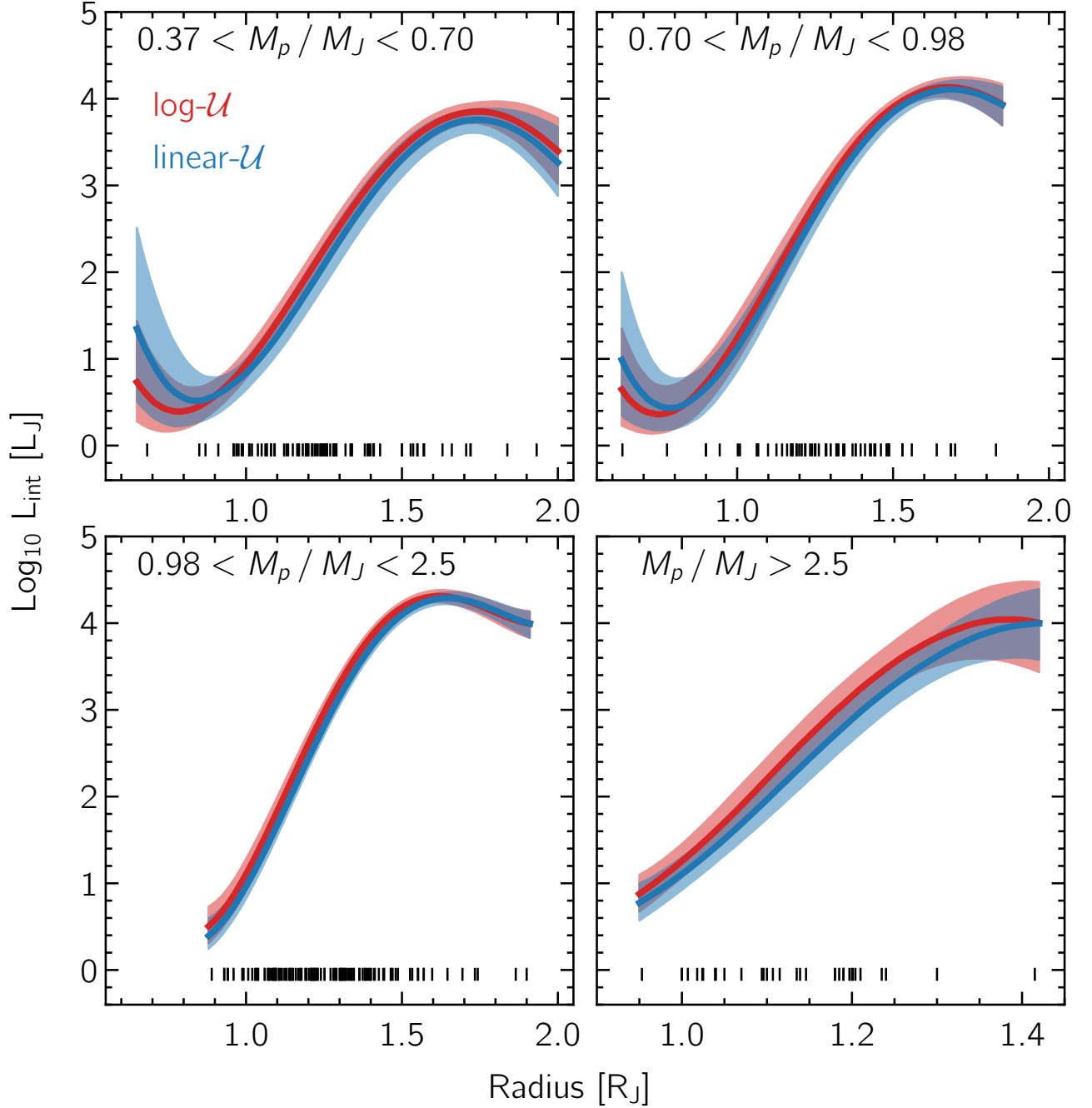


Fig. 4. MLR posterior distribution for four different mass bins showing the median (thick line) and 1σ credible interval (shaded area) assuming a uniform prior in log (blue) and linear (red) space. Using either prior leads to almost identical results. The internal luminosity is high with the largest planets having a luminosity \sim four orders of magnitude larger than Jupiter.

5. Results

We first apply the model described in Section 4.1, i.e. the lower level of the hierarchical model, to infer the distribution of L_{int} , ϵ , T_{int} , and P_{RCB} for each planet. In Section 5.1, we present diagnostic tools to validate the lower level of the hierarchical model. We then use the inferred posterior distributions to study the mass–luminosity–radius (MLR), heating efficiency – equilibrium temperature (HEET), $T_{\text{int}} - T_{\text{eq}}$, and $P_{\text{RCB}} - T_{\text{eq}}$ distri-

butions for the population of hot Jupiters following the model introduced in Section 4.2. In Section 5.2, we show that by properly correcting for the choice of prior, the MLR distribution at the population level is prior independent. We hence present the rest of the results under the uniform in linear space prior in Sections 5.3 – 5.4. For completeness, we show the results using both priors in Appendix A.

5.1. Posterior Predictive Checks

For each system, we infer the distribution of the internal luminosity that reproduces the observed radius, mass, and stellar luminosity while fixing the semi-major axis to the observed value. We visually inspect each system to double check that the marginalized posterior distributions of the observed parameters, M_p , R_p , L_* , and thus T_{eq} , are reproduced. Such plots are important to check that the model is a good fit and is thus capable of generating data that resemble the observed data. There are in total 17 systems where the observed mass and/or radius was not reproduced and thus we exclude these systems from the data set and do not include them in the analysis presented below. For most of the planets the radii are not possible from theoretical models as they are at the edge of the computed grid for a given planet mass, stellar luminosity, and semi-major axis. The observed radii tend to be larger than what is possible from the theoretical grid and most of these planets have masses $M_p > 2.5 M_J$. Note that for three systems the stellar luminosity and therefore the equilibrium temperature was not reproduced (HAT-P-20, Qatar-2, and WASP-43). We decide however to keep these systems since the difference in the equilibrium temperature is on the order of ~ 30 K and hence the change in the internal luminosity is almost insignificant.

5.2. Mass–Luminosity–Radius (MLR) distribution

We divide the samples into four mass ranges, similar to the mass bins estimated by Sestovic et al. (2018) but further divide their second mass bin into two: the sub-Jupiter planets ($0.37 - 0.7 M_J$ and $0.7 - 0.98 M_J$) and the massive-Jupiter planets ($0.98 - 2.5 M_J$ and $> 2.5 M_J$). The number of planets in each group is 86, 59, 119, and 33 planets, respectively. To infer the MLR distribution, we run the model (Equation (32) or equivalently Equation(40)) for each mass bin by specifying the functional form of $g_p(x)$ as a 4th degree polynomial,

$$g_p(x) = a_0 + a_1x + a_2x^2 + a_3x^3 + a_4x^4 \quad (41)$$

where x is the planet radius R_p and $\tau = \{a_0, a_1, a_2, a_3, a_4\}$. There are many benefits of using polynomial regression compared to other parametric and non-parametric approaches. One important factor is that these models are flexible and can take a variety of shapes and curvatures to fit the data, making the results thus less model dependent compared to parametric models. Another important factor is that polynomial regression is similar to fitting a linear model and thus is computationally inexpensive and very fast to compute, unlike non-parametric models such as Gaussian process. A disadvantage to this approach is the curse of dimensionality, where the number of model parameters grows much faster than linearly with the growth of degree of the polynomial. In our case, we use univariate polynomial regression with degree 4 and thus the total number of model parameters is 5.

At each iteration in the MCMC, we compute ϵ following Equation (21), where the semi-major axis is fixed to the observed value and L_* and R_p are drawn from the individual posterior distributions. We further impose an additional log-normal prior on $\epsilon \sim \mathcal{LN}(-1, 1)$ for the planets with an equilibrium temperature less than 1000 K. This reflects our beliefs that planets with low equilibrium temperatures are not inflated (Demory & Seager 2011), and thus ϵ should be small. We tested several prior probability distributions on ϵ and verify that our results are not affected by the choice prior. We repeat the full procedure twice

each time drawing samples from the lower level of the hierarchical model under the different priors (\mathcal{LU} and \mathcal{U}) and assign uniform uninformative priors on the hyperparameters. In Table A.1 and Table A.2 in Appendix A we give the 68% credible interval values assuming linear-uniform and log-uniform priors.

Figure 4 shows the posterior distribution inferred for all mass bins under the two priors, uniform in log (red) and linear (blue) space. Notice that the lower right panel has a different scale to better visualize the results. Each data point is represented by a small line at the bottom of the plot at the corresponding radius. Such plots are called rug plots and are used to visualize the distribution of the data. The immediate striking feature is that the distributions under both priors are almost identical and indistinguishable. There are few differences between both models, such as at small radii for the least massive planets and at large radii for the most massive ones. These differences are mainly dominated by the small number of planets in these regions. This highlights the importance of re-weighting the samples by dividing by the prior used to do the sampling at the lower level of the hierarchical model. This further confirms that the population level distributions are physical, robust, and are not affected by the choice of prior. For the rest of the paper, we show the results under the prior uniform in linear space, but confirm that the choice of prior at the lower level of the hierarchical model does not affect the main results and conclusions.

The basic shape of the MLR relation is similar across all mass bins, where as expected larger planets have higher internal luminosity with a plateau around $1.6 R_J$ beyond which the luminosity is almost constant. The small drop towards high radii has little statistical significance and likely reflects the choice of a fourth-order polynomial. The inferred internal luminosity for most of the planets is several orders of magnitude larger than Jupiter, reaching even up to four orders of magnitude. We also find that the internal luminosity is mass dependent, with the most massive planets having the highest internal luminosity.

A noticeable feature is that the sub-Jupiter planets with masses $0.37 - 0.98 M_J$ and radii less than $1 R_J$ have an internal luminosity larger than Jupiter. At first glance, one might expect such planets to have an internal luminosity smaller than Jupiter’s. We note however that the planets that have an equilibrium temperature less than 1000 K, indeed tend to have $L_{\text{int}} \sim 3 L_J$ and not more. A higher luminosity is expected because, even with $T_{\text{eq}} < 1000$ K, these planets are still much closer than Jupiter, which reduces the cooling rate and thus leads to higher internal luminosity. As for the planets that have equilibrium temperature larger than 1000 K, they tend to have higher fraction of heavy elements distributed in the envelope. There are only two sub-Jupiter planets in our sample that have radii less than $0.7 R_J$, K2-60 and WASP-86, both of which require large fraction of heavy elements, 0.64 and 0.8, respectively, ruling out values less than 0.5. The high fraction of heavy elements explains the high luminosity values and the small number of planets with radii less than $1 R_J$ is why the distribution is poorly constrained in this regime.

5.3. Heating Efficiency Equilibrium Temperature (HEET) distribution

Similar to the previous section, we also apply the model defined in Section 4.2 to study the HEET relation. We assume two different functional forms for $g(x)$, (i) g_p a 4th degree polynomial (Equation (41)) and (ii) g_g a Gaussian function defined as

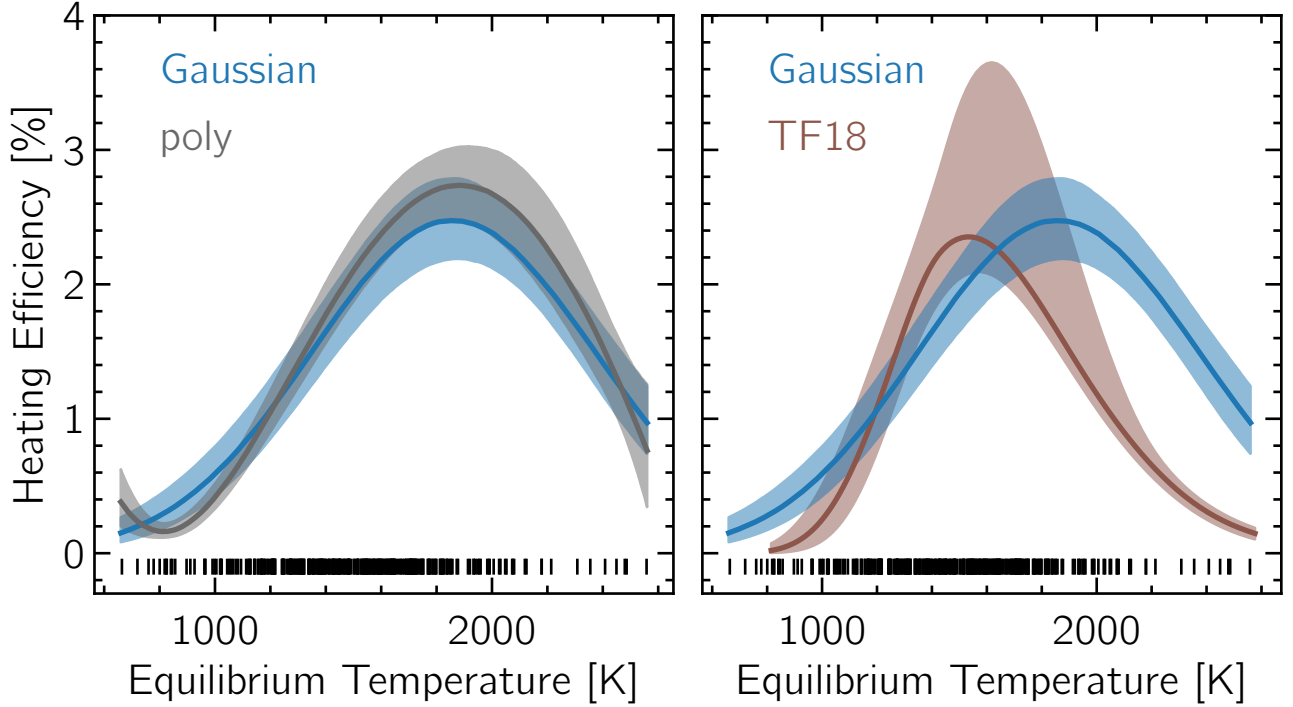


Fig. 5. (Left): HEET posterior distribution under the linear-uniform prior using a Gaussian function and a 4th degree polynomial. (Right): the Gaussian function shown on the left side in comparison to the HEET posterior distribution inferred by TF18. The shaded region show the 1 σ credible interval. There is a good agreement between the Gaussian and poly models, which shows that indeed the HEET distribution follows a Gaussian function. Our results are in agreement with the findings of TF18 although the peak in our models is shifted to higher equilibrium temperatures.

$$g_g(T_{\text{eq}}) = \epsilon_{\text{max}} \exp \left[-\frac{1}{2} \left(\frac{T_{\text{eq}} - T_{\text{eq0}}}{s} \right)^2 \right]. \quad (42)$$

The former is a flexible function that allows us to constrain the general shape of the relation by relying entirely on the data as motivated in the previous section, while the latter allows us to compare our results to TF18 and to theoretical predictions. Using the Gaussian function, the parameters are $\tau = \{\epsilon_{\text{max}}, T_{\text{eq0}}, s\}$ the amplitude, temperature at ϵ_{max} , and the width of the Gaussian function, respectively. Similar to the MLR relation, for the g_p model, we further impose a $\mathcal{LN}(-1, 1)$ prior on the heating efficiency for planets with equilibrium temperatures less than 1000 K. In Table A.3 in Appendix A we give the 68% credible interval values assuming \mathcal{LU} and \mathcal{U} priors using the polynomial model. The Gaussian models are shown in Table 1.

The left panel of Figure 5 shows that the posterior distributions are similar under both functional forms, with the polynomial function leading slightly to higher efficiencies. Using an independent interior structure model and a larger sample focused on FGK main-sequence stars, our results are qualitatively consistent with TF18. To compare our results to TF18, we report the median and the 68% credible interval in Table 1. We also show the posterior distributions in the right panel of Figure 5. The heating efficiency increases until a maximum is reached at T_{eq0} , beyond which the efficiency decreases. Our result regarding the maximum heating efficiency agrees well within 1 σ with TF18, where we determine $\epsilon_{\text{max}} \sim 2.50\%$, compared to $\sim 2.37\%$. In our model, the peak occurs at ~ 1860 K, while TF18 estimate

Table 1. Comparison of the Gaussian function using the log and linear uniform prior along with comparison to TF18 results.

τ	log- \mathcal{U}	linear- \mathcal{U}	TF18
$\epsilon_{\text{max}}[\%]$	$2.46^{+0.29}_{-0.24}$	$2.49^{+0.31}_{-0.28}$	$2.37^{+1.30}_{-0.26}$
$T_{\text{eq0}}[\text{K}]$	1982^{+83}_{-58}	1862^{+67}_{-61}	1566^{+55}_{-61}
$s[\text{K}]$	532^{+110}_{-73}	508^{+66}_{-48}	327^{+25}_{-43}

the transition at ~ 1566 K. Detailed differences in the interior structure model, in particular the EOS and opacity, may help explain this discrepancy. An important parameter in the EOS is the nature of the solids. TF18 use the SCvH for H/He (Saumon et al. 1995) and the ANEOS EOS (Thompson 1990) assuming a 50-50 ice-rock composition. In our model setup, we use the same EOSs, however we assume that the composition of the heavy elements is H_2O , where H/He and H_2O are mixed using the additive volume law (for more details on the treatment of the EOS see the Appendix B of Mordasini 2020). Differences in the EOS and the composition will lead to a different internal luminosity thus explaining this difference.

It is remarkable to see that the Gaussian pattern holds independent of the choice of prior (see Figure A.1 in Appendix A). This pattern was predicted by ohmic dissipation first based on simulations (e.g. Menou 2012) and then later supported by TF18.

Our analysis provides further evidence of the Gaussian-like distribution.

5.4. Distributions of Internal Temperature and Pressure at the RCB

Having inferred the population level distributions of the internal luminosity distribution and the heating efficiency, it is interesting to study the effect of energy dissipation on the interior structure of the planet. In particular, we show that as a consequence of transporting energy into the interior, hot Jupiters have very hot interiors which in turn pushes the RCB to low pressures. Our findings are in agreement with [Thorngren et al. \(2019\)](#) (hereafter **T19**), where they used the HEET relation presented in **TF18** to compute T_{int} and then generate PT atmospheric models for a range of T_{eq} and surface gravities to locate the P_{RCB} .

As mentioned in Section 4.1, we keep track of the PT profiles, and thus we can infer the distribution of the internal temperature and the pressure of the RCB for each planet. We again apply the model defined in Section 4.2 to study the distributions of T_{int} and P_{RCB} as a function of T_{eq} . We model the distributions, $T_{\text{int}} - T_{\text{eq}}$ and $P_{\text{RCB}} - T_{\text{eq}}$, as a Gaussian function and 4th degree polynomial, respectively. At steady state,

$$T_{\text{int}} = \epsilon^{1/4} T_{\text{eq}} \quad (43)$$

$$= g_g (T_{\text{eq}})^{1/4} T_{\text{eq}} \quad (44)$$

where the last equation was obtained by replacing $L_{\text{int}} = 4\pi R_p^2 \sigma T_{\text{int}}^4$ in Equation (8) and combining Equations (1) and (9). We use the samples from our previous analysis using the Gaussian model (see Section 5.3) to compute T_{int} using Equation (44) and compare the results to the hierarchical Bayesian approach. We refer to the former method as the analytical approach. For all the models, we assign uniform distributions on all the hyperparameters.

Figure 6 shows the inferred posterior distribution for the internal temperature (upper panel) and pressure at the RCB (lower panel) as a function of the equilibrium temperature. The analytical approach leads similar results to the Bayesian approach at the lowest and highest equilibrium temperatures. However, T_{int} is overestimated at the 2σ level for T_{eq} between 1000 and 1800 K. This difference could be because we did not account for intrinsic scatter in the model, which we leave for future work.

For both models, almost all hot Jupiters have T_{int} larger than 200 K, while, for comparison, the internal temperature of Jupiter is 100 K ([Li et al. 2012](#); [Guillot & Gautier 2014](#)). This is expected given the observed inflated radii. WASP-121 b is the only exoplanet to date whose internal temperature was constrained from observations of Mg and Fe in the transmission spectrum, with a reported value of 500 K ([Sing et al. 2019](#)). With an equilibrium temperature of $T_{\text{eq}} = 2358 \pm 52$ K ([Delrez et al. 2016](#)), we infer $T_{\text{int}} \sim 800$ K and by inspecting the individual posterior distribution of WASP-121 b, we rule out values below 500 K. This is the first hint from observations that hot Jupiters possess hot interiors, which is associated with a high internal entropy.

Another notable parameter to study is the pressure of the RCB as this partly controls the planetary cooling rate ([Arras & Bildsten 2006](#); [Spiegel & Burrows 2013](#)). It is known that high equilibrium temperature pushes the RCB deeper into the planet (e.g. [Fortney et al. 2007](#)), however high internal temperature pushes the RCB to lower pressures. Therefore, the location of the RCB is not known beforehand for planets with high equilibrium and internal temperatures. The lower panel of Figure 6

shows that the RCB is situated at low pressures or at shallow depths for high T_{eq} . The effect of the high internal temperature is thus dominant. The planets receiving high stellar irradiation tend to have hot interiors, typically around ~ 800 K, which pushes the RCB to low pressures, reaching ~ 3 bar for the most extreme cases.

Our results agree well with **T19**. While we report a maximum T_{int} of 800 K at $T_{\text{eq}} \sim 2500$ K, **T19** finds the maximum T_{int} of 700 K at $T_{\text{eq}} \sim 1800$ K. The difference is mainly due to the differences in the $\epsilon(T_{\text{eq}})$ distribution (see Section 5.3). We estimate the RCB to be at 100 bar and 4 bar for $T_{\text{eq}} = 1000$ K and 2000 K, respectively, in agreement with the findings of **T19**. Qualitatively, both models show the same pattern where the hot interior of hot Jupiters drive the RCB to lower pressures.

We provide the 68% credible interval values for the Gaussian model under both priors for the $T_{\text{int}} - T_{\text{eq}}$ distribution in Table A.4. The values for the $P_{\text{RCB}} - T_{\text{eq}}$ distribution are shown in Table A.5, also under both priors.

6. Discussion

Building on the assumption that hot Jupiters are inflated because of a process leading to high internal luminosity, we infer for each planet the internal luminosity distribution that reproduces the radius given the planet mass and equilibrium temperature from observations and using the mass–heavy-element relation ([Thorngren et al. 2016](#)) as a prior for the fraction of heavy elements. We then combine the individual distributions to constrain the population mass–luminosity–radius (MLR) distribution. Assuming that the source of extra heat in the interior is the irradiation by the host star (e.g. tides or magnetic fields), we then compute the fraction of the incident flux ϵ deposited in the interior and study the heating–efficiency–equilibrium–temperature (HEET) distribution for the full population. Finally, as a by-product of our structure model, we can also gain insights into the interior structure of the planets by inferring the distributions of the internal temperature and the pressure at the RCB.

In what follows, in Section 6.1 we discuss the consequences of the hot interior hot Jupiters possess on the internal structure. Then we discuss our results within the context of the competing heating mechanisms, mainly ohmic dissipation in Section 6.2 and advection of potential temperature in Section 6.3. In Section 6.4, we give a general comparison with analytical relations and discuss the limitations and caveats of our results in Section 6.5.

6.1. Insights into the Interior Structure of Hot Jupiters

We have shown that hot Jupiters have hot interiors, with an internal temperature as high as 800 K. This has important consequences on the location of the RCB, which in turn is important for the heating mechanism. [Komacek & Youdin \(2017\)](#) showed that heat dissipated in the convective layers suppresses cooling and thus enables the planet to maintain a large radius. Heat deposited in the radiative layer, however, does not significantly inhibit cooling. Most it is re-radiated away leading therefore to small radii. The location of the RCB is hence important to constrain the minimum depth at which the heat should be deposited and thus the efficiency of the heating mechanism. We find that the RCB is around 100 bar for planets with equilibrium temperatures of about 1000 K, and can reach 3 bar for the highly irradiated planets, which is significantly lower than previous estimates of 1000 bar without accounting for a bloating mechanism ([Fortney et al. 2007](#)). Our results are in agreement with

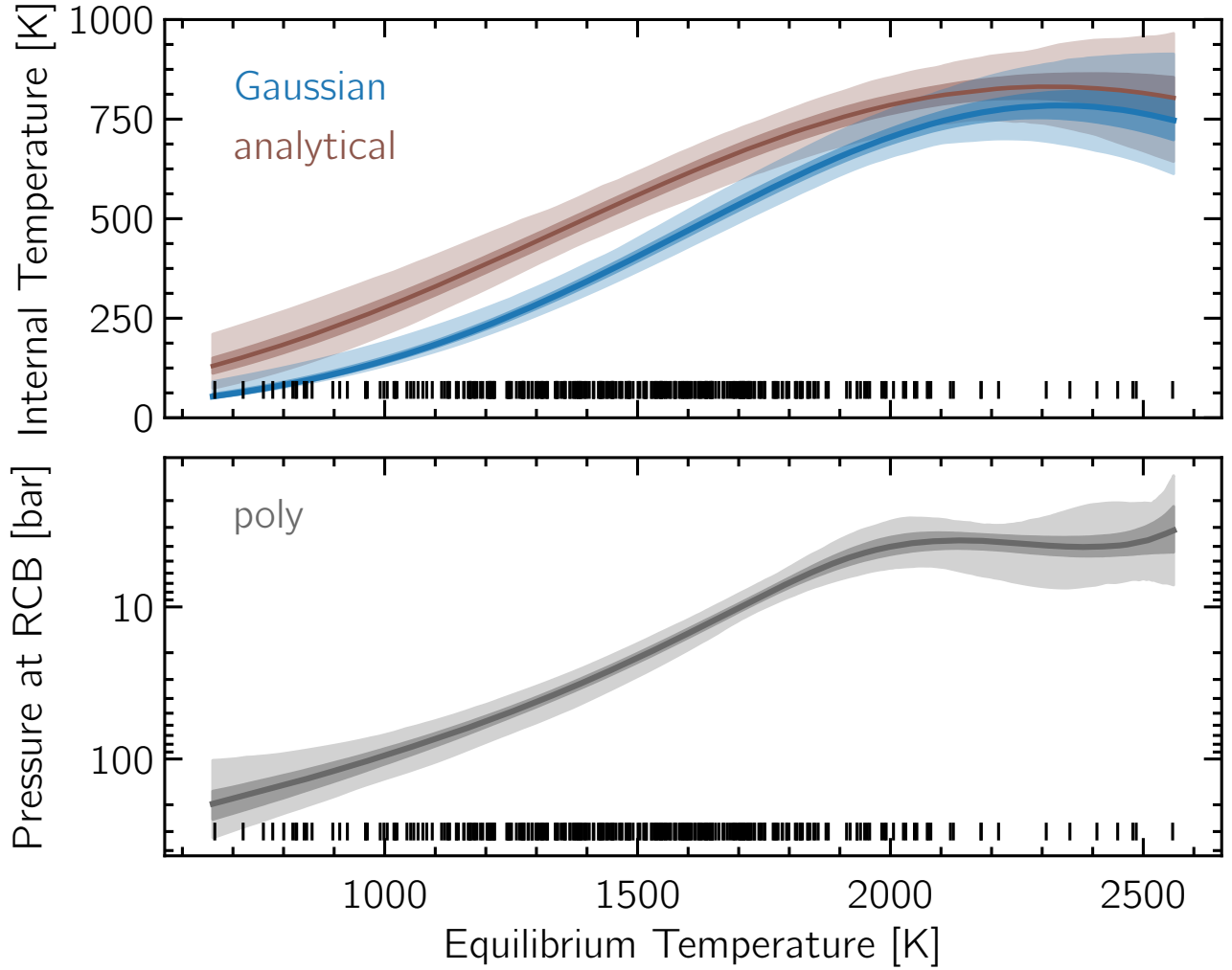


Fig. 6. $T_{\text{int}}-T_{\text{eq}}$ and $P_{\text{RCB}}-T_{\text{eq}}$ diagrams in the upper and lower panel, respectively. The dark and light shaded regions present the 1σ and 2σ credible intervals. Although the analytical approach overestimates the internal temperature at T_{eq} between 1000 – 1800 K, there is a good agreement at $T_{\text{eq}} < 1000$ K and $T_{\text{eq}} > 1800$ K. Due to the increase in the internal temperature with equilibrium temperature, the P_{RCB} moves to lower pressures with increasing T_{eq} , reaching up to ~ 3 bar for the most irradiated planets.

T19 based on coupling the heating efficiency relation (TF18) to a planetary interior structure model.

Mechanisms based on transporting heat into the deep interior, such as atmospheric circulation (Showman & Guillot 2002), ohmic dissipation (Batygin & Stevenson 2010), or advection of potential temperature (Tremblin et al. 2017) rely on the existence of winds in the interior. While the extra heat must be deposited in the convective layer in order to inflate the planet (Komacek & Youdin 2017), the actual wind speeds are not constrained from Global Circulation Models (GCMs) due to inaccurate coupling between the atmosphere and deep interior, a process still poorly understood. Recently, Carone et al. (2019) showed that through a better treatment of the lower boundary condition, i.e. by accounting for a hot interior, shallow zonal winds are present at 100 bar. With new estimates and better understanding of the internal temperature and pressure at the RCB, the depth of the wind zone and wind speeds can be constrained from GCM models, which in turn will be key inputs to further study the efficiency of the proposed mechanisms.

6.2. Comparison to Ohmic Dissipation

The general idea of ohmic dissipation is that equilibrium temperatures larger than 1000 K lead to thermally ionized atmospheres that couples to the magnetic field and in the presence of strong winds produces currents, which then dissipate thermally in the deep interior (Batygin & Stevenson 2010; Batygin et al. 2011). However, in the high equilibrium temperature regime and therefore high atmospheric ionization fraction, ions slow down the winds due to Lorentz force, which in turn decrease the efficiency of ohmic dissipation (Perna et al. 2010a,b). Scaling law relations based on ohmic dissipation showed that indeed the heating efficiency increases with equilibrium temperature until a maximum is reached beyond which the efficiency decreases (Menou 2012), which was also confirmed by TF18 and now in our study. The scaling laws also suggest that the location of the peak depends on the strength of the magnetic field. Therefore, studying the functional form of the HEET distribution provides insights within the context of ohmic dissipation.

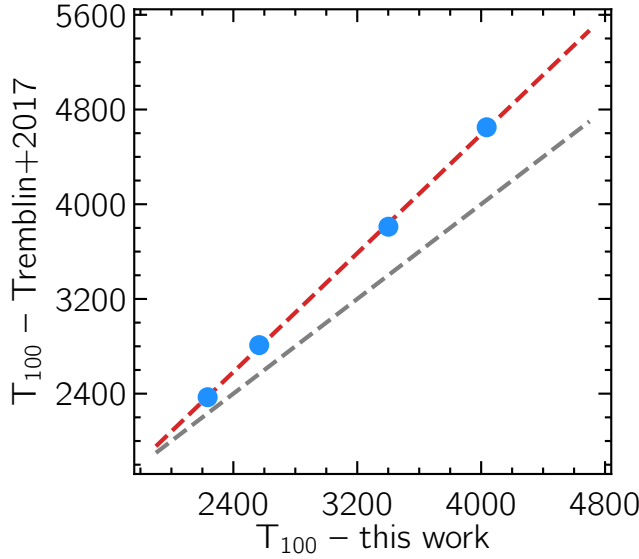


Fig. 7. Temperature at 100 bar derived from our PT structures compared to the values from the average PT profiles using 2D circulation models presented by Tremblin et al. (2017) resulting from the advection of potential temperature. All the models correspond to a planet with $\log g = 2.97 \pm 0.15$ and increasing stellar incident flux. The gray dashed line shows the 1:1 relation while the red dashed line shows the fit to the data.

Based on our analysis, we find that the HEET distribution can be modeled by a Gaussian function, in agreement with TF18 and with the theoretical predictions. We find however that the location of the peak is at 1860 K, which is higher compared to the work of TF18 that reported the peak around 1566 K (see Table 1). Menou (2012) showed that the transition is a function of the strength of the magnetic field (see his Figure 4) where stronger magnetic fields push the peak to higher equilibrium temperatures (the peak is at ~ 1800 K for a 30 G field). Ginzburg & Sari (2016) estimate the transition around ~ 1500 K based on analytical models and Rogers & Komacek (2014) at $\sim 1500 - 1600$ K based on magnetohydrodynamic simulations. Yadav & Thorngrén (2017) estimate the surface magnetic field strength of hot Jupiters using the energy flux scaling law from Christensen et al. (2009) and account for the extra heat injected using the heating efficiency relation presented by TF18. They found magnetic field strengths around 50 – 100 G for the most inflated hot Jupiters. There are no theoretical atmospheric circulation models with such strong magnetic fields, which might hence change the location of the peak. The transition is still not well constrained and might depend on the field strength but the Gaussian distribution is robust and most importantly is prior independent. Future observations of magnetic field strengths could potentially provide a better overview but for now they remain unconstrained from an observational point of view (for a current review see Griessmeier 2017; Lazio 2018).

6.3. Comparison to Advection of Potential Temperature

Another source of heat could be the movement of high-entropy fluid parcels deeper into the atmosphere, a process known as advection of potential temperature. Within this context, Tremblin et al. (2017) suggested, using two-dimensional (2D) circulation

model, that this process leads to a hot interior that can naturally explain the radius anomaly of hot Jupiters. This was further supported recently by 3D GCM simulations (Sainsbury-Martinez et al. 2019). The 2D models show that a stronger stellar incident flux leads to hotter interior adiabat (see their Figure 5). We compare our results based on the 1D model to the 2D models by selecting four planets from our sample that matches their simulation parameters, i.e. $\log g = 2.97 \pm 0.15$ with the corresponding equilibrium temperatures. We do not include the model with the lowest equilibrium temperature (~ 500 K) as it does not match any of the selected systems in our sample. The planets we selected as a function of increasing stellar incident flux are HAT-P-17 b, Corot-4 b, HD209458 b, and HATS-35 b. We then compare the temperatures at 100 bar (T_{100}) using the PT profiles based on the 2D models to the ones based on our 1D model presented in Section 3. The results are illustrated in Figure 7, where the derived temperatures at 100 bar are shown in blue circles and the red dashed line shows the fit to the data. The gray dashed line shows the 1:1 relation on which the points would lie if their model and our data derived from observations would predict identical temperatures. We find that roughly the results agree well with a slope of 1.25, deviating from the 1:1 relation. We note however that these values are model dependent and any change in the treatment of the atmospheric model, e.g. including clouds and new opacity sources, will change these values. The temperatures estimated from the average PT profiles using the 2D circulation models are larger than the values predicted by our model, varying from 6% up to 15% for the most irradiated planets. This is expected since the 2D models tend to overestimate the radii compared to the observed ones (Tremblin et al. 2017). Our results concerning the adiabatic profile are also in agreement, where the 2D and 3D atmospheric circulation models suggest a hot adiabat starting at ~ 10 bar, significantly at lower pressures compared to standard irradiated models (e.g. Fortney et al. 2007). This is in agreement with our findings and conclusions that future GCM models should account for the extra heat in the interior of inflated hot Jupiters and in-line with the work of Carone et al. (2019).

6.4. General Comparison to Previous Studies

It is useful and informative to compare the results of our model with analytical relations. We consider the analytical approximations of the internal luminosity based on ohmic dissipation (L_{Huang} ; Equation (14) of Huang & Cumming 2012) and thermal tides (L_{Socrates} ; Equation (8) of Socrates 2013):

$$L_{\text{Huang}} = 3 \times 10^{22} \text{ erg s}^{-1} \left(\frac{B_{\phi 0}}{10 \text{ G}} \right)^2 \left(\frac{\sigma_t}{10^6 \text{ s}^{-1}} \right)^{-1} \times \left(\frac{T_{\text{eq}}}{1500 \text{ K}} \right) \left(\frac{R_p}{R_J} \right)^4 \left(\frac{M_p}{M_J} \right)^{-1} \quad (45)$$

$$L_{\text{Socrates}} = 1.5 \times 10^{28} \text{ erg s}^{-1} \left(\frac{P}{4 \text{ days}} \right)^{-2} \times \left(\frac{T_{\text{eq}}}{2000 \text{ K}} \right)^3 \left(\frac{R_p}{10^{10} \text{ cm}} \right)^4. \quad (46)$$

In the above equations, $B_{\phi 0}$ is the toroidal component of the magnetic field at a reference pressure of 10 bar, σ_t is the electrical conductivity in the dissipation region, and P is the orbital period.

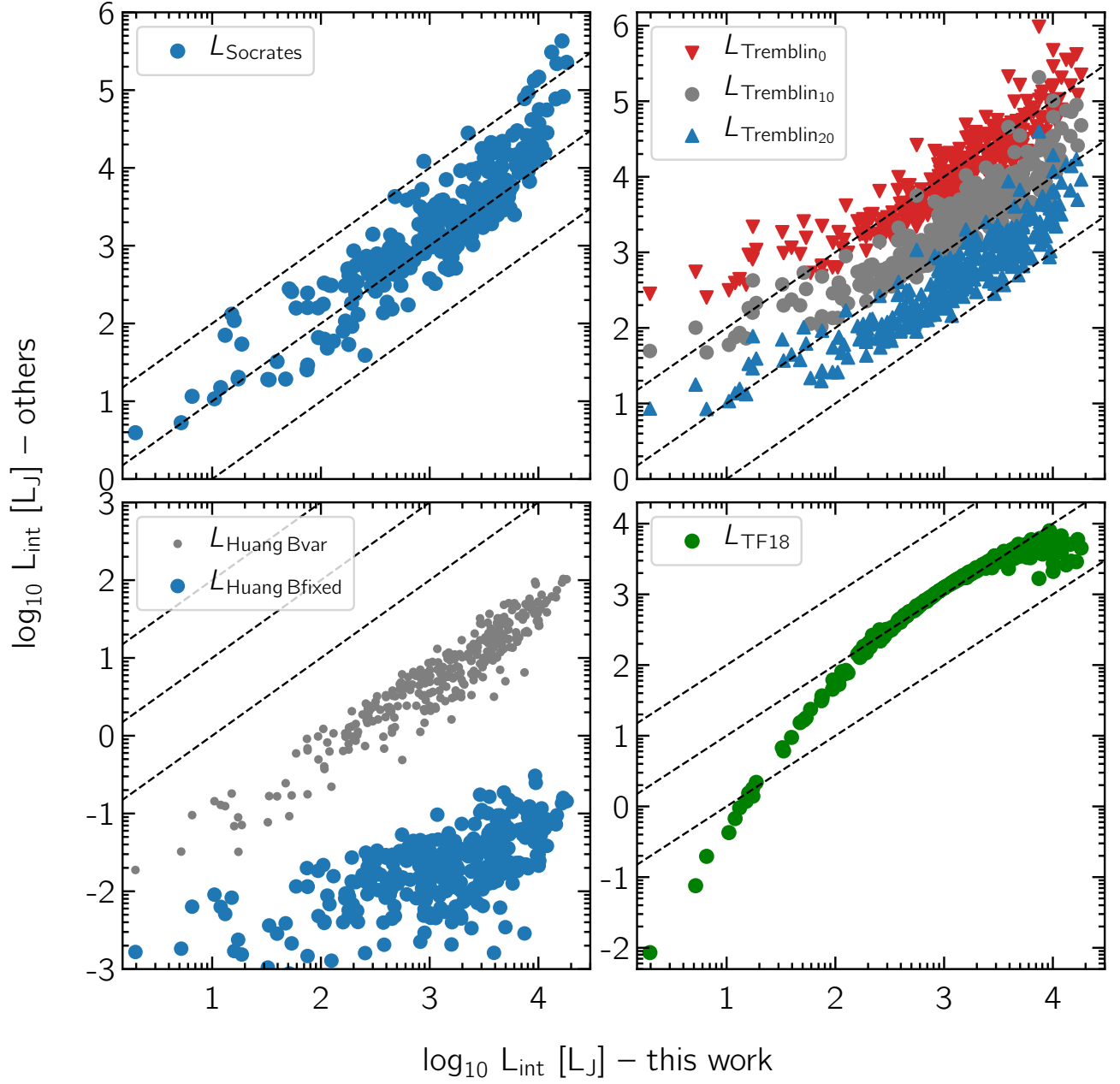


Fig. 8. Comparison of the internal luminosity derived in this work from observations and other (theoretical) studies. The solid dashed lines are from top to bottom the 1:10, 1:1, and 1:0.1 relations. The different panels show the results in comparison with analytical relations (Huang & Cumming 2012; Socrates 2013), numerical modeling (Tremblin et al. 2017), and based on a statistical approach similar to ours (TF18). Notice the different scales in each panel. The results based on the analytical approximations of Huang & Cumming (2012) underestimate L_{int} . There is an agreement with TF18, Tremblin et al. (2017), and Socrates (2013) giving thus evidence for advection of potential temperature and thermal tides as possible mechanisms to explain the radius inflation conundrum.

To compute L_{Huang} , we fix σ_t to the nominal value 10^6 s^{-1} and consider two different cases for $B_{\phi 0}$. In the first case, we fix $B_{\phi 0}$ to 10 G and in the second case, we compute the mean magnetic field strength at the surface of the dynamo based on the scaling law of Christensen et al. (2009) in the form given by Reiners & Christensen (2010):

$$B_{\text{dyn}} = 4.8 \times 10^3 \text{ G} \times \left(\frac{ML^2}{R^7} \right)^{1/6} \quad (47)$$

where M , L , and R are the mass, luminosity, and radius of the planet normalized to solar units. We assume $B_{\phi 0} = B_{\text{dyn}}$. Note that using this relation, B_{dyn} ranges roughly between 30

and 480 G for our sample, in agreement with the previous estimates of [Yadav & Thorngren \(2017\)](#). We refer to these cases as $L_{\text{Huang, Bfixed}}$ and $L_{\text{Huang, Bvar}}$, respectively. It is straightforward then to calculate L_{Socrates} , $L_{\text{Huang, Bfixed}}$ and $L_{\text{Huang, Bvar}}$ for each hot Jupiter in our sample using the relevant physical properties.

We also examine our results within the context of advection of high-entropy material based on models of [Tremblin et al. \(2017\)](#). Our aim is to compare the internal luminosity of the planets that this mechanism predicts to the internal luminosities derived in Section 4.1. However, [Tremblin et al. \(2017\)](#) did not report the internal luminosity in their models and computed 2D PT profiles only for four planets with different T_{eq} values. Therefore, we need to estimate the internal luminosity of all the planets based on the model of advection of potential temperature, for which we follow the procedure described next. We first compute the entropy using the SCvH EOS ([Saumon et al. 1995](#)) and T_{100} , which was derived from the 2D PT profiles based on four fiducial planets with different T_{eq} (see Section 6.3 for more details). Second, we fit a relation between the equilibrium temperatures of the four planets and their estimated entropy. Finally, to convert the entropy into an internal luminosity, we use the entropy–mass–luminosity relation from an updated version of the population synthesis of [Mordasini \(2018\)](#). The second step allows us to compute the entropy for all the selected hot Jupiters in our sample using the observed T_{eq} . Having calculated the entropy and knowing M_p from observations, the last step allows us to compute the internal luminosity of the planets. With this procedure, we therefore calculate the internal luminosity of the planets predicted by this mechanism based on these fits and based on T_{eq} and M_p from observations. We consider three cases for comparison by assuming the planets are composed of H/He and setting the fraction of heavy elements to 0%, 10%, and 20%. We refer to these models as L_{Tremblin_0} , $L_{\text{Tremblin}_{10}}$, and $L_{\text{Tremblin}_{20}}$, respectively. We point out that the values should be taken with caution as there are strong approximations involved in this approach.

Finally, to compare our results to [TF18](#), we use the analytical $\epsilon(T_{\text{eq}})$ (Equation (34) in their paper) to compute ϵ and then estimate L_{TF18} using Equation (8).

Figure 8 compares our results to the various studies where the dashed lines are the 1:10, 1:1, and 1:0.1 relations. The predicted luminosities based on the analytical solution of thermal tides as suggested by [Socrates \(2013\)](#) and the advection of potential temperature ([Tremblin et al. 2017](#)) are on the same order of magnitude as the ones we derive in this work based on observations. The advection of potential temperature ([Tremblin et al. 2017](#)) predicts high luminosity values for the least luminous planets in our sample. This is expected since their model tend to overestimate the radii compared to observations, even for planets with incident flux below the threshold of inflation (stellar incident flux of $\sim 2 \times 10^8 \text{ erg s}^{-1} \text{ cm}^{-2}$ or $T_{\text{eq}} \approx 1000 \text{ K}$).

The relation of [Huang & Cumming \(2012\)](#) based on ohmic dissipation leads to small internal luminosity values. Note that this relation is an order-of-magnitude estimation of the total ohmic power. We therefore caution that these results do not provide evidence against ohmic dissipation, but rather that this relation underestimates the ohmic power. Based on our results and the work of [TF18](#), there is compelling evidence from the HEET relation that ohmic dissipation can explain the radii of hot Jupiters. The ohmic power values estimated by [Batygin & Stevenson \(2010\)](#) and [Menou \(2012\)](#) are up to three orders of magnitude higher than the values predicted by [Huang & Cumming \(2012\)](#) and thus on the same order of magnitude estimated in this work. Moreover, the small internal luminosity val-

ues using the relation of [Huang & Cumming \(2012\)](#) could also explain the findings of [Lopez & Fortney \(2016\)](#), where it was shown that the relation did not lead to re-inflation of hot Jupiters.

For our models with $L_{\text{int}} < 10^2 L_J$, the model of [TF18](#) predicts smaller values of L_{int} . This difference is a direct consequence of the discrepancy in ϵ as shown in the right panel of Figure 5, where as discussed in Section 5.3 we predict higher heating efficiencies for the least and the most irradiated planets.

Converting the luminosity values to a heating efficiency using Equation (8), the models of [Socrates \(2013\)](#) and [Tremblin et al. \(2017\)](#) do not lead to a decrease in the heating efficiency at the highest equilibrium temperatures. The former predicts a continuous increase as was shown by [TF18](#) with values as high as 20–25% and the latter seems to increase moderately up to 30%, 10%, and 2% for $Z_p = 0, 0.1, \text{ and } 0.2$, respectively. This is expected given the steeper increase in the luminosity values above $10^4 L_J$ for both models. These are the highly inflated and highly irradiated hot Jupiters ($R_p > 1.4 R_J$ and $T_{\text{eq}} > 1900 \text{ K}$). Note that the peak in the HEET distribution in our model occurs close to 1900 K (see Section 5.3 and Table 1), beyond which ϵ decreases for higher T_{eq} . This explains why the models of [Socrates \(2013\)](#) and [Tremblin et al. \(2017\)](#) do not predict a Gaussian function, i.e. why ϵ does not decrease at high T_{eq} . We stress that these models can nevertheless explain the observed radii of most of the hot Jupiters and can be the dominant mechanisms responsible for inflation even in the absence of the Gaussian function. It could be thus that these mechanisms are too efficient in inflating hot Jupiters at temperatures above than 1900 K. Thermal tides have received less attention within the context of the radius anomaly problem and thus more work is needed to understand the physical regime where this mechanism is efficient.

In summary, we provide evidence that thermal tides and advection of potential temperature can reproduce the large observed radii of most of the hot Jupiters based on the internal luminosity predicted using these models. Moreover, the HEET distribution suggests that ohmic dissipation can also explain the radii of the close-in giant planets (see Section 6.2). We therefore conclude that all of these three mechanisms can explain the inflation of hot Jupiters. This is in line with our main goals where we stress that these mechanisms were tested on only a handful of exoplanets and a statistical approach is necessary to confirm or refute these mechanisms for the entire population.

6.5. Limitations and Caveats

There are important caveats and limitations related to this work that should be explicitly mentioned.

Our results and conclusions are based on a simple 1D interior structure model. Hot Jupiters however are tidally locked, which gives rise to a temperature gradient between the day-side and the night-side. The RCB at the night-side might thus be at lower pressures compared to the day-side leading to uneven cooling. As a consequence of that, [Spiegel & Burrows \(2013\)](#) showed using a 1+1D model that the net effect of incorporating night-side cooling leads to higher cooling rates compared to the default 1D models. 2D circulation models also showed that the location of the RCB differs from the day-side to the night-side, which further enhances the cooling rate ([Rauscher & Showman 2014](#)) and thus requires even higher efficiency to explain the radii of hot Jupiters. This is especially important for the highly irradiated planets as it was shown that the day-side–night-side temperature differences increases with stellar irradiation ([Komacek & Showman 2016; Komacek et al. 2017](#)).

In addition, we assume that the heat is deposited in the interior of the planet and we do not account for dissipation in the intermediate layers. A better treatment would be to deposit the heat over a range of depths similar to [Ginzburg & Sari \(2016\)](#) or [Komacek & Youdin \(2017\)](#). Moreover, even though we showed that the Gaussian profile of the HEET distribution is in agreement with ohmic dissipation there are few shortcomings to this. A key component for ohmic dissipation is the electrical conductivity σ , where the ohmic power is proportional to $1/\sigma$ ([Batygin & Stevenson 2010](#)). The electrical conductivity increases dramatically in the interior leading to efficient heating only at lower densities and thus at lower pressures. However, the layers that contribute to the inflation are not at the surface where the conductivity is maximum but rather at deeper layers (between 100 and 1000 bar; [Batygin et al. 2011](#)). [Wu & Lithwick \(2013\)](#) confirmed these results by showing that heat deposited at 100 bar requires significantly less heating efficiency in comparison to 10 or 3 bar (0.3% compared to 3% and 200%, respectively, see their Figure 3). It is therefore unclear whether the Gaussian functional form holds for energy dissipated at lower pressures.

The depth of the heating has also direct consequences on the interior structure. For example, [Huang & Cumming \(2012\)](#) included ohmic heating only in the radiative layers deeper than 10 bar and showed that as a consequence of that the RCB moves to deeper pressures. However, their model cannot reproduce the radii of massive planets. Understanding the location of the RCB is crucial as it regulates the planetary cooling rate and thus the contraction rate ([Arras & Bildsten 2006](#); [Marleau & Cumming 2014](#)). Future developments of state-of-the-art GCM models that solve the complete equations without approximations and that couple the upper atmosphere with the deep convective layers will provide a complete picture of the underlying physical processes.

Finally, in this work we did not account for observational biases. A large number of the hot Jupiters discovered to date are discovered using ground based telescopes, such as WASP ([Pollacco et al. 2006](#)) and the HATNet and HATSouth ([Bakos 2018](#)) exoplanet surveys. There is a lack of hot Jupiters with radii smaller than $\sim 1.4 R_J$ around early- and mid-F stars. This is because detecting such planets is still challenging from the ground as the transit depths are shallow and less than 0.5%. [Heng \(2012\)](#) showed that *if* ohmic dissipation can explain the anomalously large radii of hot Jupiters, then this naturally leads to scatter in the radii at a given stellar incident flux due to variations in the opacity, albedo, cloud/hazes properties, and the magnetic fields strength. It is therefore still not quite clear whether the lack of “medium-inflated” hot Jupiters around F stars is due to observational biases or variations in the efficiency of the heating mechanism. The NASA *Transiting Exoplanet Survey Satellite* mission (TESS; [Ricker et al. 2015](#)) will discover such planets if they exist and will help to better constrain the efficiency of the heating mechanisms either by the lack or existence of such planets. Subsequently high precision follow-up observations with the *CHaracterising ExOPlanet Satellite* (CHEOPS; [Broeg et al. 2013](#)) will help to get very accurate radii.

7. Conclusion

In this work, we developed a flexible and robust hierarchical Bayesian model to couple the observed physical parameters of hot Jupiters to an interior structure model. The model accounts for observational uncertainties and for the scatter in the relation between planet mass and heavy-element fraction. We applied this approach to quantify the internal luminosity needed to explain the radii of a sample of 314 hot Jupiters. We tested this

model under two different priors (assuming a log-uniform and a linear-uniform distributions for L_{int}) and showed that the population level distributions are prior independent (Figure 4). This provides useful and robust constraints on the interior structure of hot Jupiters. We find that such planets tend to have hotter interiors compared to previous assumptions, and as a result, the RCB moves to lower pressures, in agreement with recent work by [Thorngren et al. \(2019\)](#) (Figure 6).

Assuming the planet has reached steady state and assuming that the additional source of heat is the stellar irradiation, we compute the heating efficiency ϵ , defined as the fraction of stellar irradiation deposited into the interior of the planet that is needed to explain the observed inflated radii. We find that the heating-efficiency–equilibrium-temperature relation is described by a Gaussian function (Figure 5), in agreement with previous work by [TF18](#) and most importantly in agreement with theoretical predictions based on the ohmic dissipation model ([Menou 2012](#)). We also show that thermal tides ([Arras & Socrates 2010](#); [Socrates 2013](#)) and advection of potential temperature ([Tremblin et al. 2017](#)) can explain the observations of most of the planets in our sample and thus are possible mechanisms responsible for the anomalously large radii of hot Jupiters (Figure 8).

To conclude, we provide new insights into the interior of hot Jupiters by coupling observations to theoretical models within a powerful statistical framework. With a better understanding of the interior, we highlight the importance of accounting for the extra heat flux in the interior in 3D GCM models, which will further improve our understanding of wind speeds and hence on the efficiency of the heating mechanisms.

The future of hot Jupiters is exciting and bright. Simulations of the expected TESS yield ([Barclay et al. 2018](#)) predict that TESS will discover more than 250 hot Jupiters suitable for RV follow-up ($R_p > 1 R_J$) with orbital periods < 10 days orbiting bright stars ($V < 14$ mag), almost doubling the number of hot Jupiters discovered. The mission already detected few hot Jupiters (e.g. [Kossakowski et al. 2019](#); [Wang et al. 2019](#)) with many yet to be discovered. Furthermore, CHEOPS ([Broeg et al. 2013](#)) is capable of detecting the phase curves of hot Jupiters, which provide information on the day-night temperature contrast. CHEOPS will therefore play a major role in providing clues into the efficiency of energy transport in hot Jupiter atmospheres (e.g. HD189733 b; [Knutson et al. 2007](#)). With a better understanding of the interior structure of hot Jupiters thanks to the development of flexible and computationally efficient statistical tools, we will be able to provide further constraints on the radius inflation conundrum.

Acknowledgements. P.S., C.M., G.-D.M. acknowledge the support from the Swiss National Science Foundation under grant BSSG10.155816 “PlanetsInTime”. Parts of this work have been carried out within the framework of the NCCR PlanetS supported by the Swiss National Science Foundation. T.H. and P.M. acknowledge support from the European Research Council under the Horizon 2020 Framework Program via the ERC Advanced Grant Origins 83 24 28. G.-D.M. acknowledges the support of the DFG priority program SPP 1992 “Exploring the Diversity of Extrasolar Planets” (KU 2849/7-1). P.S. would like to thank David Hogg for useful discussions related to the importance sampling technique and Daniel Thorngren for sharing the posterior distributions of the individual planets. P.S. thanks Saavi and Gabriele for exchanging priority time on the aida server.

References

- Arras, P. & Bildsten, L. 2006, *ApJ*, 650, 394 [1](#), [2](#), [5.4](#), [6.5](#)
- Arras, P. & Socrates, A. 2010, *ApJ*, 714, 1 [1](#), [7](#)
- Bakos, G. Á. 2018, The HATNet and HATSouth Exoplanet Surveys, 111 [6.5](#)
- Baraffe, I., Chabrier, G., & Barman, T. 2008, *A&A*, 482, 315 [3.1](#)
- Baraffe, I., Selsis, F., Chabrier, G., et al. 2004, *A&A*, 419, L13 [2](#)

- Barclay, T., Pepper, J., & Quintana, E. V. 2018, *ApJS*, 239, 2 7
- Batygin, K. & Stevenson, D. J. 2010, *ApJ*, 714, L238 1, 3.3.2, 6.1, 6.2, 6.4, 6.5
- Batygin, K., Stevenson, D. J., & Bodenheimer, P. H. 2011, *ApJ*, 738, 1 1, 3.3.2, 6.2, 6.5
- Bodenheimer, P., Lin, D. N. C., & Mardling, R. A. 2001, *ApJ*, 548, 466 1
- Broeg, C., Fortier, A., Ehrenreich, D., et al. 2013, in *European Physical Journal Web of Conferences*, Vol. 47, *European Physical Journal Web of Conferences*, 03005 6.5, 7
- Burrows, A., Hubeny, I., Budaj, J., & Hubbard, W. B. 2007, *ApJ*, 661, 502 1
- Carone, L., Baeyens, R., Mollière, P., et al. 2019, arXiv e-prints, arXiv:1904.13334 6.1, 6.3
- Chabrier, G. & Baraffe, I. 2007, *ApJ*, 661, L81 1
- Christensen, U. R., Holzwarth, V., & Reiniers, A. 2009, *Nature*, 457, 167 6.2, 6.4
- Collins, K. A., Kielkopf, J. F., & Stassun, K. G. 2017, *AJ*, 153, 78 3.1.1
- Delrez, L., Santerne, A., Almenara, J. M., et al. 2016, *MNRAS*, 458, 4025 5.4
- Demory, B.-O. & Seager, S. 2011, *ApJS*, 197, 12 1, 4.1.1, 5.2
- Dorn, C., Harrison, J. H. D., Bonsor, A., & Hands, T. O. 2019, *MNRAS*, 484, 712 3
- Enoch, B., Collier Cameron, A., & Horne, K. 2012, *A&A*, 540, A99 1
- Folkner, W. M., Iess, L., Anderson, J. D., et al. 2017, *Geophysical Research Letters*, 44, 4694 3.3.1
- Foreman-Mackey, D., Hogg, D. W., Lang, D., & Goodman, J. 2013, *PASP*, 125, 306 4.1
- Foreman-Mackey, D., Hogg, D. W., & Morton, T. D. 2014, *The Astrophysical Journal*, 795, 64 4.2, 4.2
- Fortney, J. J., Lodders, K., Marley, M. S., & Freedman, R. S. 2008, *ApJ*, 678, 1419 3.1.1
- Fortney, J. J., Marley, M. S., & Barnes, J. W. 2007, *ApJ*, 659, 1661 1, 5.4, 6.1, 6.3
- Freedman, R. S., Lustig-Yaeger, J., Fortney, J. J., et al. 2014, *ApJS*, 214, 25 3.1
- Ginzburg, S. & Sari, R. 2016, *ApJ*, 819, 116 1, 2, 6.2, 6.5
- Griessmeier, J. M. 2017, in *Planetary Radio Emissions VIII*, ed. G. Fischer, G. Mann, M. Panchenko, & P. Zarka, 285–299 6.2
- Grunblatt, S. K., Huber, D., Gaidos, E., et al. 2017, *AJ*, 154, 254 2
- Grunblatt, S. K., Huber, D., Gaidos, E. J., et al. 2016, *AJ*, 152, 185 2
- Guillot, T. 2010, *A&A*, 520, A27 2, 3.1.1, 3.2
- Guillot, T. & Gautier, D. 2014, arXiv e-prints, arXiv:1405.3752 3.3.1, 5.4
- Guillot, T. & Showman, A. P. 2002, *A&A*, 385, 156 1, 3.1.1
- Hartman, J. D., Bakos, G. Á., Bhatti, W., et al. 2016, *AJ*, 152, 182 2
- Heng, K. 2012, *ApJ*, 748, L17 6.5
- Hogg, D. W., Myers, A. D., & Bovy, J. 2010, *The Astrophysical Journal*, 725, 2166 4.2, 4.2
- Huang, X. & Cumming, A. 2012, *ApJ*, 757, 47 1, 3.3.2, 6.4, 8, 6.4, 6.5
- Jin, S. & Mordasini, C. 2018, *ApJ*, 853, 163 3.1
- Jin, S., Mordasini, C., Parmentier, V., et al. 2014, *ApJ*, 795, 65 2, 3.1, 3.1.1
- Knutson, H. A., Charbonneau, D., Allen, L. E., et al. 2007, *Nature*, 447, 183 7
- Komacek, T. D. & Showman, A. P. 2016, *ApJ*, 821, 16 6.5
- Komacek, T. D., Showman, A. P., & Tan, X. 2017, *ApJ*, 835, 198 6.5
- Komacek, T. D. & Youdin, A. N. 2017, *ApJ*, 844, 94 1, 3.2, 3.3.1, 3.3.2, 6.1, 6.5
- Kossakowski, D., Espinoza, N., Brahm, R., et al. 2019, *MNRAS*, 490, 1094 7
- Laughlin, G., Crismani, M., & Adams, F. C. 2011, *ApJ*, 729, L7 1
- Lazio, T. J. W. 2018, *Radio Observations as an Exoplanet Discovery Method*, 9 6.2
- Li, L., Baines, K. H., Smith, M. A., et al. 2012, *Journal of Geophysical Research (Planets)*, 117, E11002 5.4
- Linder, E. F., Mordasini, C., Mollière, P., et al. 2019, *A&A*, 623, A85 3.1, 3.1.1
- Lopez, E. D. & Fortney, J. J. 2016, *ApJ*, 818, 4 2, 6.4
- Marleau, G.-D., Coleman, G. A. L., Leleu, A., & Mordasini, C. 2019, *A&A*, 624, A20 3.1, 3.1.1
- Marleau, G. D. & Cumming, A. 2014, *MNRAS*, 437, 1378 1, 2, 3.2, 6.5
- Menou, K. 2012, *ApJ*, 745, 138 5.3, 6.2, 6.4, 7
- Miller, N. & Fortney, J. J. 2011, *ApJ*, 736, L29 1
- Mollière, P., van Boekel, R., Bouwman, J., et al. 2017, *A&A*, 600, A10 3.1, 3.1.1
- Mollière, P., van Boekel, R., Dullemond, C., Henning, T., & Mordasini, C. 2015, *ApJ*, 813, 47 3.1, 3.1.1
- Mollière, P., Wardenier, J. P., van Boekel, R., et al. 2019, *A&A*, 627, A67 3.1.1
- Mordasini, C. 2018, *Planetary Population Synthesis*, 143 6.4
- Mordasini, C. 2020, arXiv e-prints, arXiv:2002.02455 3.1, 5.3
- Mordasini, C., Alibert, Y., Klahr, H., & Henning, T. 2012, *A&A*, 547, A111 3.1, 3.3.1
- Mordasini, C., Marleau, G. D., & Mollière, P. 2017, *A&A*, 608, A72 2
- Muller, S., Helled, R., & Cumming, A. 2020, arXiv e-prints, arXiv:2004.13534 3.3.1
- Owen, J. E. & Jackson, A. P. 2012, *MNRAS*, 425, 2931 2
- Perna, R., Menou, K., & Rauscher, E. 2010a, *ApJ*, 719, 1421 1, 6.2
- Perna, R., Menou, K., & Rauscher, E. 2010b, *ApJ*, 724, 313 1, 6.2
- Pollacco, D. L., Skillen, I., Collier Cameron, A., et al. 2006, *PASP*, 118, 1407 6.5
- Price-Whelan, A. M., Hogg, D. W., Rix, H.-W., et al. 2018, *AJ*, 156, 18 4.2
- Rauscher, E. & Showman, A. P. 2014, *ApJ*, 784, 160 6.5
- Reiners, A. & Christensen, U. R. 2010, *A&A*, 522, A13 6.4
- Ricker, G. R., Winn, J. N., Vanderspek, R., et al. 2015, *Journal of Astronomical Telescopes, Instruments, and Systems*, 1, 014003 6.5
- Rogers, L. A. 2015, *ApJ*, 801, 41 4.2
- Rogers, T. M. & Komacek, T. D. 2014, *ApJ*, 794, 132 6.2
- Sainsbury-Martinez, F., Wang, P., Fromang, S., et al. 2019, *A&A*, 632, A114 1, 6.3
- Saumon, D., Chabrier, G., & van Horn, H. M. 1995, *The Astrophysical Journal Supplement Series*, 99, 713 3.1, 5.3, 6.4
- Sestovic, M., Demory, B.-O., & Queloz, D. 2018, *Astronomy and Astrophysics*, 616, A76 1, 2, 5.2
- Showman, A. P. & Guillot, T. 2002, *A&A*, 385, 166 1, 6.1
- Sing, D. K., Lavvas, P., Ballester, G. E., et al. 2019, *AJ*, 158, 91 4.1.1, 5.4
- Socrates, A. 2013, arXiv e-prints, arXiv:1304.4121 6.4, 8, 6.4, 7
- Southworth, J. 2011, *MNRAS*, 417, 2166 2
- Spiegel, D. S. & Burrows, A. 2013, *ApJ*, 772, 76 2, 3.2, 5.4, 6.5
- Thompson, S. L. 1990, *Sandia Natl. Lab. Doc.* 3.1, 5.3
- Thorngrén, D., Gao, P., & Fortney, J. J. 2019, *ApJ*, 884, L6 1, 5.4, 5.4, 6.1, 7
- Thorngrén, D. P. & Fortney, J. J. 2018, *The Astronomical Journal*, 155, 214 1, 3.2, 3.3.1, 4.2, 4.2, 5, 5.3, 1, 5.3, 5.4, 6.1, 6.2, 8, 6.4, 7
- Thorngrén, D. P., Fortney, J. J., Murray-Clay, R. A., & Lopez, E. D. 2016, *The Astrophysical Journal*, 831, 64 2, 3, 3.2, 3.3.1, 4.1, 4.1, 4.1, 4.1.1, 6
- Tremblin, P., Chabrier, G., Mayne, N. J., et al. 2017, *ApJ*, 841, 30 1, 6.1, 7, 6.3, 8, 6.4, 7
- Valencia, D., Guillot, T., Parmentier, V., & Freedman, R. S. 2013, *ApJ*, 775, 10 3
- Venturini, J., Alibert, Y., & Benz, W. 2016, *A&A*, 596, A90 3.3.1
- Wahl, S. M., Hubbard, W. B., Militzer, B., et al. 2017, *Geophys. Res. Lett.*, 44, 4649 3.3.1
- Wang, S., Jones, M., Shporer, A., et al. 2019, *AJ*, 157, 51 7
- Weiss, L. M., Marcy, G. W., Rowe, J. F., et al. 2013, *ApJ*, 768, 14 1
- Wu, Y. & Lithwick, Y. 2013, *ApJ*, 763, 13 1, 2, 3.3.2, 6.5
- Yadav, R. K. & Thorngrén, D. P. 2017, *ApJ*, 849, L12 6.2, 6.4
- Youdin, A. N. & Mitchell, J. L. 2010, *ApJ*, 721, 1113 1

Appendix A: Supplemental Information

In Section 5.2, we showed that the mass–luminosity–radius (MLR) posterior distribution is similar when assuming L_{int} follows either a linear-uniform or a log-uniform prior distribution. In this Appendix we show that the heating-efficiency–equilibrium temperature (HEET), $T_{\text{int}} - T_{\text{eq}}$, and $P_{\text{RCB}} - T_{\text{eq}}$ distributions are also similar using both priors. Figure A.1 and Figure A.2 show the HEET and both the $T_{\text{int}} - T_{\text{eq}}$ and $P_{\text{RCB}} - T_{\text{eq}}$ distributions, respectively. Tables A.1 and A.2 present the 68% credible interval values for the model parameters for the MLR distribution assuming linear-uniform and log-uniform priors. Similarly, Table A.3 for the HEET distribution using a 4th degree polynomial, Table A.4 for the $T_{\text{int}} - T_{\text{eq}}$ distribution using a Gaussian function, and finally Table A.5 for the $P_{\text{RCB}} - T_{\text{eq}}$ distribution using a polynomial function.

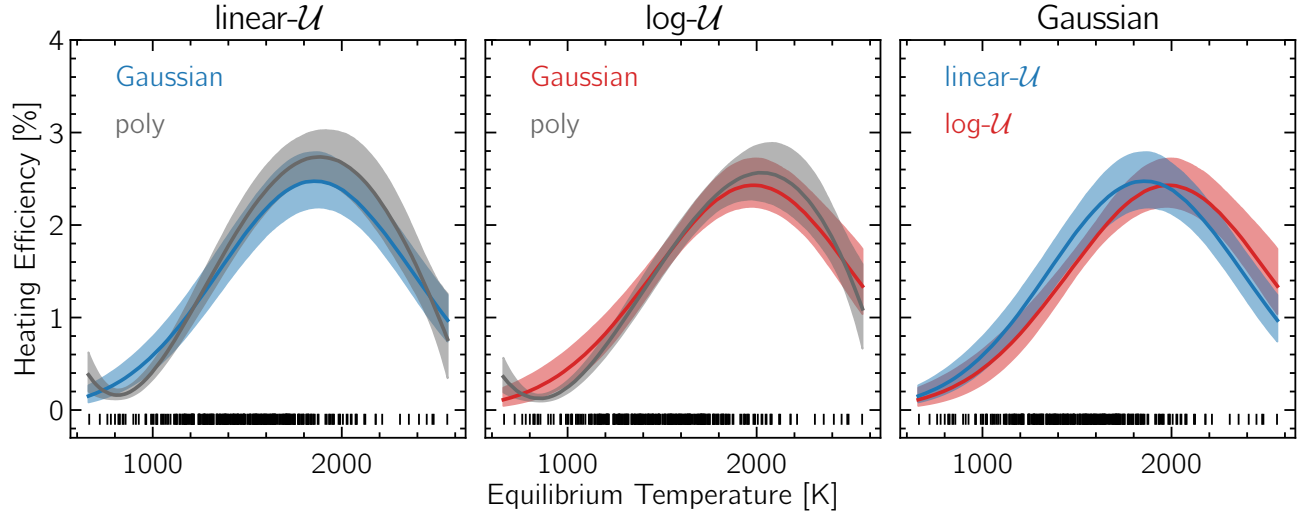


Fig. A.1. HEET posterior distribution under the linear–uniform (*left*) and the log–uniform (*middle*) priors using a Gaussian and 4th degree polynomial. There is a good agreement between both models using the same prior. To better compare the same model using different priors, the *right* panel shows the Gaussian models using log (red) and linear (blue) uniform priors.

Table A.1. 68% credible interval values of the parameters for the mass–luminosity–radius (MLR) distribution for the **linear– \mathcal{U}** case modelled as a 4th degree polynomial $g_p(x) = a_0 + a_1x + a_2x^2 + a_3x^3 + a_4x^4$ where $x = R_p$.

τ	a_0	a_1	a_2	a_3	a_4
$0.37 - 0.7 M_J$	28^{+11}_{-10}	-85^{+28}_{-31}	92^{+29}_{-29}	-39^{+12}_{-12}	6^{+1}_{-2}
$0.7 - 0.98 M_J$	27^{+14}_{-13}	-91^{+38}_{-44}	106^{+46}_{-43}	-48^{+20}_{-22}	8^{+3}_{-4}
$0.98 - 2.5 M_J$	48^{+12}_{-13}	-160^{+39}_{-38}	186^{+40}_{-45}	-88^{+21}_{-19}	15^{+3}_{-4}
$> 2.5 M_J$	72^{+52}_{-54}	-224^{+200}_{-198}	244^{+276}_{-274}	-102^{+161}_{-165}	14^{+36}_{-36}

Table A.2. 1σ credible interval values of the parameters for the mass–luminosity–radius (MLR) distribution for the **log– \mathcal{U}** case modelled as a 4th degree polynomial $g_p(x) = a_0 + a_1x + a_2x^2 + a_3x^3 + a_4x^4$ where $x = R_p$.

τ	a_0	a_1	a_2	a_3	a_4
$0.37 - 0.7 M_J$	20^{+8}_{-7}	-66^{+19}_{-22}	73^{+22}_{-21}	-32^{+9}_{-10}	5^{+1}_{-1}
$0.7 - 0.98 M_J$	23^{+12}_{-10}	-79^{+32}_{-39}	94^{+43}_{-39}	-44^{+19}_{-21}	7^{+3}_{-4}
$0.98 - 2.5 M_J$	50^{+17}_{-14}	-166^{+42}_{-51}	195^{+54}_{-48}	-94^{+22}_{-26}	16^{+4}_{-4}
$> 2.5 M_J$	86^{+70}_{-70}	-272^{+263}_{-269}	306^{+370}_{-366}	-135^{+219}_{-223}	19^{+49}_{-48}

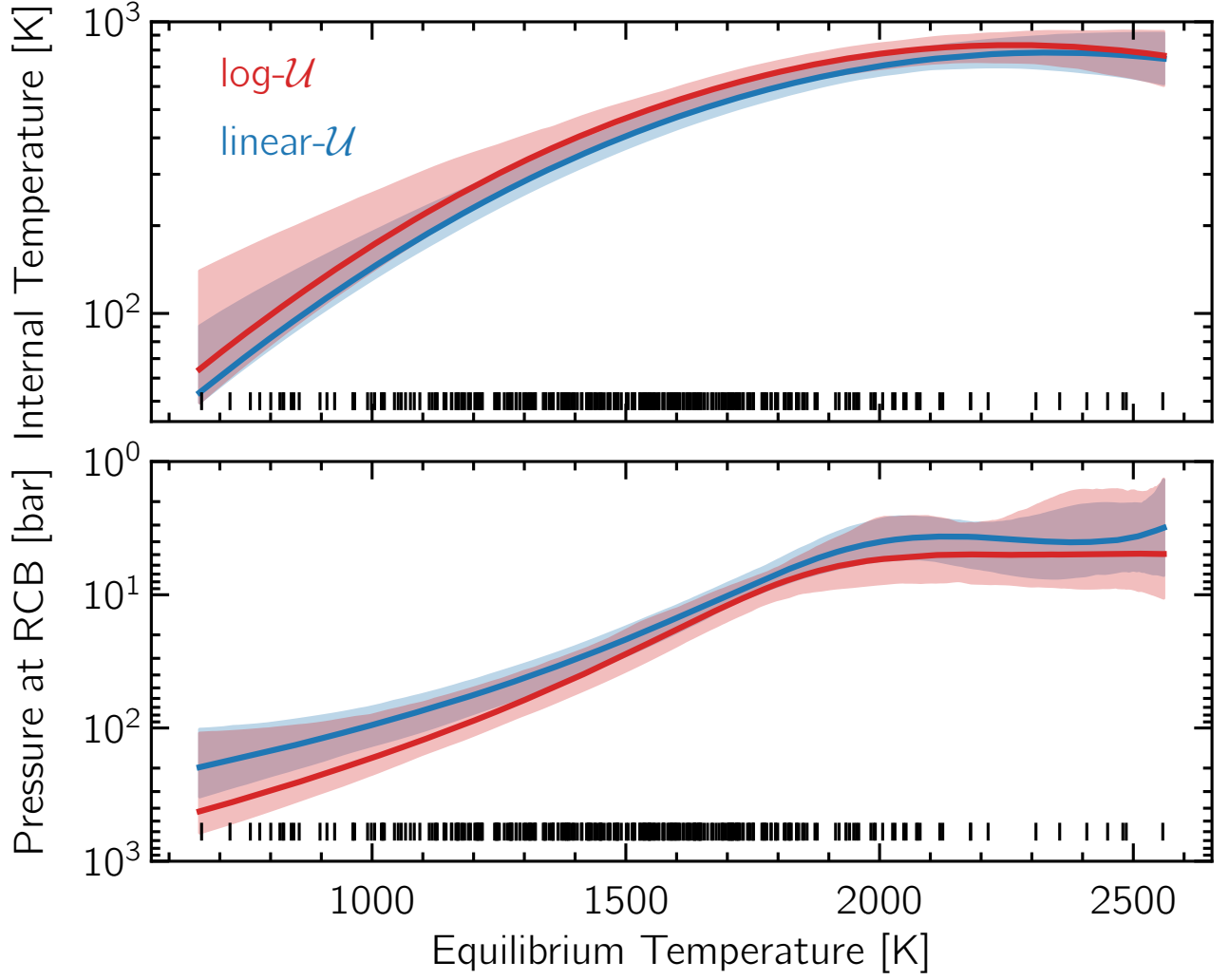


Fig. A.2. $T_{\text{int}}-T_{\text{eq}}$ and $P_{\text{RCB}}-T_{\text{eq}}$ diagrams in the upper and lower panel, respectively. The shaded regions show the 2σ credible interval. Both distributions are similar at the 2σ level using the linear-uniform (red) and the log-uniform (blue) priors.

Table A.3. 68% credible interval values of the parameters for the heating-efficiency-equilibrium temperature (HEET) distribution for the **linear-U** and **log-U** cases using the 4th degree polynomial model $g_p(x) = a_0 + a_1x + a_2x^2 + a_3x^3 + a_4x^4$, where $x = T_{\text{eq}}/1000$.

τ	a_0	a_1	a_2	a_3	a_4
log-U	11_{-5}^{+5}	-33_{-17}^{+15}	35_{-18}^{+19}	-14_{-9}^{+8}	2_{-1}^{+1}
linear-U	7_{-4}^{+4}	-21_{-15}^{+13}	19_{-16}^{+16}	-6_{-8}^{+7}	1_{-1}^{+1}

Table A.4. 68% credible interval values of the parameters for the $T_{\text{int}}-T_{\text{eq}}$ distribution for the **linear- \mathcal{U}** and **log- \mathcal{U}** cases using the Gaussian function Equation (42), where $x = T_{\text{eq}}$ and T_{int} is in K.

τ	$T_{\text{int,max}}$	T_{int0}	s
log- \mathcal{U}	835^{+69}_{-58}	2270^{+202}_{-120}	709^{+154}_{-70}
linear- \mathcal{U}	786^{+85}_{-56}	2333^{+149}_{-109}	723^{+75}_{-46}

Table A.5. 2σ credible interval values of the parameters for the $P_{\text{RCB}}-T_{\text{eq}}$ distribution for the **linear- \mathcal{U}** and **log- \mathcal{U}** cases under the polynomial function Equation (41), where $x = T_{\text{eq}}/1000$ and $g_p \times 100$ in bar.

τ	a_0	a_1	a_2	a_3	a_4
log- \mathcal{U}	16^{+6}_{-13}	-29^{+26}_{-15}	19^{+12}_{-20}	-5^{+6}_{-4}	$0.59^{+0.57}_{-0.85}$
linear- \mathcal{U}	6^{+6}_{-4}	-8^{+9}_{-14}	4^{+10}_{-8}	-1^{+2}_{-4}	$0.03^{+0.48}_{-0.37}$

6.6 Comparison to Thorngren Results

While the approach presented in the publication is similar to [Thorngren & Fortney \(2018\)](#), there are few differences in the methods and results that should be addressed. Their method relies on estimating the heating efficiency distribution ϵ , while we infer the distribution of the internal luminosity. The main advantage of our approach is that the internal luminosity is a fundamental physical property compared to the heating efficiency. This thus allows us to compare our results to heating mechanisms where the source of heat is not the stellar irradiation flux. Another advantage is that we can systematically study the effect of the high internal luminosity on the interior structure of the planets. Note that we also convert L_{int} to ϵ , which allows us to compare our results to that of [Thorngren & Fortney \(2018\)](#) and most importantly to dissipative processes powered by the stellar irradiation flux.

The main evidence for ohmic dissipation is the Gaussian pattern distribution between the heating efficiency and the equilibrium temperature. While both models infer a Gaussian-like distribution, there are a number of differences between the results of [Thorngren & Fortney \(2018\)](#) and our results (see the right panel of Figure 5 in the paper). Based on our model the peak occurs at ~ 1865 K, while [Thorngren & Fortney \(2018\)](#) find the peak at ~ 1566 K. This discrepancy could be due to differences in the treatment of the EOS and the composition of the planets. In our model the heavy elements are modeled as water and mixed with H/He using the additive volume law ([Mordasini 2020](#)), while [Thorngren & Fortney \(2018\)](#) assume the composition is 50% rock and 50% ice for the heavy elements. Furthermore, for the highly irradiated planets we find that the efficiency is above 1%, whereas [Thorngren & Fortney \(2018\)](#) find very low efficiency close to 0% in this regime. The Gaussian function hints at ohmic dissipation and it is important to quantify the location of the peak. At high equilibrium temperatures magnetic drag becomes important as it slows down the winds and thus reduces the heat dissipation efficiency. Therefore, the location of the peak provides observational clues of the critical temperature beyond which magnetic drag effects become important.

We also provide evidence for advection of potential temperature and thermal tides as possible explanations, even though [Thorngren & Fortney \(2018\)](#) argued against these mechanisms. Their main argument was that these mechanisms fail to reproduce the Gaussian-like pattern between the heating efficiency and the equilibrium temperature.

We show however, that these mechanisms predict internal luminosities in agreement with our analysis, which is based on linking observed properties to interior structure models (see Figure 8 in the paper). These models though tend to overestimate the luminosities above $10^4 L_J$. We suggest that the internal luminosity is the fundamental and the main parameter leading to the inflated radii. Therefore, a more natural comparison would be to compare the internal luminosity to the suggested mechanisms rather than comparing the functional form of the heating efficiency.

Building on the $\epsilon(T_{\text{eq}})$ relation, [Thorngren et al. \(2019\)](#) studied the distribution of the T_{int} and P_{RCB} as a function of T_{eq} . Our results agree well with their results. [Thorngren et al. \(2019\)](#) report a maximum T_{int} of 700 K at $T_{\text{eq}} \sim 1800$ K, while we find a maximum T_{int} of 800 K at $T_{\text{eq}} \sim 2500$ K. This difference is mainly due to the differences in the $\epsilon(T_{\text{eq}})$ distribution. The high T_{int} in turn pushes the RCB to lower pressures. [Thorngren et al. \(2019\)](#) finds that at $T_{\text{eq}} = 1000$ K, the RCB is at 100 bar and moves up to 1 bar for $T_{\text{eq}} = 2000$ K. We estimate the RCB is at 100 bar and 4 bar for $T_{\text{eq}} = 1000$ K and 2000 K, respectively, in agreement with their results. To conclude, both models support the idea that hot Jupiters possess hot interiors that drives the RCB to lower pressures.

6.7 Disk Migration Within the Context of Planet Population Synthesis

How hot Jupiters reached their current location is another mystery challenging theorists. The two competing mechanisms are high eccentricity migration and disk migration. Under the disk migration model, hot Jupiters need to migrate to their current locations during the disk lifetime, typically few million years after their formation. At early phases though, (i) the planets still possess high internal entropy left from formation and thus have large radii and (ii) young pre-main sequence stars are more luminous, leading to high incident stellar flux. Both of these effects lead to large bloating luminosity for a fixed heating efficiency ϵ (see Equation (6.1)). Therefore, if the planet arrives too early by disk migration, the planet radius might expand very quickly, leading to an unstable phase of runaway inflation. This will eventually lead to Roche-lobe overflow ([Baraffe et al. 2004](#)) and therefore the planet will not survive. Under this scenario, disk migration

can be ruled out as a formation mechanism and this allows us to constrain the earliest arrival time for the planets to survive.

6.7.1 Coupling Bloating Model to Planet Formation and Evolution Models

We couple the bloating model discussed in Section 6.2 to models of planet formation and evolution with one additional modification

$$L_{\text{bloat}} = \epsilon F \pi R_p^2 \exp(-\tau) \quad (6.2)$$

where τ is the optical depth in the disk midplane from the star to the planet. For the heating efficiency ϵ , we use the relation established by [Thorngren & Fortney \(2018\)](#)¹. We assume the heating efficiency is constant in time. Most likely this is not the case but little is known about the change of the heating efficiency in time. Under the ohmic dissipation model, the heating efficiency depends on the magnetic field strength, wind speeds, and depth of the heating. All of which are not constrained and therefore we focus on a simple model yet with less parameters to tweak.

At early times the disk is optically thick and the planet is at large semimajor axis, therefore bloating is inefficient. At later times, the disk dissipates, the planet migrates inwards, and the heating becomes relevant. The main focus is to study the effect of extra heat on a synthetic planet population. Particularly, we want to quantify the rate of hot Jupiters to check whether they survive or not.

6.7.2 Synthetic Planet Populations

We use the Bern planet population synthesis models ([Mordasini et al. 2012b](#)), which is based on the core-accretion model. For a recent review, see [Mordasini \(2018\)](#). The planet formation and evolution models include stellar evolution and atmospheric evaporation that accounts for the stellar X-ray and extreme-ultraviolet (XUV) flux ([Jin et al. 2014](#)). The stellar mass is fixed to $1 M_{\odot}$. In the formation model one embryo per disk is included.

¹This work was done before we estimated the HEET relation presented in the paper.

Additionally, all the heavy elements are in the core and the envelope is made up of H/He. This however should not affect our results as discussed in Section 6.3.2.

6.7.3 Results

Stable and Unstable Configurations

The bloating model has two different effects on the radial evolution of the planet. Both effects are illustrated in Figure 6.6. The evolution of the planet radius (blue) and the Hill sphere radius (red) are shown for both models. At early times the bloating luminosity does not affect the radial evolution of the planet (indicated by the dashed lines), while at later times it is the main driver characterizing the evolution (indicated by the solid lines).

One consequence of the bloating model is to keep the planet at a large radius, preventing it from contracting even further. This is identical to the model presented in Section 6.2 (see also Figure 6.1). This stable configuration is shown in the upper panel of Figure 6.6. The planet has a radius of $1.37 R_J$, significantly larger than the largest radius possible without including the heating mechanism. Note that the increase in the radius at early times is due to the gas accretion and is not related to the bloating mechanism.

The second effect is that the radius increases rapidly as soon as the bloating luminosity becomes non-negligible. Since $L_{\text{bloat}} \propto R_p^2$, as the radius increases, the heating rate also increases. This process leads to runaway inflation. Consequently, as soon as the radius of the planet becomes larger than the Hill sphere radius, the planet undergoes Roche-lobe overflow, leading to the evaporation of the H/He envelope. The planet does not survive as a giant planet under this unstable configuration, but as a naked core with a final radius of $0.25 R_J$.

Rate of Hot Jupiters and the Mass-Radius Diagram

The next result to check is whether most of the hot Jupiters are destroyed or not under this model. We simulate a synthetic planet population where we include the heating model. We find that the rate of hot Jupiters is 1.56%, which is slightly higher than the rate from observations. For comparison, the rate of hot Jupiters based on a synthetic planet population without including the effect of heating is 1%. Note that it is not possible to compare the rate of hot Jupiters of the synthetic populations to each other because they

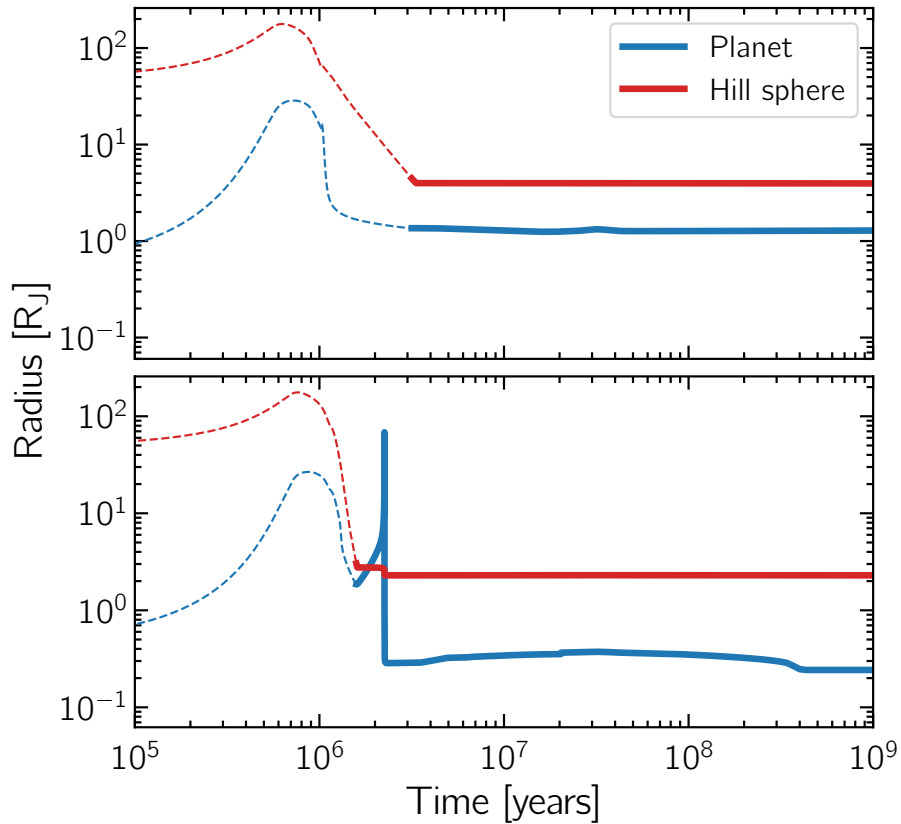


FIGURE 6.6: Effect of the extra heat dissipated into the interior before (dashed lines) and after (thick lines) the disk dissipates. This leads to a stable (upper panel) and an unstable (lower panel) configuration. In the former case, heating prevents further contraction and yields a planet with a radius $1.37 R_J$. In the latter case, the extra heat deposited in the interior drives the rapid expansion of the outer layers, which inevitably leads to Roche-lobe overflow and evaporation of the planet.

have different initial conditions. We therefore find that the hot Jupiters are not destroyed using the heating relation implemented by [Thorngren & Fortney \(2018\)](#). Rather we find that the lower mass planets are destroyed. It is not clear whether our relation will give

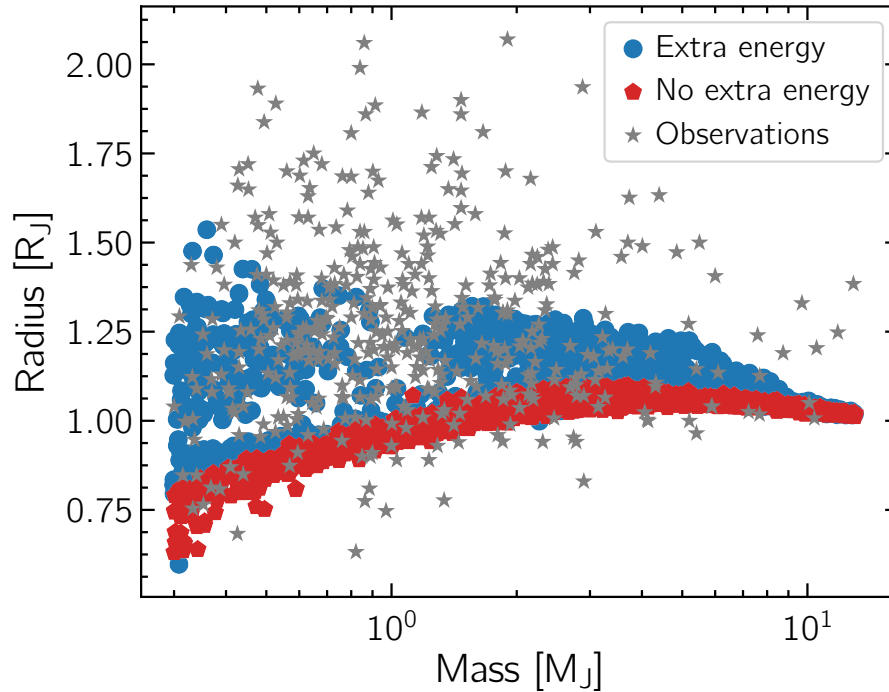


FIGURE 6.7: Comparison of the mass–radius diagram for the planet population synthesis including the bloating mechanism (blue circles) and without including it (red pentagons). The observed planets are also shown (gray stars). Larger planets are formed in comparison to not accounting for an inflation mechanism. This model however is not able to form planets with radii larger than $1.55 R_J$. The observed planets with radii smaller than the synthetic ones must have more heavy elements than predicted by the models.

significantly different results but it is worth investigating, especially that we predict a significant non-zero heating efficiency at high T_{eq} .

In Figure 6.7, we compare the mass–radius diagram under the two synthetic populations and the observed planets (gray stars). We only show planets with $M_p > 0.3 M_J$.

Coupling the formation model to an inflation mechanism is able to produce radii significantly larger than the nominal one for planets with masses less than $10 M_J$. The largest radius under this model is $1.55 R_J$. However, this model is unable to reproduce the most inflated planets detected from observations. This could be related to the setup of the simulations where we assumed the stellar mass of the host star is $1 M_\odot$. A more realistic approach would be to include this parameter as an initial condition, especially that the bloating luminosity depends on the stellar luminosity. In reality, there is also an age spread, which we do not include. The radii of some of the observed planets in Figure 6.7 are smaller than radii from the synthetic populations. The amount of heavy elements in these planets must be larger than predicted by the models, which leads to smaller radii (see also Figure 6.1).

To conclude, we find that hot Jupiters are not destroyed using the heating efficiency model developed by [Thorngren & Fortney \(2018\)](#). We cannot therefore rule out disk migration as a formation scenario. This model can form planets as large as $1.55 R_J$ but is still unable to account for the most inflated planets.

6.8 Summary

The main goal of this study is to put constraints on the radius anomaly of hot Jupiters. We show that it is still challenging to find one universal mechanism that solves the radius anomaly conundrum. We provide evidence for three mechanisms that can explain our results: ohmic dissipation ([Batygin & Stevenson 2010](#); [Batygin et al. 2011](#)), advection of potential temperature ([Tremblin et al. 2017](#)), and thermal tides ([Arras & Socrates 2010](#)). We also show that hot Jupiters have hot interiors and the RCB is located at pressures between 3 – 200 bar.

We also coupled the bloating model using the relation of [Thorngren & Fortney \(2018\)](#) to formation and evolution models. We find that disk migration is a possible formation scenario since hot Jupiters were not destroyed.

It's Louder than words this thing that we do
Louder than words - the way it unfurls
Louder Than Words – Pink Floyd

Chapter 7

Summary and Outlook

The detection of new exoplanets will continue to be an important aspect of the exoplanet field in order to further increase our understanding on planet formation and evolution. Within this context, this thesis is divided into two parts, where the first part deals with the characterization of transiting exoplanets and the second part addresses the inflated radii of hot Jupiters by linking the observed properties to theoretical models.

In the first publication (Chapter 4 and [Sarkis et al. 2018b](#)) we presented the characterization of the planetary system around the active M2.5 dwarf K2-18. The star is known to host a transiting planet K2-18 b ([Montet et al. 2015](#); [Benneke et al. 2017](#)). The location of K2-18 b in the habitable zone of the nearby host star and its equilibrium temperature, which is similar to Earth, makes it an interesting target for RV follow-up observations. We obtained 58 precise radial velocities using CARMENES, which allowed us to determine precisely the mass and mean density of the planet. We also obtained simultaneous photometric observations to better characterize stellar activity. We found that the star is indeed active and that the observed variability in the photometric and spectroscopic data is due to spots, where the active chromospheric regions are located on top of photometric spots. Fitting for stellar activity and a Keplerian signal revealed that K2-18 b is a low-mass volatile rich planet. The system was also observed with HARPS and our findings concerning the transiting planet agree well ([Cloutier et al. 2017](#)). Additionally, the HARPS RVs suggest a second non-transiting planet in the system. This signal however was marginally detected in the CARMENES data. We found that the signal is time and wavelength dependent and attributed its origins to stellar activity. Subsequent HARPS observations reveal that the signal is still present and most likely planetary in nature ([Cloutier et al. 2019](#)). The CARMENES data favor two planets only after 3 anomalous RV

measurements are omitted (Cloutier et al. 2019). This highlights the challenges in distinguishing between stellar activity and Keplerian signals.

In the second publication (Chapter 5 and Sarkis et al. 2018a) we introduced the discovery of HATS-59 b,c, the first multi-planet system within the HATSouth survey. The system is particularly interesting because the inner transiting hot Jupiter is on an eccentric orbit, unlike most hot Jupiters which tend to be on circular orbits. The outer massive planet, with a minimum mass close to the brown dwarf limit and period of ~ 4 years could have scattered HATS-59 b inwards and resulted in its eccentric orbit. The architecture of this system, namely the presence of two massive planets and the eccentric orbit of the inner planet, are valuable for theoretical studies on planet formation, migration, and evolution.

The third publication (Chapter 6 and Sarkis et al. *submitted*) consists of the theoretical work focused on constraining the radius anomaly of hot Jupiters. This has challenged astronomers for over two decades now and highlights one of the unexpected discoveries in the exoplanet field. Recently, Thorngren & Fortney (2018) provided the first evidence that ohmic dissipation can be the mechanism responsible for the large radii of close-in giant planets. With the increasing number of detected hot Jupiters, we tackled the radius inflation conundrum in a statistical approach by linking the observed properties to interior structure models. With a sample of 314 hot Jupiters, we find that high internal luminosity is needed to reproduce the observed radii. As a consequence of that, hot Jupiters possess hot interiors and the radiative–convective–boundary layer is located at low pressures between 3 – 100 bar, shallower than the previous estimates of 1000 bar that did not account for the high internal entropy. Our findings are in agreement with the recent work by Thorngren et al. (2019). With a better understanding of the interior structure of hot Jupiters, we show that the following three proposed mechanisms can all explain various aspects of the radius anomaly of hot Jupiters: ohmic dissipation, advection of potential temperature, and thermal tides. This work also highlights the importance of individual detections that lead to a large statistical sample and thus enabled to compare observations to theoretical models. While it is challenging to firmly constrain the dominant mechanism driving the inflated radii, we are one step closer in solving one of the long standing questions in the exoplanet field.

Future detections of individual systems, ranging from Earth-like to giant planets, will continue to be valuable to put constraints on planet formation and evolution models. The

current ongoing space-based surveys like *TESS* (Ricker et al. 2015) and *CHEOPS* (Broeg et al. 2013; Benz et al. 2018) and future missions such as *PLATO* (Rauer et al. 2014) in addition to ground-based surveys such as NGTS (Wheatley et al. 2018) will continue observing and discovering new transiting exoplanets. Additionally, the next generation high-resolution spectrographs mounted on large telescopes such as ESPRESSO (Pepe et al. 2010) at the Very Large Telescope and HIRES at the E-ELT (Marconi et al. 2016) will provide extremely precise radial velocity measurements enabling thus the characterization down to Earth-like planets. These contributions will lead to a more complete picture of exoplanets and will help address key questions related to planet formation and evolution.

When you open your eyes
When you gaze at the sky
When you look to the stars
As they shut down the night
You know this story ain't over

When you open your eyes
When you gaze at the sky
When you look to the stars
As they shut down the night
You feel this story ain't over
The Story Ain't Over – Avantasia

Bibliography

- Alonso, R., Brown, T. M., Torres, G., et al. 2004, *ApJ*, 613, L153 [1.1.3](#)
- Anderson, K. R. & Lai, D. 2017, *MNRAS*, 472, 3692 [3.1.3](#)
- Anglada-Escudé, G. & Butler, R. P. 2012, *ApJS*, 200, 15 [1.1.4](#)
- Arras, P. & Bildsten, L. 2006, *ApJ*, 650, 394 [3.2.3](#), [3.4](#)
- Arras, P. & Socrates, A. 2010, *ApJ*, 714, 1 [6.8](#)
- Baglin, A., Auvergne, M., Boisnard, L., et al. 2006, in 36th COSPAR Scientific Assembly, Vol. 36, 3749 [1.1.3](#)
- Bakos, G., Noyes, R. W., Kovács, G., et al. 2004, *PASP*, 116, 266 [1.1.3](#)
- Bakos, G. Á. 2018, The HATNet and HATSouth Exoplanet Surveys, 111 [3.1.3](#)
- Bakos, G. Á., Bayliss, D., Bento, J., et al. 2018, arXiv e-prints, arXiv:1812.09406 [2.2.2](#)
- Bakos, G. Á., Csubry, Z., Penev, K., et al. 2013, *PASP*, 125, 154 [1.1.3](#), [2.2](#)
- Bakos, G. Á., Noyes, R. W., Kovács, G., et al. 2007, *ApJ*, 656, 552 [1.1.3](#)
- Bakos, G. Á., Penev, K., Bayliss, D., et al. 2015, *ApJ*, 813, 111 [2.2.2](#)
- Baraffe, I., Chabrier, G., Barman, T. S., Allard, F., & Hauschildt, P. H. 2003, *A&A*, 402, 701 [3.2.3](#)
- Baraffe, I., Chabrier, G., Fortney, J., & Sotin, C. 2014, in *Protostars and Planets VI*, ed. H. Beuther, R. S. Klessen, C. P. Dullemond, & T. Henning, 763 [3.5](#)

- Baraffe, I., Selsis, F., Chabrier, G., et al. 2004, *A&A*, 419, L13 [6.7](#)
- Barman, T. S., Hauschildt, P. H., & Allard, F. 2001, *ApJ*, 556, 885 [3.2.3](#)
- Batalha, N. M., Borucki, W. J., Bryson, S. T., et al. 2011, *ApJ*, 729, 27 [1.1.3](#)
- Batista, V. 2018, *Finding Planets via Gravitational Microlensing*, 120 [1.1.2](#)
- Batygin, K. & Stevenson, D. J. 2010, *ApJ*, 714, L238 [3.5](#), [6.8](#)
- Batygin, K., Stevenson, D. J., & Bodenheimer, P. H. 2011, *ApJ*, 738, 1 [6.8](#)
- Bauer, F. F., Zechmeister, M., & Reiners, A. 2015, *A&A*, 581, A117 [2.1.1](#)
- Bayliss, D., Gillen, E., Eigmüller, P., et al. 2018, *MNRAS*, 475, 4467 [1.1.3](#)
- Bayliss, D., Hartman, J. D., Bakos, G. Á., et al. 2015, *AJ*, 150, 49 [2.2.2](#)
- Beaulieu, J. P., Bennett, D. P., Fouqué, P., et al. 2006, *Nature*, 439, 437 [1.1.2](#)
- Benneke, B., Werner, M., Petigura, E., et al. 2017, *ApJ*, 834, 187 [4](#), [4.1](#), [7](#)
- Benneke, B., Wong, I., Piaulet, C., et al. 2019, *ApJ*, 887, L14 [4.1](#)
- Benz, W., Ehrenreich, D., & Isaak, K. 2018, *CHEOPS: CHaracterizing ExOPlanets Satellite*, 84 [1.1.3](#), [7](#)
- Bhatti, W., Bakos, G. Á., Hartman, J. D., et al. 2016, arXiv e-prints, arXiv:1607.00322 [1.1.3](#)
- Bond, I. A., Udalski, A., Jaroszyński, M., et al. 2004, *ApJ*, 606, L155 [1.1.2](#)
- Bonomo, A. S., Desidera, S., Benatti, S., et al. 2017, *A&A*, 602, A107 [3.1.3](#)
- Borucki, W. J., Koch, D., Basri, G., et al. 2010, *Science*, 327, 977 [1.1.3](#), [3.1.3](#)
- Brahm, R., Jordán, A., Bakos, G. Á., et al. 2016, *AJ*, 151, 89 [2.2.2](#), [3.1](#)
- Brahm, R., Jordán, A., & Espinoza, N. 2017, *PASP*, 129, 034002 [1.1.4](#), [2.2.1](#)

- Broeg, C., Fortier, A., Ehrenreich, D., et al. 2013, in European Physical Journal Web of Conferences, Vol. 47, European Physical Journal Web of Conferences, 03005 [1.1.3](#), [7](#)
- Bryan, M. L., Knutson, H. A., Howard, A. W., et al. 2016, ApJ, 821, 89 [3.1.3](#), [5](#)
- Burrows, A., Budaj, J., & Hubeny, I. 2008, ApJ, 678, 1436 [3.2.3](#)
- Burrows, A., Guillot, T., Hubbard, W. B., et al. 2000, ApJ, 534, L97 [3.2.3](#)
- Burrows, A., Hubeny, I., Budaj, J., & Hubbard, W. B. 2007, ApJ, 661, 502 [3.5](#)
- Burrows, A. & Liebert, J. 1993, Reviews of Modern Physics, 65, 301 [3.3](#)
- Burrows, A., Marley, M., Hubbard, W. B., et al. 1997, ApJ, 491, 856 [3.2.3](#)
- Burton, J. R., Watson, C. A., Rodríguez-Gil, P., et al. 2015, MNRAS, 446, 1071 [3.2.2](#)
- Butler, R. P., Marcy, G. W., Williams, E., et al. 1996, PASP, 108, 500 [1.1.4](#)
- Carleo, I., Benatti, S., Lanza, A. F., et al. 2018, A&A, 613, A50 [1.1.4](#)
- Chabrier, G. & Baraffe, I. 1997, A&A, 327, 1039 [6.4.2](#)
- Chabrier, G., Baraffe, I., Allard, F., & Hauschildt, P. 2000, ApJ, 542, 464 [3.2.3](#)
- Charbonneau, D., Brown, T. M., Latham, D. W., & Mayor, M. 2000, ApJ, 529, L45 [1.1.3](#)
- Charbonneau, D., Brown, T. M., Noyes, R. W., & Gilliland, R. L. 2002, ApJ, 568, 377 [3.2.2](#)
- Chauvin, G., Lagrange, A. M., Dumas, C., et al. 2004, A&A, 425, L29 [1.1.1](#)
- Chen, J. & Kipping, D. 2017, ApJ, 834, 17 [3.3](#)
- Ciceri, S., Mancini, L., Henning, T., et al. 2016, PASP, 128, 074401 [2.2.2](#)
- Claudi, R., Benatti, S., Carleo, I., et al. 2017, European Physical Journal Plus, 132, 364 [1.1.4](#)
- Cloutier, R., Astudillo-Defru, N., Doyon, R., et al. 2017, A&A, 608, A35 [4](#), [4.1](#), [4.2.1](#), [7](#)

- Cloutier, R., Astudillo-Defru, N., Doyon, R., et al. 2019, *A&A*, 621, A49 ([document](#)), [4.2.1](#), [4.2.1](#), [4.2.2](#), [7](#)
- Collier Cameron, A., Bouchy, F., Hébrard, G., et al. 2007, *MNRAS*, 375, 951 [1.1.3](#), [1.1](#), [1.1.4](#)
- Conod, U., Blind, N., Wildi, F., & Pepe, F. 2016, Society of Photo-Optical Instrumentation Engineers (SPIE) Conference Series, Vol. 9909, Adaptive optics for high resolution spectroscopy: a direct application with the future NIRPS spectrograph, 990941 [1.1.4](#)
- Cosentino, R., Lovis, C., Pepe, F., et al. 2012, Society of Photo-Optical Instrumentation Engineers (SPIE) Conference Series, Vol. 8446, Harps-N: the new planet hunter at TNG, 84461V [1.1.4](#)
- Crockett, C. J., Mahmud, N. I., Prato, L., et al. 2012, *ApJ*, 761, 164 [1.1.4](#)
- Dawson, R. I. & Johnson, J. A. 2018, *ARA&A*, 56, 175 [3.1](#)
- Dawson, R. I. & Murray-Clay, R. A. 2013, *ApJ*, 767, L24 [3.1.3](#)
- Deeg, H. J. & Alonso, R. 2018, Transit Photometry as an Exoplanet Discovery Method, 117 [1.1.3](#)
- Deleuil, M., Aigrain, S., Moutou, C., et al. 2018, *A&A*, 619, A97 [3.1.1](#)
- Delisle, J. B., Ségransan, D., Dumusque, X., et al. 2018, *A&A*, 614, A133 [1.1](#), [1.1.4](#)
- Deming, D., Wilkins, A., McCullough, P., et al. 2013, *ApJ*, 774, 95 [3.2.2](#)
- Demory, B.-O. & Seager, S. 2011, *ApJS*, 197, 12 [3.5](#)
- Dumusque, X. 2018, *A&A*, 620, A47 [1.1.4](#)
- Dunham, E. W. 2018, Discovery of the First Transiting Planets, 170 [1.1.3](#)
- Espinoza, N., Brahm, R., Henning, T., et al. 2020, *MNRAS*, 491, 2982 [2.2.1](#)
- Espinoza, N., Hartman, J. D., Bakos, G. Á., et al. 2019, *AJ*, 158, 63 [2.2.2](#)
- Evans, T. M., Sing, D. K., Wakeford, H. R., et al. 2016, *ApJ*, 822, L4 [3.2.2](#)

- Fabrycky, D. & Tremaine, S. 2007, *ApJ*, 669, 1298 [3.1.3](#), [5](#), [6](#)
- Feng, F., Tuomi, M., Jones, H. R. A., et al. 2017, *AJ*, 154, 135 [1.1.4](#)
- Fischer, D. A., Anglada-Escude, G., Arriagada, P., et al. 2016, *PASP*, 128, 066001 [1.1.4](#)
- Fortney, J. J., Lodders, K., Marley, M. S., & Freedman, R. S. 2008, *ApJ*, 678, 1419 [3.2.3](#), [3.2.3](#), [6.4.1](#)
- Fortney, J. J., Marley, M. S., & Barnes, J. W. 2007, *ApJ*, 659, 1661 [3.2.3](#), [3.2](#), [3.3](#), [3.4](#), [3.6](#), [6.5](#)
- Giles, H. A. C., Osborn, H. P., Blanco-Cuaresma, S., et al. 2018, *A&A*, 615, L13 [1.1.3](#)
- Gould, A., Udalski, A., An, D., et al. 2006, *ApJ*, 644, L37 [1.1.2](#)
- Guillot, T. 2010, *A&A*, 520, A27 [3.2.3](#), [3.2.3](#), [6.4.1](#)
- Guillot, T., Burrows, A., Hubbard, W. B., Lunine, J. I., & Saumon, D. 1996, *ApJ*, 459, L35 [3.2.3](#)
- Guillot, T. & Gautier, D. 2014, arXiv e-prints, arXiv:1405.3752 [3.2.4](#)
- Guillot, T. & Showman, A. P. 2002, *A&A*, 385, 156 [3.2.3](#), [3.5](#)
- Hadden, S. & Lithwick, Y. 2014, *ApJ*, 787, 80 [3.3](#)
- Haswell, C. A. 2010, *Transiting Exoplanets* [1.1.3](#), [1.1.3](#), [1.1.3](#)
- Hatzes, A. P. 2016, *A&A*, 585, A144 [1.1.4](#)
- Henning, T., Mancini, L., Sarkis, P., et al. 2018, *AJ*, 155, 79 [2.2.2](#)
- Henry, G. W., Marcy, G. W., Butler, R. P., & Vogt, S. S. 2000, *ApJ*, 529, L41 [1.1.3](#)
- Hicks, T. R., May, B. H., & Reay, N. K. 1972, *Nature*, 240, 401 [1](#)
- Hicks, T. R., May, B. H., & Reay, N. K. 1974, *MNRAS*, 166, 439 [1](#)
- Holman, M. J., Fabrycky, D. C., Ragozzine, D., et al. 2010, *Science*, 330, 51 [1.1.3](#)

- Jin, S., Mordasini, C., Parmentier, V., et al. 2014, *ApJ*, 795, 65 [3.2.3](#), [3.2.3](#), [6.4.1](#), [6.3](#), [6.7.2](#)
- Jones, H. R. A., Butler, R. P., Tinney, C. G., et al. 2003, *MNRAS*, 341, 948 [3.1](#)
- Kaufer, A. & Pasquini, L. 1998, Society of Photo-Optical Instrumentation Engineers (SPIE) Conference Series, Vol. 3355, FEROS: the new fiber-linked echelle spectrograph for the ESO 1.52-m telescope, ed. S. D’Odorico, 844–854 [1.1.4](#), [2.2.1](#)
- Keppler, M., Benisty, M., Müller, A., et al. 2018, *A&A*, 617, A44 [1.1.1](#)
- Kipping, D. M. 2013, *MNRAS*, 434, L51 [3.1.3](#)
- Knutson, H. A., Fulton, B. J., Montet, B. T., et al. 2014, *ApJ*, 785, 126 [3.1.3](#), [5](#)
- Komacek, T. D. & Youdin, A. N. 2017, *ApJ*, 844, 94 [3.6](#)
- Konacki, M., Torres, G., Jha, S., & Sasselov, D. D. 2003, *Nature*, 421, 507 [1.1.3](#)
- Kostov, V. B., Schlieder, J. E., Barclay, T., et al. 2019, *AJ*, 158, 32 [1.1.3](#)
- Léger, A., Rouan, D., Schneider, J., et al. 2009, *A&A*, 506, 287 [1.1.3](#)
- Lin, D. N. C., Bodenheimer, P., & Richardson, D. C. 1996, *Nature*, 380, 606 [5](#), [6](#)
- Linder, E. F., Mordasini, C., Mollière, P., et al. 2019, *A&A*, 623, A85 [3.2.3](#), [6.4.2](#)
- Lissauer, J. J., Fabrycky, D. C., Ford, E. B., et al. 2011a, *Nature*, 470, 53 [1.1.3](#)
- Lissauer, J. J., Ragozzine, D., Fabrycky, D. C., et al. 2011b, *ApJS*, 197, 8 [3.3](#)
- Mahmud, N. I., Crockett, C. J., Johns-Krull, C. M., et al. 2011, *ApJ*, 736, 123 [1.1.4](#)
- Mancini, L., Hartman, J. D., Penev, K., et al. 2015, *A&A*, 580, A63 [2.2.2](#)
- Marconi, A., Di Marcantonio, P., D’Odorico, V., et al. 2016, Society of Photo-Optical Instrumentation Engineers (SPIE) Conference Series, Vol. 9908, EELT-HIRES the high-resolution spectrograph for the E-ELT, 990823 [7](#)
- Marleau, G.-D., Coleman, G. A. L., Leleu, A., & Mordasini, C. 2019, *A&A*, 624, A20 [3.2.3](#)

- Marleau, G. D. & Cumming, A. 2014, MNRAS, 437, 1378 [3.4](#)
- Marois, C., Macintosh, B., Barman, T., et al. 2008, Science, 322, 1348 [1.1.1](#)
- May, B. H. 2007, A Survey of Radial Velocities in the Zodiacal Dust Cloud [1](#)
- Mayor, M., Marmier, M., Lovis, C., et al. 2011, arXiv e-prints, arXiv:1109.2497 [3.1.1](#), [3.1.2](#)
- Mayor, M., Pepe, F., Queloz, D., et al. 2003, The Messenger, 114, 20 [1.1.4](#)
- Mayor, M. & Queloz, D. 1995, Nature, 378, 355 [1.1.4](#), [3.2.3](#)
- Mazeh, T., Naef, D., Torres, G., et al. 2000, ApJ, 532, L55 [1.1.3](#)
- Mollière, P. & Mordasini, C. 2012, A&A, 547, A105 [3.2.1](#)
- Mollière, P., van Boekel, R., Bouwman, J., et al. 2017, A&A, 600, A10 [3.2.3](#), [6.4.1](#)
- Mollière, P., van Boekel, R., Dullemond, C., Henning, T., & Mordasini, C. 2015, ApJ, 813, 47 [3.2.3](#), [6.4.1](#)
- Montet, B. T., Morton, T. D., Foreman-Mackey, D., et al. 2015, ApJ, 809, 25 [2.1.2](#), [4](#), [7](#)
- Morales, J. C., Mustill, A. J., Ribas, I., et al. 2019, Science, 365, 1441 [2.1.2](#)
- Mordasini, C. 2018, Planetary Population Synthesis, 143 [3.3](#), [6.7.2](#)
- Mordasini, C. 2020, arXiv e-prints, arXiv:2002.02455 [3.2.2](#), [6.6](#)
- Mordasini, C., Alibert, Y., Georgy, C., et al. 2012a, A&A, 547, A112 [3.3](#), [3.2](#)
- Mordasini, C., Alibert, Y., Klahr, H., & Henning, T. 2012b, A&A, 547, A111 [3.2](#), [3.2.1](#), [6.7.2](#)
- Mortier, A., Faria, J. P., Correia, C. M., Santerne, A., & Santos, N. C. 2015, A&A, 573, A101 [4.2.1](#)
- Naoz, S., Farr, W. M., & Rasio, F. A. 2012, ApJ, 754, L36 [3.1.3](#), [5](#), [6](#)
- Ngo, H., Knutson, H. A., Hinkley, S., et al. 2016, ApJ, 827, 8 [3.1.3](#)

- Ning, B., Wolfgang, A., & Ghosh, S. 2018, *ApJ*, 869, 5 [3.3](#)
- O'Donovan, F. T., Charbonneau, D., Mand ushev, G., et al. 2006, *ApJ*, 651, L61 [1.1.3](#)
- Penev, K., Bakos, G. Á., Bayliss, D., et al. 2013, *AJ*, 145, 5 [1.1.3](#)
- Pepe, F., Lovis, C., Ségransan, D., et al. 2011, *A&A*, 534, A58 [1.1.4](#)
- Pepe, F., Mayor, M., Delabre, B., et al. 2000, Society of Photo-Optical Instrumentation Engineers (SPIE) Conference Series, Vol. 4008, HARPS: a new high-resolution spectrograph for the search of extrasolar planets, ed. M. Iye & A. F. Moorwood, 582–592 [1.1.4](#), [1.1.4](#), [4](#)
- Pepe, F. A., Cristiani, S., Rebolo Lopez, R., et al. 2010, Society of Photo-Optical Instrumentation Engineers (SPIE) Conference Series, Vol. 7735, ESPRESSO: the Echelle spectrograph for rocky exoplanets and stable spectroscopic observations, 77350F [1.1.4](#), [7](#)
- Perryman, M. 2011, *The Exoplanet Handbook* [1.1.3](#), [1.1.3](#)
- Pollacco, D. L., Skillen, I., Collier Cameron, A., et al. 2006, *PASP*, 118, 1407 [1.1.3](#), [3.1.3](#)
- Prato, L., Huerta, M., Johns-Krull, C. M., et al. 2008, *ApJ*, 687, L103 [1.1.4](#)
- Pueyo, L. 2018, *Direct Imaging as a Detection Technique for Exoplanets*, 10 [1.1.1](#)
- Queloz, D., Mayor, M., Weber, L., et al. 2000, *A&A*, 354, 99 [1.1.4](#)
- Quirrenbach, A., Amado, P. J., Caballero, J. A., et al. 2014, Society of Photo-Optical Instrumentation Engineers (SPIE) Conference Series, Vol. 9147, CARMENES instrument overview, 91471F [1.1.4](#), [2.1](#), [2.1.1](#), [2.1.2](#)
- Quirrenbach, A., Amado, P. J., Caballero, J. A., et al. 2016, Society of Photo-Optical Instrumentation Engineers (SPIE) Conference Series, Vol. 9908, CARMENES: an overview six months after first light, 990812 [2.1.1](#)
- Rabus, M., Jordán, A., Hartman, J. D., et al. 2016, *AJ*, 152, 88 [2.2.2](#)
- Rasio, F. A. & Ford, E. B. 1996, *Science*, 274, 954 [3.1.3](#), [6](#)

- Rauer, H., Catala, C., Aerts, C., et al. 2014, *Experimental Astronomy*, 38, 249 [7](#)
- Reiners, A., Bean, J. L., Huber, K. F., et al. 2010, *ApJ*, 710, 432 [1.1.4](#)
- Reiners, A., Ribas, I., Zechmeister, M., et al. 2018, *A&A*, 609, L5 [2.1.2](#)
- Ribas, I., Tuomi, M., Reiners, A., et al. 2018, *Nature*, 563, 365 [2.1.2](#)
- Ricker, G. R., Winn, J. N., Vanderspek, R., et al. 2015, *Journal of Astronomical Telescopes, Instruments, and Systems*, 1, 014003 [1.1.3](#), [7](#)
- Rogers, L. A. 2015, *ApJ*, 801, 41 [3.3](#)
- Santerne, A., Moutou, C., Tsantaki, M., et al. 2016, *A&A*, 587, A64 [3.1](#), [3.1.1](#), [3.1.2](#)
- Sarkis, P., Henning, T., Hartman, J. D., et al. 2018a, *AJ*, 156, 216 [5](#), [7](#)
- Sarkis, P., Henning, T., Kürster, M., et al. 2018b, *AJ*, 155, 257 [4.1](#), [7](#)
- Saumon, D., Chabrier, G., & van Horn, H. M. 1995, *The Astrophysical Journal Supplement Series*, 99, 713 [3.2.2](#)
- Sedaghati, E., Boffin, H. M. J., Jeřabková, T., et al. 2016, *A&A*, 596, A47 [3.2.2](#)
- Sestovic, M., Demory, B.-O., & Queloz, D. 2018, *Astronomy and Astrophysics*, 616, A76 [3.5](#)
- Showman, A. P., Lewis, N. K., & Fortney, J. J. 2015, *ApJ*, 801, 95 [3.4](#)
- Snellen, I. A. G., de Kok, R. J., de Mooij, E. J. W., & Albrecht, S. 2010, *Nature*, 465, 1049 [3.4](#)
- Southworth, J. 2011, *MNRAS*, 417, 2166 [3.3](#)
- Southworth, J., Wheatley, P. J., & Sams, G. 2007, *MNRAS*, 379, L11 [1.1.3](#)
- Sozzetti, A., Torres, G., Charbonneau, D., et al. 2007, *ApJ*, 664, 1190 [1.1.3](#)
- Spergel, D., Gehrels, N., Baltay, C., et al. 2015, arXiv e-prints, arXiv:1503.03757 [1.1.2](#)

- Spiegel, D. S. & Burrows, A. 2013, *ApJ*, 772, 76 [3.2.3](#)
- Stelzer, B., Damasso, M., Scholz, A., & Matt, S. P. 2016, *MNRAS*, 463, 1844 [4.1](#)
- Stevenson, K. B., Bean, J. L., Seifahrt, A., et al. 2016, *ApJ*, 817, 141 [3.2.2](#)
- Stock, S., Kemmer, J., Reffert, S., et al. 2020, arXiv e-prints, arXiv:2002.01772 [2.1.2](#)
- Thorngren, D., Gao, P., & Fortney, J. J. 2019, *ApJ*, 884, L6 [3.6](#), [6.1](#), [6.6](#), [7](#)
- Thorngren, D. P. & Fortney, J. J. 2018, *The Astronomical Journal*, 155, 214 [3.5](#), [6.1](#), [6.6](#), [6.7.1](#), [6.7.3](#), [6.8](#), [7](#)
- Thorngren, D. P., Fortney, J. J., Murray-Clay, R. A., & Lopez, E. D. 2016, *The Astrophysical Journal*, 831, 64 [3.2.3](#), [6.3.2](#)
- Tinney, C. G., Butler, R. P., Marcy, G. W., et al. 2001, *ApJ*, 551, 507 [1.1.4](#)
- Tremblin, P., Chabrier, G., Mayne, N. J., et al. 2017, *ApJ*, 841, 30 [3.5](#), [6.8](#)
- Trifonov, T., Kürster, M., Zechmeister, M., et al. 2018, *A&A*, 609, A117 [2.1.1](#)
- Trifonov, T., Reffert, S., Zechmeister, M., Reiners, A., & Quirrenbach, A. 2015, *A&A*, 582, A54 [1.1.4](#)
- Tsiaras, A., Waldmann, I. P., Tinetti, G., Tennyson, J., & Yurchenko, S. N. 2019, *Nature Astronomy*, 3, 1086 [4.1](#)
- Udry, S., Dumusque, X., Lovis, C., et al. 2019, *A&A*, 622, A37 [1.1.4](#)
- Udry, S., Mayor, M., & Santos, N. C. 2003, *A&A*, 407, 369 [3.1](#)
- Vogt, S. S., Allen, S. L., Bigelow, B. C., et al. 1994, *Society of Photo-Optical Instrumentation Engineers (SPIE) Conference Series*, Vol. 2198, *HIRES: the high-resolution echelle spectrometer on the Keck 10-m Telescope*, ed. D. L. Crawford & E. R. Craine, 362 [1.1.4](#)
- Weiss, L. M. & Marcy, G. W. 2014, *ApJ*, 783, L6 [3.3](#)
- Wheatley, P. J., West, R. G., Goad, M. R., et al. 2018, *MNRAS*, 475, 4476 [1.1.3](#), [7](#)

- Wilson, P. A., Sing, D. K., Nikolov, N., et al. 2015, MNRAS, 450, 192 [3.2.2](#)
- Winn, J. N. 2010, arXiv e-prints, arXiv:1001.2010 [1.1.3](#), [1.1.3](#), [1.1.3](#), [1.1.3](#)
- Wolfgang, A., Rogers, L. A., & Ford, E. B. 2016, ApJ, 825, 19 [3.3](#)
- Wright, J. T. 2018, Radial Velocities as an Exoplanet Discovery Method, 4 [1.1.4](#)
- Wright, J. T., Marcy, G. W., Howard, A. W., et al. 2012, ApJ, 753, 160 [3.1.1](#)
- Wytttenbach, A., Ehrenreich, D., Lovis, C., Udry, S., & Pepe, F. 2015, A&A, 577, A62 [3.2.2](#)
- Zechmeister, M., Dreizler, S., Ribas, I., et al. 2019, A&A, 627, A49 [2.1.2](#)
- Zechmeister, M., Reiners, A., Amado, P. J., et al. 2018, A&A, 609, A12 [1.1.4](#)
- Zhou, G., Bakos, G. Á., Bayliss, D., et al. 2019, AJ, 157, 31 [2.2.2](#)
- Zhou, G., Bakos, G. Á., Hartman, J. D., et al. 2017, AJ, 153, 211 [3.1.3](#)

Declaration of consent

on the basis of Article 30 of the RSL Phil.-nat. 18

Name/First Name:

Matriculation Number:

Study program:

Bachelor Master Dissertation

Title of the thesis:

Supervisor:

I declare herewith that this thesis is my own work and that I have not used any sources other than those stated. I have indicated the adoption of quotations as well as thoughts taken from other authors as such in the thesis. I am aware that the Senate pursuant to Article 36 paragraph 1 litera r of the University Act of 5 September, 1996 is authorized to revoke the title awarded on the basis of this thesis.

For the purposes of evaluation and verification of compliance with the declaration of originality and the regulations governing plagiarism, I hereby grant the University of Bern the right to process my personal data and to perform the acts of use this requires, in particular, to reproduce the written thesis and to store it permanently in a database, and to use said database, or to make said database available, to enable comparison with future theses submitted by others.

Place/Date

Signature

Curriculum Vitae – Paula Sarkis

Education

- 2016 - 2020** **PhD in Physics**
Universität Bern, Switzerland and Max-Planck-Institut für Astronomie, Germany
- 2012 - 2015** **Master of Science in Astrophysics**
Joint program at Notre Dame University and Université Saint Joseph, Lebanon
- 2008 - 2012** **Bachelor of science in Statistics**
Lebanese University, Lebanon

List of Publications

- Sarkis et al. (2018b)** – The CARMENES Search For Exoplanets Around M Dwarfs: A Low-Mass Planet In The Temperate Zone Of The Nearby K2-18, AJ, 2018, 155
- Sarkis et al. (2018a)** – HATS-59b,c: A Transiting Hot Jupiter And A Cold Massive Giant Around a Sun-like Star, AJ, 2018, 156
- Sarkis et al. (submitted)** – Evidence of Three Mechanisms Explaining the Radius Anomaly of Hot Jupiters

Oral Presentations

Conferences

- 2019** – From Protoplanetary Discs to Planetary Systems, Ringberg, Germany
Title: **The Radius Anomaly of Hot Jupiters: Linking Observations and Theory**
- 2018** – Observing the Sun as a Star, Göttingen, Germany
Title: **K2-18: Cool Planet or Cool Spots?**
- 2018** – Exoplanets II, Cambridge, UK
Title: **The Radius Anomaly of Hot Jupiters: Linking Observations and Theory**
- 2017** – Planet Formation and Evolution, Jena, Germany
Title: **A Low-Mass Planet in the Habitable Zone of the Nearby M-dwarf K2-18**
- 2017** – 7th CARMENES scientific meeting, Göttingen, Germany
Title: **K2-18 as seen by CARMENES**

Seminars

- 2018** – ESO Thirty Minute Talks, Santiago, Chile
Title: **K2-18: Cool Planet or Cool Spots?**
- 2018** – Seminar at Pontificia Universidad Católica de Chile, Santiago, Chile
Title: **The Radius Anomaly of Hot Jupiters: Linking Observations and Theory**

2018 – Seminar at University Observatory Munich, Munich, Germany
Title: **K2-18: Cool Planet or Cool Spots?**

Schools

2017 – Nordita Winter School: Physics of Planets, Stockholm, Sweden

2016 – Astrostatistics and data mining, IMPRS Summer School, Heidelberg, Germany

2016 – Sagan Exoplanet Summer Workshop: Is There a Planet in My Data? Statistical Approaches to Finding and Characterizing Planets in Astronomical Data, Pasadena, USA

Observing Experience

La Silla Observatory, Chile – 120 nights
observing with GROND, WFI, and FEROS at the 2.2m telescope

Calar Alto, Spain – 3 nights
remote observations with the 1.23m telescope

Observational time awarded

More than 1000 hours at the MPIA 2.2m telescope at La Silla awarded for RV follow-up observations of HATSouth and TESS candidates with FEROS.